

MEASUREMENT, MODELING AND SIMULATION
OF GROUND-LEVEL TROPICAL CYCLONE WINDS

By

FORREST JAMES MASTERS

A DISSERTATION PRESENTED TO THE GRADUATE SCHOOL
OF THE UNIVERSITY OF FLORIDA IN PARTIAL FULFILLMENT
OF THE REQUIREMENTS FOR THE DEGREE OF
DOCTOR OF PHILOSOPHY

UNIVERSITY OF FLORIDA

2004

Copyright 2004

by

Forrest James Masters

ACKNOWLEDGMENTS

Kurtis Gurley, Luis Aponte, Gary Consolazio, Jennifer Jacobs, Perry Green, Lou Cattafesta, Tim Reinhold, Scott Robinette, Jon Lamb, Cos Gardener, Greg Kopp, Mark Powell, Eric Ho and Peter Vickery deeply deserve my gratitude. Only with their gracious support did this document make its way into your hands.

TABLE OF CONTENTS

	<u>Page</u>
ACKNOWLEDGMENTS	iii
LIST OF TABLES	vii
LIST OF FIGURES	viii
ABSTRACT	xiii
CHAPTER	
1 INTRODUCTION	1
The Hurricane Wind to Damage Chain	1
Research Underway	2
Florida Coastal Monitoring Program.....	3
Hurricane Loss Reduction Project.....	4
Scope of Research.....	5
2 HURRICANE DAMAGE MITIGATION RESEARCH.....	6
Sources of Wind Speed Data	6
Use of Permanent Instrumented Towers	9
Use of Portable Instrumented Towers	10
Current Wind Load Design Provisions and Standards	18
American Society of Civil Engineer’s Minimum Design Loads for Buildings and Other Structures (ASCE 7-02)	18
Applicability of the Current Standard	20
Reliability-Based Database-Assisted Design	22
Summary	25
3 ANALYSIS AND SIMULATION TECHNIQUES FOR WIND	27
Characterization of Ground-Level Hurricane Winds	27
Mean Velocity Profile	28
Turbulence Characteristics	32
Estimation of Roughness.....	37
Correlation and Spectral Relations.....	39
Stochastic Simulation Methods	42
Spectral Representation	43

Random Variable Transformation.....	44
Existing Simulation Techniques.....	46
Spectral Correction.....	53
Application of Simulation for the NIST Project: Interpolation of Existing Time Histories.....	58
Summary.....	58
4 FULL-SCALE MEASUREMENT OF TROPICAL CYLONE WINDS.....	60
Deployment History, Organization and Logistics.....	60
Irene (1999).....	61
Gabrielle (2001).....	62
Isidore (2002).....	62
Lili (2002).....	63
Isabel (2003).....	65
Satellite Tower System.....	68
Real-Time Data Acquisition.....	71
Internet Upload Capability.....	73
Continuous Data Acquisition.....	74
Automated Processing of Data.....	74
Improved Graphical Interface.....	75
Improved Flexibility.....	77
Outcomes of Hurricane Isabel.....	77
Impact on Meteorology.....	77
Impact on Emergency Management.....	80
Summary.....	81
5 ANALYSES OF TROPICAL CYCLONE WIND DATA.....	86
Experimental Assumptions.....	87
Concerning the Hurricane Boundary Layer.....	87
Concerning Experimental Rigor.....	88
Concerning the Homogeneity and Flatness of Upwind Terrain.....	88
Data Reduction.....	91
Data Analyses.....	92
Turbulence Intensities.....	93
Comparison to Known Gust Factor Curves.....	95
Formulation of Gust Factor Curves based on a 10-Minute Wind Speed for Varying Gust Durations and Roughness Lengths.....	104
Integral Length Scales.....	109
Spectral Models.....	111
Summary.....	113
6 MULTIVARIATE STOCHASTIC SIMULATION OF WIND PRESSURE OVER LOW-RISE STRUCTURES.....	115
Methodology.....	117

Overview	117
Wind Tunnel Data Sets.....	118
Cases Studied.....	119
Interpolation Overview.....	120
Interpolation of the Probability Targets	120
Validation of CDF Interpolation Concept	121
Interpolation of the Spectral Targets	124
Validation and Limitations of the Simulation Algorithm.....	126
Accuracy of the Simulation Algorithm	127
Results.....	129
Comparison of Peak Aggregate Uplift	129
Summary.....	136
7 CONCLUSIONS AND RECOMMENDATIONS FOR FUTURE RESEARCH....	137
Contributions to Full-Scale Measurement Research	137
Recommendations for Future Full-Scale Measurement Research.....	139
Wireless Data Acquisition.....	139
Roughness Estimation	140
Dissemination of Real-Time Data	142
Contributions to Stochastic Simulation Research.....	144
Recommendations for Future Stochastic Simulation Research.....	145
APPENDIX	
A FCMP DATABASE	147
B AERIAL IMAGERY OF TOWER SITES	158
C RESULTS FROM PRESSURE TAP SIMULATION OF UWO WIND TUNNEL DATA	169
LIST OF REFERENCES.....	182
BIOGRAPHICAL SKETCH	189

LIST OF TABLES

<u>Table</u>	<u>page</u>
3-1. Calculated Durst gust factors.....	35
3-2. Longitudinal turbulence PSD models.....	43
5-1. Summary of data reduction results	92
5-3. Turbulence intensity comparison.....	95
5-4. Standard deviate, departure standard deviations, and gust factors	100
5-5. Coefficients for the proposed gust factor curve.....	107
5-6. Longitudinal integral length scales (m) for 10-minute records	110
6-1. Simulation test matrix.....	120

LIST OF FIGURES

<u>Figure</u>	<u>page</u>
2-1. Weather stations (courtesy of NOAA)	7
2-2. Texas Tech WEMITE.....	12
2-3. The FCMP instrumented tower	13
2-4. Location of FCMP homes instrumented to measure wind pressure.....	16
2-5. FCMP instrumented homes: A) Sensor installation just before Hurricane Isabel and B) Pre-wiring of a south Florida home.....	17
3-1. The decomposition of an instantaneous wind velocity profile.....	28
3-2. Gust factor curves as a function of gust duration t based on an hourly mean wind speed T	33
3-3. Correlation Distortion.....	47
3-4. Yamazaki and Shinozuka univariate stochastic simulation technique	49
3-5 Grigoriu univariate stochastic simulation technique	50
3-6. Shinozuka and Deodatis correlated non-Gaussian multivariate stochastic simulation technique	54
4-1. Deployment of instrumented towers during Tropical Storm Isidore (2002).....	63
4-3. Deployment map for Hurricane Isabel	68
4-4. Tower deployment and transportation.....	69
4-5. Satellite tower stabilization	70
4-6. Satellite tower instrumentation and safety considerations	71
4-7. Computer enclosure for remote transmission of FCMP data	72
4-8. Configuration of Tower XP user interface to set up data collection	76

4-9. Hurricane Research Division surface wind field analysis (courtesy of NOAA).....	83
4-10. Track of NOAA research aircraft in Coastal Mission 20030918H1 during Isabel 2003 (courtesy of NOAA).....	84
4-11. GPS sonde splash locations during Isabel 2003 (courtesy of NOAA).....	84
4-12. Wind swath map from FEMA’s HAZUS program, based on the NOAA H*WIND model using FCMP data (courtesy of Applied Research Associates, Inc.)	85
5-1. Fetch requirements to determine the roughness length in a homogenous terrain at an observation height of 10 m	90
5-2. Convergence of the longitudinal turbulence intensity over increasing averaging times (FCMP database)	94
5-3. Ratios of vertical turbulence intensities to longitudinal and lateral turbulence intensities.....	96
5-4. Gust Factors based on a 10-minute mean wind speed.....	101
5-5. Mean and 5% / 95% quantile gust factors based on a 10-minute wind speed.....	102
5-6. Gust Factors based on a 1-hour mean wind speed.....	103
5-7. Linear regression of gust factor vs. longitudinal turbulence intensity over a variety of gust durations.....	106
5-8. Rational polynomial fits to slope α_1 and z-intercept α_0	107
5-9. Exponential fit to beta curve.....	107
5-10. Proposed gust factor relationship based on a 10-minute wind speed, roughness length and gust duration	108
5-11. Spectral analysis of tropical cyclone data.....	113
6-1 Tap geometry on the building model.....	119
6-2. PDF interpolation of 24 ft eave height for a single tap (winds parallel to the ridgeline)	122
6-3. PDF interpolation of 24 ft eave height for a single tap (cornering winds).....	123
6-4. PDF interpolation of 24 ft eave height for a single tap (winds perpendicular to the ridgeline)	123
6-5. Experimental pressure tap data.....	130

6-7. Comparison of the target and simulated spectral matrices for one realization of $H = 24$ ft and $\alpha = 180^\circ$	132
7-1. Aerial imagery of the Tower T3 deployment site in Isabel	141
7-2. Wind speed, wind direction and turbulence intensity measured by Tower T3 in Hurricane Isabel	141
A-1. Velocity and turbulence intensity records from Tower T0 in Hurricane Isabel at Elizabeth City, North Carolina	148
A-2. Velocity and turbulence intensity records from Tower T1 in Hurricane Isabel at Wilmington, North Carolina	149
A-3. Velocity and turbulence intensity records from Tower T2 in Hurricane Isabel at Atlantic Beach, North Carolina	150
A-4. Velocity and turbulence intensity records from Tower T3 in Hurricane Isabel at Frisco, North Carolina	151
A-5. Velocity and turbulence intensity records from Tower T0 in Hurricane Lili at Lafayette, Louisiana	152
A-6. Velocity and turbulence intensity records from Tower T3 in Hurricane Lili at Lydia, Louisiana	153
A-7. Velocity and turbulence intensity records from Tower T0 in Tropical Storm Isidore at Mary Esther, Florida	154
A-8. Velocity and turbulence intensity records from Tower T2 in Tropical Storm Isidore at Gulf Breeze, Florida	155
A-9. Velocity and turbulence intensity records from Tower T1 in Tropical Storm Gabrielle at Venice Beach, Florida	156
A-10. Velocity and turbulence intensity records from Tower T1 in Tropical Storm Irene at Melbourne Beach, Florida	157
B-1. Aerial Imagery of the terrain surrounding Tower T0 in Hurricane Isabel at Elizabeth City, North Carolina	159
B-2. Aerial Imagery of the terrain surrounding Tower T1 in Hurricane Isabel at Wilmington, North Carolina	160
B-3. Aerial Imagery of the terrain surrounding Tower T2 in Hurricane Isabel at Atlantic Beach, North Carolina	161

B-4. Aerial Imagery of the terrain surrounding Tower T3 in Hurricane Isabel at Frisco, North Carolina.....	162
B-5. Aerial Imagery of the terrain surrounding Tower T0 in Hurricane Lili at Lafayette, Louisiana.....	163
B-6. Aerial Imagery of the terrain surrounding Tower T3 in Hurricane Lili at Lydia, Louisiana.....	164
B-7. Aerial Imagery of the terrain surrounding Tower T0 in Tropical Storm Isidore at Mary Esther, Florida.....	165
B-8. Aerial Imagery of the terrain surrounding Tower T2 in Tropical Storm Isidore at Gulf Breeze, Florida.....	166
B-9. Aerial Imagery of the terrain surrounding Tower T1 in Tropical Storm Gabrielle at Venice Beach, Florida.....	167
B-10. Aerial Imagery of the terrain surrounding Tower T1 in Tropical Storm Irene at Melbourne Beach, Florida.....	168
C-1. Comparison of direct and interpolated simulated peak aggregate uplifts to wind tunnel data and simple averaging for winds parallel to the ridgeline on a 125 X 80 ft gable end building with a 24 ft eave height.....	170
C-2. Comparison of direct and interpolated simulated peak aggregate uplifts to wind tunnel data and simple averaging for cornering winds on a 125 X 80 ft gable end building with a 24 ft eave height.....	171
C-3. Comparison of direct and interpolated simulated peak aggregate uplifts to wind tunnel data and simple averaging for winds perpendicular to the ridgeline on a 125 X 80 ft gable end building with a 24 ft eave height.....	172
C-4. Comparison of direct and interpolated simulated peak aggregate uplifts to wind tunnel data and simple averaging for winds parallel to the ridgeline on a 125 X 80 ft gable end building with a 24 ft eave height.....	173
C-5. Comparison of direct and interpolated simulated peak aggregate uplifts to wind tunnel data and simple averaging for cornering winds on a 125 X 80 ft gable end building with a 24 ft eave height.....	174
C-6. Comparison of direct and interpolated simulated peak aggregate uplifts to wind tunnel data and simple averaging for winds perpendicular to the ridgeline on a 125 X 80 ft gable end building with a 24 ft eave height.....	175
C-7. Comparison of direct and interpolated simulated peak aggregate uplifts to wind tunnel data and simple averaging for winds parallel to the ridgeline on a 125 X 80 ft gable end building with a 32 ft eave height.....	176

C-8. Comparison of direct and interpolated simulated peak aggregate uplifts to wind tunnel data and simple averaging for cornering winds on a 125 X 80 ft gable end building with a 32 ft eave height	177
C-9. Comparison of direct and interpolated simulated peak aggregate uplifts to wind tunnel data and simple averaging for winds perpendicular to the ridgeline on a 125 X 80 ft gable end building with a 32 ft eave height	178
C-10. Comparison of direct and interpolated simulated peak aggregate uplifts to wind tunnel data and simple averaging for winds parallel to the ridgeline on a 125 X 80 ft gable end building with a 32 ft eave height	179
C-11. Comparison of direct and interpolated simulated peak aggregate uplifts to wind tunnel data and simple averaging for cornering winds on a 125 X 80 ft gable end building with a 32 ft eave height	180
C-12. Comparison of direct and interpolated simulated peak aggregate uplifts to wind tunnel data and simple averaging for winds perpendicular to the ridgeline on a 125 X 80 ft gable end building with a 32 ft eave height	181

Abstract of Dissertation Presented to the Graduate School
of the University of Florida in Partial Fulfillment of the
Requirements for the Degree of Doctor of Philosophy

MEASUREMENT, MODELING AND SIMULATION OF GROUND-LEVEL
TROPICAL CYCLONE WINDS

By

Forrest J. Masters

August 2004

Chair: Kurtis R. Gurley

Cochair: Gary R. Consolazio

Major Department: Civil and Coastal Engineering

Designing low-rise structures to prevail against strong winds requires a detailed understanding of the turbulence structure of the winds that impinge upon them. Knowledge of these descriptors has accumulated since the late 1800s, although most of the information was determined from data collected in winter storms and thunderstorms. Whether the turbulent behavior of tropical storms and hurricanes differ from these models remains an active subject of debate and is the focus of this dissertation. During the 1999-2003 Atlantic Hurricane Seasons, instrumented towers collected hundreds of hours of surface-level wind speed data from 29 instrumented towers in ten different named storms in Florida, North Carolina and Louisiana. From these data, the 19 records with the highest speeds were divided into 10-minute segments and compiled into a database from which turbulence intensity, gust factors, integral length scales and power spectra were measured. In this dissertation, turbulence intensity ratios and longitudinal length scales are analyzed over a range of roughness regimes and wind speeds. Gust

factor relationships are presented for 10-minute and 1-hour mean wind speeds, and a formula relating gust factors to gust duration and roughness length is developed for a 10-minute mean wind speed. From these analyses, it is shown that tropical cyclones produce “gustier” winds than extratropical data. Additionally, the use of a non-Gaussian multivariate simulation algorithm to recreate aggregate pressure loading on untested building shapes is investigated.

CHAPTER 1 INTRODUCTION

The Hurricane Wind to Damage Chain

The likelihood that another intense hurricane will strike a major population center remains high. As evidence, consider that metropolitan areas including Miami, Tampa, New Orleans and New York City will surpass their return period for hurricane landfall after 2005 (Williams 2003) and that tropical meteorologists predict that the post-1994 trend of reduced wind shear and elevated ocean temperatures in the Atlantic basin will persist, increasing hurricane activity throughout the next few decades (Gray and Klotzbach 2003). In addition to increased strike probability, the rising coastal population has elevated the potential for catastrophe. Presently, over 45 million residents live in hurricane prone coastlines (Noserale 2001) and by 2010, the population of Florida is expected to grow to more than 16 million residents, which is twice its 1960 population (Hinrichsen 1999).

Although the casualty rate associated with hurricane landfall has rapidly declined despite the population increase, the economic repercussion of a tropical cyclone remains staggering. According to the Insurance Information Institute, the world's most costly insurance loss from a disaster (from 1970-2002) occurred during Hurricane Andrew in 1992. Miami-Dade County suffered an estimated \$20.5 billion in insured damages (in 2002 dollars), which is commensurate to the insured losses from the terrorist attacks on the World Trade Center and the Pentagon. Eleven insurance companies emerged insolvent, and another forty withdrew or severely limited their underwriting in the state of

Florida. Ten percent of the businesses in six south Florida counties closed in Andrew's aftermath (Rappaport 1993, Barnes 1998, Hartwig 2003). On a longer timeline, the destructive forces of hurricanes and other extreme wind events—including tornadoes and thunderstorms—is tremendous. The United States sustains an average of \$6.3 billion dollars in damage from windstorms annually (Meade and Abbot 2003).

Research seeking to reduce loss of life and property during extreme wind events, such as Hurricane Andrew, is conducted in the wind engineering community. Born from the Tacoma Narrows Bridge collapse in 1940, when a suspension bridge collapsed at one-third of its design wind load from dynamic wind effects (Scott 2001), wind engineering has evolved from the field of industrial aerodynamics (as it was originally known in the 1950-60s) to a multidisciplinary research focus, working in conjunction with meteorologists, emergency managers and social scientists in addition to designers of wind-resistant structures, risk assessment experts and modelers of wind-structure interaction.

The research presented herein is a contribution to wind engineering, particularly to improve the current understanding of ground level hurricane winds and to develop the ability to simulate wind loading on low-rise structures in hurricane prone regions. This dissertation documents the measurement of tropical cyclone winds in the field during the 1999-2003 Atlantic hurricane seasons, presents the analyses of collected data and details computer simulation methods to recreate wind loading on low-rise structures.

Research Underway

Modern design of wind resistant structures relies heavily on wind tunnel testing to estimate dynamic pressure loading. The pressure loading on low-rise buildings—which reside within the lowest 5% of the atmospheric boundary layer—is deeply sensitive to the

turbulence characteristics of the wind field, which in turn, is dependent on the roughness of the upwind terrain. To better understand turbulent wind fields in situ, engineering research has complemented the testing laboratory with modern techniques to measure wind fields from hurricanes and thunderstorms. Since the late 1990s, full-scale research—i.e., in-field measurement to capture real environmental loading and actual structural response—has grown significantly, providing valuable insight into surface level winds and the resultant loads on residential structures during extreme wind events.

The research presented in this document is the result of two such programs involved in full-scale measurement activities: the Florida Coastal Monitoring Program (FCMP) and the National Institute of Standards and Technology (NIST) Hurricane Loss Reduction project. These projects are described below, followed by the list of original contributions discussed in detail within this dissertation.

Florida Coastal Monitoring Program

The FCMP, a joint venture between the University of Florida and Clemson University, focuses on full-scale experimental methods to quantify near-surface hurricane wind behavior and the resultant loads on residential structures. Before storm landfall, portable instrumentation is deployed in the path of the cyclone. Four 10-meter tower systems (capable of withstanding 90 m/s wind gusts) measure high-resolution time histories of wind velocity and transmit data to a web server where meteorologists from the National Oceanic and Atmospheric Administration (NOAA) and analysts contracted by the Federal Emergency Management Agency (FEMA) ingest data into surface wind field models (H*Wind and HAZUS, respectively). Additionally, the FCMP will instrument a series of residential houses should the storm make landfall in the proximity of the 30 homes participating in the project. Collected data from an individual house

include time histories of pressure at various locations on the roof, soffit, and attic as well as wind speed and direction. Chapter 2 provides greater detail concerning the tower and house experimental configurations. Chapter 4 discusses the history and logistics of FCMP deployments into tropical cyclones. Chapter 5 contains analyses of surface-level wind speed data collected in those deployments.

Hurricane Loss Reduction Project

The overarching goal of the Hurricane Loss Reduction Project is to strengthen the scientific and engineering basis for measures that reduce losses from windstorms and particularly, from hurricane events striking the United States. The consortium, composed of research teams from Clemson University (CU), Virginia Polytechnic Institute and State University, the University of Illinois at Urbana-Champaign, Johns Hopkins University and the University of Florida (UF), has established a coordinated series of research activities in four thrust areas:

1. Dependence on wind load magnitudes and distributions on wind characteristics
2. Hurricane wind loads and wind characteristics
3. Physical modeling and computer simulation of structural capacities and responses to wind loads
4. Simulation and modeling tools for database-assisted, reliability-based design

UF is responsible for objectives 2 and 4. The research aims of objective 2 are coincident to the goals of the FCMP, as both programs seek to characterize the ground level wind field during the landfall of tropical cyclones. Original contributions concerning objective 2 are located in Chapter 5. Contributions towards objective 4 are located in Chapter 6.

Scope of Research

This document provides the background of wind hazard mitigation research conducted at UF and its partnering universities. Chapter 2 documents the full-scale measurement of hurricane boundary layer winds, specifically efforts to measure surface level wind speeds and the resultant pressures on low-rise buildings during extreme wind events. The design of wind-resistant structures under the guidance of the American Society of Civil Engineers *Minimum Design Loads for Buildings and Other Structures* (ASCE 2002) and recent efforts to enhance design with reliability-based, database-assisted design (DAD) techniques are also explored in Chapter 2. Chapter 3 covers aspects of atmospheric turbulence that are of interest to structural and wind engineers and explains the principles and methods of stochastic simulation techniques. Chapter 4 presents the history, organization and logistics of deployments and presents original contributions to full-scale measurement, namely the development of the satellite tower system and the first real-time data acquisition to transfer continuous, high frequency, digital observations to NOAA meteorologists from a U.S. landfalling hurricane. Chapter 5 presents analyses of surface-level wind speed data collected from the FCMP mobile instrumented towers during the 1999-2003 Atlantic hurricane seasons, including a new model to represent extreme departures of wind gusts from the sustained wind speed for coastal regions. Chapter 6 focuses on the use of a stochastic simulation algorithm for the generation of the pressure coefficient time histories on buildings geometrically similar to those tested in wind tunnel facilities. Finally, Chapter 7 summarizes conclusions about full-scale measurement and the application of stochastic simulation in wind engineering and presents suggestions for future research.

CHAPTER 2 HURRICANE DAMAGE MITIGATION RESEARCH

This chapter chronicles research efforts to measure surface level wind speeds and the resultant pressures on low-rise buildings during extreme wind events, outlines the design of wind-resistant structures under the guidance of the American Society of Civil Engineers *Minimum Design Loads for Buildings and Other Structures* (ASCE 7-02), and details recent efforts to enhance design practice with reliability-based, database-assisted design (DAD).

Sources of Wind Speed Data

Meteorological data of interest to wind engineers include high-resolution time histories of three-dimensional (3D) wind velocities observed at ground level (<20 m) from fixed points of observation. This information allows engineers to characterize the turbulent wind fields that envelop low-rise structures in extreme wind events. A variety of weather stations collect ground-level wind speed data in the United States (as seen in Figure 2-1), including

- Offshore and coastal stations operated by NOAA's National Data Buoy Center (NDBC), such as moored buoys and the Coastal Marine Automated Network (CMAN)
- Airport stations, such as the National Weather Service (NWS) Automated Surface Observing System (ASOS)
- Regional networks of automated environmental monitoring systems with real-time data collection and dissemination capabilities. Examples include the Florida Automated Weather Network (FAWN) and the Texas MesoNet Program

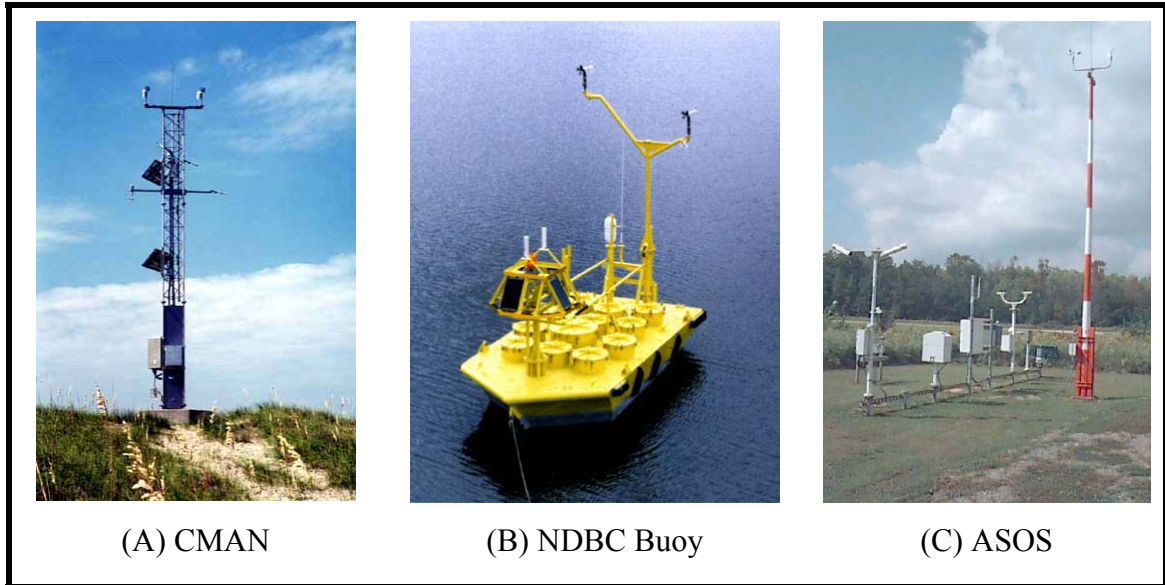


Figure 2-1. Weather stations (courtesy of NOAA)

While these weather monitoring stations are useful for normal operation—as tools for meteorological prediction, assessment of flight level conditions, air pollution studies, and climate monitoring in agrarian regions—they are unreliable for measurement in extreme wind events. Tree branches succumbing to high winds ($> 20\text{-}30\text{ m/s}$) commonly disrupt power service, and absence of backup power prevents further data collection. Stations also fail from debris impact and wind loading—particularly due to damage to the structure supporting the anemometry (e.g., masts, crossarms and/or guywires). Some stations lack recording capability altogether, and the remainder sample at rates ($\sim 0.3\text{-}2\text{ Hz}$) too low to capture dynamic wind effects. In Hurricane Andrew, only 10 out of the 34 weather stations in Miami-Dade County survived with a record (Powell et al. 1996). Meteorologists have issued recommendations concerning the implementation of backup power, improved archival abilities and better construction techniques to ameliorate the current observational configuration (Powell 1993), but the ability to record high-

resolution time histories of hurricane winds from these stations has yet to reach implementation.

In addition to employing ground- and ocean-based weather stations, the U.S. Air Force Reserves and the National Oceanic and Atmospheric Administration (NOAA) Hurricane Research Division (HRD) fly reconnaissance aircraft into hurricanes to measure winds at heights of 2.1-3.7 km. NOAA meteorologists linearly reduce—typically 63-90%—those wind speeds measured at the cruising height of the aircraft to estimate the ground level wind speeds of interest to wind engineers. Comparison to ground observations, however, has demonstrated the potential to underestimate (Hurricane Bonnie) and overestimate (Hurricane Mitch) wind speeds (Franklin et al. 2000). From the aircraft, the research crew also drops instrument packages called Global Positioning System (GPS) sondes to measure pressure, temperature and position throughout their descent. While GPS sondes provide useful data to describe the velocity profile of the hurricane boundary layer, they do not provide a time history at a fixed position. Additionally, it is difficult to glean ground level wind speeds due to the high rate of descent (10-15 m/s) before splashdown (Powell et al. 1999).

While modern weather stations provide valuable insight for meteorological prediction and the monitoring of decaying weather conditions during hurricane landfall, they do not meet the needs of wind engineers. They do not provide the high-resolution time histories of wind speeds over a variety of different terrains needed to quantify the turbulence structure of the gusts that cause damage to low-rise structures. In order to address the need for such data sets, researchers have employed permanent and portable instrumented towers since the 1950s to collect wind speed data.

Use of Permanent Instrumented Towers

Towers instrumented to record high-resolution time histories are scarce in hurricane prone regions. The earliest documented digital measurements in civil engineering literature occurred during Hurricanes Carol and Edna (1954), Connie (1955) and Donna (1960) by an instrumented tower at Brookhaven National Laboratory (BNL) on Long Island, New York. The 100-m tower provided the time series that would form the basis of the first ground-level wind spectral models (van der Hoven 1957, Davenport and Stagg 1962). During Hurricanes Eloise (1975) and Frederic (1975), the US Army Corps of Engineers (USACE) collected data from oil rigs in the Gulf of Mexico as part of its Ocean Current Measurement Program (Forristall 1988). The USACE has also measured waves, winds, tides, and currents from its Field Research Facility located in Duck, North Carolina, since 1977. In 1987, the USACE relocated its anemometry from the central building to a tower at the end of a 560 m pier, where it sits at 19 m above the National Geodetic Vertical Datum (NGVD). Most recently, the facility collected wind speeds from Hurricanes Bob (1991) and Isabel (2003). In Asia, typhoon wind speeds have been collected from instrumented towers in Nakagawa (Japan, 1964-1967), Tokyo (Japan, 1959 and 1961) and Tarama Island (Japan, 1975-1977) and in Hong Kong (1959 and 1961). Analyses of these data may be found in Ishizaki (1983).

Data from many storms are necessary to evaluate the velocity field and its turbulence characteristics in a statistically meaningful way. To increase the likelihood of recording hurricane winds, NOAA's Hurricane Research Division (HRD) implemented the Hurricanes at Landfall Time Series Data Recorders (HAL-TSR) program. Before tropical cyclone landfall, research personnel augmented existing weather stations in the path of the storm with portable instrumentation packages equipped with backup power

and high-resolution data acquisition software. The HAL-TSR experiment provided digital ground observations for Hurricanes Dennis, Floyd and Irene in 1999 (personal communication with Mark Powell, January 19, 2004). The HAL-TSR program represents a significant transitioning point for full-scale measurement of surface-level tropical cyclone winds. Prior to that experiment, data collection only occurred if the path of the cyclone brought it within close proximity of an observation site.

Use of Portable Instrumented Towers

Engineers need wind records from a variety of terrain exposures, but a fixed observation point only provides velocity field data for the local terrain exposure. Additionally, most weather stations operate in flat expanses—such as airports and beachfronts—that do not generate the turbulence of built-up terrains such as suburban neighborhoods. These conditions are of great interest to engineers as they reveal the turbulent wind fields that envelop low-rise structures. To collect these data, two other programs were formed to add portability and flexibility to hurricane data collection efforts.

In 1998, the Federal Emergency Management Agency (through the State of Florida Department of Community Affairs) and the Idaho National Engineering and Environmental Laboratory (INEEL) funded the development of two university research programs to collect full-scale hurricane data: the Wind Engineered Mobile Tower Experiment (WEMITE) and the Florida Coastal Monitoring Program (FCMP). This dissertation is concerned in large part with contributions made to the FCMP.

Wind Engineered Mobile Tower Experiment (WEMITE). Civil engineering and atmospheric science faculty at the Texas Technological University (TTU) Wind Science and Engineering Research Center jointly administer the WEMITE program.

Instrument capabilities include five towers, specially equipped vehicles (mobile mesonets), and a Shared Mobile Atmospheric Research and Teaching Doppler on Wheels (SMART-DOW) used in conjunction with Oklahoma and Texas A&M Universities. Of the five towers, Texas Tech employs two towers capable of withstanding 67 m/s (150 mph) wind gusts: WEMITE I and II. WEMITE I collects data at 3.1 m, 6.1 m and 10.7 m, and the second generation tower, WEMITE II, collects data at five levels: 2.13 m, 3.96 m, 6.1 m, 10.06 m, and 15.2 m. Both systems collect temperature, barometric pressure and relative humidity and maintain stability from outrigger arms, guy wires and ground screws. Instruments and the data acquisition system receive power from a wind generator and a bank of four deep-cycle batteries. Figure 2-2 provides pictures of WEMITE II. The remaining three towers are lightweight 10-m aluminum towers that use guy wires and shear pins to remain stable in high winds.

Florida Coastal Monitoring Program. The FCMP is a unique joint venture—led by structural engineering faculty at Clemson University and the University of Florida—that focuses on full-scale experimental methods to quantify near-surface hurricane wind behavior and the resultant loads on residential structures. The aim of the project is to provide the data necessary to identify methods to cost-effectively reduce hurricane wind damage to residential structures.



Figure 2-2. Texas Tech WEMITE

Similar to the WEMITE deployment strategy, FCMP teams remain on standby throughout the hurricane season to respond rapidly when the threat of a tropical storm arises. When a cyclone approaches, FCMP teams leave their home universities to meet the inbound hurricane with four—soon to expand to six—portable tower systems (as seen in Figure 2-3). Based on advisories issued by the National Hurricane Center, research personnel deploy the towers in the vicinity of anticipated landfall approximately 8-24 hours before impact.



Figure 2-3. The FCMP instrumented tower

Designed to capture hurricane winds in a variety of exposures and to survive a hurricane episode, the towers are highly mobile and rugged. They meet U.S. Department of Transportation (DOT) requirements for transport as a conventional trailer, and with the tow capabilities of the FCMP's four-wheel drive vehicles, the towers can be erected in a wide variety of off-road terrains.

Several performance measures were implemented to simplify tower setup and to increase the window of time for research personnel to evacuate the impacted region. The tower is stable without guy wires, requires only six bolts during assembly and is hoisted into place with an electric winch in seconds. These time-saving measures allow three research personnel to erect each tower in less than 30 minutes.

Designed to withstand extreme service conditions, the tower can resist a peak gust wind speed of 90 m/s (200 mph), which corresponds to a strong Saffir-Simpson Category

5 hurricane (Simpson and Riehl, 1981). The main tower is built from a structural steel lattice, bolstered by structural tubing that connects the tower to its trailer. All computer, generator and battery enclosures are built from 16 gauge steel or diamond-plated aluminum. Wiring for power and data cables are encased in conduit for protection. The towers resist sliding and overturning from impinging wind loads through its 2700 kg of self weight, an outrigger system which places supports 6 m from the tower base, and earth screws (similar to those used in manufactured housing), which are augured into the ground and attach to the end of the outriggers. The natural frequencies of the tower—5.66 Hz and 6.45 Hz perpendicular and parallel to the axles of the trailer, respectively—render dynamic effects negligible as the practical upper frequency limit of ground level hurricane wind spectra is approximately 1-2 Hz.

Three levels of sensors outfit the tower at 3, 5 and 10 m. The data acquisition system measures 3D wind speed and direction at the top two levels and collects temperature, rainfall, barometric pressure, and relative humidity data at the tower's base. Two RM Young anemometry systems—a wind monitor and a custom array of three gill propellers—collect data at the 10-m level, which the World Meteorological Organization deems as the standard wind speed observation height. A second array of gill propellers collects wind speed data at the 5-m level to measure winds at the approximate eave height of a single-story home. Dynamic characteristics of the anemometer's four-blade polypropylene helicoid propellers include a 2.7 m 63% recovery distance constant and a damped natural wavelength of 7.4 m. The wind monitor 50% recovery vane delay distance is 1.3 m and is rated for a 100 m/s gust survival.

A contractor-grade gasoline generator powers a linked uninterruptible power supply system, which in turn powers the onboard computer and instrumentation. The equipment can operate for up to 24-36 hours before research personnel must refuel the generator. All data are stored in digital form on two hard disks in the tower's computer system. Customized C++ data acquisition software samples at a rate of 100 Hz, which provides excellent resolution of high-speed wind field dynamics (Poss 2000).

The FCMP has produced data sets from the portable towers for Tropical Cyclones Georges (1998), Dennis (1999), Floyd (1999), Irene (1999), Gordon (2000), Gabrielle (2001), Michelle (2001), Isidore (2002), Lili (2002) and Isabel (2003).

In addition to the mobile tower experiments, the FCMP conducts full-scale measurement of wind pressures on low-rise structures during hurricane landfall. The following section explains this program.

FCMP House Experiments: The purpose of the house component of the FCMP is to collect uplift pressure data on the roofs of real residential homes during landfalling hurricanes. Together, the towers and houses provide critical data to engineers developing wind-resistant designs in hurricane prone regions by tying together ground level wind speeds and the resultant pressure forces that impinge upon low-rise structures. To date, the project has funded the instrumentation of 30 homes (Figure 2-4) along the Southeastern and Panhandle coasts of Florida.

Private homeowners agree to participate in the program in exchange for retrofits to their homes to increase wind resistance. These retrofits can include a new roof, braced garage door, hurricane shutters, gable-end bracing, and other measures. An inspection of the home determines the individual measures taken for each home. Before any data

collection work is done on a house, the promised retrofits are performed on the participant's home. In the event that a hurricane impacts one or more of the homes, the FCMP will compare damage between the retrofitted houses and neighboring structures to assess the effectiveness of the retrofits.

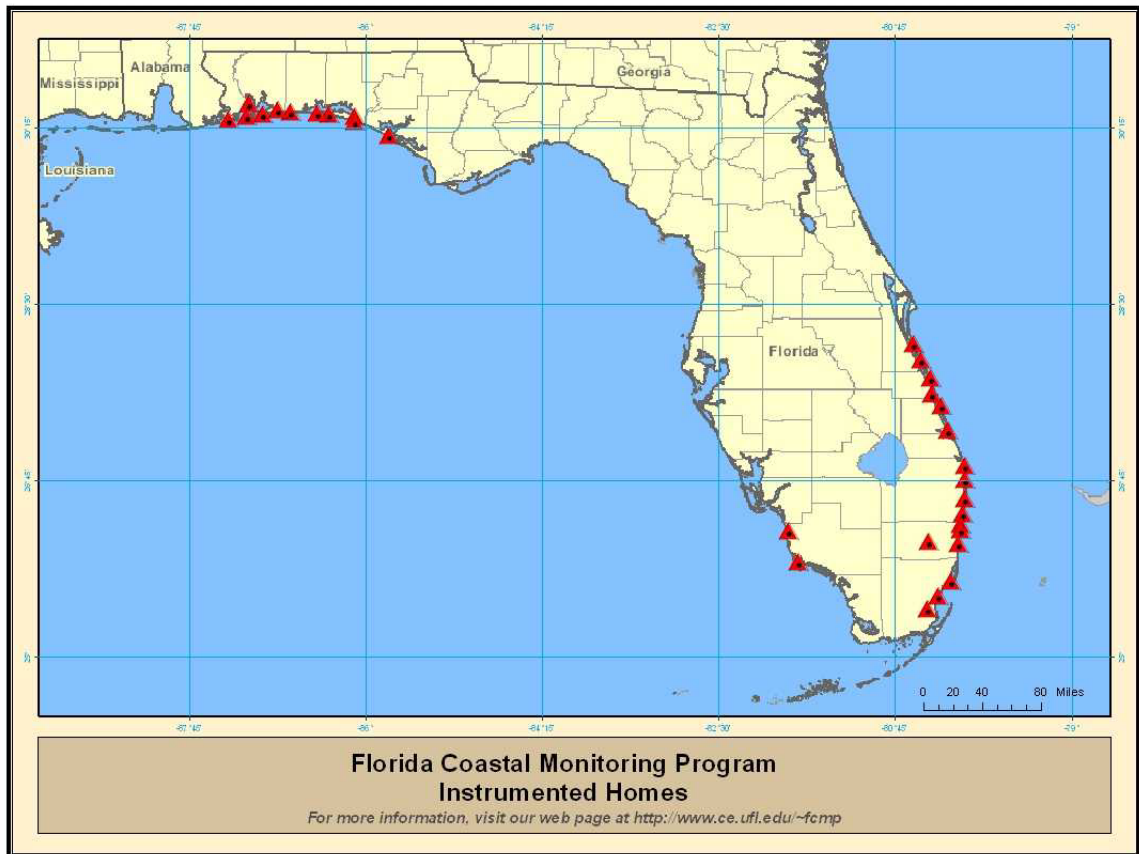


Figure 2-4. Location of FCMP homes instrumented to measure wind pressure

Microswitch pressure transducers housed in 30.5 cm diameter aluminum pans collect data on the roof. Each pan anchors to three stainless steel brackets permanently attached to the roof. A shielded cable connects the transducer to wiring encased in CPVC piping discretely located under the eave. In addition to the pan sensors, an anemometer and a pressure sensor located in the attic tie into the conduit. The CPVC pipes terminate at a disconnect box, where each instrument is separately fused in the event debris severs a

cable and disrupts the electronics. Weatherproof flexible conduit extends from the disconnect box to the data acquisition system, which, along with its backup power, is located inside a rugged steel enclosure. Sequential 15-minute data records are recorded at a sampling rate of 100 Hz. Left alone, the system can operate up to 12 hours after a power outage. Figure 2-5 illustrates the experimental setup.

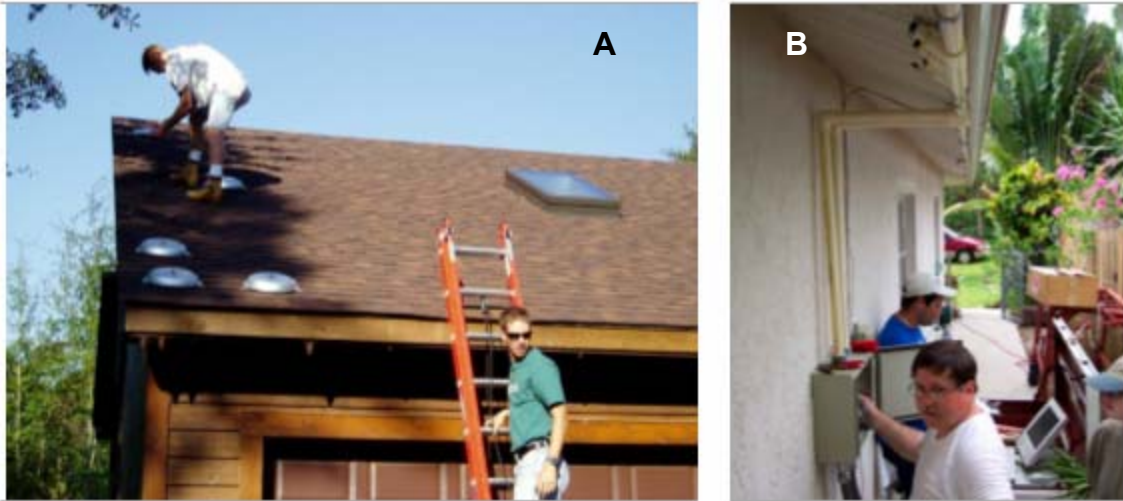


Figure 2-5. FCMP instrumented homes: A) Sensor installation just before Hurricane Isabel and B) Pre-wiring of a south Florida home

To date, the home instrumentation systems have not collected data from hurricane-force winds but did succeed in capturing the outer bands of Floyd, Michelle, Isidore and Isabel. Recently, Clemson University conducted wind tunnel studies of models of two instrumented homes that collected data in Tropical Storm Isidore (Dearheart 2003).

The portable tower and house components of the FCMP operate independently, while providing complementary data sets to quantify wind field and structural load behavior. A portion of this dissertation focuses on the portable tower component, while the house data system is not a subject directly addressed.

Current Wind Load Design Provisions and Standards

Currently, engineers seeking guidelines to design modern low-rise buildings resistant to wind loads usually turn to the American Society of Civil Engineers *Minimum Design Loads for Buildings and Other Structures* (ASCE 7-02) for guidance. ASCE 7-02 is referenced by most major building codes, including the *International Building Code* (IBC 2003) and the *Florida Building Code* (FBC 2003).

American Society of Civil Engineer's Minimum Design Loads for Buildings and Other Structures (ASCE 7-02)

The provisions offer three sets of guidelines for design: simplified, analytical and wind tunnel. The simplified and analytical methods are applicable to buildings without unusual geometric irregularities and response characteristics making it subject to aeroelastic vibrations such as flutter, vortex shedding, etc. Application of the simplified method is further restricted to buildings not subject to topographic effects with

- A mean roof height that does not exceed 60 ft
- An approximately symmetrical building cross section in each direction
- An angle of plane of roof from horizontal $\theta \leq 45^\circ$ for a gable-end roof or $\theta \leq 27^\circ$ for a hip roof
- A natural frequency > 1 Hz

In the simplified case, wind pressures are extracted from a table. For the analytical case, the provisions hinge upon the calculation of the dynamic velocity pressure (in psf),

$$q_z = 0.00256 K_z K_{zt} K_d V^2 I \quad (\text{lb/ft}^2) \quad (1)$$

(ASCE 7-02 Eq 6-15)

where K_z = a terrain exposure coefficient, K_{zt} = a topographic effect factor to account for wind speed up over hills, K_d = a directionality factor, V = the design wind speed dependent on location of the structure (mph), and I = the building importance factor, which ranges from 0.87 (e.g., agricultural structures) to 1.15 (e.g., hospitals).

For the design of low-rise buildings, design pressures p are calculated by the following equations:

1. **Main Wind-Force Resisting System**—the structural system that provides support and stability to the overall structure. Examples include roof and floor diaphragms, rigid and braced frames, shear walls and truss anchorages

$$\begin{array}{l} \text{ASCE 7-02} \\ \text{Eq. 6-18} \end{array} \quad p = q_h [(GC_{pf}) - (GC_{pi})] \quad (2)$$

where

- q_h = the velocity pressure evaluated at the mean roof height
- GC_{pf} = external pressure coefficient (See ASCE 7-02 Figure 6-10)
- GC_{pi} = internal pressure coefficient (See ASCE 7-02 Figure 6-5)

2. **Components and Cladding**—elements that transfer wind loading to the MWFRS. Examples include curtain walls, sheathing, trusses and exterior windows and doors

$$\begin{array}{l} \text{ASCE 7-02} \\ \text{Eq. 6-22} \end{array} \quad p = q_h [(GC_p) - (GC_{pi})] \quad (3)$$

where

- q_h = the velocity pressure evaluated at the mean roof height
- GC_p = external pressure coefficient (See ASCE 7-02 Figures 6-11 through 6-16)
- GC_{pi} = internal pressure coefficient (See ASCE 7-02 Figure 6-5)

The dimensionless pressure coefficients C_p provide the empirically determined relationship between upstream wind velocity and the pressure on the building in different regions. For example, the coefficients on the windward wall will be positive (inward pressure), while the coefficients on a flat roof may be strongly negative (suction).

Pressure coefficients are calculated from the following equation

$$C_p = \frac{p - p_0}{1/2 \rho V^2} \quad (4)$$

where $p - p_0$ = the pressure difference between the local and far upstream pressure p_0 , ρ = the density of air, V = the mean value of the velocity (taken from far upstream or point above the boundary layer) and $1/2 \rho V^2$ is the mean dynamic pressure of the far upstream wind or the free-stream wind at a point out of the boundary layer (Simiu and Scanlan 1996).

In terms of application of the standard, the most likely extreme wind speed in a 50-year period (dependent on building location and found in the ASCE 7-02's wind map) is used as the design wind speed in combination with the pressure coefficient C_p and the gust effect factor G to envelope dynamic effects to formulate design pressures acting on the exterior of the structure.. The gust effect factors accounts for gust load effect and dynamic structural response (which is negligible for a rigid structure).

Applicability of the Current Standard

The framework of ASCE 7-02 relies on tables and figures to extract parameters for equations that determine the design loads. The wind tunnel studies used to create the pressure coefficient information were only performed on a few very simple shapes over a range of directions. From this information, a worst-case scenario approach was used to determine pressure coefficient values for the provisions using an enveloping approach. Loading on structures or buildings with reentrant corners, geometrical asymmetries and/or distinguishing architectural treatments are approximated based on the handful of building shapes offered in the provisions. The conservative nature of the enveloping procedure is intended to account for these limitations (Rigato et al. 2001).

Additionally, ASCE 7-02 does not explicitly account for directional effects on cladding and components and the main wind-load resisting system, even though the worst-case scenarios for both cases may occur at different incident wind angles. Rather than explicitly account for directional issues, ASCE 7-02 relies on the directionality reduction factor coefficient K_d (which for low-rise buildings = 0.85) that places the design load at 85% of the worst possible enveloped value. Simiu and Heckert (1998) and Rigato et al. (2001) have shown that the reduction factor may underestimate loads since K_d is not dependent upon the mean recurrence interval of landfalling hurricanes. The study also indicated that the same building that is over-designed in some areas of the structure is under-designed in other areas. While over-design (within reason) is the intent of the ASCE prescriptive approach, the simultaneous occurrence of under-designed regions was an unintended (and unacceptable) consequence of this simplified approach to account for a very complex phenomenon.

The methodology of ASCE 7-02 draws upon three series of tests to provide an assessment of wind forces on a low-rise building:

- Irmingier's 1894 aerodynamic tests
- Flachsbart's 1932 boundary layer wind tunnel experiments
- The University of Western Ontario's (UWO) tests sponsored by the Metal Building Manufacturers Association (MBMA) in the 1970s and early 1980s

Clearly, the investigators could not avail themselves to the benefits of modern technology, particularly the digital computer and today's high resolution data acquisition systems. Only the latter study employed computing hardware to record and store data. This statement does not imply that the original tests are inaccurate but instead recognizes that the resolution gains (e.g., denser clusters of pressure tap arrays) and greater data

storage capabilities offered by modern data acquisition systems can provide a more complete view of the complex phenomenon of wind-structure interaction.

Recent high-resolution wind tunnel tests performed by UWO in 1997 and 2001-2004 have called the adequacy of the ASCE 7 pressure coefficient values into question. While state-of-the-art computer based models can calculate bending moments, shear forces and axial forces to within a 5% deviation from experimental results, the models used to develop ASCE 7 can result in wind pressure load deviations as high as 50% (Rigato et al. 2001).

Reliability-Based Database-Assisted Design

One concept to modernize wind load provisions envisions the use of an online database containing the wind load time histories over a building surface for a huge variety of structural shapes. These time histories will be comprised of wind tunnel tests and computer generated simulations. Advanced (and proven) analysis methods that have been developed since the creation of the existing pseudo-static design procedure can then be applied to determine the maximum critical stresses in a statistically reliable sense. As a result, engineers can rationally create a uniformly conservative design based on a detailed analysis of structural response to wind loads created for that building shape.

Whalen et al. (1998) and Rigato et al. (2001) established the foundations for database-assisted design (DAD) concept for wind loads in hurricane prone regions:

1. The development of technology for recording and storing simultaneous wind tunnel or full-scale pressure time histories over the external and internal surfaces of building models
2. The development of climatological databases containing large numbers of simulated hurricane wind speed data

3. Computational capabilities allowing the use of pressure and climatological databases for the calculation of bending moments, shear forces and axial forces in wind-resistant structures

Item 2 above is supported in part by Objective 4 set forth by the Hurricane Loss Reduction Project introduced in Chapter 1. Computer simulation of these pressure coefficients using multivariate stochastic simulation techniques is a component of the successful implementation of this procedure and is addressed in Chapter 6.

DAD is intended as a natural extension to analytical design, providing more accurate loads for a wide variety of building types. The development of electronic standards for wind load provisions has elicited the interest of many private, government and educational institutions including the UWO, Purdue University, Texas Technological University (TTU), Colorado State University, Ceco Building Systems, MBMA, Clemson University, University of Notre Dame, Virginia Polytechnic Institute and State University, Johns Hopkins University, the University of Illinois at Urbana-Champaign, and the University of Florida. Additionally, industry professionals developing vulnerability models for insurance and reinsurance companies have taken an interest, because the DAD concept will provide considerably more building shapes than the set of building geometries currently found in ASCE-7.

Several paths of research have manifested to further DAD aims. Efforts have been made to determine internal force peaks from stochastic simulation methods (Sadek and Simiu 2002) and to quantify the resultant sampling errors (Sadek et al. 2002). Additionally, the analysis of wind tunnel data collected at the Wind Load Test Facility at Clemson University has been used to characterize the probabilistic content and correlation structure of pressure coefficients on the roof of low-rise buildings (Cope and Gurley 2001).

Chapter 6 addresses methods to generate time histories of loads on untested buildings based on interpolation of load time histories between building shapes tested in the wind tunnels. The problem statement under consideration is: Given the wind tunnel measured time histories of pressure coefficients at multiple roof taps on two similar but not identical buildings, develop methods to accurately represent the pressure coefficient time histories of a building whose geometry lies between the two measured buildings. For example, consider three buildings identical in all respects other than roof pitch. If wind tunnel studies are conducted on models with 3 on 12 and 8 on 12 roof pitches, one can infer appropriate time histories for the roof taps on a 5 on 12 roof pitch building. The resulting aggregate loads in the structural members should be statistically similar to the actual loads in terms of mean, rms, and peak values. The highly non-Gaussian and strongly correlated nature of uplift on low-rise roofs renders this a challenging problem. A viable solution to the problem statement will serve to increase the applicability of the intended online DAD database by making a wider array of low-rise building geometries available.

Recently, UWO researchers have addressed this issue through re-scaling of the measured pressure time histories of tested buildings. Using the example above, the time histories from the 3 on 12 roof pitch building are translated and dilated to adjust the mean and rms values, with the resultant serving as the inferred time histories for the unmeasured 5 on 12 roof pitch building. The translation and dilation parameters are determined using neural network training of a handful of tested buildings of similar shape (Chen, Kopp and Surry, 2003a). Another approach reconstructed the resultant aggregate loads using linear stochastic estimation (Chen, Kopp and Surry 2003b). In both studies

the added complexity of direct simulation of the time histories was avoided in order to explore the efficacy of simpler methodologies. The tradeoff is the inability to capture differences in higher order statistics between time histories on different geometries, potentially influencing the ability to reproduce accurate peak value magnitudes and rates of occurrence.

Chapter 6 presents the use of a stochastic simulation algorithm for the generation of the pressure coefficient time histories on a building similar to tested geometries. This method goes beyond the translation and dilation of time histories of tested buildings, potentially improving the accuracy of the load time histories. The use of simulation preserves the spectral content, correlation, and the non-Gaussian probability distribution, thereby maintaining higher moments and accurate fluctuating peak values. The spectral and probabilistic models used as input to the stochastic simulation algorithm are derived from interpolation of models fitted to data from similar buildings. Background on simulation methods is provided in Chapter 3, and the development and results of this interpolation – simulation methodology are presented in Chapter 6.

Summary

This chapter has introduced two avenues of hurricane damage mitigation research including full-scale ground level wind velocity and structural load data collection, and new concepts for providing structural wind loading for design via Database Assisted Design. The research in this dissertation focuses on contributions to both these avenues of research. Chapter 3 will present the background necessary to provide a proper context for the original contributions in Chapters 4 through 6. Chapter 4 discusses the data collection efforts of the FCMP. Chapter 5 presents the results of detailed analyses of the FCMP datasets, including new models of turbulent gust behavior for coastal regions.

Chapter 6 presents the development of computational simulation algorithms combined with interpolation schemes using existing wind tunnel data sets to expand the utility of the DAD concept for prescriptive structural wind loading.

CHAPTER 3 ANALYSIS AND SIMULATION TECHNIQUES FOR WIND

This chapter provides a brief description of the aspects of atmospheric turbulence that are of interest to structural and wind engineers and explains the principles and methods of stochastic simulation techniques required to computationally simulate wind loading. This is necessary background material for the research presented in Chapters 4 through 6.

Of principal interest to structural engineers are winds in the surface layer region of the atmospheric boundary layer (ABL), where surface friction primarily influences wind structure. Wind speeds and pressure loading vary with time inside the ABL, and require probabilistic and spectral analyses to characterize their turbulent nature. In addition to characterizing surface level wind fields, these analyses also yield the target statistical models required to recreate wind loading in Monte Carlo simulation techniques.

Characterization of Ground-Level Hurricane Winds

Data collected by the portable towers are processed to quantify the data in terms of steady and fluctuating components, and their relationship to terrain roughness. The wind velocity is observed at a fixed point (x,y,z) in a right-handed Cartesian coordinate system over the time duration T . The longitudinal or along-wind (u), lateral or across-wind (v), and vertical (w) components decompose into the superposition of its steady state or mean velocity and its fluctuating or turbulent components.

Assuming stationary, horizontally homogeneous and neutrally stratified flow, the velocity field reduces to a two-dimensional instantaneous vertical velocity profile $u(z)$ and constituents $\bar{u}(z)$ and $u'(z)$ (shown in Figure 3-1).

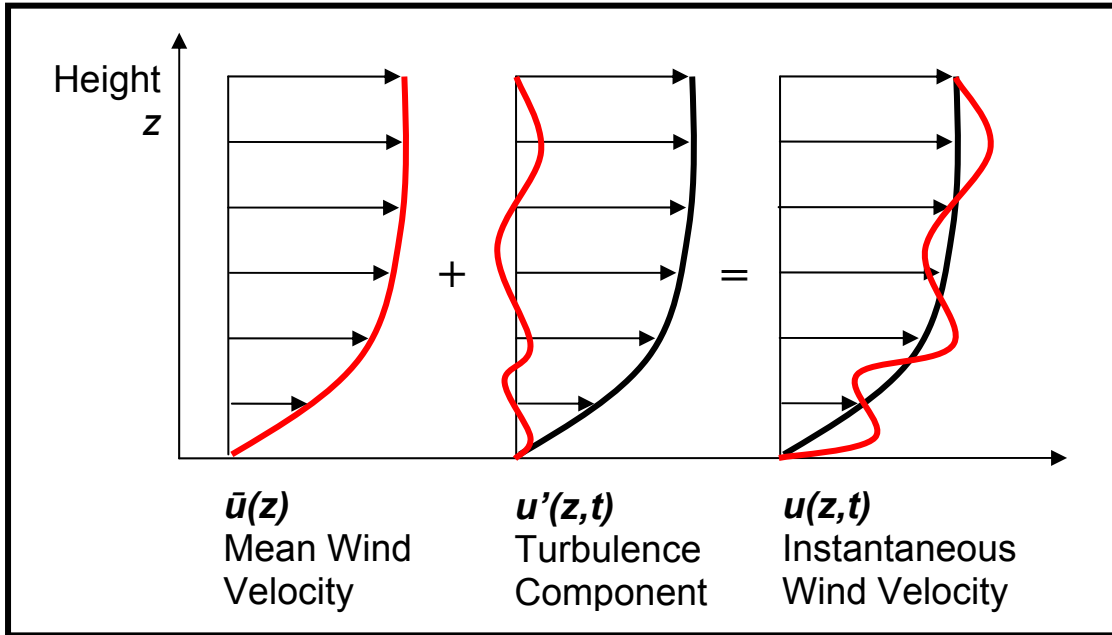


Figure 3-1. The decomposition of an instantaneous wind velocity profile

Mean Velocity Profile

Many velocity profiles exist to describe the variation in mean wind speed with height. The two most widely used profiles are presented in this section. The first profile (and also one of the earliest profiles proposed) is the power law,

$$\begin{aligned}\bar{u}(z) &= \bar{u}_g \left(\frac{z}{z_g} \right)^\alpha & 0 \leq z \leq z_g \\ &= \bar{u}_g & z > z_g\end{aligned}\quad (5)$$

which relates a gradient wind speed \bar{u}_g at height z_g to velocity over a range of heights z with knowledge of the non-dimensional surface roughness parameter α . Typical values

of α range from 0.10 in open terrain to 0.33 in metropolitan exposures. Its mathematical simplicity has made it a popular choice for many building codes and standards, including ASCE 7, *Eurocode*, AS1170.2 (Standards Australia) and the RLB (Architectural Institute of Japan). ASCE 7 uses the following form

$$\bar{u}(z) = \bar{U}_0 E(z) = \bar{U}_0 \bar{b} (z/10)^{\bar{a}} \quad (6)$$

where the mean velocity is a function of the mean wind speed \bar{U}_0 and the wind exposure category $E(z)$, which is determined from the observation height z (units of meters) and the terrain dependent constants \bar{a} and \bar{b} (Zhou and Kareem 2002).

The second profile, proposed by Sverdrup (1934), is based on flat-plate boundary layer theory of Prandtl and von Kármán. The logarithmic law is valid from several meters off of the ground to 50-100 m depending on the surface roughness and the wind speed (Wieringa 1993),

$$\bar{u}(z) = \frac{1}{k} u_* \ln \frac{z}{z_0} \quad (7)$$

and defines the mean velocity $\bar{u}(z)$ as a function of von Kármán's constant (observed experimentally to be $k \cong 0.40 \pm 0.01$), the shear velocity u_* , the observation height z , and the roughness length z_0 .

Like the coefficient α in the power law, the roughness length provides a mathematical description of the degree of roughness in the upwind terrain. Physically, it represents the size of the characteristic eddy size that is formed from the friction between the air and the ground surface (Dyrbye and Hansen 1999), and mathematically, it is

equivalent to the z -intercept of the logarithmic profile. Extensive effort has been undertaken to produce reliable estimates of α and z_0 for varying roughness conditions, but considerable variability exists in the literature, possibly due to the assumptions about the flow field (e.g., adiabatic equilibrium) or the upwind terrain (e.g., that sufficient homogeneous fetch exists to develop a boundary layer fully). Counihan (1972) and Wieringa (1993) provide the most complete review and analysis of available data.

The shear velocity,

$$u_* = \sqrt{\frac{\tau_0}{\rho}} \quad (8)$$

is dependent on the turbulent shear stress τ_0 and the density of air ρ . The shear stress can be calculated directly using a drag plate (or floating-element skin friction balance), which typically consists of a 1-2 m representative ground sample mounted on a sensitive balance mechanism buried beneath the ground, by measuring the tangential force of the wind (Kaimal 1994). More commonly, the shear velocity is calculated from measured eddy fluxes in the constant shear stress region close to the surface.

At least four definitions of u_* exist in the literature. Some authors use the length of the horizontal Reynolds stress vector in the direction of the mean wind vector,

$$u_{*f} = \left(E[u'w']^2 + E[v'w']^2 \right)^{1/4} \quad (9)$$

where $E[\]$ = the expectation operator or in this case, the covariance of the turbulence components. Others employ the absolute value of the horizontal Reynolds stress vector to define friction velocity,

$$u_{*II} = \sqrt{E[u'w']} \quad (10)$$

For complex terrain, Zemann and Jensen (1987) suggested a coordinate transformation of the turbulence components to align the longitudinal axis with the 3D mean wind vector such that the mean vertical and lateral components equal zero. From the new longitudinal (u'_{3D}) and vertical (w'_{3D}) components, the friction velocity is calculated as

$$u_{*III} = \sqrt{E[u'_{3D}w'_{3D}]} \quad (11)$$

Finally, McMillen (1988) modified Eq. 11 to account for rotation about the longitudinal axis (i.e., instrument tilts relative to the vertical axis). In cases where the rotation angle $< 10^\circ$, he suggests rotating the coordinate system to reduce the lateral-vertical covariance to zero (i.e., $E[v'w'] = 0$).

Weber (1998) performed least-square fits of the logarithmic profile to wind speed data collected on a 70-m instrumented tower and compared results to four methods. He determined that Eq. 9 yielded the lowest mean square error in fitted profile. Based on his conclusion, the research presented in Chapter 5 relies on that estimation technique. Important to note, however, is the significant amount of scatter and error associated with z_0 estimation using eddy fluxes. Wind tunnel studies (e.g., Iyengar and Farell 2001) have shown that Reynolds stress measurements can be off by more than 15% (using hot-wire anemometry), which produce substantial deviations in z_0 . Full-scale measurement, devoid of the idealness of a laboratory, is considerably more problematic.

Turbulence Characteristics

Turbulence Intensity. A simple measure of the fluctuating component of the wind is turbulence intensity (TI), which is a ratio of the root mean square (rms) of the turbulence component to the mean wind speed \bar{u} . In practice, decomposition of the measured wind speed and direction removes the mean from the turbulence component u' , so the rms value is a standard deviation σ_u . Assuming negligible influence of rotational and convective effects, only the longitudinal, lateral and vertical TI components remain,

$$TI_u = \frac{\sigma_u}{\bar{u}} \quad TI_v = \frac{\sigma_v}{\bar{u}}, \quad TI_w = \frac{\sigma_w}{\bar{u}} \quad (12)$$

Gust Factors. The gust factor GF relates the peak gust wind speed u_{max} to the mean wind speed \bar{u} over the selected gust duration t and record length T

$$GF(t, T) = \frac{u_{\max}(t)}{\bar{u}(T)}, \quad t < T \quad (13)$$

Choice of gust duration varies in the literature, but meteorologists and engineers commonly use $t = 2$ - and 3 -second gusts, respectively, over $T = 10$ -minute to 1 -hour durations. Structural design of low-rise structures, in particular, typically references peak gusts to an hourly mean wind speed.

Three hourly mean wind speed gust factor models—Durst (1960), Cook (1985) and Krayner and Marshall (1992)—are presented in this study (shown in Figure 3-2). The Durst and Cook models are similar in that: (1) their models were not developed from observations in the hurricane boundary layer, and (2) these gust factor models provide the reference wind speed for structural design (ASCE 7 and Eurocode, respectively).

Krayer and Marshall (1992) developed a gustier model from tropical cyclone data for the design of low-rise structures in hurricane prone regions predicated on the methodology (and assumptions) of Durst. The model replaced the Durst curve in the 1995 edition of ASCE-7 but was replaced by its predecessor in the 1998 edition.

A new gust factor model has been developed based on the FCMP database and is presented in Chapter 5. Its development required a complete reanalysis of Durst (1960). Details concerning these studies follow.

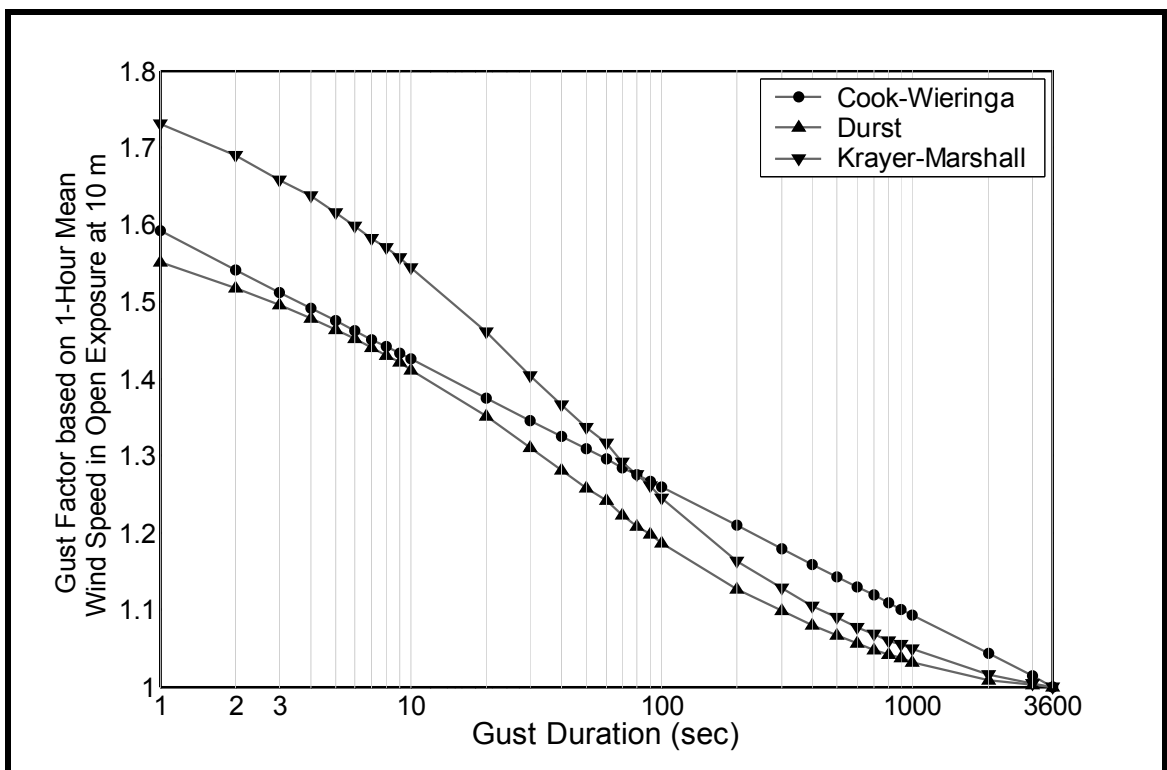


Figure 3-2. Gust factor curves as a function of gust duration t based on an hourly mean wind speed T

The first gust model, proposed in Durst (1960), was generated from wind speed records obtained from Dines pressure tube recorders in an open countryside at Cardington, England (detailed are provided in Giblett 1932). From these data, Durst divided $T = 10$ -minute records into N_{gust} t -duration segments,

$$N_{gust} = T/t \quad (14)$$

and averaged each segment to calculate the short-duration gust u_{gust} (e.g., from a 10-minute record, he calculated 120 five-second u_{gust} values). Next, he calculated the population standard deviation of the gust sequence u_{gust} with its mean wind speed \bar{u} removed,

$$\sigma(t) = \sqrt{\frac{\sum (u_{gust}(t) - \bar{u})^2}{N_{gusts} - 1}} \quad (15)$$

and divided the results of Eq. 15 by the mean wind speed \bar{u} before averaging the values to produce the first row of values in Table 3-1. The ratio of σ to \bar{u} represents the standard deviation of the gust departures of duration t (sec) from the mean wind speed over interval T (sec), for which subsequent literature has adopted the notation $SD(t, T)$. In order to produce gust factor estimates for a one hour time frame rather than the 10-minutes used in the measurements, the values in row one of Table 3.1 must be manipulated as detailed next.

Transforming $SD(t, 600)$ into an hourly mean wind speed gust factor relationship required three additional steps. First, Durst transformed the experimental $SD(t, 600)$ values to an hourly mean wind speed basis $SD(t, 3600)$ through a Gaussian translation of variance, which assumes that the mean square of the instantaneous t -second average velocity u_t may be decomposed by the following relationship,

$$E[u_t^2] = \bar{u}^2 + E[u_1(t, T_{\bar{u}})] + \sum_{i=2}^{n_{gust}} E[u_i(t, t_{i-1})] \quad (16)$$

where $E[]$ = the expectation operator, u_i = the gust departure sequence inside of the duration T_{i-1} , T_{ii} = the duration of the record and n_{gust} = the number of points in the gust.

Since the terms in Eq. 16 have a common mean, it may be reduced further and rearranged into the form employed by Durst (1960, pg. 185) to calculate

Table 3-1. Calculated Durst gust factors

Period in seconds (t)	5	10	15	20	25	30	40	50	60
$SD(t,600) = \sigma/\bar{u}$	0.145	0.135	0.128	0.124	0.120	0.115	0.107	0.098	0.095
$SD(t,3600)$	0.159	0.150	0.144	0.140	0.137	0.132	0.125	0.118	0.115
$SU(t,3600)$	2.99	2.77	2.64	2.54	2.46	2.39	2.29	2.20	2.13
$GF(t,3600)$	1.48	1.42	1.38	1.36	1.34	1.32	1.29	1.26	1.24

Note: $SD(t,600)$ can be found in Table II of Durst (1960)

$$SD(t,3600) = \sqrt{SD^2(600,3600) + SD^2(t,600)} \quad (17)$$

Three anemograms available from the Cardington site indicated that $SD(600,3600)$ equaled 0.055, 0.065 and 0.075 at a 50 ft observation height. Durst chose the median value of 0.065 to estimate $SD(t,3600)$ from row one of Table 3-1 and Eq. 17.

Next, the standardized normal deviate $SU(t,T)$ —i.e., the number of standard deviations from zero in a standardized normal cumulative distribution function CDF —was calculated for the gust duration t inside of the record interval T

$$SU(t,T) = CDF^{-1}(1-t/T) \quad (18)$$

Finally, the gust factor was calculated from Eq. 19. Values of $SD(t,3600)$, $SU(t,3600)$ and $GF(t,3600)$ are provided in Table 3-1.

$$GF(t,T) = 1 + SU(t,T) \cdot SD(t,T) \quad (19)$$

The second model, proposed in Krayner and Marshall (1992), resulted from an analysis of strip-chart data from several post-disaster investigations of wind damage by Hurricanes Frederic (1979), Alicia (1983), Elena (1985) and Hugo (1989). Records with wind speed anomalies generated from the presence of structures and trees near the anemometry were eliminated. The remaining 13 records were divided into 10-minute sequential segments, and 2-second peak gusts were extracted from spikes in the pen trace. Following Durst (1960), the observed $GF(2,600)$ were transformed into estimates of $GF(2,3600)$. Subsequent analysis supported an upward adjustment of the gust factors estimated from extratropical storms.

The third model, proposed in Cook (1995), simplified an empirical curve offered by Wieringa (1973) that assumes a linear dependence on the longitudinal turbulence intensity and a logarithmic dependence on the gust duration t .

$$GF(t, T = 1 \text{ hour}) = 1 + 0.42 TI_u \ln(3600/t) \quad (20)$$

The large volume of high fidelity wind velocity data recorded by the FCMP during tropical storms and hurricanes provides a significant database for the characterization of turbulent wind behavior in coastal areas. As coastal structures are typically most vulnerable to the worst of the damage associated with high winds during storm landfall, a gust factor model was developed exclusively from wind records collected near the coast. The development of this new coastal hurricane gust factor model is presented in Chapter 5, and contrasted with the three models shown in Figure 3-2.

Estimation of Roughness

Methods to estimate the roughness length z_0 commonly employ the logarithmic law. Neutral stability, horizontal homogeneity and stationary imply that the statistical properties of the vertical velocity profile changes only with height z . Accordingly, given enough observations, z_0 can be estimated by fitting the observed vertical wind profile to Eq. 7. To calculate a roughness length within a factor of two, Wieringa (1993) suggests at least three profile levels over rough terrain ($z_0 \approx 1$ m), four profile levels over moderately rough terrain ($z_0 \approx 0.1$ m) and five profile levels over smooth terrain ($z_0 \approx 0.01$ m).

The longitudinal TI is useful to estimate an associated roughness length of the approach terrain (Wieringa 1993). Assuming that the variance of the longitudinal turbulence component σ_u^2 is linearly proportional to the shear velocity squared by a factor β ,

$$\sigma_u^2 = \beta(u_*')^2 \quad (21)$$

and further that von Kármán's constant k and β share the relationship,

$$k\sqrt{\beta} = 1 \quad (22)$$

The logarithmic law can be rearranged to solve for the roughness length z_0 in terms of the longitudinal turbulence intensity TI_u

$$z_0 = \exp[\ln(z) - \bar{u}(z)/\sigma_u(z)] \quad (23)$$

$$z_0 = \exp[\ln(z) - 1/TI_u(z)] \quad (24)$$

Strictly speaking, application of Eq. 24 is limited to homogeneous, flat terrains (where $\beta = 6.25$) because the calculation of z_0 in a heterogeneous terrain will cause its overestimation. In heterogeneous terrain, the upwind fetch must be divided into homogeneous patches for assessment of surface roughness, before an “effective” z_0 value can be calculated from the area (Claussen 1991). Counihan (1975) hypothesized that the TI-based roughness estimation is only valid for values of $z_0 < 0.10$ m and suggested a downward adjustment for values beyond that limit.

Gust factors can also be used to estimate z_0 . Wieringa (1993) presented the following equation,

$$z_0 = z \cdot \exp\left[-\frac{f_T A [1.42 + 0.3 \ln(-4000/Ut)]}{\langle u_{\max}/U \rangle - 1 + A - f_T A}\right] \quad (25)$$

where $\langle u_{\max}/U \rangle$ = the median gust factor taken from at least 15 gust observations, A = the attenuation factor (~ 0.9) of the anemometry, f_T = a factor which is unity for 10-minute averaging periods and increases to 1.1 for hourly averages and Ut = the average wavelength of maximum gusts observed by the anemometer-recorder (usually varying between 50 and 100).

Finally, z_0 can be estimated directly from a rearrangement of Eq. 7,

$$z_0 = z \cdot \exp\left[-\frac{k\bar{u}(z)}{u_*}\right], \quad (26)$$

with the knowledge of a mean longitudinal wind speed $\bar{u}(z)$ and the shear velocity u_* . Since the momentum fluxes are assumed to be independent of height in the surface layer, 3D turbulence measurements at the 10-m observation height can be used to estimate the

shear velocity from Eq. 9. This methodology is the basis of the roughness-dependent turbulence analyses presented in Chapter 5.

Correlation and Spectral Relations

Integral Length Scales. Quantifying the length and width of an average gust in an extreme wind event is of special interest to design engineers because a gust's dimensions and velocity determine the pressure loading a structure experiences. To quantify the average length of a gust in a stationary wind record, engineers calculate the autocorrelation function $R_{xx}(\tau)$ of the longitudinal turbulence component u' over a range of time lag values τ . Noting that u' is mean-removed, $R_{xx}(\tau)$ equals the covariance function $Cov(\tau)$

$$Cov(\tau) = R_{uu}(\tau, \bar{u}' = 0) = E[u'(t)u'(t + \tau)] \quad (27)$$

The covariance function is scaled by the variance and integrated to produce the time scale T , which equals the average gust duration,

$$T = \frac{1}{\sigma_{u'}^2} \int_0^{\infty} Cov(\tau) d\tau \quad (28)$$

In practice, the upper limit of integration is reduced to the lag value where $Cov(\tau)$ dips below zero. To calculate the average gust length L_u^x , the time scale is multiplied by the mean velocity (Simiu and Scanlan 1996).

$$L_u^x = T \cdot \bar{u} \quad (29)$$

In all there are nine integral length scales L_j^i , corresponding to the direction i (x, y, z) and the turbulence component j (u, v, w). The notation in Eq. 29 corresponds to the size of the fluctuation in the direction x with respect to the longitudinal component of the wind.

Below 200-300 m elevations, the integral length scale grows as the surface roughness decreases and the elevation increases. Counihan (1975) compiled and analyzed data from 1880-1972 to propose one such empirical relationship,

$$L_u^x = Cz_0^m \quad (30)$$

where C and m are obtained graphically (the figure is available in Simiu and Scanlan 1996) from the roughness length z_0 . Assuming that $C = 145$ and $m = 0.13$ for $z_0 = 0.01$ m and $C = 90$ and $m = 0.19$ for $z_0 = 0.03$ m, Eq. 30 estimates L_u^x to be 196 m and 139 m, respectively.

Dyrbe and Hansen (1996) have proposed a conservative relationship between longitudinal length scale and roughness for structural design,

$$L_u^x = L_{10} \left(\frac{z}{z_{10}} \right)^{0.3}, \quad 10 \text{ m} \leq z \leq 200 \text{ m} \quad (31)$$

where $z_{10} = 10$ m and $L_{10} = 100$ m are independent of surface roughness.

Chapter 5 will present the results of a length scale analysis of tropical storm and hurricane level winds collected by the FCMP that demonstrate a dependence of length scale not only on roughness, but on mean wind speed as well.

Power Spectra. Accurate prediction of structural response to pressure loading requires an understanding of the distribution of wind energy with respect to frequency.

In wind, larger or low-frequency eddies generate turbulent energy and smaller or high-frequency eddies dissipate it through viscous effects. This phenomenon is referred to as the energy cascade, which consists of three major spectral regions. In the lower frequency range, energy is produced by buoyancy and shear. In the highest frequency range, kinetic energy is converted into internal energy (viscous dissipation). In the intermediate or inertial subrange, energy is neither produced nor dissipated if the flow is horizontally homogenous and neutrally stratified (Kaimal 1994).

Power spectral density functions (PSD) of turbulent wind energy employed for structural design purposes include those found in von Kármán (1948), Davenport (1961), Kaimal et al. (1972) and Harris (1990). More recently, Tieleman (1995) proposed unified spectral models for three-component velocity fluctuations at all frequencies in two different exposures: (1) flat, smooth and uniform and (2) complex or perturbed terrain. Equations for these models are presented in Table 3-2. PSD ordinates are normalized by the variance of the longitudinal turbulence component and multiplied by the frequency. To invoke similarity, wind PSD ordinates are plotted against reduced frequency or the nondimensional quantity f known as the Monin coordinate,

$$f = \frac{nz}{\bar{u}} \quad (32)$$

where $n = \text{frequency (Hz)}$, $z = \text{the observation height}$ and $\bar{u} = \text{the mean wind speed}$. For engineering purposes, the Monin coordinate is valid for $f > 0.2$ (Simiu and Scanlan 1996).

Chapter 5 will present the results of a PSD study of the FCMP wind velocity database, and compare the resulting empirical estimates with several of the models in Table 3-2.

Stochastic Simulation Methods

Chapter 6 presents the development and results of a study to enhance the database of wind tunnel tested building shapes through interpolation of existing data sets and application of stochastic simulation algorithms to digitally create loading time histories on untested building shapes. This section presents background material for the simulation work presented in Chapter 6.

Reliability-based structural design and analysis often rely on the Monte Carlo approach to quantify the probability of occurrence of various failure modes. The accuracy of such techniques depends on both appropriate system modeling and the proper representation of stochastic loads.

To characterize the pressure fields acting on bluff bodies immersed in a turbulent flow field, engineers draw from model testing in the wind tunnel, full-scale experimental data and computational fluid dynamics (CFD). Testing requires time, money and research personnel to conduct the experiment, and CFD requires significant computational resources.

Preferably, structural engineers would like to have an efficient means to produce an unlimited number of loading inputs for their models. For this reason, stochastic simulation techniques emerged as an alternative to enhance existing methods. Considerable work has been done in the simulation of Gaussian processes (Shinozuka and Jan 1972, Borgman 1990, Shinozuka and Deodatis 1991, Grigoriu 1993, Shinozuka and Deodatis 1996) and elements of these methods as well as new techniques have been applied to the simulation of non-Gaussian sample functions (Cai and Lin 1996, Gurley et al. 1997, Popescu et al. 1998, Masters and Gurley 2003), non-stationary sample functions (Priestly 1967, Vanmarcke and Fenton 1991, Zhang and Deodatis 1996, Li and Kareem

1997), non-Gaussian and non-stationary sample functions (Phoon et al. 2002, Sakamoto and Ghanem 2002, Sakamoto and Ghanem 2002) and conditional non-Gaussian sample functions (Elishakoff et al. 1994, Gurley and Kareem 1998, Hoshiya et al. 1998).

Table 3-2. Longitudinal turbulence PSD models

Name	Equation	Parameters	Reference	
von Kármán	$\frac{nS(z, n)}{\sigma_u^2} = \frac{0.33\beta f}{(1 + 70.8f^2)^{5/6}}$	$f = \frac{nL_u^x}{\bar{u}(z)}$	von Kármán (1948)	(33)
Davenport	$\frac{nS(z, n)}{\sigma_u^2} = \frac{0.33x^2}{(1 + 50x^2)^{4/3}}$	$x = \frac{1200n}{\bar{u}(10\text{m})}$	Davenport (1961)	(34)
Kaimal	$\frac{nS(z, n)}{\sigma_u^2} = \frac{33.33f}{(1 + 50f)^{2/3}}$	$f = \frac{nz}{\bar{u}(z)}$	Kaimal et al. (1972)	(35)
Harris	$\frac{nS(z, n)}{\sigma_u^2} = \frac{0.33x^2}{(2 + x^2)^{5/6}}$	$x = \frac{1800n}{\bar{u}(10\text{m})}$	Harris (1990)	(36)
Flat, Smooth and Uniform (FSU) Terrain	$\frac{nS(z, n)}{\sigma_u^2} = \frac{20.53f}{1 + 475.1f^{5/3}}$	$f = \frac{nz}{\bar{u}(z)}$	Tieleman (1995)	(37)
Perturbed Terrain	$\frac{nS(z, n)}{\sigma_u^2} = \frac{40.42f}{(1 + 60.62f)^{5/3}}$	$f = \frac{nz}{\bar{u}(z)}$	Tieleman (1995)	(38)

The majority of these methods rely on two numerical techniques to infuse prescribed spectral and probabilistic contents into each random signal or field: the Spectral Representation method and the random variable transformation.

Spectral Representation

Simulation of uplift pressure on roofs of low-rise structures requires multivariate, non-Gaussian algorithm capability in order to properly capture the peak and aggregate loading experienced in separation zones. The simulations will be based on empirical models of turbulent wind behavior, including both probabilistic and spectral models.

Spectral representation-based methods are therefore used in the Chapter 6 simulation work.

The use of the fast Fourier transform (FFT) to impart the desired distribution of energy with respect to frequency is known as the spectral representation method of simulation. Comprehensive descriptions of the spectral representation method exist in many works (Shinozuka and Jan 1972, Shinozuka and Deodatis 1991). Shinozuka and Jan (1972) present the principal formulation of the spectral representation method for a 1D process

$$y(j\Delta t) = 2 \sum_{k=0}^{M-1} \sqrt{S_{yy}(k\Delta\omega)\Delta\omega} \cdot e^{i\phi_k} \cdot e^{i(k\Delta\omega)(j\Delta t)} \quad (39)$$

where S_{yy} = two-sided power spectral density (PSD) of the sample function y , M = index of the highest contributing frequency, and ϕ = phase angles. If ϕ is uniformly and independently distributed over $[0 \dots 2\pi]$, the probability content of y will be Gaussian as M gets large, and the statistical properties measured over multiple realizations at a given time instant will be invariant to the time instant chosen.

Random Variable Transformation

Fitting a probabilistic model to a non-Gaussian random process in practical engineering application (e.g., wind pressure in the separation zones of a residential structure) typically involves matching moments measured from the time history with those integrated from the distribution being fitted. This implies the need to match moments beyond second order to describe the manner of deviation from Gaussian statistics.

Since the spectral representation method produces a Gaussian signal from a prescribed PSD and a uniformly and independently distributed random phase, additional methods must be employed to infuse a prescribed non-Gaussian content into the signal. For real-valued stationary random variables, a reliable technique is a class of memoryless translations that transform the probability content of a random variable into a prescribed probability density function (PDF). Three typical random variable transformations are given below:

1. **Analytical Filter.** When available, a deterministic nonlinear equation is an efficient approach to altering the probability content of a stochastic sample function
2. **Empirical or Analytical Gaussian to non-Gaussian Mapping (Translation Process).** (Grigoriu 1984) used the following relationship to map a Gaussian signal $u(t)$ into a prescribed non-Gaussian signal $x(t)$ through their respective cumulative distribution (CDF) functions:

$$x(t) = F_X^{-1}(\Phi_U[u(t)]) \quad (40)$$

where the prescribed non-Gaussian cumulative distribution function is F_X and the Gaussian cumulative distribution function is Φ_U . This translation can either take the form of an analytical relation or an empirical mapping scheme.

3. **Empirical non-Gaussian Mapping.** Deodatis and Micaletti (2001) expanded the Gaussian to non-Gaussian CDF mapping (translation) concept by generalizing it to an empirically based non-Gaussian to non-Gaussian CDF mapping

$$x(t) = F_X^{-1}(F_{\hat{x}}[\hat{x}(t)]) \quad (41)$$

where the arbitrary non-Gaussian sample function \hat{x} is mapped through its CDF $F_{\hat{x}}$ into the target cumulative distribution F_x to create a sample function x with the desired

marginal PDF. A refinement to this procedure was recently developed by Masters and Gurley (2003).

Existing Simulation Techniques

Non-Gaussian spectral representation-based methods may be sorted into two categories of simulation ideology: Correlation Distortion and Spectral Correction. Both are designed to simultaneously satisfy the spectral and probabilistic target information.

Correlation Distortion

The goal of Correlation Distortion is the simultaneous imparting of a desired power spectral density function (PSD) and a non-Gaussian probability content to a sample function (simulated time history). Correlation Distortion methods seek to identify a PSD to assign to the initial Gaussian sample function. This underlying PSD differs from the target PSD desired for the final non-Gaussian sample function. This “underlying Gaussian” PSD is chosen such that the nonlinear transformation to non-Gaussian probability distorts the spectral content of the Gaussian sample function into the target PSD without sacrificing an accurate representation of the target PDF.

Figure 3-3 illustrates this process. First, the underlying PSD S_{uu} and a uniformly distributed random phase ϕ are combined, and a Gaussian process u is generated using the Spectral Representation Method (SRM). Second, the Gaussian process u is passed through a random variable transformation to produce a non-Gaussian process x that possesses the target probability and spectral contents.

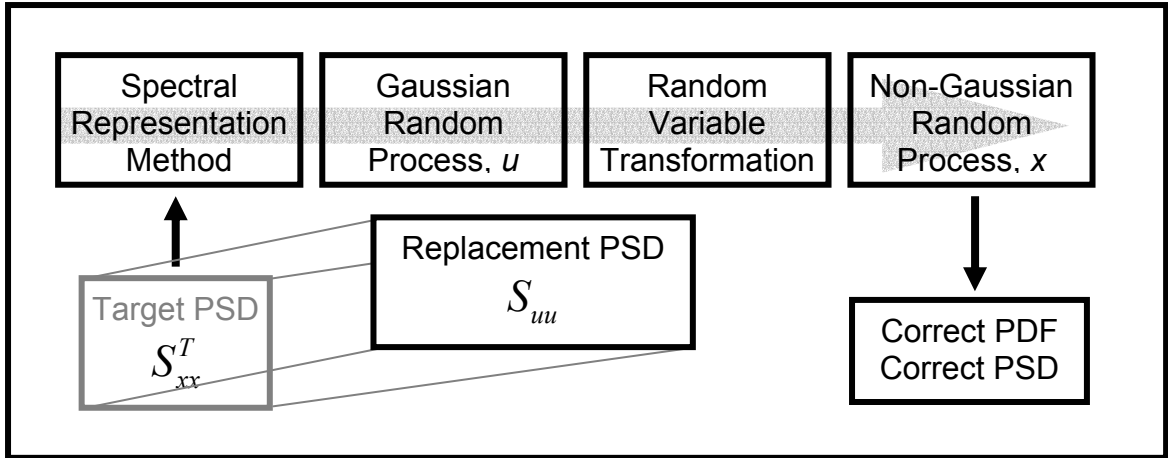


Figure 3-3. Correlation Distortion

Yamazaki and Shinozuka (1988) presented a Correlation Distortion simulation algorithm that iteratively alters the PSD associated with the Gaussian sample function before transformation (see Figure 3-4). During each iteration, a Gaussian sample function u is generated from the current S_{uu} and passed through a Gaussian to non-Gaussian CDF Map. If the resultant PSD S_{xx} matches the target S_{xx}^T as measured by the chosen error quantification, the simulation is successful and the algorithm exits. If S_{xx} is deemed an unacceptable match of S_{xx}^T , an updated version of S_{uu} is produced via the following equation,

$$S_{uu}^{i+1} = S_{uu}^i \frac{S_{xx}^T}{S_{xx}} \quad (42)$$

where i = iteration index. Generally, the first underlying Gaussian PSD S_{UU}^0 is seeded with the target S_{xx}^T for simplicity. The resultant underlying Gaussian PSD is unique to the individual sample function, and cannot be re-used to generate multiple sample functions.

For faster convergence and greater robustness, Deodatis and Micaletti (2001) suggested a modification to Eq. 42:

$$S_{uu}^{i+1} = S_{uu}^i \left(\frac{S_{xx}^T}{S_{xx}} \right)^\beta \quad (43)$$

where the β factor is included to attenuate the iterative modification to the underlying Gaussian PSD. For most applications, β may be set to 0.3 (as determined by trial and error to optimize convergence).

Grigoriu (1995, 1998) offered another Correlation Distortion method that utilizes the relationship between the scaled covariance function ξ_{xx}^T of the target process and a Gaussian image ξ_{UU} (see Figure 3-5). For a process with a variance of unity the scaled covariance function is

$$\xi_0(\tau) = \int_{-\infty}^{\infty} \int_{-\infty}^{\infty} (g(y) - \mu)(g(z) - \mu) \phi[y, z, \rho_0(\tau)] dy dz \quad (44)$$

where g is a monotonic translation (CDF mapping function) and $\phi(y, z, \rho_0(\tau))$ is the density function of a standard bivariate Gaussian distribution with Gaussian variables of integration y and z and the corresponding Gaussian correlation coefficient ρ_0 (which is bounded by \pm unity). ξ_0 is the corresponding correlation between the non-Gaussian variables $g(y)$ and $g(z)$. Eq. 44 is used to map the relationship between the target non-Gaussian scaled covariance function ξ_{xx}^T and the underlying Gaussian scaled covariance function ξ_{UU} corresponding to ξ_0 and ρ_0 respectively. The underlying Gaussian PSD S_{uu} is then identified from ξ_{uu} via the Wiener-Khintchine relationship. For multivariate simulation, Eq. 44 is modified to map between pairs of variates as:

$$\xi_{u_1 u_2}(\tau) = \int_{-\infty}^{\infty} \int_{-\infty}^{\infty} (g_1(y) - \mu_1)(g_2(z) - \mu_2) \phi[y, z, \rho_0(\tau)] dy dz \quad (45)$$

where g_1 and g_2 are the CDF mapping functions for the two random variables with potentially different marginal PDFs imparted by the operators g_1 and g_2 . Eq. 45 is required to calculate the off-diagonal terms in the underlying scaled covariance matrix (Grigoriu 1995, 1998).

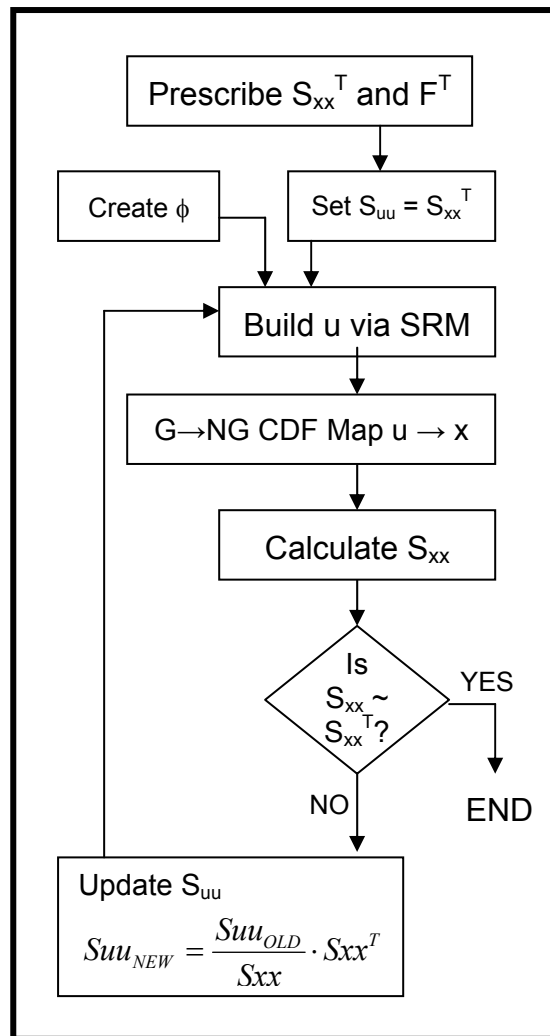


Figure 3-4. Yamazaki and Shinozuka univariate stochastic simulation technique

For large-scale Monte Carlo simulation, Grigoriu's method holds one major advantage. Since the underlying Gaussian spectrum is a function of the target PSD and

not the PSD of an individual sample function, it may be reused for each new simulation. Convergence to the target PSD can be shown in the ensemble sense, although any individual sample function will contain variance (ordinate) error in the PSD.

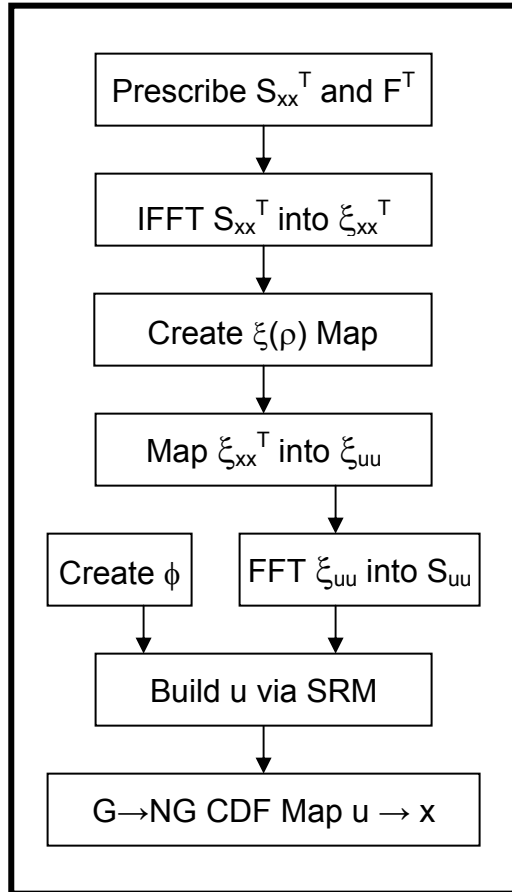


Figure 3-5 Grigoriu univariate stochastic simulation technique

Shinozuka and Deodatis (1996) presented an efficient algorithm to simulate ergodic Gaussian multivariate stochastic processes, and Gioffre et al. (2001) utilized a modified algorithm using Eq. 45 that is suitable for the simulation of stationary non-Gaussian random variables. An outline of this methodology (illustrated in Figure 3-6) is presented below:

Steps 1-6. Calibration: Random Variable Prescription and Correction for Non-Gaussian

The following steps need only be performed once for each set of probabilistic, spectral and cross-spectral targets.

1. For each random variable $X_1 \dots X_N$ (where N = number of correlated random variables under simulation), prescribe the following:
 - marginal PDF f_x (with mean $\mu_x = 0$ and variance $\sigma_x^2 = 1$)
 - PSD $S_{xx}^T(\omega)$ —appropriately discretized
 - $\sum_{k=1}^{N-1} k$ coherence functions $\gamma_{ij}(\omega, p_1, p_2, \dots, p_M)$ for each pair of i^{th} and j^{th} variates
2. Create an $N \times N$ target PSD matrix $S_{x_i x_j}^T$

$$S_{xx}^T = \begin{bmatrix} S_{x_1 x_1}^T & S_{x_1 x_2}^T & \dots & S_{x_1 x_N}^T \\ S_{x_2 x_1}^T & S_{x_2 x_2}^T & \dots & S_{x_2 x_N}^T \\ \vdots & \vdots & \ddots & \vdots \\ S_{x_N x_1}^T & S_{x_N x_2}^T & \dots & S_{x_N x_N}^T \end{bmatrix} \quad (46)$$

where the diagonal terms are the auto-PSDs (S_{xx}), and the off-diagonal terms are calculated from the coherence function and the respective auto-PSDs between the i^{th} and j^{th} variates:

$$S_{ij}(\omega) = \sqrt{S_{ii}(\omega)S_{jj}(\omega)} \cdot \gamma_{ij}(\omega, p_1, p_2 \dots p_M) \quad (47)$$

3. Using the Wiener-Khinchine Relationship,

$$\xi_{ij} = R_{ij}(\mu_i = \mu_j = 0, \sigma_i^2 = \sigma_j^2 = 1) = \int_{-\infty}^{\infty} S_{ij}(\omega) e^{i\omega t} d\omega \quad (48)$$

calculate the target scaled covariance function matrix ξ^T from the cross PSD S_{xx}^T

$$\xi_{xx}^T = \begin{bmatrix} \xi_{x_1x_1}^T & \xi_{x_1x_2}^T & \cdots & \xi_{x_1x_N}^T \\ \xi_{x_2x_1}^T & \xi_{x_2x_2}^T & \cdots & \xi_{x_2x_N}^T \\ \vdots & \vdots & \ddots & \vdots \\ \xi_{x_Nx_1}^T & \xi_{x_Nx_2}^T & \cdots & \xi_{x_Nx_N}^T \end{bmatrix} \quad (49)$$

4. Create the underlying Gaussian scaled covariance function ξ_{uu} by mapping the diagonal terms of Eq. 49 through Eq. 44 and the off-diagonal terms of Eq. 49 through Eq. 45
5. Using the Wiener-Khinchine Relationship,

$$S_{ij}(\omega) = \frac{1}{2\pi} \int_{-\infty}^{\infty} \xi_{ij}(\tau) e^{-i\omega\tau} d\tau \quad (50)$$

convert ξ_{uu} into the underlying PSD S_{uu}

$$S_{uu} = \begin{bmatrix} S_{u_1u_1} & S_{u_1u_2} & \cdots & S_{u_1u_N} \\ S_{u_2u_1} & S_{u_2u_2} & \cdots & S_{u_2u_N} \\ \vdots & \vdots & \ddots & \vdots \\ S_{u_Nu_1} & S_{u_Nu_2} & \cdots & S_{u_Nu_N} \end{bmatrix} \quad (51)$$

6. Perform a Cholesky decomposition of S_{uu} at each frequency point

$$S(\omega) = \begin{bmatrix} S_{11}(\omega) & S_{12}(\omega) & \cdots & S_{1N}(\omega) \\ S_{21}(\omega) & S_{22}(\omega) & \cdots & S_{2N}(\omega) \\ \vdots & \vdots & \ddots & \vdots \\ S_{N1}(\omega) & S_{N2}(\omega) & \cdots & S_{NN}(\omega) \end{bmatrix} = H(\omega)H^*(\omega)^T = \quad (52)$$

$$\begin{bmatrix} H_{11}(\omega) & 0 & \cdots & 0 \\ H_{21}(\omega) & H_{22}(\omega) & \cdots & 0 \\ \vdots & \vdots & \ddots & \vdots \\ H_{N1}(\omega) & H_{N2}(\omega) & \cdots & H_{NN}(\omega) \end{bmatrix} \begin{bmatrix} H_{11}^*(\omega) & 0 & \cdots & 0 \\ H_{21}^*(\omega) & H_{22}^*(\omega) & \cdots & 0 \\ \vdots & \vdots & \ddots & \vdots \\ H_{N1}^*(\omega) & H_{N2}^*(\omega) & \cdots & H_{NN}^*(\omega) \end{bmatrix}^T$$

Steps 7-10. Simulation of Correlated Random Variables

The following procedure is performed for each set of unique realizations.

7. Generate a complex white noise vector $\phi = \eta + \zeta i$ from two independent Gaussian white noise vectors η and ζ with means and variances

$$E[\eta] = E[\zeta] = 0 \quad (53)$$

$$E[\eta^2] = E[\zeta^2] = \Delta\omega \quad (54)$$

8. Multiply the cholesky decomposition $H(\omega)$ and ϕ to get the underlying correlated Gaussian PSDs $U(\omega)$

$$\begin{bmatrix} U_1(\omega) \\ U_2(\omega) \\ \vdots \\ U_N(\omega) \end{bmatrix} = \begin{bmatrix} H_{11}(\omega) & 0 & \cdots & 0 \\ H_{21}(\omega) & H_{22}(\omega) & \cdots & 0 \\ \vdots & \vdots & \ddots & \vdots \\ H_{N1}(\omega) & H_{N2}(\omega) & \cdots & H_{N2}(\omega) \end{bmatrix} \begin{bmatrix} \phi_1(\omega) \\ \phi_2(\omega) \\ \vdots \\ \phi_N(\omega) \end{bmatrix} \quad (55)$$

9. Inverse Fourier transform each $U(\omega)$ into its correlated Gaussian time series $u(t)$
10. CDF Map the correlated normal random variables through their respective target non-Gaussian probability distributions through Eq. 40. The underlying Gaussian PSD and cross-PSD will then distort to the final desired targets

Spectral Correction

Recent publications have presented alternatives to the Correlation Distortion methods to simulate univariate (Gurley et al. 1997, Masters and Gurley 2003) and multivariate (Gurley and Kareem 1998) non-Gaussian sample functions using a technique known as spectral correction. This method does not seek an underlying Gaussian PSD for the initial sample function and thus is not properly classified as a Correlation Distortion method. Rather, Spectral Correction iteratively applies corrective transformations to the probability and spectral content of the signal in the time and frequency domain, respectively, until the signal converges to the PDF and PSD targets.

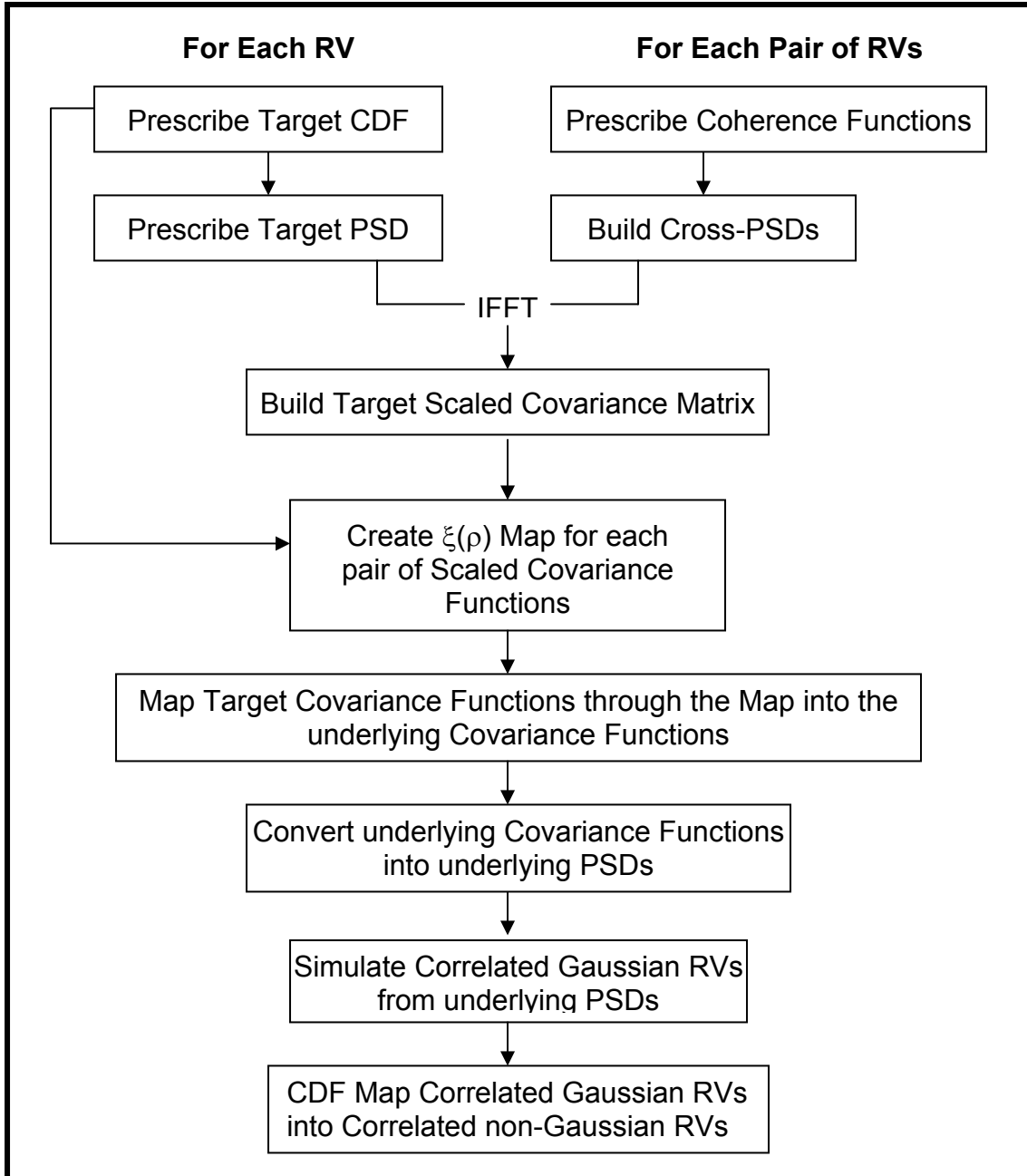


Figure 3-6. Shinozuka and Deodatis correlated non-Gaussian multivariate stochastic simulation technique

Two Spectral Correction methods are available for univariate simulation, and they differ by technique of random variable transformation. The original method by Gurley and Kareem (1997) relies on a Hermite-based probability filter to correct the statistical content of the simulated random process. Four-parameter models like the modified

Hermite polynomial (i.e., PDF models that require knowledge of the mean, variance, skewness and kurtosis to generate the parameters that affect the shape of the distribution) have been used with excellent results in a variety of applications where traditional models fail to properly represent the time series under consideration. The third order Hermite polynomial is one such four-parameter model that has been used in civil engineering applications. The coefficients in the polynomial are selected based on the desired first four moments (Winterstein 1995).

$$x = \mu_x + \kappa\sigma_x \left[u + c_3(u^2 - 1) + c_4(u^3 - 3u) \right] \quad (56)$$

$$\kappa = \left(1 + 2c_3^2 + 6c_4^2 \right)^{-0.5} \quad (57)$$

where the normalized Gaussian sample function u is translated to the non-Gaussian sample function x . The parameters c_3 and c_4 are dependent upon the desired third and fourth central moments (skewness γ_3^T and kurtosis γ_4^T):

$$c_3 = \frac{\gamma_3^T}{6} \cdot \left[\frac{1 - 0.015|\gamma_3^T| + 0.3(\gamma_3^T)^2}{1 + 0.2(\gamma_4^T - 3)} \right] \quad (58)$$

$$c_4 = c_{40} \cdot \left[1 - \frac{1.43(\gamma_3^T)^2}{\gamma_4^T - 3} \right]^{1 - 0.1(\gamma_4^T)^{0.8}}; \quad c_{40} = \frac{\sqrt[3]{1 + 1.25(\gamma_4^T - 3)} - 1}{10} \quad (59)$$

Eqs. 58 and 59 provide an approximate solution to identifying the parameters c_3 and c_4 . For higher accuracy, an optimization routine (using c_3 and c_4 as initial guesses) is employed to determine the parameters needed to provide a sample function with the desired moments (Gurley and Kareem 1997).

Limitations

The stochastic simulation methods outlined in the previous sections work well for many engineering applications, including the generation of environmental loads in the analysis of structural response, but are subject to limits concerning the choice of target probabilistic and spectral content. This section details those limitations.

Four Parameter Hermite Polynomial Transformation. Unlike the Correlation Distortion methods that utilize the CDF mapping concept, Hermite-based Spectral Correction uses only the first four moments to define the desired probability. The resulting PDF in the sample function is always described by a four-parameter third-order Hermite polynomial PDF model (Gurley and Kareem 1997, 1998a). The probability correction requires an optimization routine to identify the Hermite polynomial coefficients needed for an accurate transformation to the desired moments. This presents two limitations to the Spectral Correction method. The first is the computational expense of the simulation due to the embedded optimization. The second is a limit in the range of probability contents that can be simulated. Since the Hermite PDF (with its domain of $\pm \infty$) has unbounded tails, it may not accurately recreate a PDF that is bounded. Additionally, the absence of higher order moments (i.e., $> 4^{\text{th}}$ order, such as hyper-skewness and hyper-kurtosis) as inputs to the polynomial affects the tails and peaks adversely for some families of probability distribution functions.

A solution to these limitations replaces the Hermite polynomial transform with a modified CDF mapping technique to impart the desired probability to the realization (Masters and Gurley 2003). This improves numerical efficiency by eliminating the embedded Hermite optimization, and expands the range of probability content to any desired PDF model.

Spectral and Probabilistic Incompatibilities. The methods presented by Grigoriu (1998) perform well for symmetrically non-Gaussian and/or wide-banded systems, but incompatibilities will arise for certain combinations of highly-skewed and/or narrow-banded processes. This observation made by Grigoriu (1998) was addressed in several works (Deodatis and Micaletti 2001, Gioffre et al. 2001) by presenting two forms of incompatibility that arise during the translation of a Gaussian process u into a non-Gaussian process x :

1. Successfully mapping the target scaled covariance function ξ_{xx}^T through the mapping scheme is only possible if every ordinate of ξ_{xx}^T lies between ξ^* and 1, where ξ^* equals the evaluation of the double integral at $\rho = -1$. If any value of ξ_{xx}^T falls outside this range (i.e., $\xi_{xx}^T \in [-1, \xi^*]$), an incompatibility exists. The off-diagonal cross-covariance functions are also susceptible to this incompatibility with the additional constraint that the map is bounded above ($\rho = 1$) as well as below ($\rho = -1$)
2. The underlying autocorrelation function ξ_{uu} as determined through the application of Eqs. 44 and 45 can be non-positive definite, producing an underlying Gaussian power spectral density S_{uu} with values < 0 . This is a physically unrealizable condition

The Efficacy of Large-Scale Simulation. In addition to the above-mentioned mathematical obstacles associated with the algorithm, large-scale multivariate simulation also carries storage limit issues. The use of cross-spectral matrices inherently requires tremendous data storage and handling capacity. For example, multivariate simulation via the method offered by Grigoriu requires $\frac{1}{2}(N^2 + N)$ integrations of Eqs. 44 and 45, where N is the number of random variables under simulation.

One collaborator in the NIST project, Massimiliano Gioffre of the University of Perugia, reported extreme difficulty in simulating more than 8 correlated random variables at one time at the expense $\frac{1}{2}(8^2 + 8) = 36$ integrations. The practical bottleneck is the solution of the Cholesky decomposition of the spectral matrix. The spectral matrix

associated with $N > 8$ strongly correlated variables leads to ill-conditioned spectral matrices, and the decomposition fails. While this can be numerically avoided using an ad-hoc adjustment procedure, eventually enough frequencies are affected that the resultant simulations diverge from the intended cross-spectral targets.

Application of Simulation for the NIST Project: Interpolation of Existing Time Histories

As presented in Chapter 2, the specific application of stochastic simulation in this research is to digitally create uplift loading on the roofs of low-rise structural shapes that were not tested in wind tunnel studies. The spectral and probabilistic targets for the simulations are derived by interpolating models from time histories of tested buildings of similar shape. Given the restrictions in the number of variables that may be simulated, efforts focus on simulation of aggregate loads over large sections of the roof. Evaluating the efficacy of deriving appropriate models using interpolation schemes is a major contribution to the NIST project. The direct interpolation of peak loads from measured time histories was also found to be valid, thus deemphasizing the need to rely on full simulation algorithms to characterize key load parameters on untested buildings. Details of the study are found in Chapter 6.

Summary

This chapter presented the background material for the original contributions to be discussed in Chapters 4 through 6. The statistical characterization of hurricane winds has been discussed, and will be applied in Chapter 5 to the analysis of FCMP datasets collected since 1999. Non-Gaussian stochastic simulation has also been discussed, including the limitations which partially determined the direction of the research

presented in Chapter 6. The next chapter presents FCMP data collection efforts, and the impact of the program on meteorological and emergency management interests.

CHAPTER 4 FULL-SCALE MEASUREMENT OF TROPICAL CYLONE WINDS

During the 1998-2003 Atlantic hurricane seasons, the FCMP deployed instrumented towers for ten named storms—Georges, Dennis, Floyd, Irene, Gordon, Gabrielle, Michelle, Isidore, Lili and Isabel—and collected 29 data records at locations throughout Florida, Louisiana and North Carolina. Nineteen of these records were selected for analysis in Chapter 5.

This chapter addresses four aspects of the experimental process. First, the history, organization and logistics of deployments for selected storms are discussed. Second, the satellite tower system employed during Isabel (2003) to calculate lateral integral length scales is presented. Third, this chapter details the development and implementation of the first mobile real-time data acquisition system to transmit detailed coastal tower wind data to National Oceanic and Atmospheric Administration (NOAA) meteorologists during a landfalling hurricane. Finally, outcomes of the real-time data acquisition system are addressed, specifically the response from meteorological and emergency management interests.

Deployment History, Organization and Logistics

This section provides a brief narrative of the events that occurred during four storm deployments and details the involvement of research teams at the University of Florida (UF) and Clemson University (CU). Synoptic history and track data for each cyclone were taken from the National Hurricane Center Tropical Cyclone Report archives, available at the agency's website: www.nhc.noaa.gov. Pictures of the deployment sites

are located in Appendix B and may also be found at the project website:

www.ce.ufl.edu/~fcmp.

Irene (1999)

At 1200 UTC on October 13, 1999, Irene reached tropical storm status in the northwestern Caribbean Sea and kept a general northward track before slowing down and curving to the north-northeast southwest of the Isle of Youth, Cuba. The center of the storm crossed the Havana and Ciudad Havana provinces on the 14th. Irene reached hurricane status over the Florida Straits before its center moved over Key West and made landfall near Cape Sable, Florida as a tropical storm. The cyclone trekked across southeast Florida, eventually reemerging back over water in northern Palm Beach County near Jupiter at approximately 0000 UTC on the 16th.

UF and CU teams arrived in Melbourne Beach prior to the storm's arrival on the evening of the 15th, where colleagues from Florida Institute of Technology and local authorities assisted in the location of deployment sites. With their assistance, teams were able to begin acquiring data by 1100 UTC.

During the night, Irene regained hurricane strength and began a northward track paralleling the Florida east coast heading for the Carolinas. An upper-level trough, sweeping eastward across the eastern United States, sped its progress. On the morning of the 16th, teams collected the towers and caravanned up the I-95 corridor to intercept the storm. Within a few hours, the convoy was traveling parallel to Irene, where buffeting winds and unavailability of fuel (gasoline pumps require power to operate) significantly impeded the team's progress.

At 0100 UTC on the 17th, twenty-five hours after the departure from Melbourne Beach, teams arrived in Wilmington, NC, where two towers were deployed. Residential

and shoreline exposure were chosen—the shoreline site would be later reused by Tower T1 in Hurricane Isabel. The FCMP only succeeded in capturing the outer bands of Irene in North Carolina because the cyclone veered away from the mainland and brushed the Outer Banks before moving out to sea.

Gabrielle (2001)

The shortest deployment in FCMP history occurred during Gabrielle, which made landfall in Venice, Florida around 1200 UTC on September 14, 2001. The cyclone moved in a small counterclockwise loop over the southeastern Gulf of Mexico for two and a half days before reaching tropical storm strength on the 13th. At that time, Gabrielle was located 325 km southwest of the landfall site.

One UF team with tower T1 in tow left Gainesville around 2200 UTC on the 12th to intercept the storm and arrived in Venice Beach immediately prior to landfall. Data collection continued into the early afternoon, and the team returned to the University of Florida by late evening.

Isidore (2002)

Isidore became a hurricane at 1800 UTC on September 19, 2002 as it tracked west-northwest across the Cayman Islands. As the cyclone neared the southwest coast of the Isle of Youth, Cuba, the FCMP deployed one UF team to monitor the storm from Key West, Florida. Isidore moved westerly, however, and the team only succeeded in capturing the outermost bands of the cyclone. Isidore moved west and southwestward toward the Yucatan Peninsula, reaching its maximum intensity of 56.6 m/s (126.7 mph) at 1800 UTC on the 21st. The cyclone remained nearly stationary for 24 to 36 hours over northern Yucatan and weakened to a minimal tropical storm, before it moved northward over the Gulf of Mexico. Figure 4-1 contains a map of the deployment region.



Figure 4-1. Deployment of instrumented towers during Tropical Storm Isidore (2002)

UF and CU FCMP teams remained on standby as the cyclone moved northward into the Gulf of Mexico, anticipating the possibility that Isidore might strike somewhere in the array of instrumented homes located on the west end of the panhandle of Florida (shown in Figure 2-4). On the 24th, UF met CU in Gulf Breeze, Florida, to ready three instrumented homes and set up three towers (T0, T1 and T2) in close proximity.

Isidore made landfall with winds of 28.3 m/s (63.4 mph) with a minimum pressure of 984 mb just west of Grand Isle, Louisiana at 0600 UTC on the 26th. Although it weakened to a minimal tropical storm in the Gulf of Mexico, its circulation expanded which provided significant wind (as high as 26.9 m/s) approximately 350 km away.

Lili (2002)

As the center of Hurricane Lili trekked past the southwest tip of the Isle of Youth over western mainland Cuba on October 1st, FCMP teams from CU and UF traveled to

Mobile, Alabama. On the morning of the 2nd (while the cyclone turned northward through the Gulf of Mexico), FCMP personnel and equipment caravanned to Baton Rouge, Louisiana and set up base camp. In the afternoon, the team split into two deployment groups. The first team traveled west along I-10 inserting towers in Lafayette (T0) and Baton Rouge (T1). The second team traveled south placing towers in Donaldsonville (T2) and Lydia (T3). With nine personnel working, the four towers went operational over a 7-hour period (between 2/2303 and 3/0616 UTC). Figure 4-2 illustrates the tower locations with respect to the path of the cyclone.

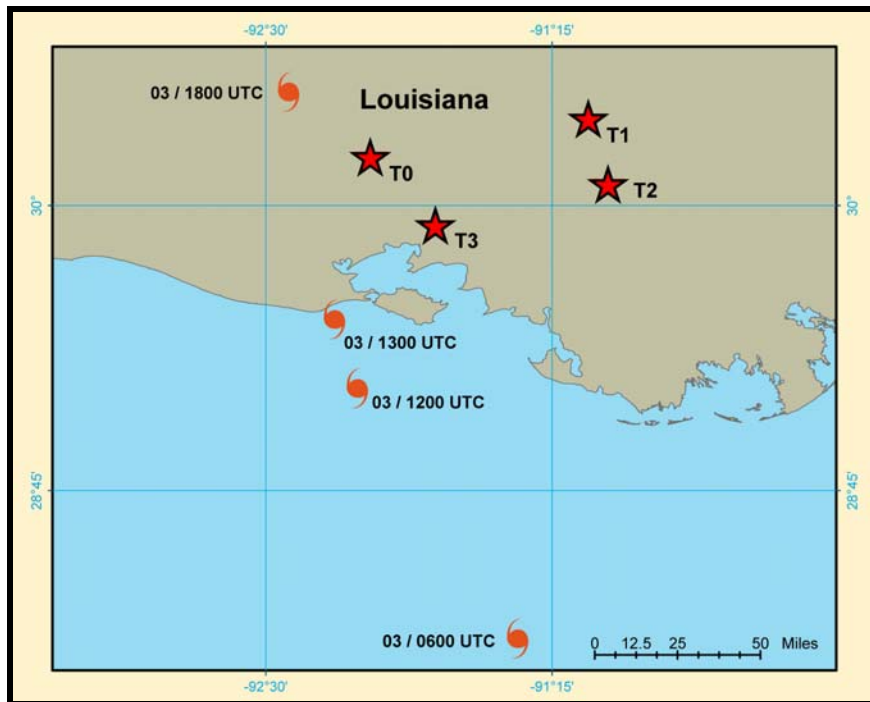


Figure 4-2. Deployment of instrumented towers during Hurricane Lili (2002)

Between Cuba and Louisiana, Lili intensified to 64.4 m/s (144 mph) early on the 3rd over the north-central Gulf of Mexico and then rapidly weakened during the 13 hours until landfall. Lili made landfall on the Louisiana coast with an estimated 41.2 m/s (92.2 mph) maximum wind speed.

Isabel (2003)

Isabel captured the attention of the FCMP during the second week of September 2003. Initially, it appeared that the storm's path would bring in within striking distance of Florida's Atlantic coastline as it emerged from the Greater Antilles. Uncertainty in the forecast beyond that point, namely the influence of troughs/ridges that would eventually steer the storm, brought great trepidation to communities in hurricane prone regions along the Atlantic coast. At its peak intensity, the hurricane, with Saffir-Simpson Category 5 winds and a 90 km eye, represented a potential major threat to lives and property.

By the end of the week, meteorologists at NOAA's Tropical Prediction Center had narrowed the projected path of the storm to landfall somewhere in or above the Carolinas. On the 13th, FCMP teams were put on standby, anticipating deployment to that region. Final testing of the new "internet-capable" data acquisition system was completed earlier in the week, and for the first time, the FCMP mobile towers were synchronized with forecasters at the Hurricane Research Division of NOAA to transmit real-time high resolution data every 15 minutes from the field. Equipped with this new technology, the team from the University of Florida left Monday with towers T1 and T2 and arrived in Morehead City, NC early Tuesday.

The optimal location for a tower (to capture the highest winds) is north of the predicted landfall for a hurricane striking the Atlantic coast. To achieve this end required tower deployment around the Outer Banks, a great challenge for the FCMP. First, traveling on barrier islands required that the team arrive well in advance of the closures of inbound traffic lanes. Secondly, potential tower sites were limited by the storm surge potential for that area.

After coordinating with the Clemson University FCMP team and researchers from Texas Tech University, the UF team decided to deploy T2 in the vicinity of Morehead City (north of the latest forecasted landfall). With the help of South Carolina Sea Grant, the team contacted the North Carolina Department of Environment and Natural Resources and received permission to erect a tower at Fort Macon State Park. T2 went operational at 1530 UTC, and afterwards, the team secured lodging in Morehead City.

For the remainder of the afternoon, the team scouted Craven and Pamlico counties to locate a site amenable to the new satellite tower system, which required an open 60 m swath of land to erect the three towers. As nightfall approached, it became apparent that the majority of the coastline was unacceptable for deployment, given the reach of the estuary system and its favorable environment for flooding and storm surge. The team backtracked its survey and received permission to deploy the towers on a horse ranch in Oriental, a small town five miles inland. Meanwhile, the Clemson FCMP team arrived in Wilmington to begin instrumentation of a home the following day.

Early Wednesday morning, the UF team traveled from Morehead City to Wilmington to reorganize teams. The first (southern) team remained in Wilmington to instrument the home, and the second (northern) team pulled the remaining towers northward to deploy in Elizabeth City (T0) and Cape Hatteras (T3), two population centers with established local contacts and potential for higher ground. As the northern team split off, 36 hours remained until the expected landfall of Isabel.

The T0 Team secured a site at the Elizabeth City Coast Guard Airstation. Bordering Pamlico Sound, the flat expanse of terrain afforded by the airport provided a significant amount of upwind open exposure. After some modifications to the new

software were made, T0 went operational at 0541 UTC. The team secured lodging for the entire northern team nearby.

The T3 team traveled through Manteo to reach the outer banks. After conferring with locals, the team decided to deploy the tower at Billy Mitchell Airport, purportedly the highest ground in Cape Hatteras. T3 went operational at 0214 UTC on the 18th, and afterwards, the team drove to Elizabeth City to join up with the remainder of the northern team.

Meanwhile, the southern team had split, allowing one group to complete the home instrumentation and the other to refill the onboard generator on T1 in Oriental. New information concerning flooding at the existing site, however, prompted the team to relocate T1. With the preparations to instrument the home in Wilmington nearing completion, the team decided to relocate T1 to capture the wind field in the vicinity of the house. The teams recombined and erected the tower system at a nearby boat ramp. T1 restarted at 0420 UTC on the 18th.

After the storm passed, the priority of all teams involved became retrieval of instrumentation. For T0, T1 and T2, this was a relatively straightforward operation, but extracting T3 from Cape Hatteras required significantly more effort than inserting it. Multiple roadblocks separated the team from the tower, each progressively more difficult to negotiate. After acquiring the proper permit, the team stopped in Kill Devil Hills to perform damage surveys. The imposed mandatory curfew throughout the Outer Banks forced the team to continue south to collect the remaining tower, however.

The storm surge that impacted the strip of land between Nags Head and Rodanthe rendered US 12 impassable in some areas, leaving up to 2 m of aerated sand across the

roadway. Using 4-wheel drive and bypassing the road via the beach, the team inched their way down the coastline, arriving in Cape Hatteras in the early afternoon. A map of the impacted region and the location of FCMP instrumentation is provided in Figure 4-3.



Figure 4-3. Deployment map for Hurricane Isabel

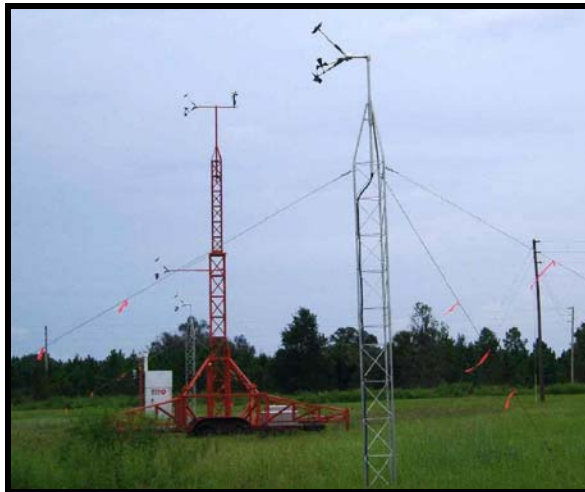
Satellite Tower System

Studies of the correlation structure and integral length scales of lateral turbulence have been conducted since the 1920s. The earliest experiments were conducted to study the strength of wind loading on electric power lines in winter storms (Sherlock and Stout 1937). Through 1960-1972, extensive three-dimensional turbulence data were obtained (Counihan 1975), and relationships between the longitudinal and lateral components were

developed (Shiotani 1967, Harris 1971, Deacon 1971). In the summer of 2003, two of the four instrumented towers were outfitted with additional towers to conduct similar experiments, but in a wider range of exposures and in tropical cyclone winds.

Lightweight (<37 kg) and highly portable, the 5-m aluminum towers may be erected up to 37 m (120 ft) from the main tower. In practice, the satellite towers are separated from the main tower by 15.2 m (50 ft) and 30.5 m (100 ft). This asymmetric configuration allows the FCMP teams to investigate correlations of wind speeds of lateral separation distances < 45.7 m (150 ft). The left picture in Figure 4-4 illustrates the deployment geometry and orientation (as configured for testing in Tropical Storm Henri)

A team of three people can assemble one tower in less than 30 minutes. The main tower is erected with the tongue of the trailer facing the direction of anticipated maximum winds (into the path of the storm at landfall). Next, the team removes the satellite towers from the main tower (shown in the right picture in Figure 4-4) and places them on opposite sides of the main tower.



(a) Tower array



(b) Transportation

Figure 4-4. Tower deployment and transportation

The satellite towers employ two measures to resist the wind: four shear pins are driven with a sledgehammer to resist sliding (shown in the left picture in Figure 4-5) and three guy wires attach the top of the tower to earth screws to provide lateral stability (shown in the right picture of Figure 4-5).

Once the guy wires are attached at the top of the tower, research personnel auger the earth screws into the ground and attach RM Young three-axis gill anemometers to the same assembly hub found on the larger towers. Then, the tower is raised and the guy wires are connected to the earth screws. The turnbuckles are tightened to remove slack and to level the tower. Finally, safety ribbons are tied to the guy wires for visibility, and a shielded cable is connected from the main tower's computer enclosure to the satellite tower. Figure 4-6 illustrates this process.



(a) Shear Pins



(b) Earth Screws
and Guy Wires

Figure 4-5. Satellite tower stabilization

During Isabel, the satellite tower system was tested successfully at the Wilmington and Frisco, North Carolina sites. Preliminary results of length scale analysis, site details and suggestions for future deployments may be found in Aponte (2003).



(a) Anemometry



(b) Safety measures

Figure 4-6. Satellite tower instrumentation and safety considerations

As the goal of this research is the estimation of lateral and longitudinal length scales in different roughness lengths, many additional experiments will have to be performed to produce statistically meaningful results. For this reason, the FCMP will construct six additional lightweight 5-m towers for the 2004 season. The 5-m tower design has been modified for the construction of two 10-m lightweight tower systems. The 10-m towers will operate independently of the main tower—data collection will be performed on a notebook computer encased at the base of the tower. These systems will also be internet capable, the subject of the next section.

Real-Time Data Acquisition

Recognizing that real-time access to surface level wind speeds during hurricane landfall would aid:

- meteorological institutions forecasting the hurricane's path and local news affiliates providing weather updates to the public
- federal, state and local agencies conducting emergency management operations including both evacuation and assignment of limited recovery resources post-disaster

- utility companies assessing potential damage and estimating a time of safe entry to begin restoration of power, water, telephones, etc.
- the FCMP teams, which need to respond quickly to any problem that might occur during data acquisition,

the FCMP team enhanced its existing hardware and software on its mobile tower system to disseminate real time data over the internet. Each of the four 10-meter towers is now equipped with new hardware and software that orchestrate collection, post-processing and internet connectivity on National Instrument's LabVIEW platform. The new software, dubbed Tower XP, was developed at the University of Florida and represents an original contribution to FCMP research efforts.

For redundancy, the FCMP team used the original tower computer system (detailed in Chapter 2) in conjunction with the new hardware/software. Additional storage space was needed and new computer enclosures were constructed to house the laptops, cellular modem and CDMA antenna (shown in Figure 4-7).



(a) Enclosure Fabrication



(b) Mounted Enclosure

Figure 4-7. Computer enclosure for remote transmission of FCMP data

The Tower XP software retained all of the capabilities of the original software (used since 1998) and received five major enhancements: real-time data transfer to the internet, continuous data acquisition, automatic data processing, an improved graphical interface and the flexibility to make changes to the software in the field if necessary.

Internet Upload Capability

Given the number of available coverage plans and technologies available to implement the real-time data acquisition system, a study was carried out to determine the optimum plan for the FCMP's needs. Four of the major cellular technologies in the United States were considered: Global System for Mobile Communications (GSM), Iden/Nextel, Time Division Multiple Access (TDMA) and Code Division Multiple Access (CDMA). TDMA and CDMA dominate the American markets, with GSM gaining in popularity but still lacking in coverage. CDMA is considered the more advanced digital technology and generally has better performance than TDMA because it separates channels by giving each user a unique code that is used to identify his or her conversation.

For this project, a CDMA dual mode digital cell phone that works in the 850 MHz band was chosen to transmit data from the tower to remote network servers every 15 minutes. Verizon's wireless data service plan was chosen from the subset of companies offering this service because it carries the largest area of coverage in the southeastern United States. With this plan, the laptop dials into one of two services depending on availability. In larger cities, the modem connects to Verizon's Express Network (CDMA2000 1X) and transfers data at speeds up to 144 Kbps (averaging 40-60 Kbps). Otherwise, the modem dials into Verizon's Quick 2 Net service on regular CDMA with

speeds up to 14 Kbps. Either way, the modem dials directly into an internet service provider (ISP), making file transfers out of LabVIEW possible.

The modem is connected to the notebook by a serial port connection, and TCP/IP connections are managed by Microsoft Windows' built-in command window dial-up capabilities (rasdial.exe). Once the notebook connects to Verizon's internet service, files are transferred through execution of customized file transfer protocol (FTP) scripts. If the transfer is successful, the modem disconnects and the software waits until the next transfer request. If the transfer fails, Tower XP tries connecting once more with the high speed connection before attempting a final connection with the slower service. The software also supports the option to use either an ethernet or a phone line to connect to the internet and can be configured to disable its upload capability if required.

Continuous Data Acquisition

The original system collected data and paused 2-4 seconds to store it to the hard drive after every 15 minutes of operation, which left gaps in the data. In Tower XP, data are stored at 10 Hz in a circular memory buffer on the data acquisition card, which allows for seamless acquisition and storage.

Automated Processing of Data

The original software (prior to summer 2003) did not process data during acquisition and required considerable effort to extract the data. Raw voltages were written to binary data files and reloaded into the program post-storm to retrieve the data. Voltages were scaled into engineering units, and records from gill anemometry were converted from the non-orthogonal experimental configuration into wind speed, wind direction and the vertical fluctuation. As the system did not possess batch processing capabilities, research personnel were required to spend three to four hours extracting the

individual files. Additionally, corrections for the tower orientation and time gaps had to be made in post-analysis. All of these procedures had to occur before analysis (turbulence intensities, gust factors, length scales and spectra) could begin.

Tower XP was designed to obviate these issues. The software calculates turbulence intensities, peak gusts, roughness length estimates, and averages of temperature, humidity, rainfall and barometric pressure information every 15 minutes and writes a summary text file for transfer to the internet through its built-in upload feature. After the storm, research personnel activate a subprogram that batch processes the data into text files, which are formatted to be read into several analysis programs (including Matlab, Mathcad and Excel). Wind direction records are automatically adjusted with regard to the orientation of the tower, and each instantaneous data point is uniquely time stamped. For 2004, a new module is under development to write (serialize) data directly to Matlab binary files to improve processing times.

Improved Graphical Interface

This interface allows users to input considerably more information about the deployment site and its terrain than the original software. Figure 4-8 illustrates the configuration of the user interface of the data acquisition software developed for Tower XP. After the program is started, the user activates the configuration algorithm (user interface), which consists of five components (dialog boxes). First, the sampling rate and the number of scans are set. Based on the number of channels, the size of the binary files is estimated. Second, information about the storm and the location and orientation of the tower is input. This information is written to a text file that can be sent to the web server if desired. Third, easy-to-read gauges and digital readouts provide 1 Hz measurements from all of the instrument channels to assist research personnel during the system

checkout. Fourth, descriptions of the upwind fetch are entered into the program. If the user has captured digital photos of the site, a dialog box can be activated to load the picture into the program for uploading to the web server. This feature can only be used with the high speed cellular or ethernet connections. Finally, the user selects the connection type and initiates a test of the software's upload capability.

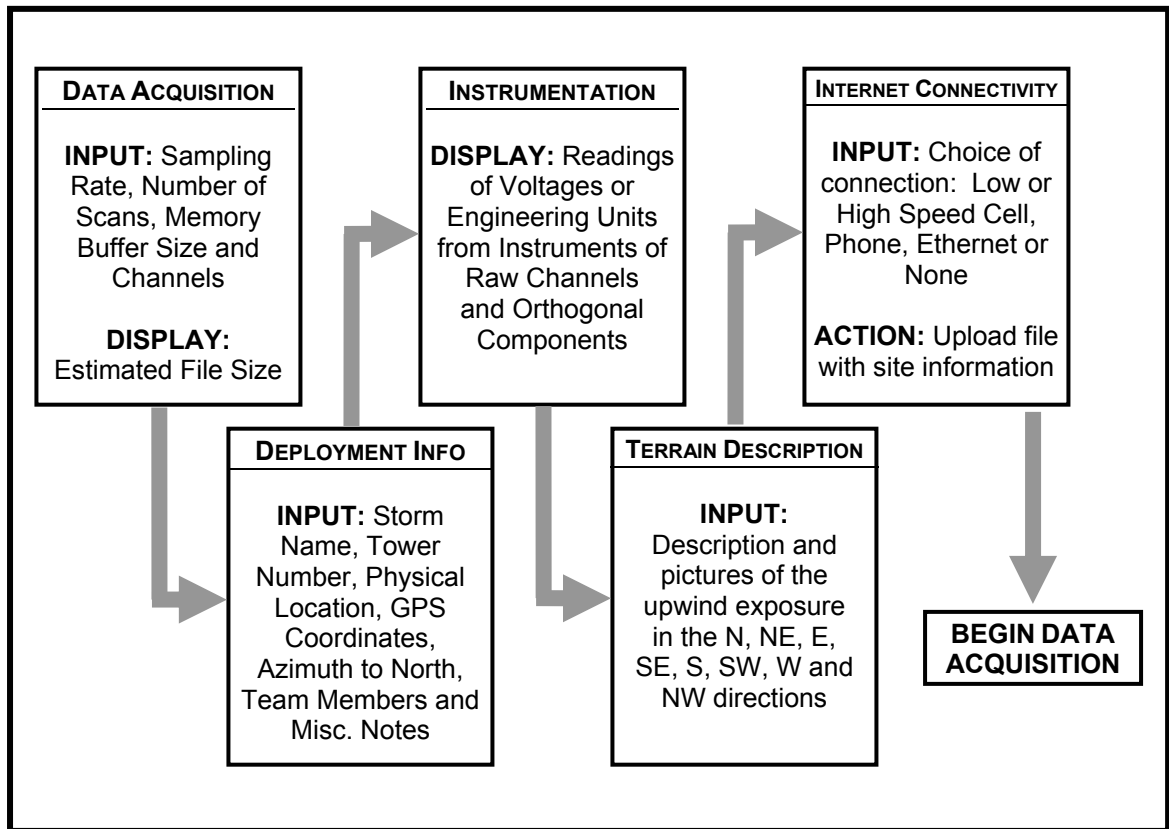


Figure 4-8. Configuration of Tower XP user interface to set up data collection

Tower XP's graphical interface is updated every time data are stored to the hard drive. Research personnel can view 3-second and 1-minute time histories of wind velocity data recorded in the previous 15-minute segment.

Improved Flexibility

Tower XP is a flexible program that can easily be reconfigured to collect data over any length interval. Unlike the original software, the LabVIEW platform is an interpreted, graphical language that does not require recompilation of the source code if a change is made. The capability to record data from the satellite tower system was added to the program's functionality. In a future version, this feature will be activated.

Outcomes of Hurricane Isabel

The FCMP intended Hurricane Isabel to be the proving grounds to test the prototype real-time data acquisition system. Within 24 hours of the first upload, however, its role in a research experiment shifted to that of an operational tool for meteorologists and hazard loss estimators. Each of the four tower systems reliably transmitted data to web servers even while a number of METAR and CMAN weather stations lost communication with their network.

This section addresses the importance of continuing synergistic research in the wind engineering community, specifically through the efforts of the FCMP to meet the needs of forecasters and emergency managers during Hurricane Isabel. The feedback from the various users of the real-time data systems deployed during Isabel indicates a strong need for continuation of this program and the further development of its capabilities.

Impact on Meteorology

The concept of developing a real-time data acquisition capable of transferring summary files to the internet was borne from the recognition that meteorologists and FCMP researchers could equally benefit from a remote monitoring capability. During its development, considerable interaction occurred with scientists at the Hurricane Research

Division (HRD). HRD is the unit of NOAA dedicated to advancing the basic physical understanding of hurricanes and to improving the forecasts of tropical meteorological systems. Based on their recommendations, the summary format and transmission scheme were developed.

During Isabel, the collected data were ingested into HRD's real-time hurricane wind analysis system, H*Wind, and utilized to validate measurements from reconnaissance aircraft. Additionally, observations at the northern sites were used to monitor decaying weather conditions.

H*Wind. Since 1996, the Hurricane Research Division has operated the H*Wind Project to integrate wind data in and around a hurricane into a single surface-level wind analysis for use by hurricane specialists at the National Hurricane Center. Continual development over this period was intended to evolve H*Wind from a hind-casting to a now-casting model of overland surface level hurricane winds. Data sources include ships, buoys, coastal platforms, surface aviation reports and reconnaissance aircraft data. The evolution to now-casting is dependent upon the availability of data in near-real time rather than post storm recovery of wind velocity data.

During Isabel, FCMP data were ingested into eight runs of the H*Wind model over September 17th and 18th. Figure 4-9 contains a map of the 1-minute maximum gusts at 1630 UTC as determined by the H*Wind software. Note at the top of the figure the reference to TOWER_LD_T0 as a source of data for this analysis. These analyses were also used by the National Hurricane Center as a part of the Joint Hurricane Testbed, a consortium between NASA, NOAA and the U.S. Navy seeking to expedite the transfer of

technology from the United States Weather Research Program (USWRP) to operational meteorologists.

Aircraft Reconnaissance. Meteorologists at NOAA's Hurricane Research Division conduct aircraft experiments to support multiple ongoing research activities at the center. Research aircraft deploy expendable instrument packages called Global Positioning System (GPS) sondes to measure pressure, temperature and position throughout their descent, which is retarded by a parachute. During Isabel (Mission 20030918H1), research aircraft deployed numerous sondes near the Diamond Shoals area specifically for comparison with real-time data reported by Tower T3 at Cape Hatteras. The track of the aircraft through North Carolina is shown in Figure 4-10, and shows the reliance of the path upon the location of the FCMP tower. Sonde splashdown locations are shown in Figure 4-11, showing significant and intentional clustering near FCMP tower locations. Data from several other sensors were compared to the incoming data from the instrumented towers, including emissivity records from the stepped frequency microwave radiometer and surface wind speed estimates from flight-level data.

Forecasting. The observations made by the Frisco, NC tower (Tower T3) constitute the highest ground level wind speeds recorded during Isabel and are also the highest wind speeds for which continuous, high frequency, digital observations have been recorded in a U.S. landfalling hurricane. The reaction from meteorologists was encouraging. On October 19th (the day preceding landfall), Peter Black, Director of the Coupled Boundary Layers/Air-Sea Transfer (CBLAST) project, contacted the FCMP in regards to the real-time transmission. An excerpt from his email follows:

“The placing of your towers appeared just about optimal and the reliability of your real time reports while I was doing the HWIND analysis at NHC on Wed night was

fantastic. The CMAN sites went down for a time due to communications problems at Wallops and your data were the only wind reports from the coast that were coming in. I was able to relay the reports to the NHC forecasters and keep them abreast of the rate of wind increase at the coast as Isabel approached. Your effort is a terrific example of how a research project can make a valuable contribution to operations while at the same time gather a research data set that will be studied for years. ... Not only did it make the HWIND product invaluable to forecasters but gave them a sense for how quickly conditions on the coast were deteriorating.”

Impact on Emergency Management

The towers were in close proximity to the Atlantic Ocean, which meant that they provided some of the first inland wind speed observations in the impacted region. They also provided these data four times an hour, a considerably higher frequency than existing weather stations. Unknown to FCMP research personnel during Isabel, these two characteristics prompted hazard loss estimators contracted by the Federal Emergency Management Agency (FEMA) and several major (re)insurance companies to use the real-time data to monitor decaying weather conditions. Modelers at several internationally recognized consultant firms, including Applied Research Associates (ARA) and Risk Management Services (RMS), conducted loss estimates throughout the storm’s landfall (personal correspondence with Auguste Boissonnade, RMS, April 4, 2004). Once discovered, this fact explained why the FCMP project website—initiated one week earlier and known only to project personnel and collaborators at NOAA—received almost 4000 hits in the 24 hours preceding the storm’s landfall.

The largest of these models is FEMA’s hurricane risk-assessment software (HAZUS-MH), which estimates the physical damage, economic loss and social impact from a hurricane impact. In the weeks preceding Isabel’s arrival, contractors at the National Institute of Building Science and ARA were beta testing the latest release. FEMA decided to implement the program to produce its official damage estimates

through the storm. Wind swath data generated from the H*Wind software was ingested into the model (shown in Figure 4-12), and wind speed estimates were validated against FCMP real-time data.

According to presentations at the 2004 National Hurricane Conference (NHC) in Orlando, the developers of the FEMA HAZUS-MH model were able to project damages within 20% of the final actual tallies. Specific credit was given to the FCMP real-time data systems for providing accurate wind speed information. The potential impact of a forecasting / now-casting model of hurricane wind damage lies in the ability of emergency management personnel to allocate recovery resources better in the immediate aftermath of a storm and to make more informed decisions regarding evacuation. The FCMP personnel presented the details of the real-time data system at the 2004 National Hurricane Conference, and received immediate commitments from emergency managers for special assistance with logistics for future deployments, including special access to restricted areas and identification of ideal deployment locations. Such feedback and cooperation underscores the potential impact of this research in the eyes of both federal and local emergency managers.

Summary

This chapter details the FCMP deployment histories for those storms that are used for the analyses to be presented in Chapter 5. The development of new hardware and software implemented during the 2003 season is also presented. The significance of these contributions is documented in terms of their impact upon the hurricane meteorology and emergency management communities.

Beyond providing nearly instantaneous information on peak winds and roughness estimates, the data collected from the FCMP towers also serves engineers seeking to

better characterize the localized ground-level behavior of landfalling hurricane winds and their interaction with structures. The detailed analysis of these wind records from the perspective of wind and structural engineers is presented in Chapter 5.

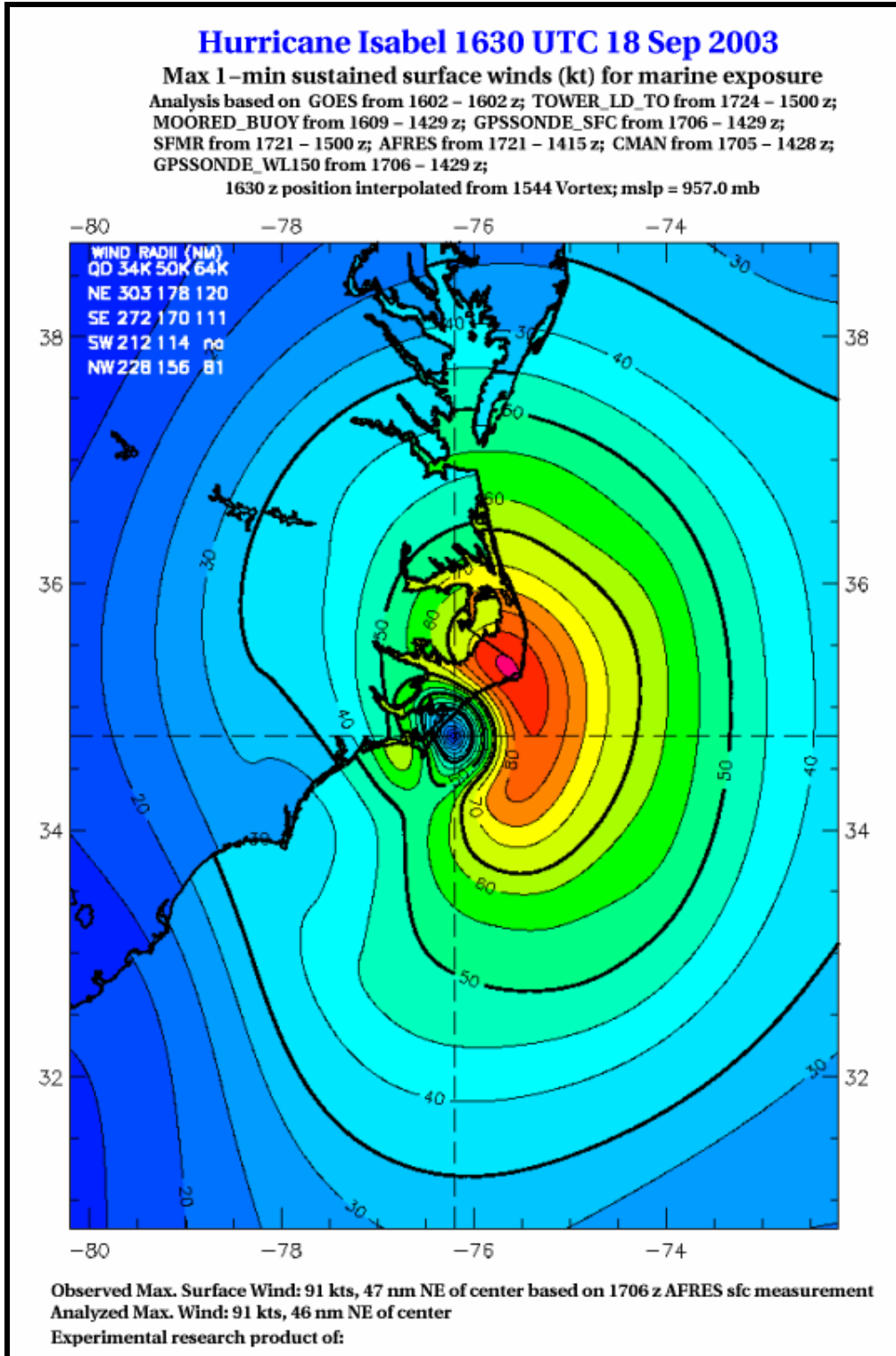


Figure 4-9. Hurricane Research Division surface wind field analysis (courtesy of NOAA)

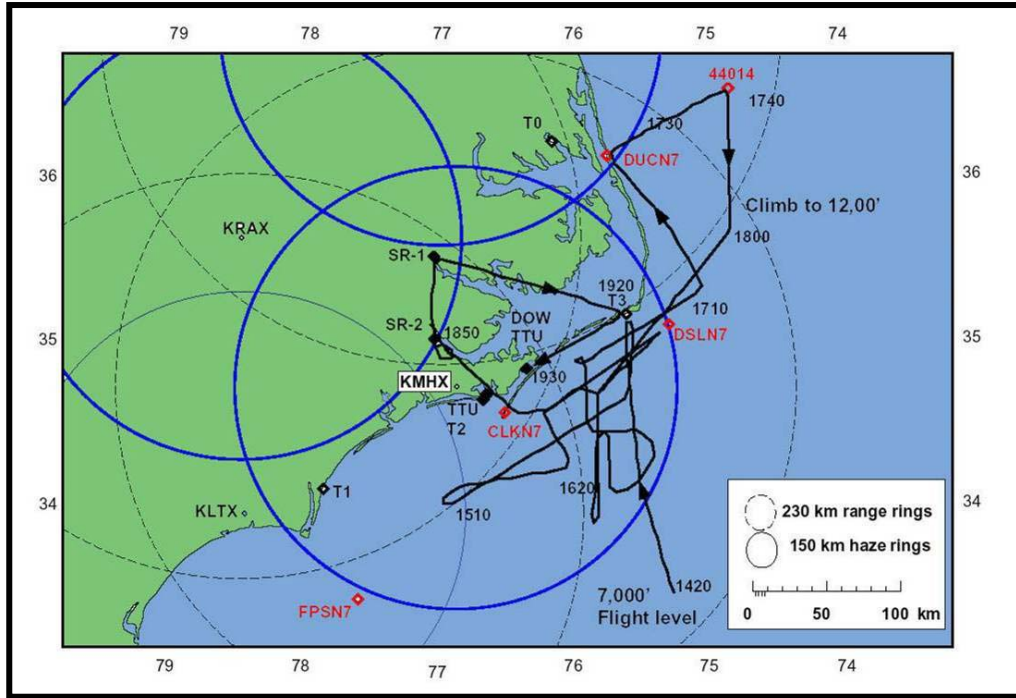


Figure 4-10. Track of NOAA research aircraft in Coastal Mission 20030918H1 during Isabel 2003 (courtesy of NOAA)

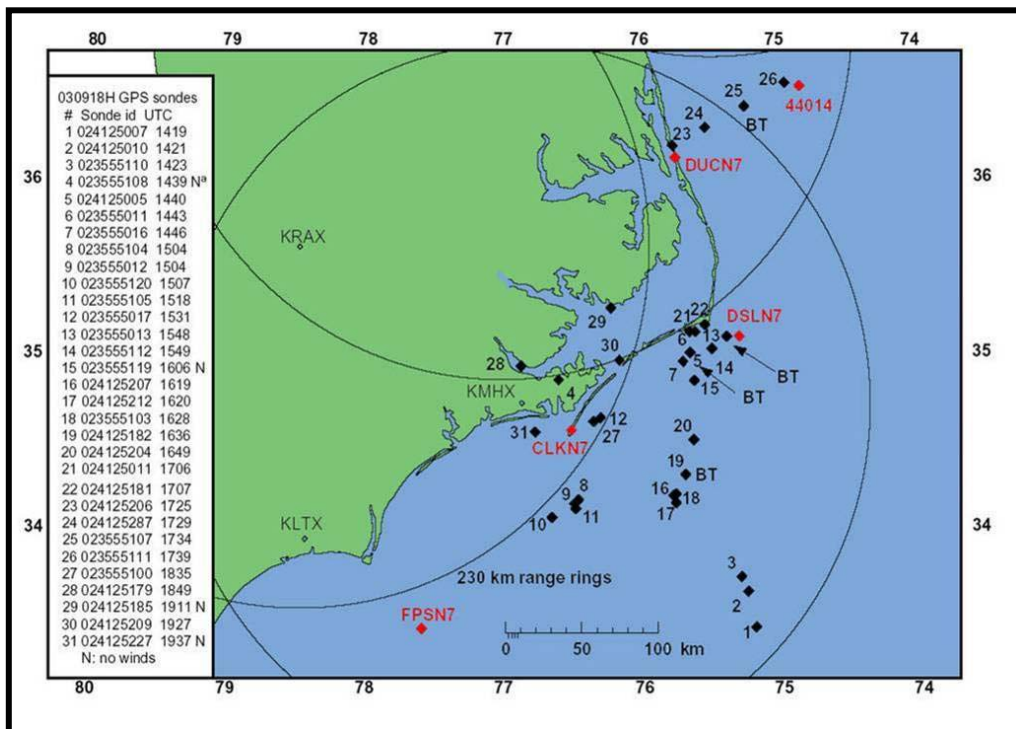


Figure 4-11. GPS sonde splash locations during Isabel 2003 (courtesy of NOAA)

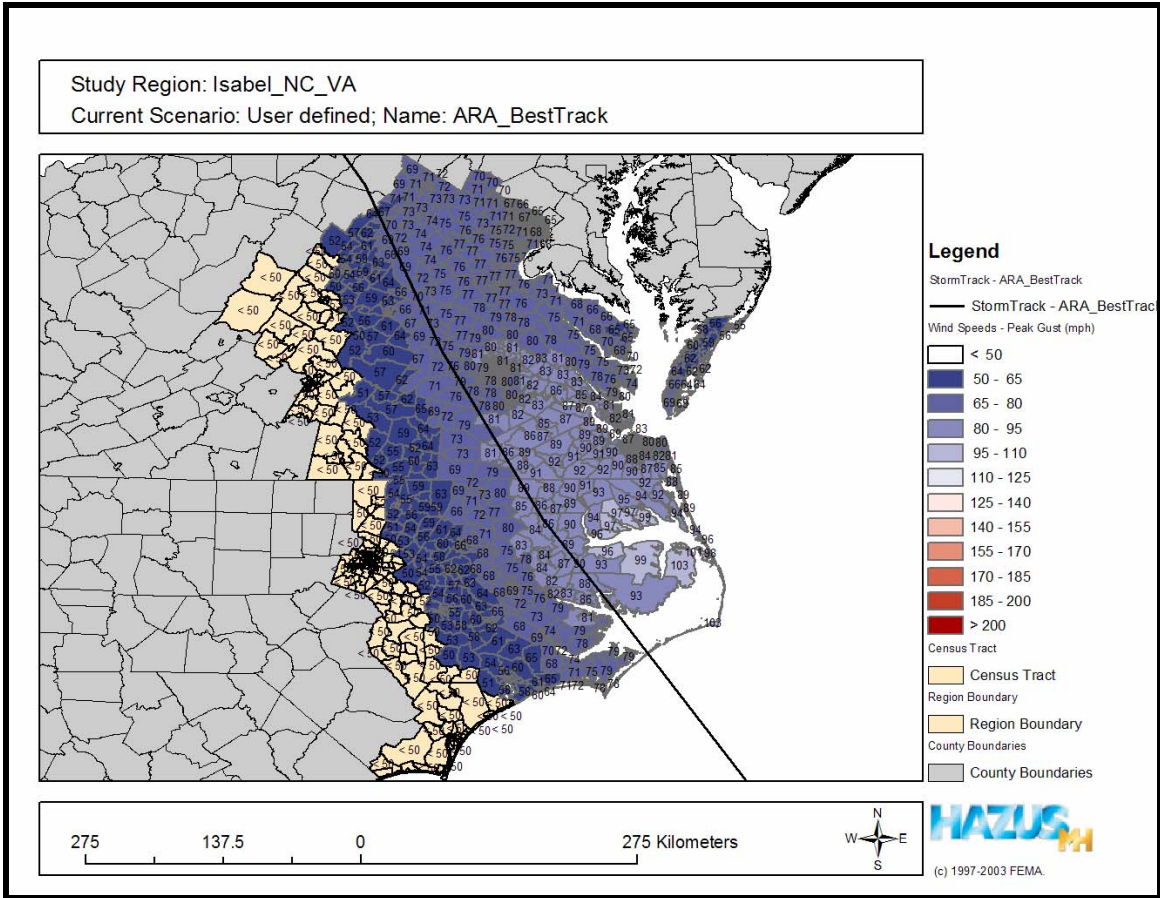


Figure 4-12. Wind swath map from FEMA’s HAZUS program, based on the NOAA H*WIND model using FCMP data (courtesy of Applied Research Associates, Inc.)

CHAPTER 5 ANALYSES OF TROPICAL CYCLONE WIND DATA

This chapter presents analyses of velocity data records from tropical cyclone collected from the FCMP mobile instrumented towers during the 1999-2003 Atlantic Hurricane Seasons. The goal of the project is to characterize overland turbulent wind behavior by quantifying the statistical descriptions of interest to structural designers. In particular, these data will provide wind tunnel modelers with turbulence information to validate that the model flow field is similar to actual conditions in a landfalling tropical cyclone. Analyses of turbulence intensity, gust factors (ratios of peak short-duration gusts to mean wind speeds of longer durations), integral length scales (statistical estimates of the physical dimensions of turbulent eddies) and power spectra (the distribution of energy with respect to frequency) are presented herein. Knowledge of these descriptors has accumulated since the late 1800s, although most were derived empirically from data sets collected from winter storms and thunderstorms (Counihan, 1975). Whether the turbulent behavior of tropical storms and hurricanes differ from these models remains an active subject of debate (Kramer and Marshall, 1992).

This chapter is divided into three sections. The first section outlines the experimental assumptions that guided data reduction and are the basis of analysis. The second section explains the data reduction algorithm employed to evaluate segments for admission to the FCMP storm database and summarizes the quantities of segments by roughness length and mean wind speed. In the final section, results from turbulence intensity (TI), gust factor (GF), integral length scale and power spectral density (PSD)

analyses are presented and compared against winter- and thunderstorm research, when available.

Experimental Assumptions

A small window of time is available for research personnel to deploy instrumentation and safely retreat from the incoming storm. At the earliest, teams arrive 60-70 hours prior to landfall to the impacted region, and the first 30-40 hours are spent locating potential sites for tower insertion based on the National Hurricane Center tropical cyclone track forecasts that are issued every six hours prior to landfall. To capture the highest winds, however, tower insertion is often delayed until 8-24 hours prior to landfall when forecast position error is reduced. Even in this timeframe, significant deviation from the projected path may occur, which requires last minute maneuvering of instrumentation along the coastline. A recent study by Powell and Abernethy (2001) found that during the 1976-2000 Atlantic Hurricane Seasons, the mean position error 7-18 hours prior to landfall was 98 km.

Research personnel employ considerable experimental rigor in the full-scale measurement of tropical cyclone winds but are not afforded the idealness of laboratory testing. Safety and logistics demand a high degree of practicality in its execution. Accordingly, a series of assumptions about the velocity field, experimental procedure and upwind terrain must be made.

Concerning the Hurricane Boundary Layer

The roughness estimation techniques employed in this chapter are shear velocity based and dependent upon the validity of the logarithmic mean velocity profile, which was developed for neutral conditions. As it is not within the technological capability of the FCMP to measure thermal conditions throughout the atmospheric boundary layer,

neutral thermal stratification was assumed a priori. This condition assumes that in extreme winds, mechanical turbulence significantly dominates heat convection. Additionally, the identification of rain bands, downdrafts and any other unusual meteorological phenomena was not pursued, although this item has been prioritized for future study.

Concerning Experimental Rigor

Once towers are operational, deployment teams evacuate the region for up to 48 hours, leaving the towers unattended to measure the incoming cyclone. Research personnel were not available to monitor the performance of the onboard computer and instrumentation nor to witness or prevent any interaction of local citizenry with the tower (which was observed after the fact on several deployments).

Measures taken to improve the quality of analysis include the proper leveling of the tower during erection to ensure proper alignment of the axes of measurement to the longitudinal, lateral and vertical components of wind, and the use of two different anemometry systems at the 10-m height to identify erratic behavior by the sensors. Recently, Aponte (2003) completed a validation study of the time histories in the storm database and found that data collected by the gill array and the wind monitor compared favorably. Additionally, segments with voltage irregularities are identified and removed from the storm database.

Concerning the Homogeneity and Flatness of Upwind Terrain

The mean velocity profile and its turbulence characteristics are deeply sensitive to surface roughness of the upwind terrain. For this reason, the FCMP has targeted a wide range of coastal terrains (e.g., shoreline, open, suburban and city exposures) for tower deployment. During analysis, wind records were divided into contiguous segments, and

for each segment, a roughness length was estimated from the shear velocity and the mean wind speed (as discussed in Chapter 3). Experimental determination of roughness lengths requires some prudence, however. Terrain inhomogeneities of sufficient scale can induce the formation of internal boundary layers, and the terrain density can invoke semi-smooth and wake-interference flows. Both conditions will alter the turbulence characteristics and ultimately, the classification of surface roughness if it is determined from turbulence characteristics.

To avoid these features, research teams scout the projected landfall area for exposures free of hills, escarpments and abrupt changes in roughness. Locating four separate homogeneous terrains in hundreds of kilometers of coastline, however, is a difficult if not unachievable task, especially if given a window of opportunity of less than 24 hours. This task is further complicated by the fact that wind shifts approximately 180° as the tropical cyclone approaches and leaves the impacted region. The upwind terrain, which extends radially from the tower, must be considered over the entire arc. To estimate the required terrain area, the fetch length may be calculated from an equation provided by Wieringa (1993), which is based on the work of Merry and Panofsky (1976) and Peterson (1969). The required fetch distance to ensure that the equilibrium layer is fully adapted to the upwind roughness is approximately

$$F \approx 2z_0 \left(\frac{10z}{z_0} \left[\ln \frac{10z}{z_0} - 1 \right] + 1 \right) \quad (60)$$

where F = fetch distance, z_0 = roughness length and z = observation height. This relationship is plotted in Figure 5-1 for an observation height of 10 m, which corresponds to the elevation of the anemometry on the FCMP instrumented towers. Assuming an

open exposure ($z_0 = 0.03$ m), Eq. 60 predicts that the sufficient fetch length is ~ 1400 m. To meet the conditions for sufficient fetch, the FCMP must locate $\pi \cdot (1400 \text{ m})^2 = \sim 620$ hectares (~ 1500 acres) of homogeneous terrain, which to date, has not occurred.

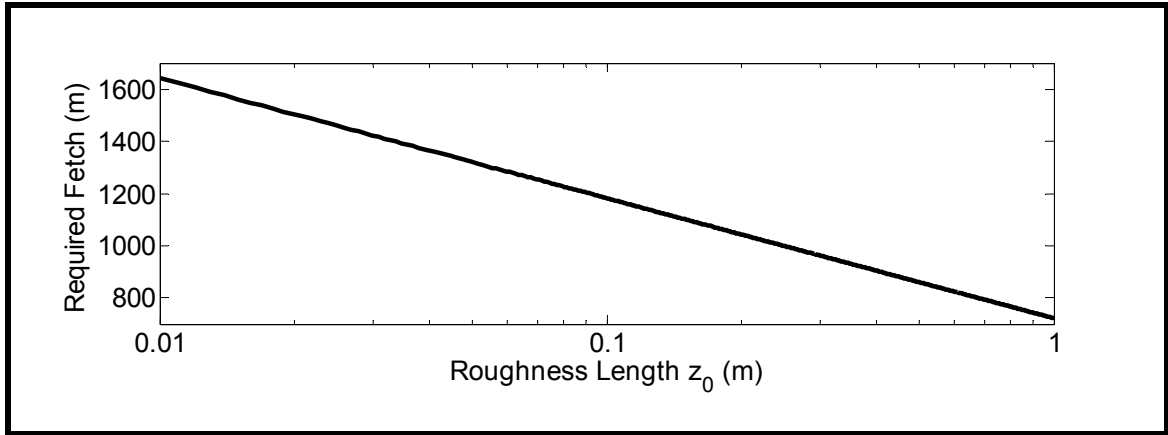


Figure 5-1. Fetch requirements to determine the roughness length in a homogenous terrain at an observation height of 10 m

In almost every case except for marine exposure, the approach terrain of the tower deployment location cannot be said to be homogeneous over the recommended fetch distance. In this study, however, terrains were treated as “homogeneous” through the use of the logarithmic law presented in Chapter 3, reproduced below

$$\bar{u}(z) = \frac{1}{k} u_* \ln \frac{z}{z_0} \quad (61)$$

although the aerial imagery provided in Appendix B indicates that the majority of upwind terrains consist of surface patches of varying roughness.

This assumption of homogeneity will always overestimate the “effective” roughness length in a heterogeneous terrain because rougher surface patches generate turbulence with greater ease than less rough patches can dissipate it (Wieringa 1993).

Data Reduction

The FCMP collected hundreds of hours of full-scale tropical cyclone wind field data from 29 instrumented towers in ten different storms, but only a portion of these records are suitable for analysis. For the study, the 19 storm records with the highest wind speeds were selected. Ten-minute segments were subjected to a series of elimination tests to identify segments for exclusion from the FCMP storm database based on the following quality control procedures:

- Based on the work of Aponte (2003), segments were eliminated if instrument mechanical failures and voltage irregularities in the onboard power system were observed
- A minimum 10-minute mean wind speed of 5 m/s was required for admission to the database. This threshold will rise with the addition of new data sets with higher wind speeds, which are of the greatest interest to design engineers and meteorologists
- Aerial imagery and site photos were studied to identify the presence of large obstructions (e.g. buildings and treelines) within 100 m upwind of the observation site that can cause blockage and interference effects in the observed flow field
- Records that included abrupt changes in topography (e.g., hills and escarpments) in the upwind terrain were removed to avoid effects of speed-up
- One-minute mean directions were analyzed inside of the 10-minute record to quantify the change in wind direction. Segments with an observed 1-minute maximum shift $> 20^\circ$ (or equivalently a 520 m arc length at 1500 m) were eliminated to limit the variability of the upwind exposure
- Data sets were evaluated for 1st and 2nd order nonstationarities through the reverse arrangement test. Operated on a time series alone, the reverse arrangement test is highly sensitive to trends in the mean but is not a good indicator of trends in variance. For this reason, 10-minute files were segmented into 1-minute means and standard deviations, and reverse arrangement tests were performed at the $\alpha = 0.025$ level of significance to identify candidates for elimination (Bendat and Piersol 2000)

As a result, 40% of the segments were eliminated for candidacy. Table 5-1 summarizes the results of this procedure. Quantities of 10-minute segments possessing

mean wind speeds less than 5 m/s, shifts in 1-minute mean directions $> 20^\circ$, immediate upwind obstructions or changes in terrain elevation, or 1st or 2nd order nonstationary behavior deemed unacceptable are listed. The total number of unique segments removed—i.e., the quantity of segments meeting at least one criterion for elimination—and the number of segments admitted to the database are listed. Table 5-2 lists the number of segments admitted to the storm database by mean velocity range and roughness regime.

Table 5-1. Summary of data reduction results

Storm	Year	Location	Tower	Number of 10-Minute Segments							
				TOTAL	Mean Wind Speed < 5 m/s	Wind Direction Drift > 20°	Poor Fetch Choice	Nonstationarity 1st Order	Nonstationarity 2nd Order	ELIMINATED	ACCEPTED
Isabel	2003	Elizabeth City, NC	T0	350	--	--	--	15	6	21	329
Isabel	2003	Wilmington, NC	T1	377	48	32	--	9	14	95	282
Isabel	2003	Atlantic Beach, NC	T2	758	--	25	502	47	23	543	215
Lili	2002	Lafayette, LA	T0	452	186	90	--	29	10	222	230
Lili	2002	Lydia, LA	T3	452	218	54	98	34	9	251	201
Isidore	2002	Mary Esther, FL	T0	470	255	175	--	20	13	298	172
Isidore	2002	Gulf Breeze, FL	T2	470	101	69	130	52	20	196	274
Michelle	2001	Homestead, FL	T1	545	366	72	--	23	23	399	146
Gabrielle	2001	Venice Beach, FL	T1	38	--	3	12	8	2	19	19
Gordon	2000	Dunedin, FL	T0	218	31	13	--	17	6	58	160
Gordon	2000	Port Richie, FL	T1	236	--	19	--	15	2	35	201
Gordon	2000	Honeymoon Island, FL	T3	233	--	2	--	15	6	20	213
Irene	1999	Melbourne, FL	T0	125	--	4	--	3	3	9	116
Irene	1999	Melbourne Beach, FL	T1	140	--	1	--	14	4	18	122
Floyd	1999	Jupiter, FL	T3	212	--	8	--	7	7	21	191
Dennis	1999	Kure Beach, NC	T0	167	--	2	--	13	3	18	149
Dennis	1999	Wrightsville Beach, NC	T1	251	--	14	--	14	10	36	215
Dennis	1999	Topsail, NC	T2	149	--	19	--	9	5	27	122
Dennis	1999	Emerald Isle, NC	T3	107	--	--	--	5	1	5	102

Number of Segments Admitted to Database = 3459

Data Analyses

Following data reduction, 10-minute segment turbulence characteristics—including turbulence intensities, gust factors, longitudinal integral length scales and power spectral density—were studied. When appropriate, segments were separated into roughness and velocity regimes to observe trends of dependency.

Table 5-2. Summary of FCMP storm database segments by mean wind speed and roughness lengths

Storm	Year	Location	Tower	Number of 10-Minute Segments													
				5 - 10	10 - 15	15 - 20	20 - 25	25 - 30	> 30 m/s	0.00 - 0.02	0.02 - 0.04	0.04 - 0.10	0.10 - 0.20	0.20 - 0.40	0.40 - 0.70	> 0.70 m	
Isabel	2003	Elizabeth City, NC	T0	59	90	83	75	22	--	285	34	10	--	--	--	--	
Isabel	2003	Wilmington, NC	T1	219	63	--	--	--	--	5	10	37	77	93	54	6	
Isabel	2003	Atlantic Beach, NC	T2	170	45	--	--	--	--	211	2	2	--	--	--	--	
Lili	2002	Lafayette, LA	T0	125	78	27	--	--	--	30	17	66	77	34	6	--	
Lili	2002	Lydia, LA	T3	93	58	36	14	--	--	89	45	26	13	13	4	11	
Isidore	2002	Mary Esther, FL	T0	112	60	--	--	--	--	--	--	--	3	50	74	45	
Isidore	2002	Gulf Breeze, FL	T2	91	96	87	--	--	--	185	11	28	28	14	5	3	
Michelle	2001	Homestead, FL	T1	146	--	--	--	--	--	1	4	6	42	81	12	--	
Gabrielle	2001	Venice Beach, FL	T1	5	9	3	2	--	--	--	1	2	--	4	6	6	
Gordon	2000	Dunedin, FL	T0	119	41	--	--	--	--	--	--	2	17	56	58	27	
Gordon	2000	Port Richie, FL	T1	52	113	36	--	--	--	149	16	21	12	3	--	--	
Gordon	2000	Honeymoon Island, FL	T3	50	26	125	12	--	--	212	--	1	--	--	--	--	
Irene	1999	Melbourne, FL	T0	50	66	--	--	--	--	--	--	--	1	24	59	32	
Irene	1999	Melbourne Beach, FL	T1	9	2	37	56	18	--	111	1	1	2	7	--	--	
Floyd	1999	Jupiter, FL	T3	89	94	8	--	--	--	--	5	39	13	26	58	50	
Dennis	1999	Kure Beach, NC	T0	--	71	76	2	--	--	12	21	47	50	19	--	--	
Dennis	1999	Wrightsville Beach, NC	T1	56	118	41	--	--	--	6	27	74	59	47	2	--	
Dennis	1999	Topsail, NC	T2	43	79	--	--	--	--	--	--	--	6	42	43	31	
Dennis	1999	Emerald Isle, NC	T3	--	49	53	--	--	--	6	5	48	26	17	--	--	
TOTAL				1488	1158	612	161	40	0	1302	199	410	426	530	381	211	
				10-Minute Mean Velocity						Roughness Length							

Turbulence Intensities

Turbulence intensities (TI), which describe the variability of a particular wind component with respect to the mean wind speed, were analyzed for comparison against observed data in the literature. To produce a reliable estimate, the segment must contain enough points to achieve a reliable estimate. Typically, 5-, 10- and 15-minute segments are chosen in full-scale measurement application. The World Meteorology Organization guidelines suggest using a 10-minute average to acquire a sustained measurement, which is the choice of averaging duration for this analysis.

To validate that the longitudinal TI stabilizes within that duration, a study was performed to determine the mean observed convergence time in open, roughly open, suburban and city exposures. The observed longitudinal TI (from which roughness was estimated) normalized by the 10-minute estimate is plotted against its averaging time in Figure 5-2. Differences between the convergence rates over the roughness ranges listed

in Figure 5-2 (and for others tested but not shown) were inconsistent but indicate that longitudinal TI estimates stabilized after 7 minutes or 70% of the chosen averaging time.

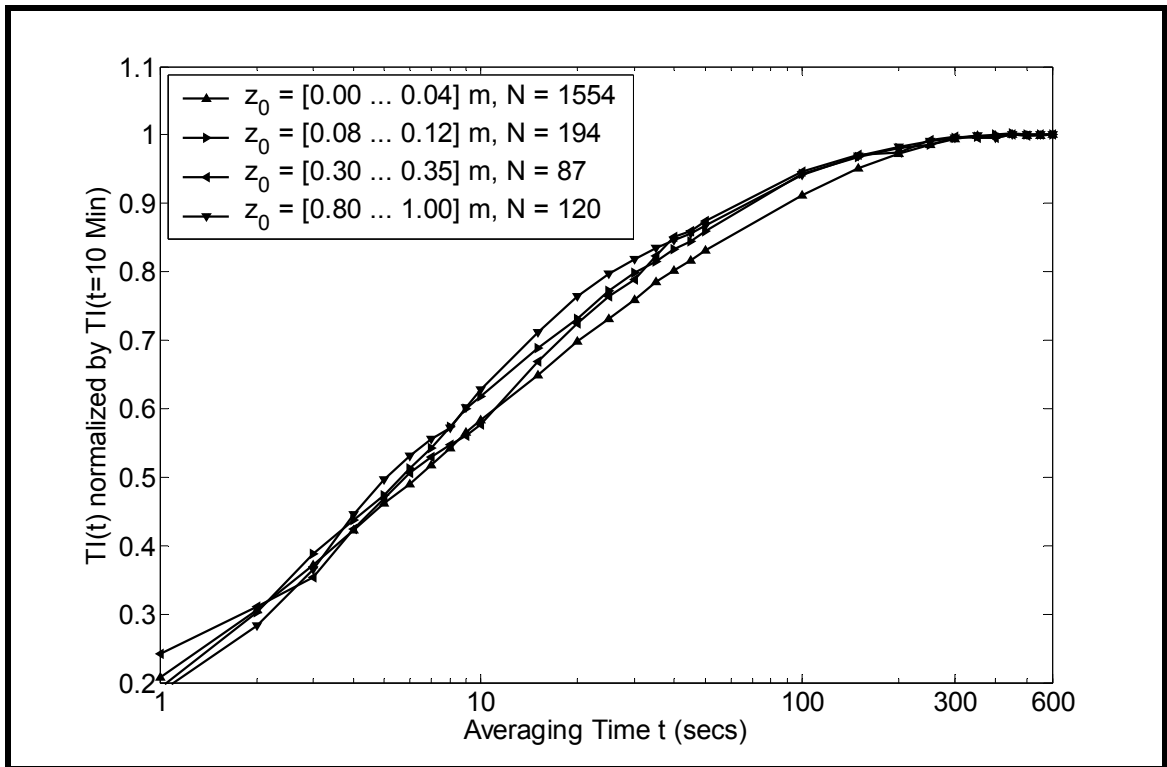


Figure 5-2. Convergence of the longitudinal turbulence intensity over increasing averaging times (FCMP database)

Longitudinal, lateral and vertical TIs were calculated for five different ranges of estimated roughness lengths. Table 5-3 compares the mean turbulence intensity ratios from experimental data taken from the FCMP storm database to observations from other experiments performed by Friedman (1953), Cermak et al. (1983) and Schroeder and Smith (2003). The number of observations N and the standard deviation of the TI ratios are also tabularized.

Over the entire range of roughness lengths, the experimental lateral/longitudinal TI ratios generally agree with observations made by wind tunnel boundary layer experimentalists (Cermak et al. 1983) and full-scale measurements in flat and open

terrains (Friedman 1953 and Schroeder and Smith 2003). Mean ratios involving vertical turbulence intensity averaged over all roughness ranges compared well with observed values, but sensitivity to roughness was noted.

Table 5-3. Turbulence intensity comparison

	Roughness Length (m)	Lateral/Longitudinal			Vertical/Longitudinal			Vertical/Lateral		
		Mean	Std	N	Mean	Std	N	Mean	Std	N
FCMP Experimental	0.00 - 0.02	0.77	0.17	1394	0.39	0.06	1394	0.52	0.12	1394
FCMP Experimental	0.02 - 0.04	0.70	0.14	160	0.45	0.07	160	0.65	0.14	160
Friedman (1953)		0.75	--	--	--	--	--	--	--	--
Cermak et al. (1983)		0.76	--	--	0.52	--	--	0.68	--	--
Schroeder and Smith (2003)		0.76	--	--	0.52	--	--	0.68	--	--
FCMP Experimental	0.04 - 0.10	0.69	0.11	365	0.46	0.08	365	0.68	0.11	365
FCMP Experimental	0.10 - 0.20	0.76	0.13	411	0.50	0.08	411	0.67	0.11	411
FCMP Experimental	0.20 - 0.40	0.74	0.13	388	0.51	0.09	388	0.70	0.11	388
FCMP Experimental	0.40 - 0.70	0.71	0.12	370	0.52	0.07	370	0.74	0.10	370
FCMP Experimental	> 0.70	0.72	0.08	371	0.54	0.06	371	0.76	0.08	371
	Mean	0.73			0.48			0.67		

Ratios of vertical to longitudinal and lateral TIs compared favorably to values found by Cermak et al. (1983) and Schroeder and Smith (2003) in the mean sense. Analyzed over a range of roughness values, however, data from the FCMP database indicate the presence of logarithmic dependency of vertical TI ratio on surface roughness. These values and their trendlines are plotted in Figure 5-3. The effect of these increased vertical turbulence intensities on pressure loading of low-rise buildings in built-up areas will require further study.

Comparison to Known Gust Factor Curves

Recall from Chapter 3 that a gust factor $GF(t, T)$ is a measure of the most likely extreme peak gust of duration t (sec) as a multiple of the mean wind speed in a given interval T (sec). In this section, $GF(t, 600)$ and $GF(t, 3600)$ curves calculated from 10-minute open exposure ($z_0 = 0.02-0.04$ m) segments in the FCMP database are compared to an analytical model offered by Cook (1985) and empirical models offered by Durst

(1962) and Krayer and Marshall (1992) for open exposure terrains ($z_0 = 0.03$ m).

Comparison was not straightforward, however, and merits further discussion.

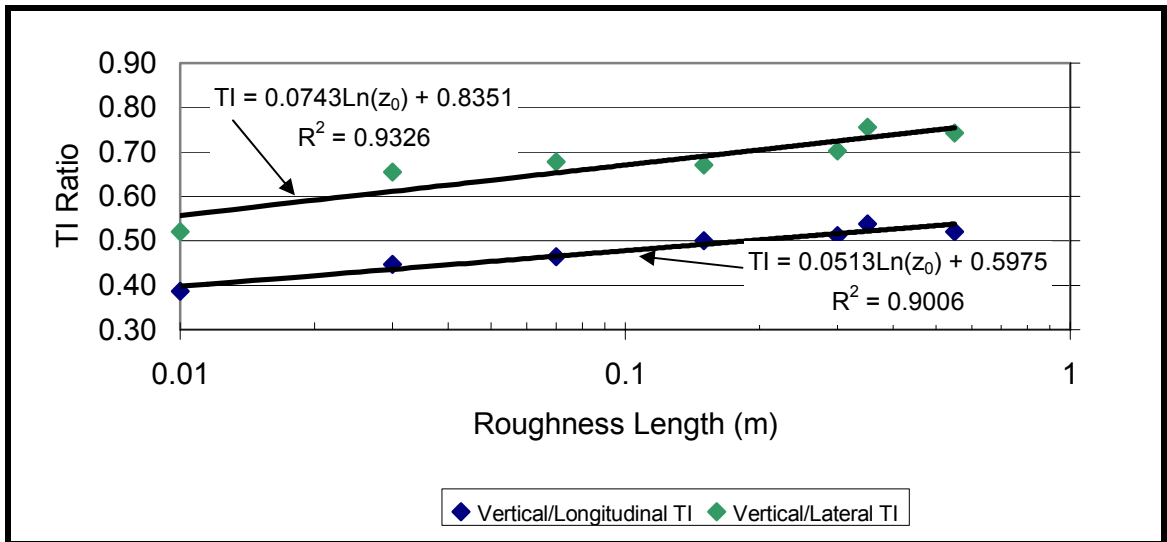


Figure 5-3. Ratios of vertical turbulence intensities to longitudinal and lateral turbulence intensities

Concerning the empirical models, Durst provided $GF(t,600)$ data for a limited range of gust durations t in a table, and Krayer and Marshall provided a $GF(t,3600)$ curve in a figure in their paper (*sans* accompanying data). Accordingly, to calculate $GF(t,600)$ data from the Krayer and Marshall $GF(t,3600)$, required scanning of Figure 1 from *Gust Factors Applied to Hurricane Winds* (Krayer and Marshall 1993) and digitization in AutoCAD. Axes were scaled, and $GF(t,3600)$ was established discretely from coordinate pairs. Secondly, standard deviations of departures were calculated from a rearrangement of Durst's gust factor equation (presented in Chapter 3),

$$GF(t,T) = 1 + SU(t,T) \cdot SD(t,T) \quad (62)$$

to solve for the standard deviation of the gust departures from the mean wind speed,

$$SD(t,3600) = \frac{GF(t, T = 1 \text{ hour}) - 1}{SU(t, T = 1 \text{ hour})} \quad (63)$$

where SU is the standard normal deviate calculated from inverse zero-mean unit-variance Gaussian CDF of $1 - t/T$. Thirdly, $SD(t,3600)$ was converted from 1-hour duration to a 10-minute duration through a Gaussian translation (offered first by Durst and later employed by Krayner and Marshall)

$$SD(t,600) = \sqrt{SD^2(t,3600) - SD^2(600,3600)} \quad (64)$$

where $SD(600,3600) = 0.065$ (Table V, Durst). Finally, Eq. 62 was used to calculate $GF(t,600)$. A similar conversion was performed on the Cook $GF(t,3600)$ curve. The SU, SD and GF values used in these calculations are presented in Table 5-4. Figures 5-4 and 5-6 show the $GF(t,600)$ and $GF(t,3600)$ curves. The following subsections discuss the curves in greater detail.

Relating Peak Gusts to a 10-Minute Mean Wind Speed. $GF(t,600)$ curves from each of the known models and three experimental curves generated from 199 ten-minute $z_0 = 0.03 \pm 0.01$ m observations extracted from the FCMP database are plotted in Figure 5-4. Gust factors in the red curve were calculated from the methodology employed by Durst and Krayner/Marshall using FCMP data. Standard deviations of departures divided by the mean wind speeds were calculated over a range of durations and averaged and converted into an equivalent gust factor. The blue and green curves are averages of gust factors directly measured from each segment from segmental (i.e., sequential and contiguous) and moving averages, respectively. The $GF(3,600)$ values calculated from

the FCMP database—1.46, 1.50 and 1.52 for the Gaussian translation, segmental average and moving average, respectively—are 6-10% larger than the Cook/Durst value of 1.38.

Figure 5-4 shows that as the gust duration decreases, the segmental-average GF curve and the moving-average GF curve converge. The reasoning for this trend is purely mathematical. Consider that, if m represents the number of points in a given gust duration and M represents the number of points in the segment, the total number of samples N available to identify the peak gust is

$$\begin{aligned} N &= M/m && \text{(Segmental Average)} \\ &= M - m + 1 && \text{(Moving Average)} \end{aligned} \tag{65}$$

As m approaches 1, which corresponds temporally to the inverse of the sampling rate of the data acquisition system, N approaches M . As M increases, the likelihood of locating the maximum gust in the record decreases. This drop-off is significant: for $M = 6000$, the ratio of sample sizes decreases by almost 97% at $m = 30$ (which in this study corresponds to a 3-second gust in a 10-minute record). Comparison between the moving-average GF and Durst yields a similar trend, which is to be expected as the standard deviation estimated from the gust departures used to translate Gaussian variables was computed from the segmental average.

The measured gust factors exhibit considerable scatter over all roughness regimes. Figure 5-5 provides the mean and 5% / 95% quantile gust factors for open exposure observations. At short (< 10 sec) durations, coefficients of variation exceed 10%, and over all durations, the histograms demonstrate positive skewness (> 1). Figure 5-5 also includes longitudinal gust factor means and quantiles. For structural design, Solari (1990) has suggested the use of the longitudinal gust factor—i.e., the peak gust parallel to

the mean direction of a segment—to model gust buffeting and alongwind response with greater accuracy. Comparison indicates no significant difference between the curves—separating the longitudinal component from the magnitude of the velocity appears unnecessary.

Relating Peak Gusts to a 1-Hour Mean Wind Speed. Many building codes reference the 1-hour mean wind speed. Accordingly, the $GF(t,3600)$ curve calculated from the FCMP storm database is shown in Figure 5-6 with the 1-hour GF curves offered by Cook (1985), Durst (1960) and Krayner and Marshall (1992), which are the basis for Eurocode, ASCE 7-02 and ASCE 7-95, respectively. The FCMP curve (calculated by Durst's methodology) is very similar to the Durst curves for gust durations > 1 minute, but exhibits higher GF values for gust durations between 1-60 seconds. The calculated GF curve does not support the degree of upward adjustment proposed by Krayner and Marshall but does suggest that the Durst curve, which is employed by ASCE 7-02, underestimates the gustiness of ground-level winds generated from tropical cyclones.

Table 5-4. Standard deviate (SU), departure standard deviations (SD), and gust factors (GF)

Gust Duration	SU		10-Minute SD				1-Hour SD				10-Minute GF						1-Hour GF			
	10-Minute	1-Hour	Cook	Durst	Krayer Marshall	Gaussian Translation	Cook	Durst	Krayer Marshall	Gaussian Translation	Cook	Durst	Krayer Marshall	Gaussian Translation	Segmental Average	Moving Average	Cook	Durst	Krayer Marshall	Gaussian Translation
1 s	2.94	3.45	0.159	0.150	0.202	0.19	0.171	0.164	0.212	0.20	1.47	1.44	1.59	1.56	1.58	1.60	1.59	1.56	1.73	1.69
2	2.71	3.26	0.153	0.149	0.201	0.18	0.166	0.162	0.212	0.19	1.41	1.40	1.55	1.50	1.53	1.55	1.54	1.53	1.69	1.63
3	2.58	3.14	0.149	0.148	0.199	0.18	0.163	0.161	0.209	0.19	1.38	1.38	1.51	1.46	1.50	1.52	1.51	1.51	1.66	1.59
4	2.47	3.06	0.147	0.146	0.198	0.17	0.161	0.160	0.208	0.18	1.36	1.36	1.49	1.43	1.46	1.50	1.49	1.49	1.64	1.56
5	2.39	2.99	0.145	0.145	0.195	0.17	0.159	0.159	0.205	0.18	1.35	1.35	1.47	1.40	1.44	1.48	1.48	1.48	1.61	1.54
6	2.33	2.94	0.143	0.143	0.193	0.16	0.157	0.157	0.204	0.18	1.33	1.33	1.45	1.38	1.43	1.46	1.46	1.46	1.60	1.52
7	2.27	2.89	0.142	0.141	0.191	0.16	0.156	0.155	0.202	0.17	1.32	1.32	1.43	1.36	1.41	1.44	1.45	1.45	1.58	1.50
8	2.22	2.84	0.141	0.139	0.189	0.16	0.155	0.153	0.200	0.17	1.31	1.31	1.42	1.35	1.39	1.43	1.44	1.44	1.57	1.48
9	2.17	2.81	0.140	0.137	0.187	0.15	0.154	0.152	0.198	0.17	1.30	1.30	1.41	1.34	1.37	1.41	1.43	1.43	1.56	1.47
10	2.13	2.77	0.139	0.135	0.185	0.15	0.153	0.150	0.196	0.16	1.30	1.29	1.39	1.32	1.37	1.40	1.43	1.42	1.54	1.46
20	1.83	2.54	0.133	0.124	0.169	0.13	0.148	0.140	0.181	0.15	1.24	1.23	1.31	1.24	1.28	1.32	1.38	1.36	1.46	1.37
30	1.64	2.39	0.129	0.115	0.156	0.12	0.144	0.132	0.169	0.14	1.21	1.19	1.26	1.20	1.23	1.27	1.35	1.32	1.40	1.32
40	1.50	2.29	0.126	0.107	0.146	0.11	0.142	0.125	0.160	0.13	1.19	1.16	1.22	1.16	1.19	1.23	1.33	1.29	1.37	1.29
50	1.38	2.20	0.124	0.098	0.139	0.10	0.140	0.118	0.153	0.12	1.17	1.14	1.19	1.14	1.17	1.21	1.31	1.26	1.34	1.26
60	1.28	2.13	0.123	0.095	0.133	0.09	0.139	0.115	0.148	0.11	1.16	1.12	1.17	1.12	1.15	1.19	1.30	1.24	1.32	1.24
70	1.19	2.07	0.122	0.093	0.125	0.09	0.138	0.114	0.141	0.11	1.14	1.11	1.15	1.10	1.13	1.17	1.28	1.23	1.29	1.23
80	1.11	2.01	0.120	0.091	0.120	0.08	0.137	0.112	0.137	0.10	1.13	1.10	1.13	1.09	1.12	1.16	1.27	1.23	1.28	1.21
90	1.04	1.96	0.119	0.090	0.116	0.08	0.136	0.111	0.133	0.10	1.12	1.09	1.12	1.08	1.11	1.15	1.27	1.22	1.26	1.20
100	0.97	1.91	0.119	0.088	0.110	0.08	0.135	0.109	0.128	0.10	1.11	1.09	1.11	1.07	1.10	1.14	1.26	1.21	1.25	1.19
200	0.43	1.59	0.114	0.070	0.079	0.04	0.131	0.096	0.102	0.08	1.05	1.03	1.03	1.02	1.04	1.07	1.21	1.15	1.16	1.12
300	0.00	1.38	0.112	0.053	0.065	0.02	0.130	0.084	0.092	0.07	1.00	1.00	1.00	1.00	1.01	1.04	1.18	1.12	1.13	1.09
400	0.00	1.22	0.113	0.035	0.055	0.00	0.130	0.074	0.085	0.07	1.00	1.00	1.00	1.00	1.00	1.02	1.16	1.09	1.10	1.08
500	0.00	1.09	0.114	0.018	0.050	0.00	0.131	0.067	0.082	0.07	1.00	1.00	1.00	1.00	1.00	1.01	1.14	1.07	1.09	1.07
600	0.00	0.97	0.117	0.000	0.046	0.00	0.134	0.065	0.080	0.07	1.00	1.00	1.00	1.00	1.00	1.00	1.13	1.06	1.08	1.06

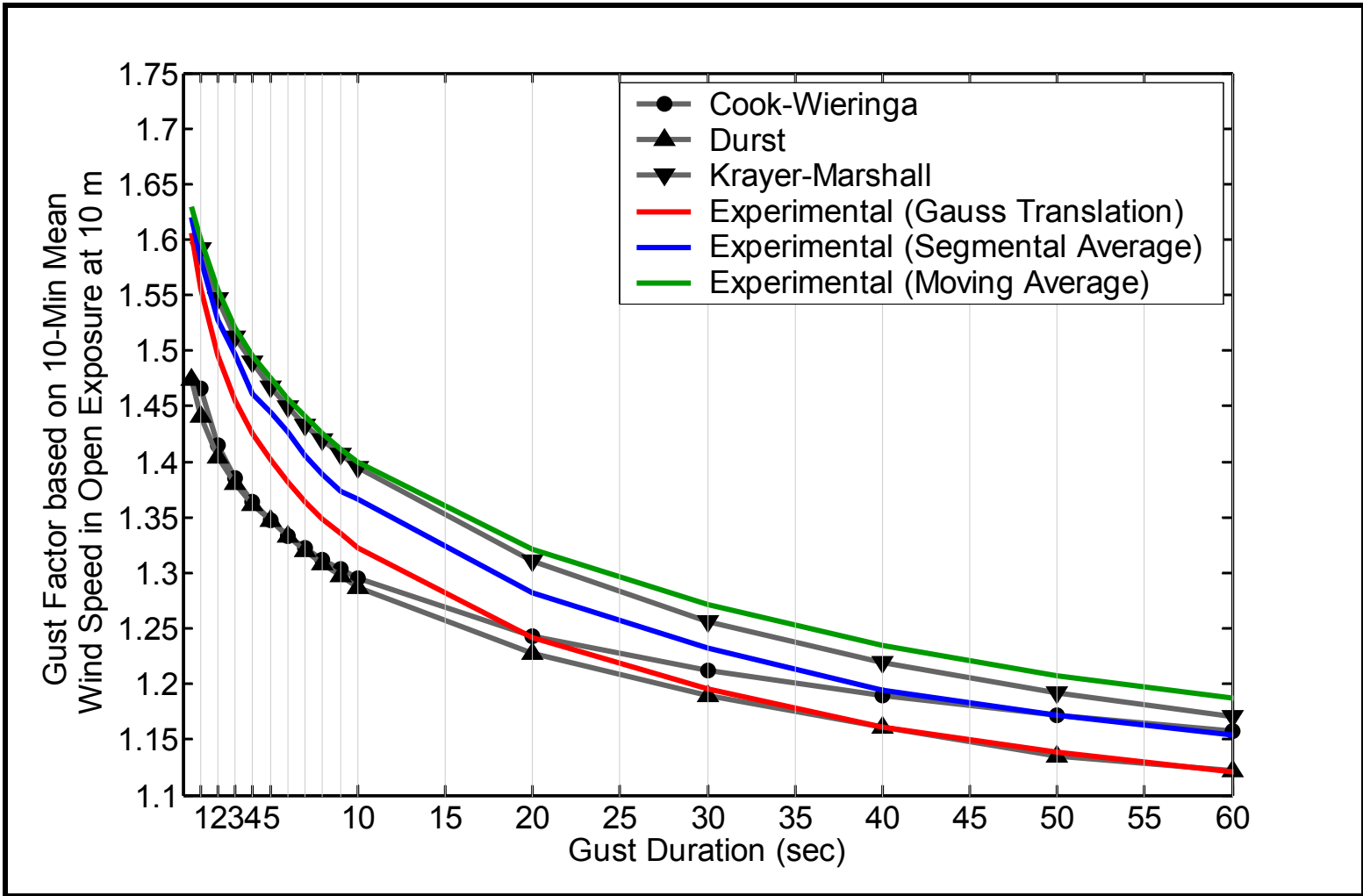


Figure 5-4. Gust Factors based on a 10-minute mean wind speed

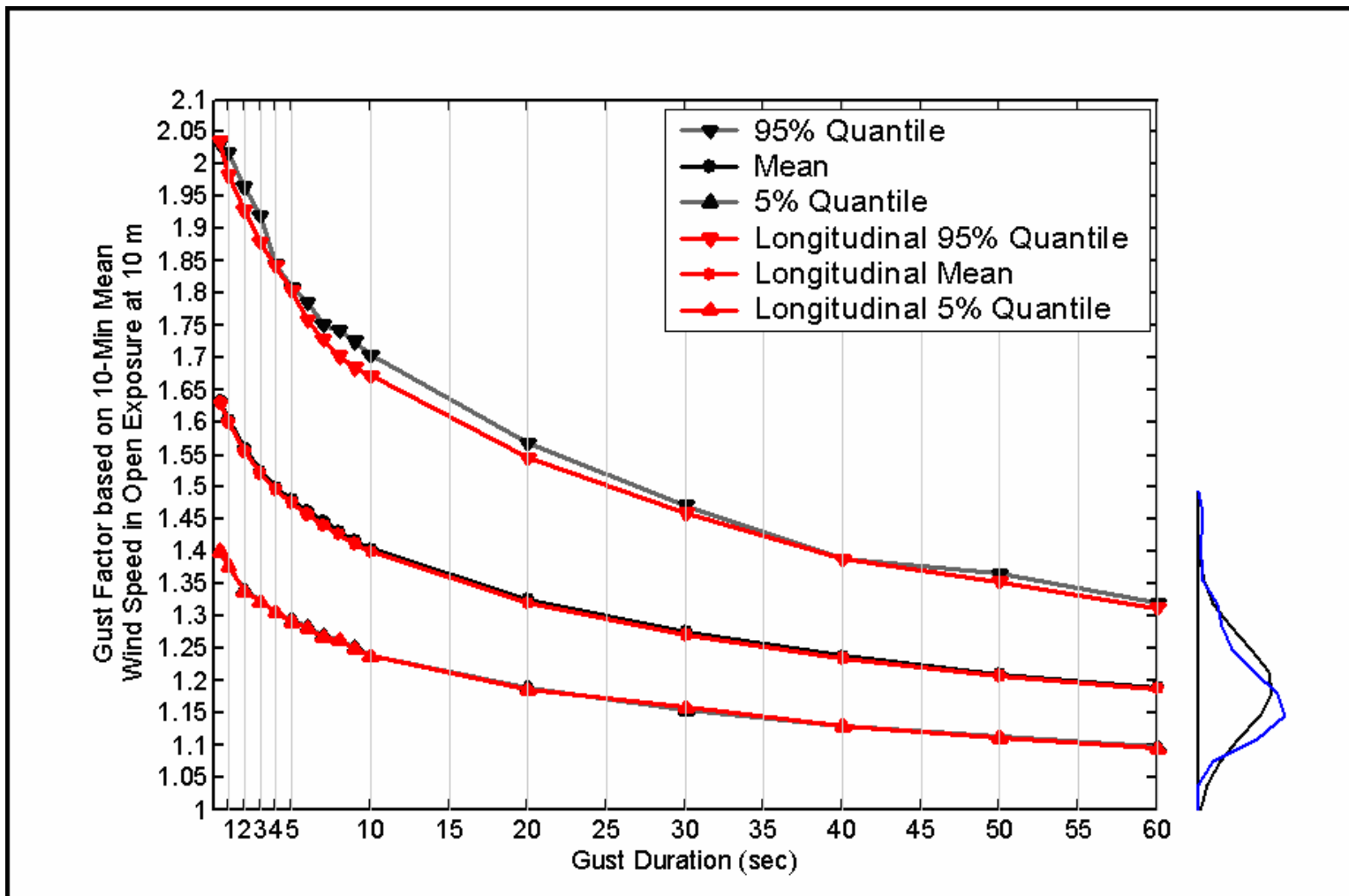


Figure 5-5. Mean and 5% / 95% quantile gust factors based on a 10-minute wind speed

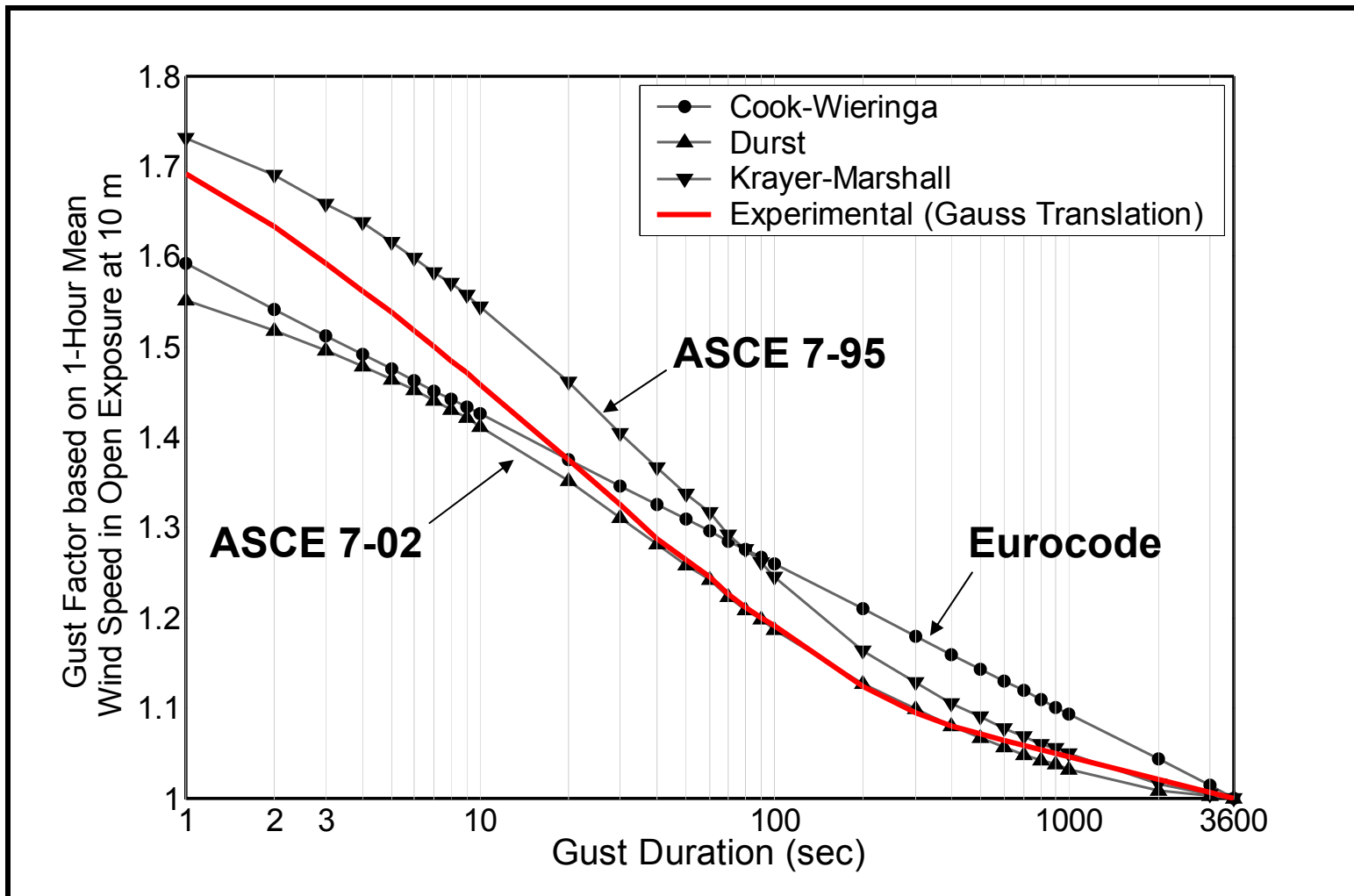


Figure 5-6. Gust Factors based on a 1-hour mean wind speed

Formulation of Gust Factor Curves based on a 10-Minute Wind Speed for Varying Gust Durations and Roughness Lengths

Based on the differences observed between the FCMP gust factors and the commonly used models, it was determined that a generalized model could be of use for future versions of wind load standards. In this section, the gust factors calculated from the FCMP database are used to formulate a series of curves for hurricane prone coastal structures.

Gust factors were calculated from moving averages inside of 10-minute open exposure segments as a function of TI_u for 20 different gust durations (the fitted curves are illustrated in Figure 5-6). For each gust duration t , linear regression was applied to the data to determine intercept and slope coefficients as a function of $\alpha_1(t)$ and $\alpha_2(t)$.

$$GF(TI_u, t, 600) = \alpha_1(t) + \alpha_2(t)TI_u \quad (66)$$

The intercept and slope demonstrated a high degree of nonlinearity as a function of duration t , so Matlab's Curve Fitting Toolbox was employed to estimate parameters to α_1 and α_2 in Eq. 66 for over 20 different potential models, including varying orders of polynomial, exponential, power and rational curves. It was determined that a 2nd order numerator/2nd order denominator rational curve (Eq. 67) fit the intercept curve α_1 best and a 2nd order numerator/1st order denominator rational curve (Eq. 68) fit the slope α_2 best.

$$\alpha_1(t, p_{11}, p_{12}, p_{13}, q_{11}, q_{12}) = \frac{p_{11}t^2 + p_{12}t + p_{13}}{t^2 + q_{11}t + q_{12}} \quad (67)$$

$$\alpha_2(t, p_{21}, p_{22}, p_{23}, q_{21}) = \frac{p_{21}t^2 + p_{22}t + p_{23}}{t + q_{21}} \quad (68)$$

The resulting fitted curves are plotted in Figure 5-8, and the coefficients are listed in Table 5.5. Next, the logarithmic mean velocity profile was rearranged for substitution into Eq. 66,

$$TI_u(z_0) = \frac{k\sqrt{\beta(z_0)}}{\ln(z/z_0)} \quad (69)$$

where z = the 10-m observation height, z_0 = the roughness length, $k = 0.40$ (von Kármán's constant) and the function $\beta(z_0)$ = the ratio of the longitudinal turbulence variance σ_u^2 to the shear velocity squared u_*^2 . Again, Matlab's Curve Fitting Toolbox was employed to determine $\beta(z_0)$. An exponential curve of the following form,

$$\beta(z_0, a, b, c, d) = ae^{bz_0} + ce^{dz_0}, \quad (70)$$

provided the best fit to empirical data and is shown in Figure 5-9. Additionally, β values provided in Simiu and Scanlan (1996) and the observed values (averaged over roughness regimes) are compared to the model. The model coefficients are listed in Table 5-5.

The resultant formula is given in Eq. 71 and plotted for $t = 1, 2, 3, 5, 20, 30$ and 600 seconds in Figure 5-10.

$$GF(t, z_0) = \alpha_1(t) + k[\alpha_2(t)][\beta(z_0)]^{0.5} [\ln(10/z_0)]^{-1} \quad (71)$$

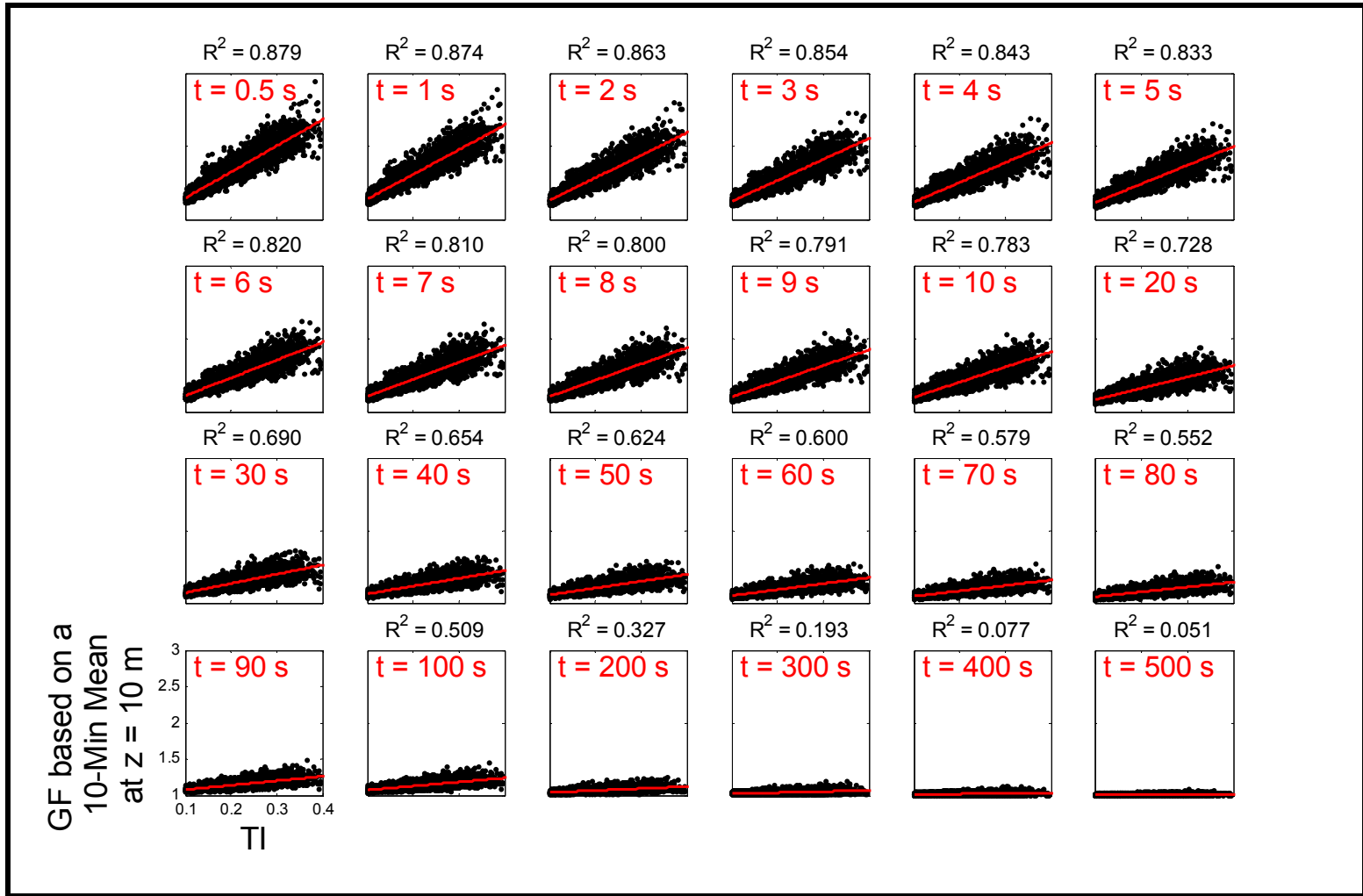


Figure 5-7. Linear regression of gust factor vs. longitudinal turbulence intensity over a variety of gust durations

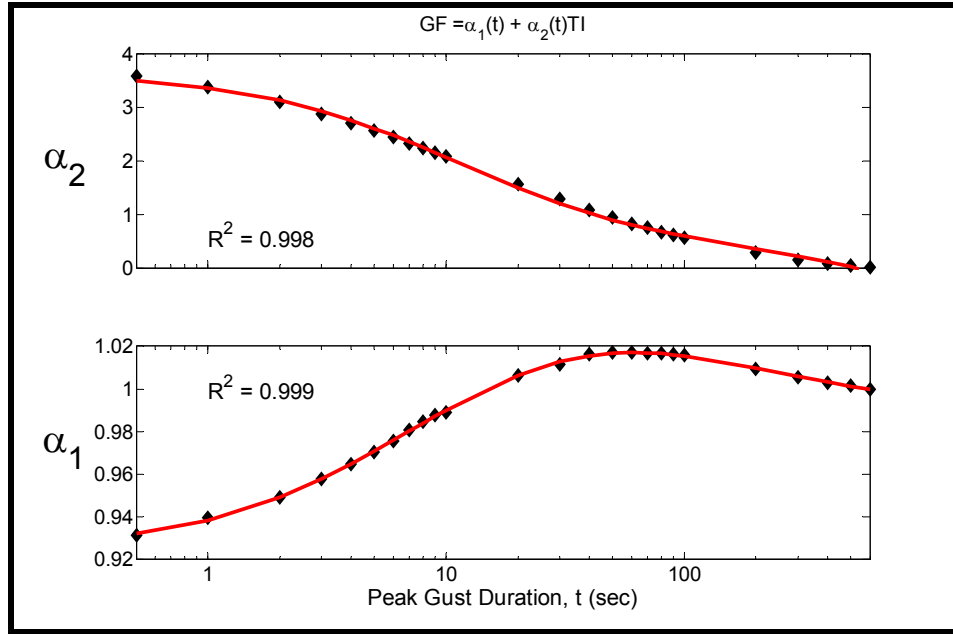


Figure 5-8. Rational polynomial fits to slope α_1 and z-intercept α_2

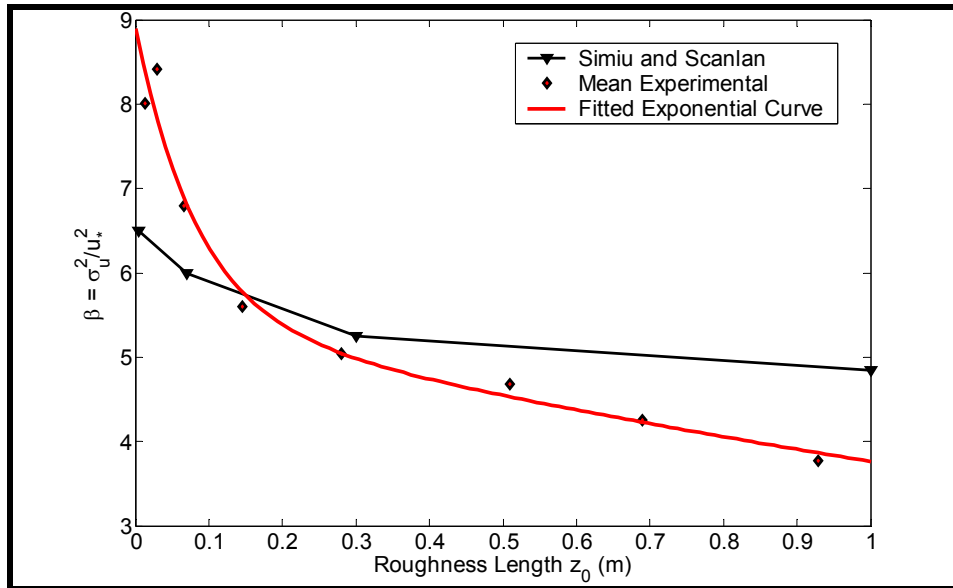


Figure 5-9. Exponential fit to beta curve

Table 5-5. Coefficients for the proposed gust factor curve

Intercept $\alpha_1(t)$		Slope $\alpha_2(t)$		$\beta(z_0)$	
p_{11}	= 9.9033E-01	p_{21}	= -7.6703E-04	a	= 3.4704E+00
p_{12}	= 1.5267E+02	p_{22}	= 3.2527E-01	b	= -1.2090E+01
p_{13}	= 1.0337E+03	p_{23}	= 4.0421E+01	c	= 5.4731E+00
q_{11}	= 1.4686E+02	q_{21}	= 1.1152E+01	d	= -3.7428E-01
q_{12}	1.1174E+03				

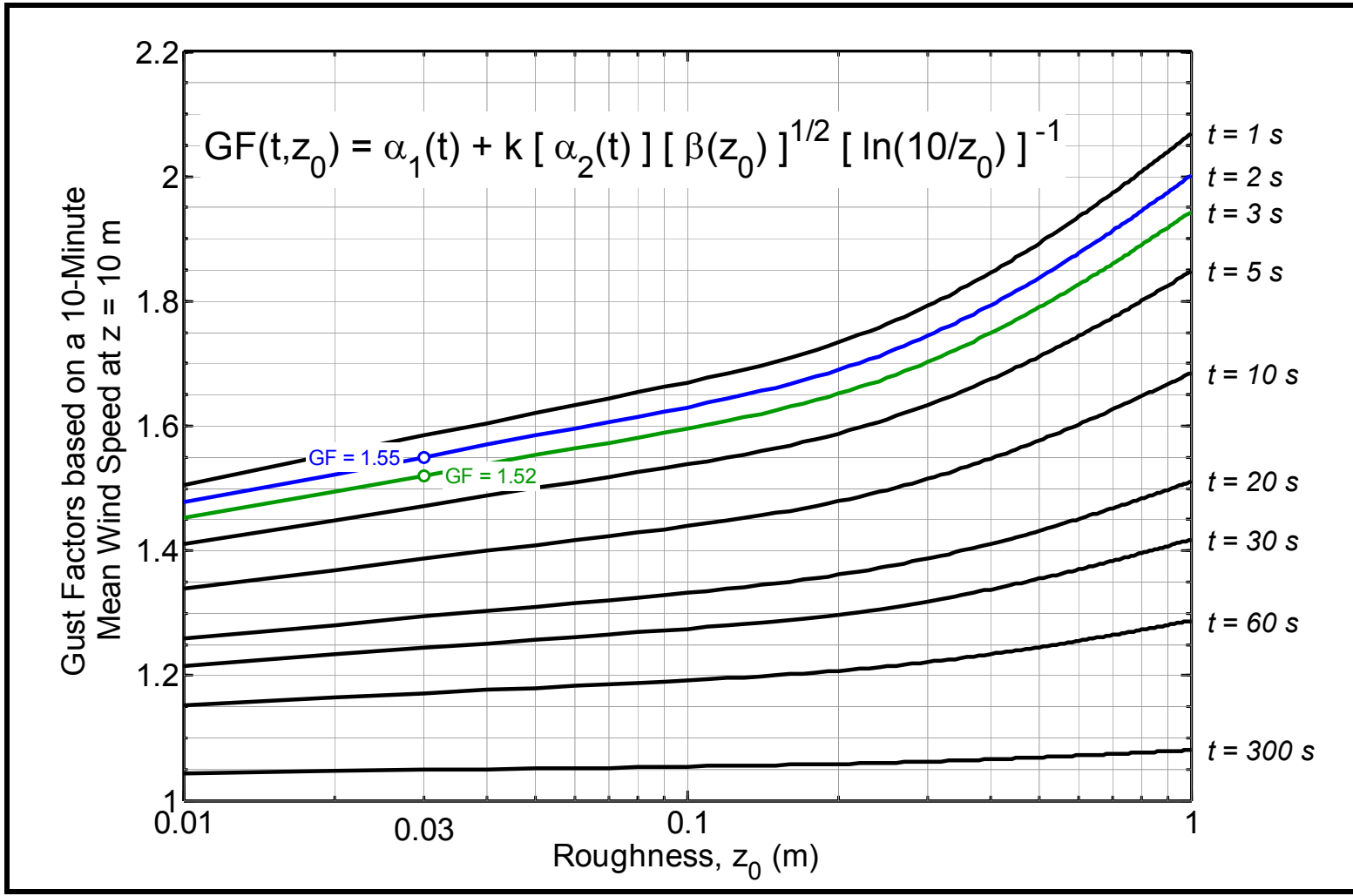


Figure 5-10. Proposed gust factor relationship based on a 10-minute wind speed, roughness length and gust duration

This curve has significant potential to benefit engineers and meteorologists but is offered with some reservation. A reliable estimate of gust factors based on surface roughness will require analysis of a full population of high resolution records from many additional exposures and at higher observed mean wind speeds. Additionally, the roughness estimation technique is very sensitive to the von Kármán constant ($k = 0.4$ in this study). Even slight adjustments, on the order of ± 0.01 , affect the estimation significantly.

Integral Length Scales

Integral length scales quantify the mean dimensions of a typical gust and with knowledge of a mean wind speed, provide the average duration a structure undergoes pressure loading associated with the passage of that gust. This section presents analysis of the longitudinal length scales measured by the FCMP instrumented towers.

Sequential segments from the storm database were linearly detrended, and their along-wind velocity components were calculated. The scaled covariance function was then computed through Wiener-Khinchine relations, specifically through an inverse Fourier transform of the autospectrum estimate. Finally, the scaled covariance function (zero-mean and unit variance autocorrelation) was integrated numerically from $\tau = 0$ s to the first crossing of the time lag (τ) axis and multiplied by the segment's mean wind speed to estimate the length scale (Simiu and Scanlan 1996).

These length scales were separated by their associated roughness lengths and mean wind speeds to produce the 10-minute summaries found in Tables 5-6. The table provides the mean longitudinal length scale L_u^x , the number of records N in the average, and the coefficient of variation CoV for 25 different roughness/10-minute mean wind

speed combinations. The maximum velocity range of 25-30 m/s encompasses the highest winds recorded by the FCMP during the 1999-2003 hurricane seasons.

Table 5-6. Longitudinal integral length scales (m) for 10-minute records

Roughness Length (m)	U = 5 - 10 m/s			10 - 20 m/s			20 - 25 m/s			25 - 30 m/s			0 - 30 m/s		
	L _{ux}	N	CoV	L _{ux}	N	CoV	L _{ux}	N	CoV	L _{ux}	N	CoV	L _{ux}	N	CoV
0.001 - 0.010	65	174	0.57	114	202	0.46	174	85	0.45	158	29	0.37	110	490	0.61
0.010 - 0.020	105	47	0.48	158	108	0.44	146	63	0.40	189	11	0.39	145	229	0.46
0.020 - 0.030	88	17	0.61	172	32	0.40	155	14	0.60	206	4	0.53	149	67	0.55
0.030 - 0.040	87	16	0.78	135	21	0.53	148	17	0.43	98	5	0.33	122	60	0.56
0.040 - 0.060	72	34	0.54	113	17	0.72	143	8	0.33	40	2	0.01	90	64	0.67
0.060 - 0.080	64	39	0.40	102	18	0.50	105	2	0.21	129	1	--	77	61	0.51
0.080 - 0.100	69	36	0.28	96	21	0.31	81	3	0.28	71	2	0.63	79	62	0.34
0.100 - 0.150	75	74	0.55	104	53	0.37	86	1	--	38	3	0.32	86	132	0.49
0.150 - 0.200	67	62	0.35	72	63	0.51	--	--	--	33	2	0.41	69	127	0.45
0.200 - 0.250	70	57	0.47	71	68	0.44	--	--	--	32	1	--	70	126	0.45
0.250 - 0.300	67	48	0.47	78	38	0.58	--	--	--	--	--	--	72	88	0.53
0.300 - 0.350	60	49	0.43	58	18	0.19	--	--	--	--	--	--	60	67	0.39
0.350 - 0.400	64	31	0.63	94	12	0.38	--	--	--	--	--	--	72	43	0.56

Analysis indicates that low wind speeds, approximately <20 m/s, produce lower longitudinal length scales than tropical cyclone force winds (> 15 m/s ten-minute sustained winds) for the same roughness of approach terrain. For example, in the roughness range $z_0 = [0.01 \dots 0.02]$ m, the length scale increases from 105 m over 5-10 m/s wind speeds to 189 m over 25-30 m/s wind speeds. Fewer records are available for higher wind speeds, but the available data suggest a convergence to a limiting length scale with wind speed.

Averages of L_u^x for $z_0 = 0.01$ -0.02 m and 0.02-0.03 m over the entire velocity range yield 145 m and 149 m for 10-minute segment calculations. These values are higher than the 100 m values estimated conservatively for structural design by Dyrbe and Hansen (1997) and observed by Schroeder and Smith (2003) during Hurricane Bonnie. The observed length scales compare more favorably to the values determined from the equation offered by Counihan (1975), which would predict $L_u^x = 196$ m for $z_0 = 0.01$ m

and $L_u^x = 139$ m for $z_0 = 0.03$ m. Table 5-6 also supports Counihan's observation that length scales decrease with increased surface roughness. The differences in observed length scale might be attributed to the storm environment, as Counihan's model is largely based on data accumulated in extratropical and winter storms.

Spectral Models

Structures with low fundamental frequencies of vibration are often subject to the dynamic effects of wind since its energy content decays exponentially in the 0-2 Hz frequency range in full-scale conditions in the surface layer. Design of low-rise buildings, such as single family homes and commercial buildings, typically does not require measures to mitigate dynamic response, but components and cladding on the structure can respond to the dynamic effects of wind loading (such as fatigue in connections from cyclic loading). This section presents spectral analysis of data collected by the FCMP, with special attention to the effects of surface roughness on the distribution with respect to frequency.

Ten-minute sequential segments from the storm database were linearly detrended, and their along-wind velocity components were calculated. Increasing the segment duration beyond 10 minutes introduced adverse nonstationary effects. Following recommendations by Bendat and Piersol (2000) in the application of Welch's method, segments were divided into m contiguous blocks and $m-1$ overlapping blocks sharing the immediate 50% data common to the neighboring contiguous blocks. Each block was tapered with a Hanning window to suppress side-lobe leakage and passed through a FFT. The $2m-1$ Fourier amplitudes were converted to PSDs and ensemble averaged. Using a 50% overlap in conjunction with the Hanning window causes successive overlapped

segments to become correlated by 16.7%, so the number of averages in the ensemble average was scaled by 94.7%.

For this analysis, $m = 6$. Higher values of m produced smoother PSD estimates but decreased the frequency resolution enough to preclude the examination of the convective mesogamma range, which has scales of motion in the 30 sec – 6 minute range. Figure 5-11 presents observed ensemble-averaged PSDs for four different roughness regimes (and 10-minute mean wind speed = 12.5 m/s). For comparison purposes, the Flat, Smooth and Uniform (FSU), Perturbed Terrain and Kaimal (neutral Kansas) models are shown in the same figure (Tielman 1995). These models were prescribed for terrains with low vegetation, complex terrains and open exposures, respectively. For visualization purposes (and to keep meteorological convention), the normalized PSD ordinates were multiplied by the appropriate frequency (Hz) and plotted against reduced frequency, determined from the nondimensional Monin coordinate f (described previously in Chapter 3).

For approximately open ($z_0 = 0.01$ - 0.05 m) to roughly open ($z_0 = 0.05$ - 0.10 m) exposures, results agree with previous observations made by Powell et al. (1996) and Schroeder and Smith (2003)—the distribution of energy in the low frequency range is higher than the available models would suggest. Over the first three roughness regimes, the empirical data collapse in the inertial subrange (indicated by the black line), but attenuates at the highest end of the frequency range. This is likely due to the response characteristics of the propeller anemometry since it mechanically filters the amplitudes of short wavelength gusts (Schroeder and Smith 2003). As the surface roughness increases ($> z_0 = 0.15$ m), however, the energy shifts to higher frequencies and similarity does not

appear to hold. As the FCMP database expands (especially from open exposure records), model development will be initiated to provide a functional form of the spectra estimates shown in Figure 5-11.

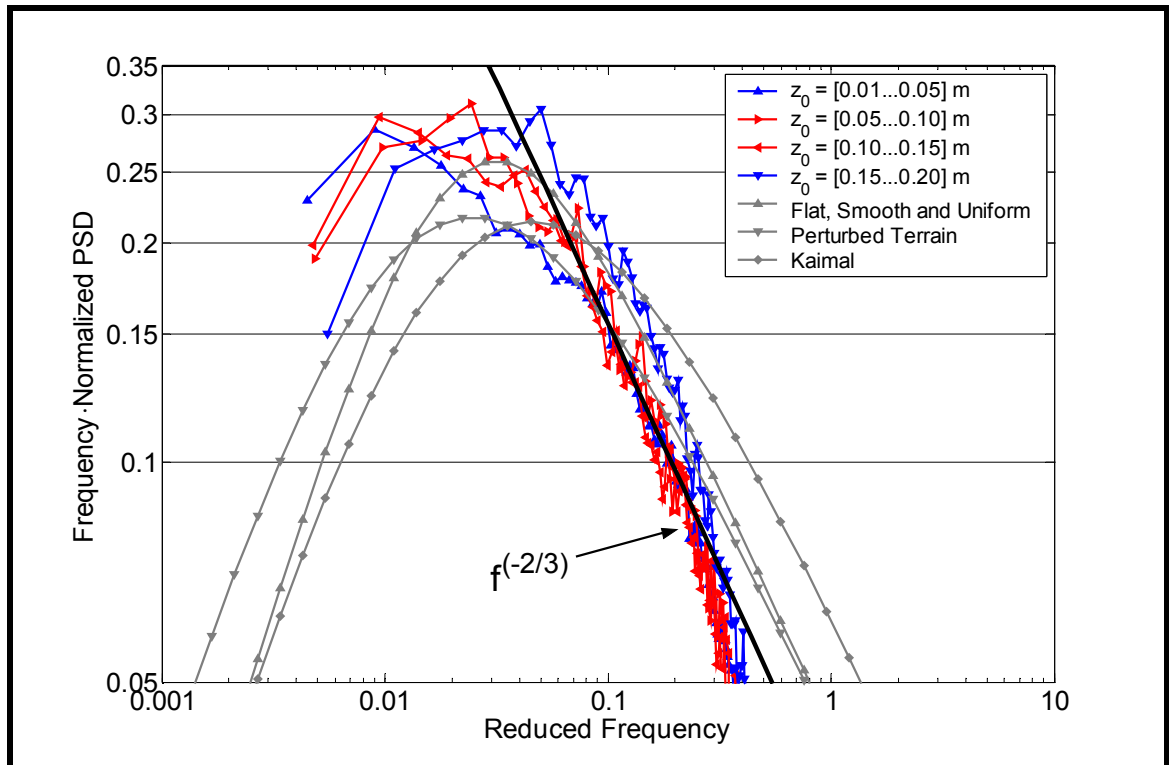


Figure 5-11. Spectral analysis of tropical cyclone data

Summary

In this chapter, turbulence intensity, gust factors, integral length and power spectra were analyzed from a subset of the FCMP storm database that passed criteria established to eliminate 10-minute segments with mean wind speeds less than 5 m/s, shifts in 1-minute mean directions $> 20^\circ$, immediate upwind obstructions or changes in terrain elevation and 1st or 2nd order nonstationarities. Analysis of the longitudinal, lateral and vertical turbulence intensities indicates a logarithmic increase in the ratios of vertical to longitudinal and lateral turbulence intensities for increasing surface roughness. Three

gust factor relationships—based on segmental averages, moving averages and the method proposed by Durst (1960)—were developed for a 10-minute mean wind speed and compared to the models used by design standards. The moving average produced the highest gust factor curve and is recommended for use. A gust factor curve was also developed for 1-hour mean wind speed. The analysis of the FCMP database indicates that tropical cyclones produce “gustier” winds than extratropical (e.g., winter storm) data, which was the basis of Durst (1960), but does not support the degree of upwind adjustment of gust factors for hurricane winds to the level proposed by Krayer and Marshall (1993) for a 1-hour mean wind speed. A formula relating gust factors to gust duration and roughness length was developed for a 10-minute mean wind speed. Analysis of longitudinal integral length scales indicates that lower wind speeds produce shorter estimates of gust lengths. While fewer records are available for higher wind speeds, the data suggests a convergence to a limiting length scale with wind speed. Finally, power spectra measured from segments over four different roughness regimes in 10-15 m/s winds were studied and indicates that the distribution of energy in the low frequency is higher than the available models would suggest for open exposures.

CHAPTER 6 MULTIVARIATE STOCHASTIC SIMULATION OF WIND PRESSURE OVER LOW- RISE STRUCTURES

Prescriptive measures for the design of structures to resist wind loads are under continual refinement as wind-tunnel, full-scale, and computational methods improve our understanding of wind-structure interaction. The database assisted design (DAD) concept now under development (see Chapter 2) will offer an online database of wind load time histories, and has the potential to further enhance load definitions. Several university-affiliated wind tunnel facilities have been contracted by the National Institute of Standards and Technology (NIST) to generate an extensive library of such time histories for a large variety of building shapes and terrains. These physical testing efforts will be complimented by computational load generating methodologies including computational fluid dynamics and stochastic simulation techniques. The intent is to use these means to extend existing records and interpolate between building shapes tested in wind tunnels.

This chapter focuses on the use of a stochastic simulation algorithm for the generation of pressure coefficient time histories on a building similar to tested geometries. The problem statement under consideration is: given wind tunnel measured time histories of pressure coefficients at multiple roof taps on two alike though not identical buildings, develop methods to accurately represent the pressure coefficient time histories of a building whose geometry lies between the two measured buildings. For example, consider three buildings identical in all respects other than roof pitch. If wind

tunnel studies are conducted on models with 3 on 12 and 8 on 12 roof pitches, infer appropriate time histories for the roof taps on a 5 on 12 roof pitch building. The resulting aggregate pressure loads acting on the structure should be statistically similar to the actual loads in terms of mean, rms and peak values. A viable solution to the problem statement will serve to increase the applicability of the intended online DAD database by making a wider array of low-rise building geometries available.

Recently, researchers have addressed this issue through re-scaling of the measured pressure time histories of tested buildings (Chen et al. 2003a, 2003b). A description of these efforts was provided in Chapter 2. In these studies, the complexity of direct simulation of the time histories was avoided in order to explore the efficacy of simpler methodologies. Second order methods, however, are unable to capture differences in higher order statistics between time histories on different geometries, potentially influencing the ability to reproduce accurate peak value magnitudes and rates of occurrence.

The avenue of research presented herein focuses on the direct use of a stochastic simulation algorithm for the generation of pressure coefficient time histories on a building similar to tested geometries. This method goes beyond the translation and dilation of time histories of tested buildings (e.g., Chen et al., 2003a), potentially improving the accuracy of the inferred load time histories by preserving the spectral content, correlation and the non-Gaussian probability distribution, and thereby maintaining higher moments and accurate fluctuating peak values. The auto- and cross-power spectral density (PSD/CSD) and cumulative distribution functions (CDF) used as

the “target” input to the stochastic simulation algorithm are derived from interpolation of models fitted to data from similar buildings.

The simulation method is capable of accurately generating realizations that match the input PSD and CDF models. Thus the main issue is the accuracy of the interpolation scheme used to create these models. The following sections discuss (1) the simulation methodology and the test matrix of data, (2) the accuracy of the CDF and PSD interpolation schemes, (3) the effectiveness of the algorithm to recreate aggregate pressure loading on a low-rise building, and (4) the direct interpolation of peak values as an alternative to simulations.

Methodology

Overview

Wind tunnel data sets were provided for four model buildings differing only by height. Spectral and probability models of the pressure coefficient time histories were created for each building. Pairs of these models were then selected to serve as the “bounding” buildings, and a building of height between those of the bounding buildings was used as the “subject” building whose roof pressure is to be simulated. The spectral and probabilistic models for this subject building were created by interpolation of the models from the bounding buildings, and simulation was applied to create pressure time histories for the interpolated building. The statistics of the resultant simulated pressures were then compared to those actually measured in the wind tunnel for the subject building. For all combinations under consideration, there are measured data to compare with the simulated data, but the measured data from the subject building were not used to create the simulation. Thus, the efficacy of the methodology can be directly verified.

Simulation Technique

The multivariate non-Gaussian simulation algorithm developed by Grigoriu (1998) is employed in this study, using modifications as outlined by Deodatis and Micaletti (2001)—details may be found in Chapter 3. Simulation software and its accompanying validation algorithms were developed in the Matlab environment. The algorithm is designed to generate realizations of multiple correlated non-Gaussian variables given the CDFs and cross-spectral matrix as targets. This method is widely accepted for a variety of applications and was determined in this study to reliably produce realizations that match the target PSD, CSD and CDF models typical of roof uplift data. A detailed analysis of several non-Gaussian simulation algorithms including performance comparisons can be found in Masters and Gurley (2003).

Wind Tunnel Data Sets

Time histories of pressure coefficients were provided for this study by the Allen G. Davenport Boundary Layer Wind Tunnel at the University of Western Ontario (UWO). The UWO facility is one of several wind tunnels that have been contracted by NIST to provide time histories of pressure coefficients for a variety of building shapes for use in the DAD. Actual data sets to be used within the DAD database are used in this study.

The subject is a 1:100 scaled gable-roofed building with a rectangular 80 ft by 125 ft plan (24.4 m by 38.1 m) and 1:12 roof slope with the ridgeline parallel to the long wall. The model was raised or lowered through the floor of the wind tunnel to change its eave height. Four scaled heights were used: 16, 24, 32 and 40 ft (4.9, 7.3, 9.8 and 12.2 m). A total of 665 pressure taps were instrumented over the building, with 335 taps on the roof. The reference wind speed was 45 ft/s (13.7 m/s), with eave height speeds about 64% of this velocity. Open exposure ($z_0 = 0.03$ m) was used for all data sets under consideration.

The data acquisition system collected 49,792 scans at 500 Hz (~100 seconds), which is equivalent to one full-scale hour. Figure 6-1 contains a photo of the model, the tap grid used in this study (which are evenly spaced at 5 ft in full-scale), and the grid's corresponding tap numbers as assigned at UWO. Further details concerning the data acquisition system and experimental configuration can be found in Chen et al. (2003a).

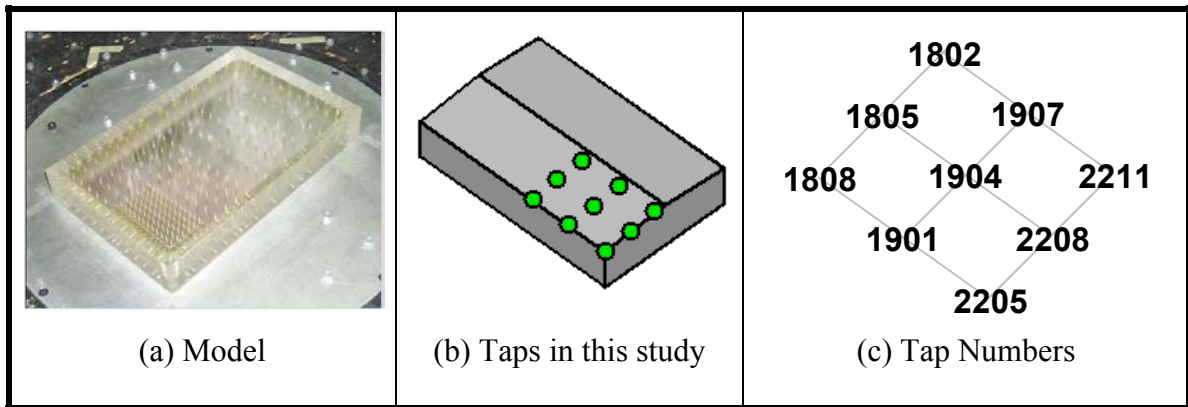


Figure 6-1 Tap geometry on the building model

Cases Studied

The data sets, simulation algorithm and interpolation scheme utilized in this study were applied to a 12-case test matrix. All cases share similar tap location geometry—the same nine taps were used to collect pressure data—but each case has a unique pair of eave heights and wind direction. Table 6-1 provides each case number (1-12). Bounding eave heights refer to the lower and upper eave heights from which models for the subject eave height are interpolated.

Table 6-1. Simulation test matrix

CDF	Bounding Eave Heights	16 and 32 ft	16 and 40 ft	24 and 40 ft	16 and 40 ft
	Interpolated Eave Height	24 ft	24 ft	32 ft	32 ft
Wind Direction	Parallel to Ridgeline ($\alpha = 180^\circ$)	1	4	7	10
	Cornering ($\alpha = 225^\circ$)	2	5	8	11
	Perpendicular to Ridgeline ($\alpha = 270^\circ$)	3	6	9	12

Interpolation Overview

A linear weighting scheme was applied to the test matrix to ensure that targets for the interpolated eave height share the greatest similarity to those of the closest bounding eave height. In the event that the differences between the bounding and interpolated eave heights are identical (such as Cases 1-3 and 7-9), the interpolated target reduces to an average of the bounding cases. For example, consider the interpolation of the means in Case 4, where the 16 and 40 ft targets are used to estimate the 32 ft target. Using the linear weighting scheme, the 24 ft mean is equal to 2/3 of the 16 ft mean and 1/3 of the 40 ft mean. This linear interpolation procedure was applied to define the probabilistic and spectral targets for the simulation of pressure on the interpolated eave heights (subject building). In all cases, the interpolations and simulations were conducted separately for each of the nine taps shown in Figure 6-1. For presentation of results, the pressure coefficients at the nine taps were aggregated to represent total uplift over that portion of the roof. Details are provided in the following sections.

Interpolation of the Probability Targets

Interpolation of the probability targets is a two-stage process. In the first stage, the interpolated first and second order moments are calculated. These values are weighted and summed to produce the interpolated estimates. The CDF and PSD interpolations and simulations are conducted within a normalized framework (zero mean, unit variance). In

the last step of the stochastic simulation procedure, the normalized simulations are translated and dilated with the appropriate interpolated first and second moments.

In the second stage, empirical CDFs were estimated from the normalized eave height data of the bounding buildings through the nonparametric estimation technique offered by Kaplan and Meier (1958). Since the domains of these estimates are unique, direct interpolation between ordinates is not possible. CDFs were linearly interpolated over a domain common to the bounding data sets, which produced two abscissas for each discrete value of probability. Next, the bounding CDFs were weighted and summed to produce the interpolated CDF.

Consider the interpolation between the 16 and 40 ft eave heights to determine the 32 ft target CDF (Cases 10 - 12 in Table 6-1). Following the procedure outlined above, normalized CDFs are calculated for the 16 and 40 ft data sets, which results in the domain bounds of $[x_a, x_b]$ and $[x_c, x_d]$, respectively. Next, each CDF is linearly interpolated over the lowest and highest values in the bounding CDFs to produce CDFs with a common domain of $[\min(x_a, x_c), \max(x_b, x_d)]$. Then, the CDFs are weighted relative to the eave height difference. In this example the lower bounding CDF is scaled by $(1 - (32-16)/24) = 1/3$ and the higher bounding CDF is scaled by $1 - (40-32)/24 = 2/3$. Finally, the scaled CDFs are summed to produce the interpolated CDF for the 32 ft eave height.

Validation of CDF Interpolation Concept

The results of the CDF interpolation scheme for the 24 ft eave height interpolation of Tap 1904 (see Figure 6-1c) for winds perpendicular to the ridgeline, cornering winds and winds parallel to the ridgeline (Cases 1 – 6 in Table 6-1) are shown in Figures 6-2 through 6-4. For visualization purposes, the probability density function (PDF)

equivalents of the CDFs are shown. PDF estimates of the experimental data (in gray) are compared to interpolated estimates from two combinations (16 and 32 ft, 16 and 40 ft) of bounding CDFs. The PDF estimated from wind tunnel data sets of the subject 24 ft subject building (noted ‘Experimental, $H = 24$ ft’ in the figures) are provided for direct comparison of the interpolated models to those from the actual data. These plots show results after the interpolated first two moments have been applied to the normalized PDFs.

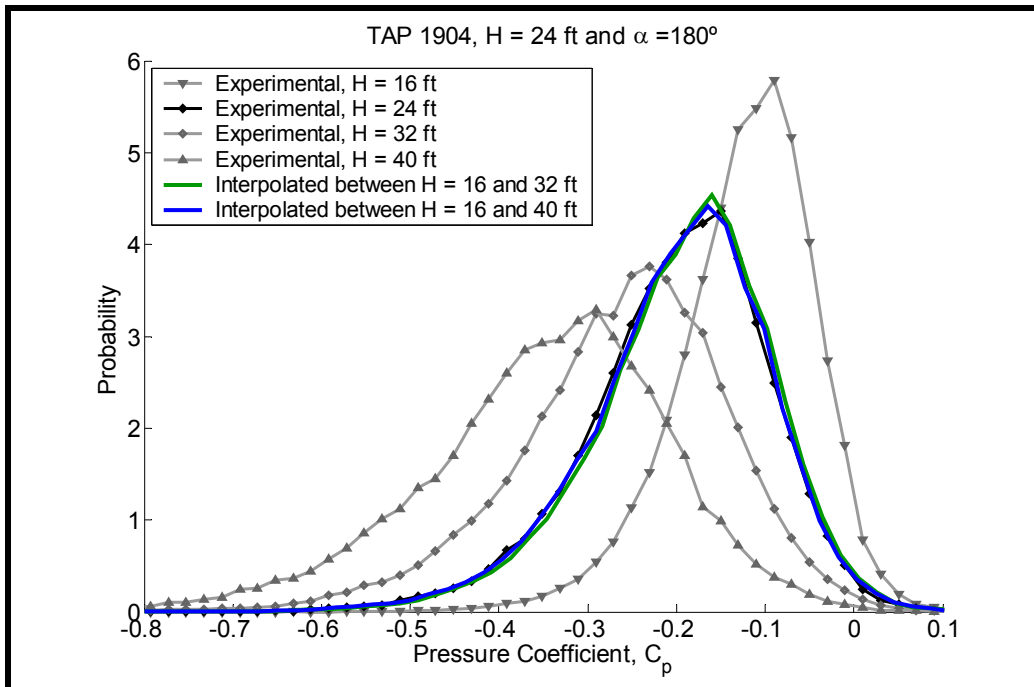


Figure 6-2. PDF interpolation of 24 ft eave height for a single tap (winds parallel to the ridgeline)

These figures (and the results of interpolation to the 32 ft building height not shown) indicate that the interpolation scheme produces a reasonable estimate of the “true” probability content without direct access to the measured time history. The greatest deviation between the interpolated target and the true target occurs at the peak of the distribution. The tails, which describe the likelihood of a peak value occurring, fit

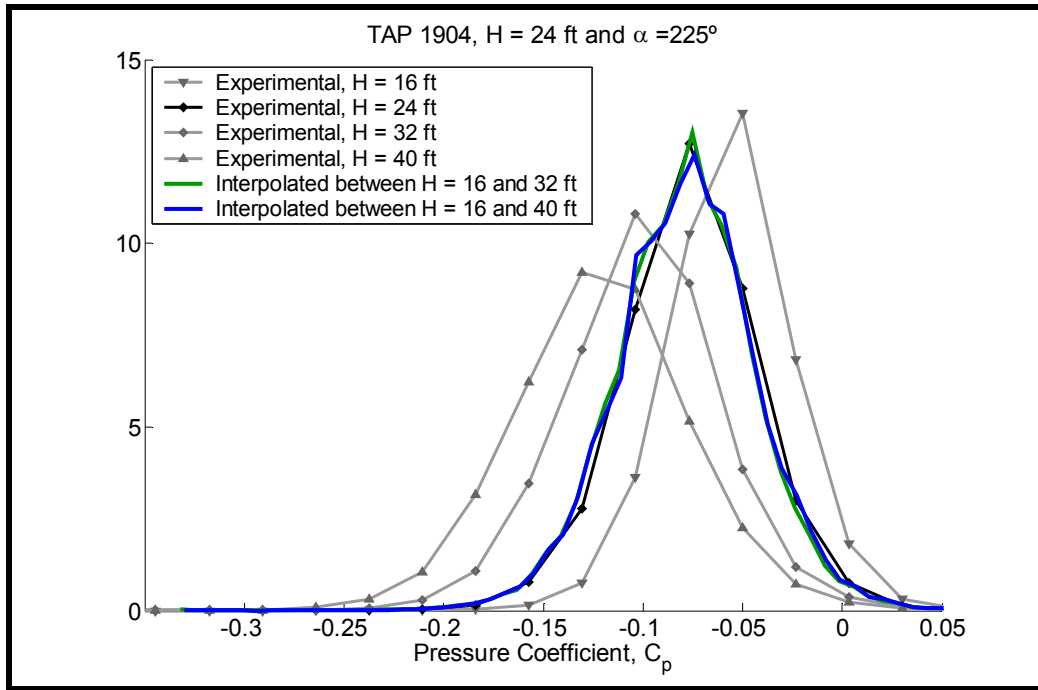


Figure 6-3. PDF interpolation of 24 ft eave height for a single tap (cornering winds)

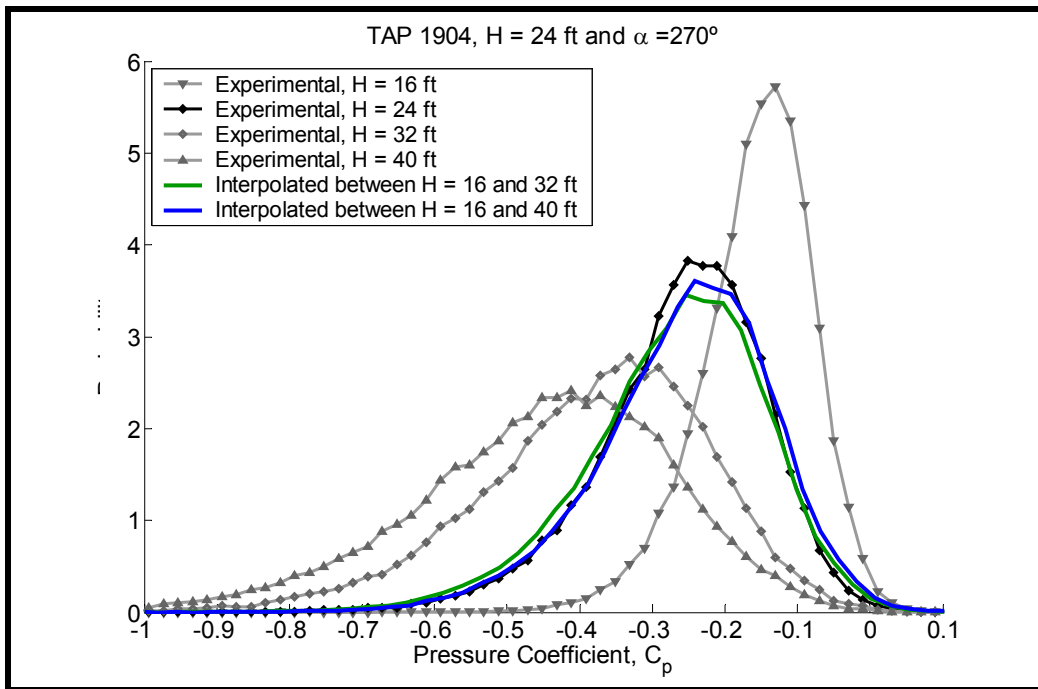


Figure 6-4. PDF interpolation of 24 ft eave height for a single tap (winds perpendicular to the ridgeline)

closely to the true target (confirmed by analysis of the mean square error). The results from this simple interpolation scheme are encouraging, as the ability to accurately model higher moment information on the subject building is critical to simulation of peaks at individual taps and aggregate peak loads over a large area such as that covered by the nine taps shown in Figure 6-1b.

Interpolation of the Spectral Targets

An approach similar to the CDF interpolation scheme was adopted for the interpolation of the PSD models. First, the lower and upper bounding data were normalized to a unit variance and zero mean. PSDs were estimated from Welch's (1967) method using six contiguous segments and a 50% overlap to produce spectra for the ensemble-averaged estimate.

In most cases, the use of empirical PSDs from a single realization in the target spectral content leads to problems with non-positive definite matrices in the cholesky decomposition used within the simulation algorithm. In order to produce smoother targets, a multidimensional unconstrained nonlinear minimization technique was used to fit a four-parameter exponentially decaying spectral model to the empirical PSD,

$$S_{xx}(n) = \frac{A}{(B + Cn)^D} \quad (72)$$

where $S_{xx}(n)$ = the weighted PSD, A , B , C and D = the shape parameters of the PSD and n = the frequency (Hz). The resulting PSD models for the data sets from the bounding buildings were weighted and summed to produce the PSD targets for the interpolated eave height.

Interpolation of cross-spectra required three steps. First, interpolated PSDs were calculated from the same procedure as above and weighted. Second, coherence functions were calculated from the bounding data. In conjunction with the weighted PSDs, the real-valued CSD was calculated from

$$S_{xy}(n) = \sqrt{\gamma_{xy}^2(n) S_{xx}(n) S_{yy}(n)} \quad (73)$$

where $S_{xy}(n)$ = the interpolated CSD, $\gamma_{xy}^2(n)$ = the coherence squared function, $S_{xx}(n)$ = the weighted PSD of the lower bounding data and $S_{yy}(n)$ = the weighted PSD of the higher bounding data.

Correlation coefficients were calculated from the lower and upper bounding data, weighted by the eave height, and added in quadrature (the square root of the sum of the squares) to produce the interpolated value of the correlation coefficient. Finally, the interpolated CSD was normalized and scaled by this correlation coefficient to produce a target CSD with the correct area.

During the development of the simulation software, several exponentially decaying spectral models (adapted from wind PSDs) were tested to improve the accuracy and robustness of the algorithm. It was generally noted that slight changes in these spectral models (and the optimization algorithm used to fit the parameters) resulted in no significant difference as long as the area under the interpolated PSD/CSD models equaled the second central moment.

Last, it should be noted that the phase component of the CSDs were ignored in this study. This exclusion affects the temporal correlation structure but reduces the number of

non-positive definite matrices in the cholesky decomposition. Given the close proximity of the pressure taps, this simplification was determined to have a negligible effect on simulation results. Spectral analysis revealed that imaginary components made up less than 2% of the magnitude of the CSD ordinates (the phase $< \sim 0.02$ radians).

Validation and Limitations of the Simulation Algorithm

This section discusses the efficiency, limitations and accuracy of the multivariate stochastic simulation algorithm developed in this study. Using a workstation with 2.5 GHz processor and 512 MB of RAM, the simulation algorithm was capable of creating 20 simulations on nine correlated 49,792-point time histories of pressure tap data in approximately 10 minutes in the Matlab programming environment. It is conceivable that the use of a compiled language (such as C++) could lessen simulation times to a few minutes. However, simulation time did not appear to present a major obstacle.

The algorithm simulated up to eleven pressure taps of varying correlation successfully. Beyond eleven simultaneous taps, the cholesky decomposition necessary in the algorithm encountered non-positive definite matrices at enough frequencies with significant energy to prohibit further simulation. To increase this threshold, multiple adjustments were made to the algorithm, including the use of modified (or incomplete) cholesky decomposition techniques, three- and five-parameter spectral models, relaxed correlation requirements and increased ensemble averaging of the experimental data to produce spectral targets. The effect of these modifications was at best minimal and at worst detrimental, and only one modification was adopted for use in the simulation algorithm. When the cholesky decomposition encountered a non-positive definite matrix, the off-diagonal terms of the offending column were reduced until the cholesky decomposition could proceed. This operation was typically necessary at very few

frequency points (typically < 100 points in the 24897-point frequency domain), but did result in an artificial reduction of correlation among variables at those frequencies.

Accuracy of the Simulation Algorithm

Two critical components of this simulation study are the accuracy of the interpolation schemes used to create target spectral and probabilistic models and the ability of the simulation method to reproduce these targets. This section concerns the latter without regard to the former.

The simulation algorithm is used in this portion of the study to create realizations of uplift loading from spectral and probabilistic target models created directly from the experimental data of the subject building (i.e., no interpolation is utilized). Simulations were run for each eave height and wind direction and compared against the spectral and probabilistic target models to validate the accuracy of the algorithm.

The case presented herein is the simulation of nine pressure taps on a 24 ft building experiencing winds parallel to the ridgeline ($\alpha = 180^\circ$). The experimental data and one realization of the simulated pressure coefficient time histories are presented in Figures 6-5 and 6-6. The minimum and maximum instantaneous (500 Hz) pressure coefficients are provided in the right margin of the plots. These values compare well because of the use of an empirical CDF map in the simulation algorithm (Masters and Gurley, 2003), which offers very accurate matching of the target CDF and thus higher order moments of the target probability distribution. The extreme value of each tap simulation varies by no more than 4% from the extreme values of the experimental data. A visual comparison of the experimental and simulated histories at individual taps qualitatively demonstrates the

ability of the simulation to capture the highly non-Gaussian nature of the loads. Further quantitative comparison is presented in terms of PSD and correlation statistics.

The algorithm performed well in the reproduction of the correlation structure measured from the experimental data. The mean correlation coefficients measured from 20 simulations are compared to the correlation coefficients measured from the target data in Table 6-2, along with the standard deviation among the 20 simulations and the residual between the experimental and simulated data. The standard deviation indicates very little fluctuation in the correlation structure from one realization to the next, and the residual between the target and the measured correlation coefficients is nearly zero.

Further comparison is provided in terms of the auto- and cross-spectral densities from experimental and simulated data. Figure 6-7 illustrates the comparison of the upper triangle of the target spectral matrix (gray lines) to 20-realization ensemble average of simulated data (blue lines). The number(s) in each plot correspond to one of the nine spectral terms. The numbers 1 – 9 in Figure 6-7 refer to the tap labels in Figure 6-1c in the following sequence: 2205, 1901, 1808, 2208, 1904, 1805, 2211, 1907 and 1802. For example, the plot labeled 3-5 refers to the CSD between Taps 3 and 5, which are taps 1808 and 1904 in the UWO tap configuration. The ensemble-average spectra match the targets best at the lower number taps and experience slight degradation in the cross-spectra as the tap numbers increase from 1 to 9. Note, however, that the auto-spectra continue to be matched very accurately through tap 9. The degradation in the cross-spectral matching is due to the order of operations in the cholesky decomposition and the use of the relaxation technique discussed in the previous section. Diagonal terms are calculated followed by the off-diagonal terms, which are calculated from the lowest to

highest rows for each column. The end result is a slight under-representation of the correlation among simulated taps. Referring to Table 6-2, however, it is clear that this under-representation is of little significance in terms of correlation coefficient matching.

In this simulation algorithm, the CDF mapping procedure is applied to the individual taps as the last step before dilation and translation to install the proper first and second moments. The accuracy of this mapping procedure has been shown to be highly accurate, and thus the probability descriptors for the individual taps will match the targets without fail (Masters and Gurley, 2003). Therefore, an explicit comparison of target and simulated PDFs is not provided. However, accuracy was confirmed for this study. A quantitative comparison of higher moments is provided in the results section when the interpolation and simulation algorithms are combined.

The end result of this portion of the study is an acceptable validation of the accuracy of the multi-variate non-Gaussian simulation algorithm employed. The next section presents results of simulations on subject buildings using PSD and PDF targets interpolated from bounding buildings.

Results

The interpolation and simulation algorithms have been verified independently in the previous sections. This section now addresses their combined application to the simulation of aggregate uplift on a gable-end roof based on knowledge only of the time histories on the bounding buildings.

Comparison of Peak Aggregate Uplift

This section discusses the results of the simulations corresponding to Cases 1 – 12 as defined in Table 6-1. Correlated pressure coefficient time histories were simulated for the nine taps illustrated in Figure 6-1 and averaged at each time step to produce an

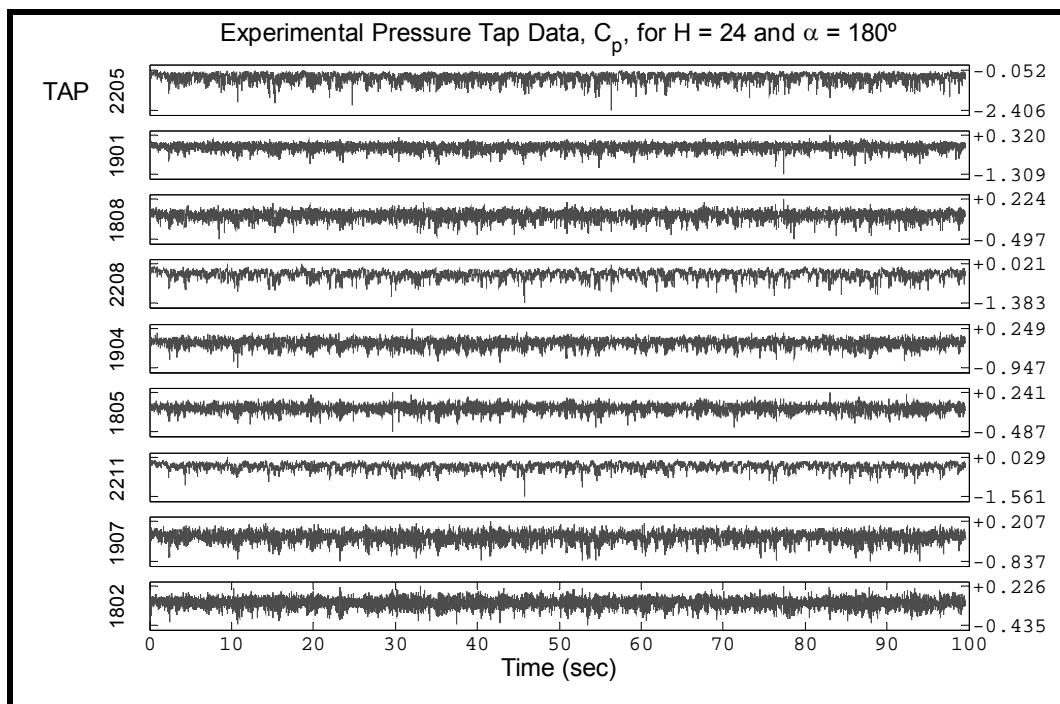


Figure 6-5. Experimental pressure tap data

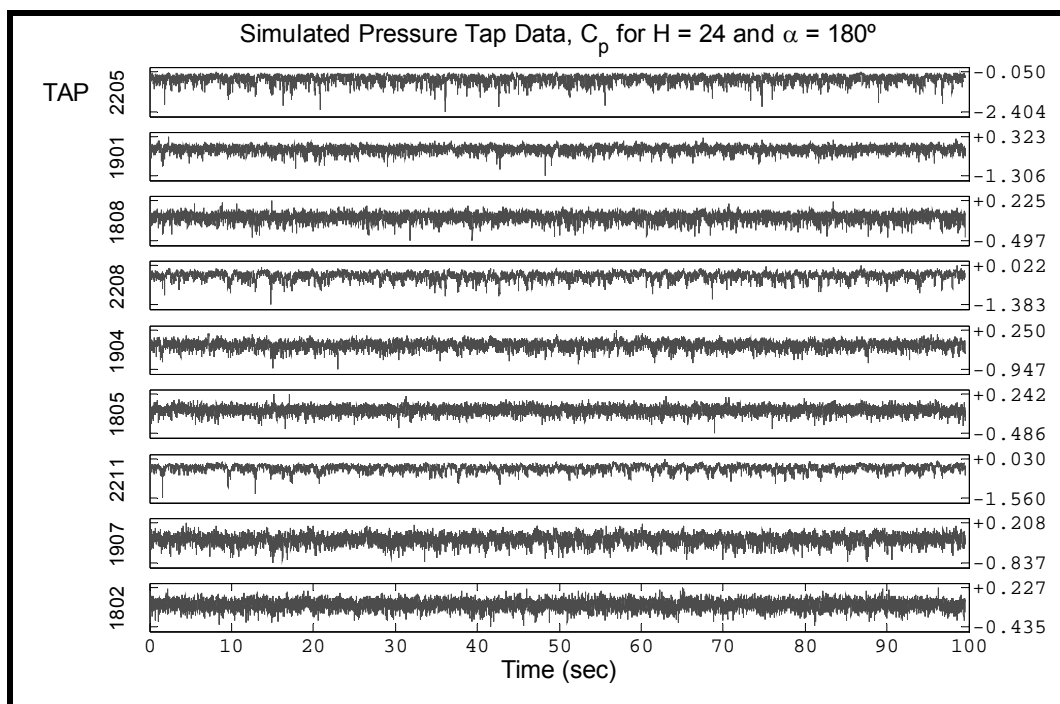


Figure 6-6. One realization of simulated pressure tap data

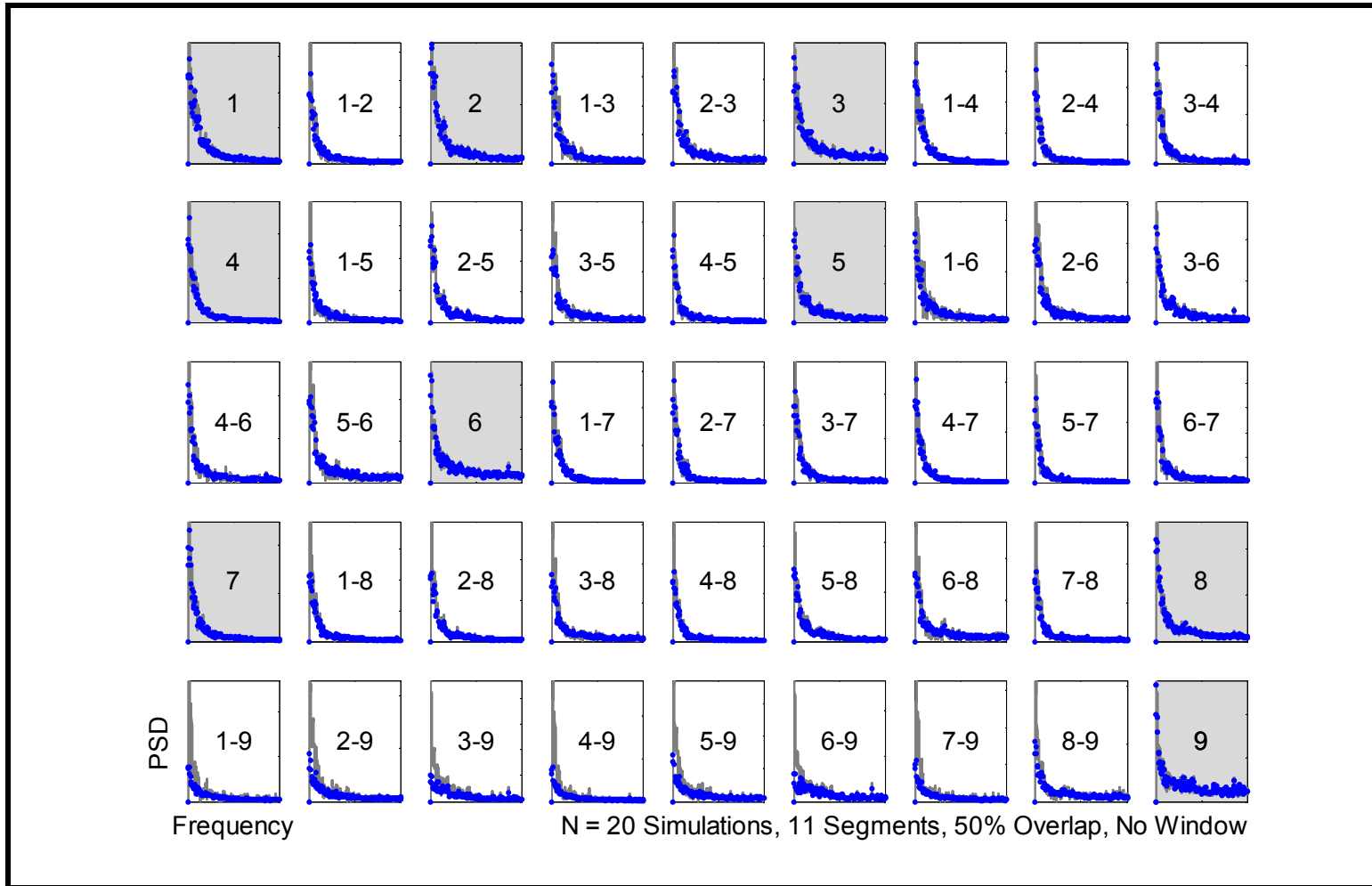


Figure 6-7. Comparison of the target and simulated spectral matrices for one realization of $H = 24$ ft and $\alpha = 180^\circ$

aggregate uplift (the pressure coefficients were not weighted by tributary area). Peak uplifts were calculated over durations ranging from 1 second to 1 hour.

Comparisons are shown for average observed peak values as a function of duration in Appendix C. In each plot, the peak pressure coefficients shown are determined from four different sources:

1. Experimental time histories for the bounding eave heights (in gray with triangle markers) and the subject eave height (in black)
2. Simulated time histories using models interpolated from buildings of lower and higher bounding eave heights (in green)
3. Simulated time histories of the subject eave height with knowledge of the spectral and probabilistic targets (in blue)
4. Linear interpolation from measured peak values of the buildings of lower and higher eave heights (solid gray). No simulations are required to calculate these values

Percent errors—the ratio of the difference between the observed and actual peaks to the actual peak—is provided in the lower portion of each graph in Appendix C. Peak uplifts compared better as the peak duration approached 1 hour (the segment duration). The simulations from interpolated CDFs are as accurate in most cases as the simulations based on models directly from the experimental data at the test height. This shows the potential for CDF interpolation to provide models for roof uplift simulation on untested buildings. However, it is notable that the majority of comparisons in Appendix C show an underestimation of aggregate peak pressure coefficients (on the order of 10%) for gust durations of less than 3 seconds.

Table 6-3 provides the mean, rms, minimum, maximum, skewness and kurtosis values of the 12 cases in the test matrix. The linear interpolation weighting scheme estimates the 1st and 2nd order statistics with <7% and <13% errors if the bounding cases

correspond to the immediate eave heights—interpolation from wider bounds produces greater error (as high as 44% in the rms). Peak instantaneous suctions in the interpolated cases varied by no more than 7% for the immediate eave heights. The 3rd and 4th order moments from the simulations fluctuated about the targets from the experimental data—no discernible trend is present.

Monte Carlo simulation studies may find use in applying the interpolation / simulation methodology presented in this study. Capturing rates of occurrence of peak pressures may be desired, such as studies of fatigue-type failure of building components (e.g., Lynn and Stathopoulos 1985, Xu 1996), and would justify the application of the simulation. If average peak values are the quantity of interest, however, direct interpolation of experimental data from the higher and lower height building geometries provides acceptable results, and simulations do not appear to provide added accuracy. This is significant in its implications. These results suggest that an average of peaks from buildings of similar geometry may be sufficient.

The methods in this study provide a potential solution for the generation of time histories for buildings at eave heights that have not been wind tunnel tested. However, the stochastic simulation and interpolation schemes do not directly incorporate knowledge of the physical flow mechanisms producing the uplift. The cases in this study were carefully selected such that only a single geometric descriptor of the building varied from case to case. The close similarity in geometry leads to flow mechanisms over the roof that are also similar. The results will begin to suffer as multiple geometric descriptors vary. Additional studies will be conducted on such cases when the data are made available from the UWO test facility, with the intent of highlighting the limiting

Table 6-3. Resultant errors in the first four moments and peak values of the simulations

$H = 24$ ft, $\alpha = 180^\circ$ cases 1 & 4	Mean	RMS	Min	Max	Skewness	Kurtosis
Target	-0.213	0.050	-0.648	-0.042	-0.76	3.85
Simulated from Experimental Data	-0.213	0.050	-0.715	-0.026	-0.70	3.94
<i>Error</i>	<i>0.0%</i>	<i>0.2%</i>	<i>10.4%</i>	<i>37.4%</i>	<i>7.1%</i>	<i>2.2%</i>
Simulated from $H = 16$ ft and $H = 32$ ft	-0.207	0.047	-0.662	-0.014	-0.61	3.83
<i>Error</i>	<i>2.8%</i>	<i>5.3%</i>	<i>2.2%</i>	<i>66.9%</i>	<i>19.3%</i>	<i>0.5%</i>
Simulated from $H = 16$ ft and $H = 40$ ft	-0.256	0.072	-0.745	-0.029	-0.71	3.98
<i>Error</i>	<i>20.2%</i>	<i>43.6%</i>	<i>14.9%</i>	<i>31.2%</i>	<i>5.8%</i>	<i>3.3%</i>

$H = 24$ ft, $\alpha = 225^\circ$	Mean	RMS	Min	Max	Skewness	Kurtosis
Target	-0.268	0.076	-0.659	-0.041	-0.530	3.640
Simulated from Experimental Data	-0.268	0.076	-0.683	-0.060	-0.553	3.671
<i>Error</i>	<i>0.0%</i>	<i>0.2%</i>	<i>3.6%</i>	<i>46.5%</i>	<i>4.4%</i>	<i>0.9%</i>
Simulated from $H = 16$ ft and $H = 32$ ft	-0.272	0.079	-0.673	-0.046	-0.479	3.414
<i>Error</i>	<i>1.7%</i>	<i>3.9%</i>	<i>2.0%</i>	<i>12.5%</i>	<i>9.7%</i>	<i>6.2%</i>
Simulated from $H = 16$ ft and $H = 40$ ft	-0.256	0.072	-0.745	-0.029	-0.712	3.982
<i>Error</i>	<i>4.2%</i>	<i>5.6%</i>	<i>13.0%</i>	<i>29.1%</i>	<i>34.3%</i>	<i>9.4%</i>

$H = 24$ ft, $\alpha = 270^\circ$	Mean	RMS	Min	Max	Skewness	Kurtosis
Target	-0.294	0.092	-0.759	-0.107	-0.800	4.044
Simulated from Experimental Data	-0.294	0.092	-0.745	-0.070	-0.621	3.760
<i>Error</i>	<i>0.0%</i>	<i>0.6%</i>	<i>1.8%</i>	<i>34.2%</i>	<i>22.4%</i>	<i>7.0%</i>
Simulated from $H = 16$ ft and $H = 32$ ft	-0.299	0.096	-0.725	-0.063	-0.549	3.402
<i>Error</i>	<i>1.8%</i>	<i>3.8%</i>	<i>4.4%</i>	<i>41.3%</i>	<i>31.4%</i>	<i>15.9%</i>
Simulated from $H = 16$ ft and $H = 40$ ft	-0.350	0.131	-0.912	-0.070	-0.600	3.665
<i>Error</i>	<i>19.2%</i>	<i>41.6%</i>	<i>20.2%</i>	<i>34.7%</i>	<i>25.0%</i>	<i>9.4%</i>

$H = 32$ ft, $\alpha = 180^\circ$	Mean	RMS	Min	Max	Skewness	Kurtosis
Target	-0.242	0.064	-0.708	-0.058	-0.784	3.946
Simulated from Experimental Data	-0.242	0.064	-0.709	-0.010	-0.626	3.691
<i>Error</i>	<i>0.0%</i>	<i>0.1%</i>	<i>0.2%</i>	<i>82.7%</i>	<i>20.2%</i>	<i>6.5%</i>
Simulated from $H = 24$ ft and $H = 40$ ft	-0.256	0.072	-0.745	-0.029	-0.712	3.982
<i>Error</i>	<i>6.1%</i>	<i>12.7%</i>	<i>5.2%</i>	<i>50.4%</i>	<i>9.2%</i>	<i>0.9%</i>
Simulated from $H = 16$ ft and $H = 40$ ft	-0.257	0.072	-0.715	-0.033	-0.577	3.656
<i>Error</i>	<i>6.5%</i>	<i>12.5%</i>	<i>1.1%</i>	<i>43.1%</i>	<i>26.3%</i>	<i>7.4%</i>

$H = 32$ ft, $\alpha = 225^\circ$	Mean	RMS	Min	Max	Skewness	Kurtosis
Target	-0.343	0.125	-0.803	-0.105	-0.596	3.658
Simulated from Experimental Data	-0.343	0.125	-0.809	-0.071	-0.590	3.726
<i>Error</i>	<i>0.0%</i>	<i>0.2%</i>	<i>0.8%</i>	<i>32.3%</i>	<i>1.0%</i>	<i>1.9%</i>
Simulated from $H = 24$ ft and $H = 40$ ft	-0.336	0.120	-0.818	-0.036	-0.473	3.568
<i>Error</i>	<i>2.1%</i>	<i>4.0%</i>	<i>2.0%</i>	<i>66.0%</i>	<i>20.5%</i>	<i>2.5%</i>
Simulated from $H = 16$ ft and $H = 40$ ft	-0.337	0.120	-0.844	-0.077	-0.532	3.609
<i>Error</i>	<i>1.9%</i>	<i>3.3%</i>	<i>5.1%</i>	<i>27.2%</i>	<i>10.7%</i>	<i>1.3%</i>

$H = 32$ ft, $\alpha = 270^\circ$	Mean	RMS	Min	Max	Skewness	Kurtosis
Target	-0.369	0.147	-0.972	-0.116	-0.650	3.608
Simulated from Experimental Data	-0.369	0.146	-0.830	-0.088	-0.498	3.282
<i>Error</i>	<i>0.0%</i>	<i>0.6%</i>	<i>14.6%</i>	<i>24.4%</i>	<i>23.4%</i>	<i>9.0%</i>
Simulated from $H = 24$ ft and $H = 40$ ft	-0.350	0.131	-0.912	-0.070	-0.600	3.665
<i>Error</i>	<i>5.2%</i>	<i>11.0%</i>	<i>6.1%</i>	<i>39.9%</i>	<i>7.6%</i>	<i>1.6%</i>
Simulated from $H = 16$ ft and $H = 40$ ft	-0.347	0.129	-0.851	-0.059	-0.550	3.589
<i>Error</i>	<i>6.0%</i>	<i>12.3%</i>	<i>12.4%</i>	<i>48.6%</i>	<i>15.3%</i>	<i>0.5%</i>

boundaries of what constitutes acceptably similar building shapes to justify use of this procedure. Until such time, this procedure is cautiously recommended for application, constrained to buildings with only a single varying geometric descriptor.

Summary

A multivariate non-Gaussian simulation algorithm developed by Grigoriu (1998) and modified by Deodatis and Micaletti (2001) was employed to generate realizations of multiple correlated non-Gaussian pressure coefficient time histories given probabilistic and spectral target information. An interpolation scheme was developed to generate spectral and probabilistic models of pressure loading on a subject building using data sets from buildings with similar geometries to the subject. Pressure loading was then simulated and aggregated for building shapes with 24 and 32 ft eave heights based on data collected from building shapes with eave heights that bound the subject eave height. The resulting models compared well with the models developed directly from data sets of the subject building.

In this application, the simulation method is capable of simulating 9-11 correlated time histories before numerical instabilities in the cholesky decomposition prevent its use. If peak pressure coefficient magnitudes for a given duration are of the greatest interest in application, weighted linear interpolation between the bounding peak values will provide nearly the same uplift pressure as the simulation method with considerably less computational expense.

CHAPTER 7 CONCLUSIONS AND RECOMMENDATIONS FOR FUTURE RESEARCH

This dissertation documents contributions to wind damage mitigation efforts, specifically the characterization of surface-level tropical cyclone winds, and the simulation of wind loading for simple building shapes untested in the wind tunnel.

The following sections summarize contributions to and conclusions about the research found in this document and present recommendations for future research (many of which are underway by the FCMP). These sections are ordered according to research topic to preserve continuity.

Contributions to Full-Scale Measurement Research

During the 1999-2003 Atlantic Hurricane Seasons, instrumented towers collected surface-level wind speed data from 29 instrumented towers in ten different named storms in Florida, North Carolina and Louisiana. Hundreds of hours of data were collected, and 19 storm data sets were used in this study. A data reduction algorithm was developed to build the FCMP storm database from 10-minute segments in the records. Segments with immediate upwind obstacles, 1st and 2nd order non-stationary behavior in the wind speed, extreme shifts in wind direction, and low mean wind speeds were eliminated. From the remaining segments, turbulence intensities, gust factors, integral length scales and power spectra were analyzed over a variety of roughness lengths and mean wind speeds.

Turbulence intensity ratios were studied to characterize the contribution of the longitudinal, lateral and vertical components to the total kinetic energy budget. The lateral to longitudinal ratio measured between 0.71-0.77 over all roughness ranges, which

is consistent with the literature. Analysis of vertical to longitudinal and lateral turbulence intensities indicated a dependency on surface roughness—only the ratio calculated over all roughness regimes (0.67) agreed from previous full-scale and wind tunnel studies (0.68).

Three gust factor relationships—based on segmental averages, moving averages and the method proposed by Durst (1960)—were developed for a 10-minute mean wind speed and compared to the models used by design standards. The moving average produced the highest gust factor curve and is recommended for use—values of 2- and 3-second gust factors are 1.52 and 1.55, respectively.

Following the methodologies of Durst (1960) and Krayner and Marshall (1993), a gust factor relationship was developed for 1-hour mean wind speed based on a Gaussian translation of variance. The analysis of the FCMP database indicates that tropical cyclones produce “gustier” winds than extratropical (e.g., winter storm) data, which was the basis of Durst (1960), but does not support the upwind adjustment of gust factors for hurricane winds proposed by Krayner and Marshall (1993).

Next, linear regression was performed on gust factor vs. longitudinal turbulence intensities for multiple gust durations ranging from 1 second to 10 minutes. Rational polynomials were fit to the intercepts and slopes, and this information was used to develop a formula relating gust factors to gust duration and roughness length based on a 10-minute mean wind speed.

Finally, power spectra were analyzed to determine the effect of surface roughness on the distribution of energy with respect to frequency. Analysis of open exposure data indicates higher energy in the lower frequency range, which is in agreement with analysis

of hurricane winds performed by Powell et al. (1993) and Schroeder and Smith (2003). Increased roughness indicates a shift in energy to higher frequencies.

Additional contributions include the development of a satellite tower system to measure gust widths and a real-time data acquisition system capable of transferring summary information to the internet over a cellular modem. One such system—employed by the instrumented tower (Tower T3) at Frisco, NC—collected the highest ground level wind speeds of record during Hurricane Isabel, and those measurements are also the highest wind speeds for which continuous, high frequency, digital observations have been recorded in a U. S. landfalling hurricane.

Recommendations for Future Full-Scale Measurement Research

The existing experimental framework has surpassed the proof-of-concept stage, and the FCMP is now in a position to improve its abilities to collect, analyze and disseminate data. Suggestions for future research activities are provided for three areas: wireless data acquisition, surface roughness estimation and the dissemination of real-time data.

Wireless Data Acquisition

Beginning in 2003, FCMP research has evolved into correlation studies of multi-tower systems. Deploying more instrumentation, however, increases setup time and reduces the time of safe retreat from the storm. By the 2004 season, the FCMP research infrastructure will have grown to five 10-m towers, four pairs of 5-m lightweight towers, two 10-m lightweight towers, and 12 sets of house instrumentation.

To expedite deployment, the same technologies that drive high-performance, scalable, wireless "broadband" to residences and public spaces should be harnessed to collect data at multiple locations, providing greater wind field resolution without

involving additional resources (such as personnel and wiring). The savings in cost and time will be tremendous if that research finds its way into application.

Additionally, wireless data acquisition will allow for the development of a new multi-tower system to study surface level winds in the transitional boundary layer that develops as hurricane winds move from ocean to land. Six to eight lightweight 10-meter aluminum towers spaced evenly between the shoreline and one of the existing FCMP steel towers located 2 km inland can collect data throughout landfall. Laptops or PDA devices in each tower can coordinate execute data collection and wireless transmission to the most inland tower, which will upload reports to the web every 15 minutes through its PCMCIA cellular modem. Equipped with RM Young gill anemometry (which is unpowered) and computers with intelligent power distribution processors (e.g., Intel Centrino), the data acquisition system will consume considerably less power than the system in the steel towers. An industrial generator/UPS system will not be required because several parallel backup batteries can power the computer for the duration of the storm.

Roughness Estimation

Every 15 minutes, the Tower XP data acquisition system estimates the roughness length from the longitudinal turbulence intensity and uploads that value to the internet for ingestion into surface wind field analyses. Post-analysis from Isabel indicates that these values may not be representative of the upwind fetch, particularly due to the heterogeneous nature of the terrain and the presence of either convective activity or wave action at the shoreline. The latter is discussed here.

During Isabel, Tower T3 recorded anomalously high turbulence intensity values between 1200 – 1400 UTC on September 18th in Frisco, NC. Aerial imagery illustrates

that the upwind exposure (shaded in yellow in Figure 7-1) shifted from an inland exposure to a marine exposure during those two hours, but anemometry at a 10-m observational height measured peak turbulence intensities representative of boundary layer flow over a sparsely built-up suburb (shaded in yellow in Figure 7-2).

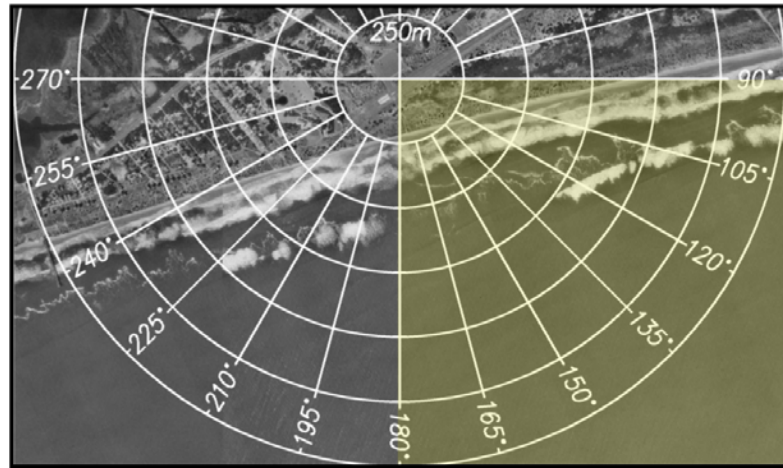


Figure 7-1. Aerial imagery of the Tower T3 deployment site in Isabel

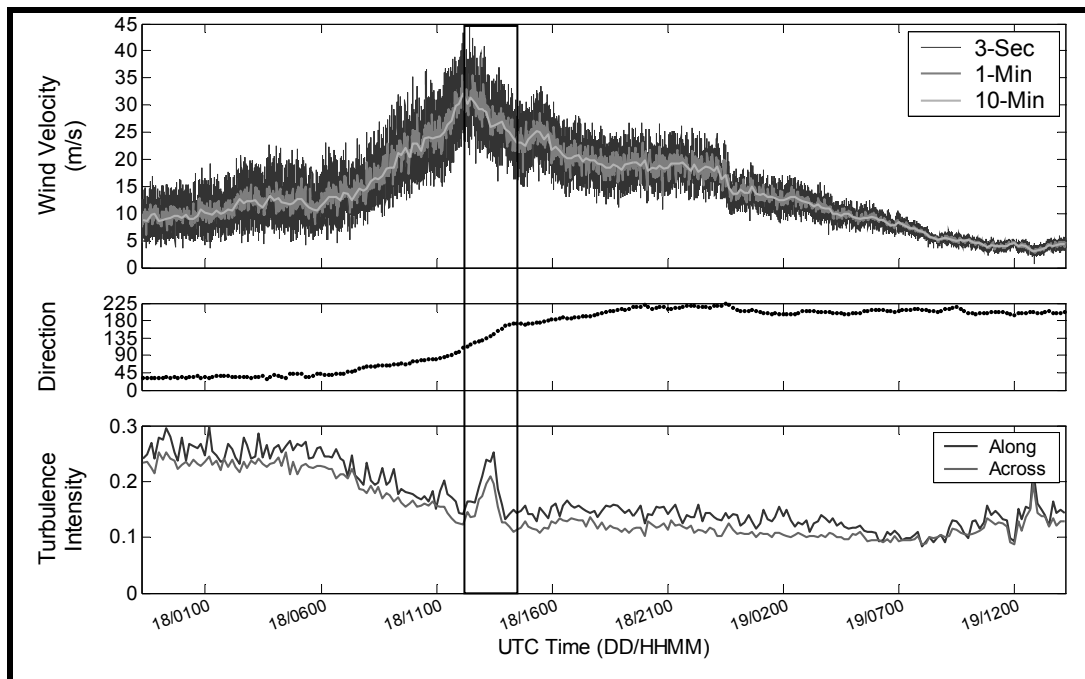


Figure 7-2. Wind speed, wind direction and turbulence intensity measured by Tower T3 in Hurricane Isabel

Since these inflated roughness lengths affect the standardization of the observed velocity to an open exposure wind speed, the FCMP should investigate other methods to estimate roughness length. Options include:

- The use of taller towers equipped with sensors at multiple levels to estimate roughness lengths directly from the observed mean velocity profile
- Estimation from gust factors (Weiringa 1993)
- Comparison to the National Land Cover Database
- Use of LIDAR data for surface roughness estimation

The last item, in particular, has a larger outcome: the development of high-resolution directional roughness maps will improve the ability of researchers to study evolutionary wind fields and allow FCMP research personnel to estimate surface roughness of prospective deployment sites before towers are dispatched to those regions. Recently, researchers at UF have begun development of strategies to use LIDAR elevation data from NOAA's Topographic Change Mapping Project (TCMP) online database to characterize surface roughness from spectral and probabilistic analysis of that data.

Dissemination of Real-Time Data

Development of robust solutions to transfer data remotely to researchers represents the state-of-the-art in full-scale measurement research. The real-time transmission capabilities of the tower can benefit from:

Greater transmission range. Presently, the practical range that the system can transmit data to a cell tower is approximately 15 km, which greatly restricts deployments in regions with poor cellular service. Areas such as the Louisiana coast and the Florida panhandle, which lack the dense array of cell towers found in other areas, will present a

challenge should a hurricane threaten. The use of signal boosters and better antenna configurations, however, could increase that range to nearly 50 km.

Mirrored upload sites. As configured, the system transmits data to two web servers at the University of Florida. If the network inside the university should fail, the data will become inaccessible. The software should receive an upgrade to transmit data to servers at multiple universities and a NOAA designated FTP site

Improved monitoring. For safety reasons, research personnel cannot remain with the portable towers during the hurricane landfall to monitor the performance of the data acquisition system, instrumentation and the power supplies. Diagnostic data, however, can be uploaded to the web server in the 15-minute summary files. Should the system detect erratic behavior from the instrumentation or low power from the uninterruptible power supply (UPS), research personnel will be alerted in the 15-minute summary file. Premature power failures and malfunctioning sensors that have occasionally hindered the project can be identified rapidly and corrected before cyclone landfall.

Geographic Information System (GIS) Online Repository. An online repository built from the ArcGIS/IMS environment to display incoming real-time weather observations—such as meteorological data from ASOS, CMAN, METAR, NDBC Buoys and the FCMP weather stations—in an interactive map of the impacted region would

- Serve as a tool to coordinate hurricane research activities across universities and government agencies
- Improve deployment strategies by aiding in the location of potential sites to erect portable instrumented towers
- Provide meteorologists and emergency managers with a centralized monitoring system to view a significant amount of data in an easy-to-use and customizable graphical framework, which will eliminate the need to parse through hundreds of uploaded summary files. This concept is unique in that it will provide incoming operational and full-scale measurement research data on one site

The site should be responsive to the needs of both the general public seeking simple levels of information and researchers that require more in-depth analysis of the real-time data. Once the site is operational, additional sources of data can be added, including historical tropical cyclone tracks (HURDAT), aircraft reconnaissance, surface wind field analyses (HURSIM, H*Wind), and hazard loss estimation maps (HAZUS, FPHLPM). Additionally, the feasibility of including radar (WSR-88D, SMART-DOW), satellite/aerial imagery, surge models (SLOSH, FIRM, ARA, WES) and roughness maps (NLCD) should be explored and implemented if logistics and operational expenses allow.

Contributions to Stochastic Simulation Research

The numerical instability associated with the cholesky decomposition of the target spectral matrix was found to be the limiting factor in the stochastic simulation algorithm used in this study.

Peaks from simulated records compare well with peaks measured directly from the data. The simulations from interpolated CDFs are as accurate in most cases as the simulations based on models calculated directly from the experimental data at the test height. This shows the potential for CDF interpolation to provide models for roof uplift simulation. In the cases where the interpolation scheme did not work well, the directly averaged peaks deviated significantly from the “true” measured peaks. In these cases (see Figures C-9 and C-12), the aggregate uplift (measured over a range of durations) did not remain within the bounding cases. In other words, the spectral and probabilistic targets of the middle (interpolated) eave height were not bounded by the lower and upper eave height cases.

When average peak values are the quantity of interest, direct interpolation of experimental data from the higher and lower height building geometries provides acceptable results, and simulations do not appear to provide added accuracy.

Recommendations for Future Stochastic Simulation Research

Once a methodology is in place to simulate large numbers of correlated random variables (> 128), memory allocation will limit the practical application of stochastic simulation programs.

During program execution, the software avails itself of the system's physical memory (RAM) before it accesses the system's virtual memory, which is a portion of the hard disk (called the swap file). Since today's 32-bit architectures are limited by the length of an instruction (or number) that can be sent to the processor, virtual memory addresses can be a maximum of 32 bits long. This results in a maximum of 2^{32} possible memory addresses, or equivalently 4 gigabytes (GB) of virtual address space. The Microsoft Windows operating system further reduces that limit down to 2 GB because of a design decision to reserve the upper 2 GB for system use.

With that consideration in mind, studies were performed with relaxed correlation targets to determine the limits of the algorithm in the early phases of development. On a workstation equipped with a 2.5 GHz Intel Pentium IV processor with 512 MB of RAM, approximately 90 pressure taps could be simulated before the available memory was depleted. Modifications were made to the program to store intermediate calculations (such as underlying PSDs) to the hard drive in binary files, but the computational expense of the input/output procedures far outweighed the benefits afforded by reduced virtual memory requirements.

The 64-bit microprocessor will make this issue obsolete and is recommended for use in future studies. Both Intel and AMD, the largest microprocessor companies in the world have released 64-bit architectures (Itanium and Opteron, respectively). Windows has begun to distribute its 64-bit operating system based on the XP platform.

APPENDIX A FCMP DATABASE

This appendix contains time histories of 10-minute, 1-minute and 3-second time histories of velocity data, 10-minute mean directions, and three-dimensional turbulence intensities from the selected storms in the FCMP database. Time histories of all storms may be found at the project website: <http://www.ce.ufl.edu/~fcmp>.

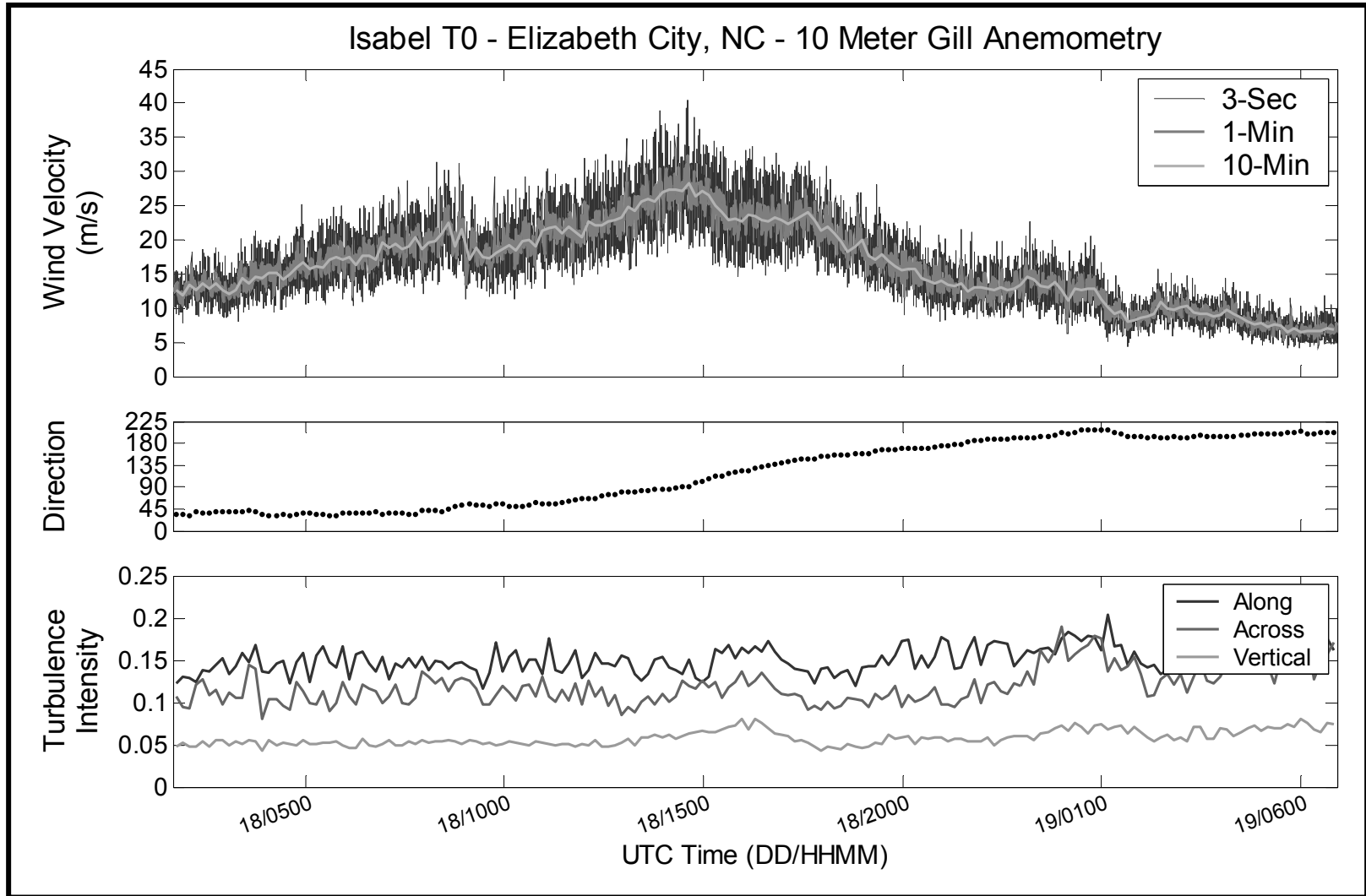


Figure A-1. Velocity and turbulence intensity records from Tower T0 in Hurricane Isabel at Elizabeth City, North Carolina

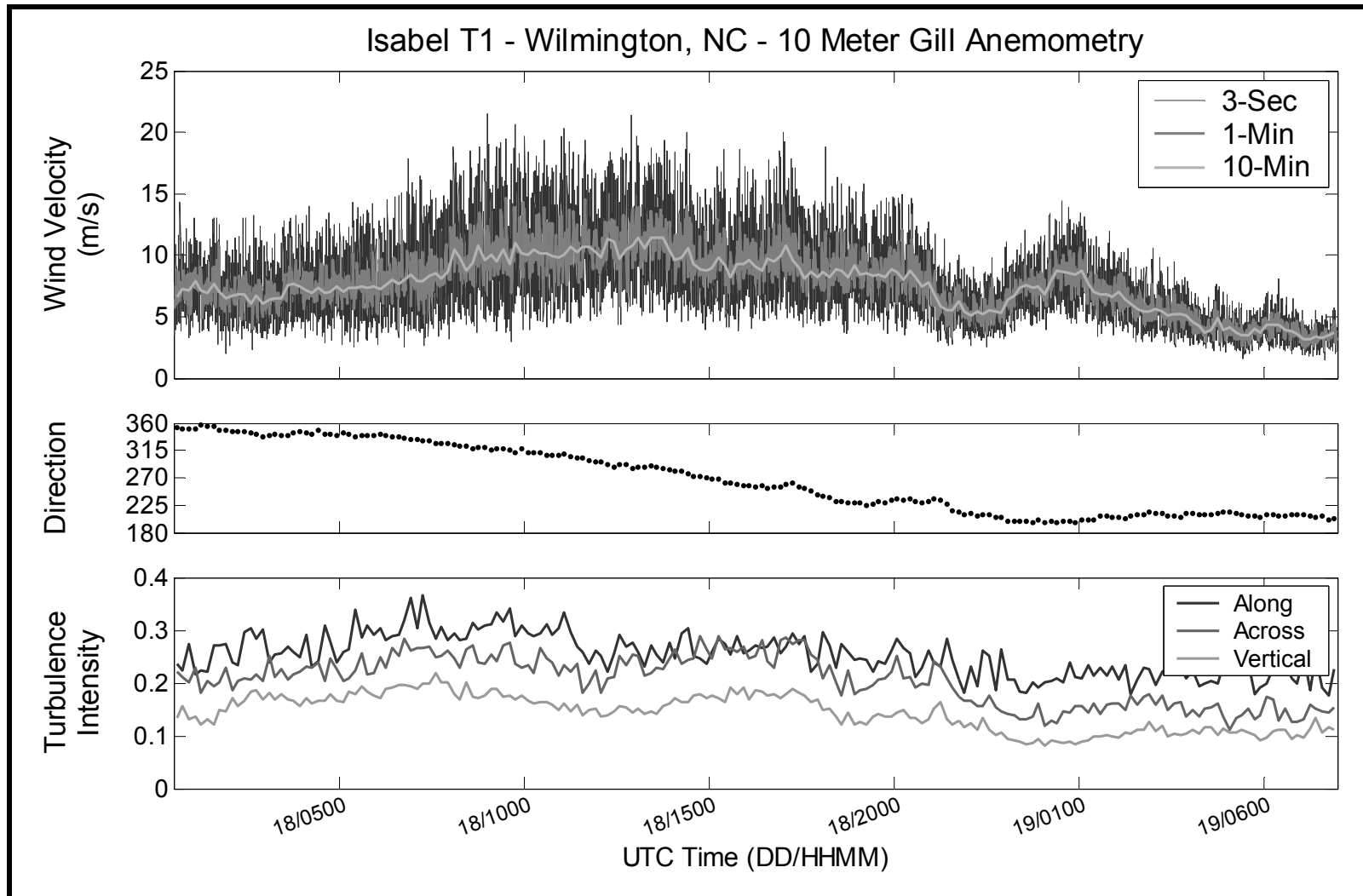


Figure A-2. Velocity and turbulence intensity records from Tower T1 in Hurricane Isabel at Wilmington, North Carolina

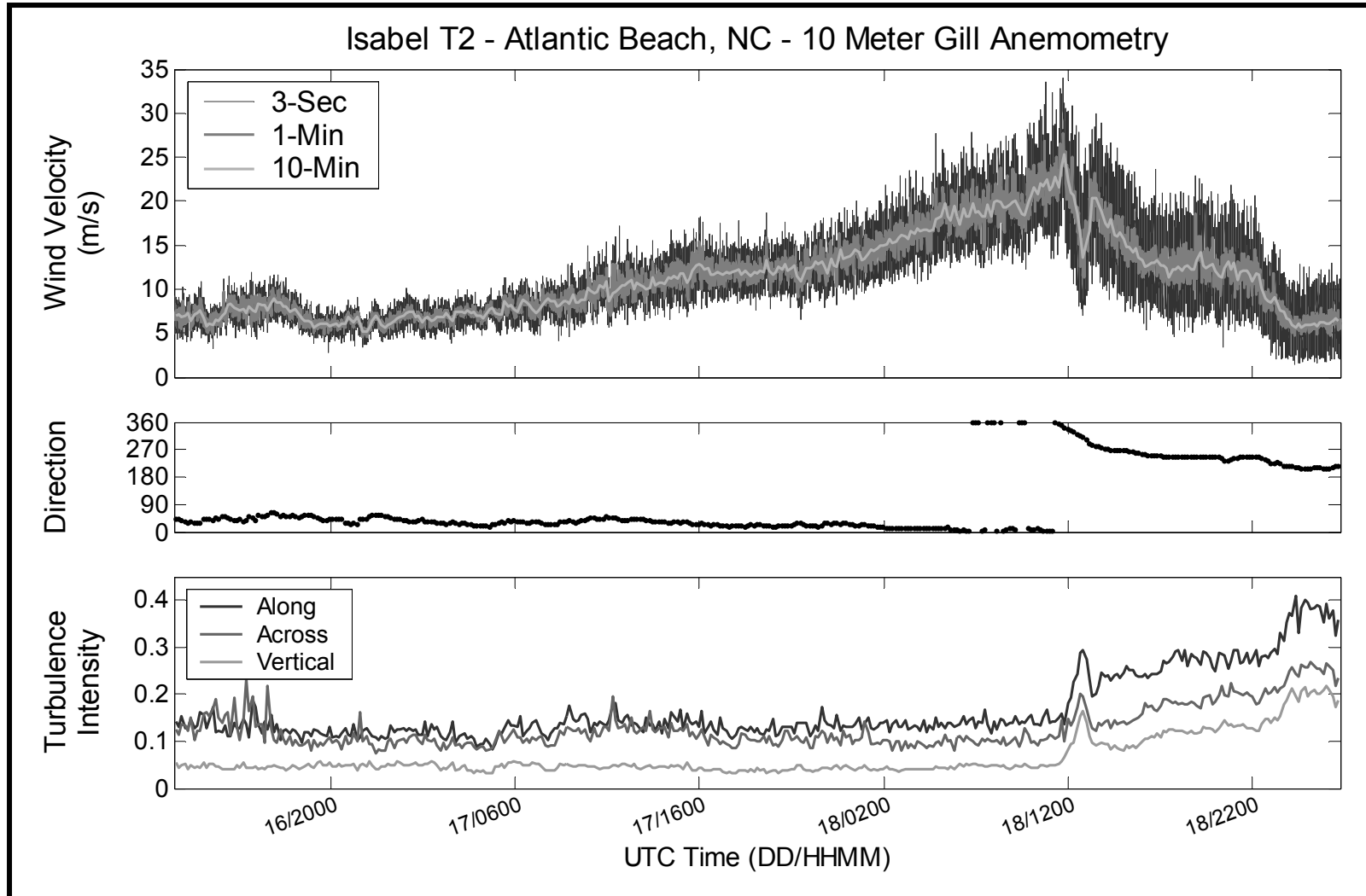


Figure A-3. Velocity and turbulence intensity records from Tower T2 in Hurricane Isabel at Atlantic Beach, North Carolina

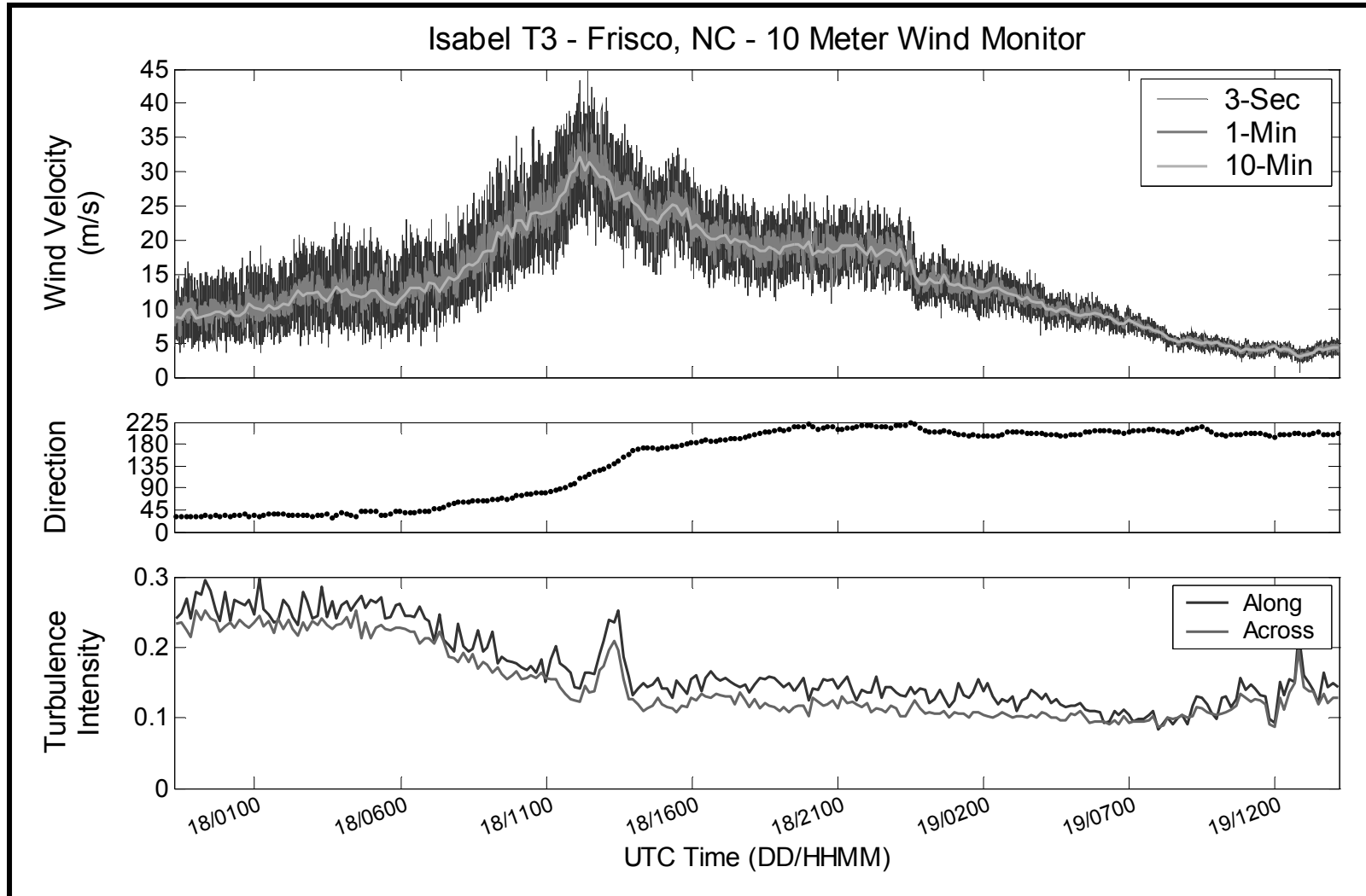


Figure A-4. Velocity and turbulence intensity records from Tower T3 in Hurricane Isabel at Frisco, North Carolina

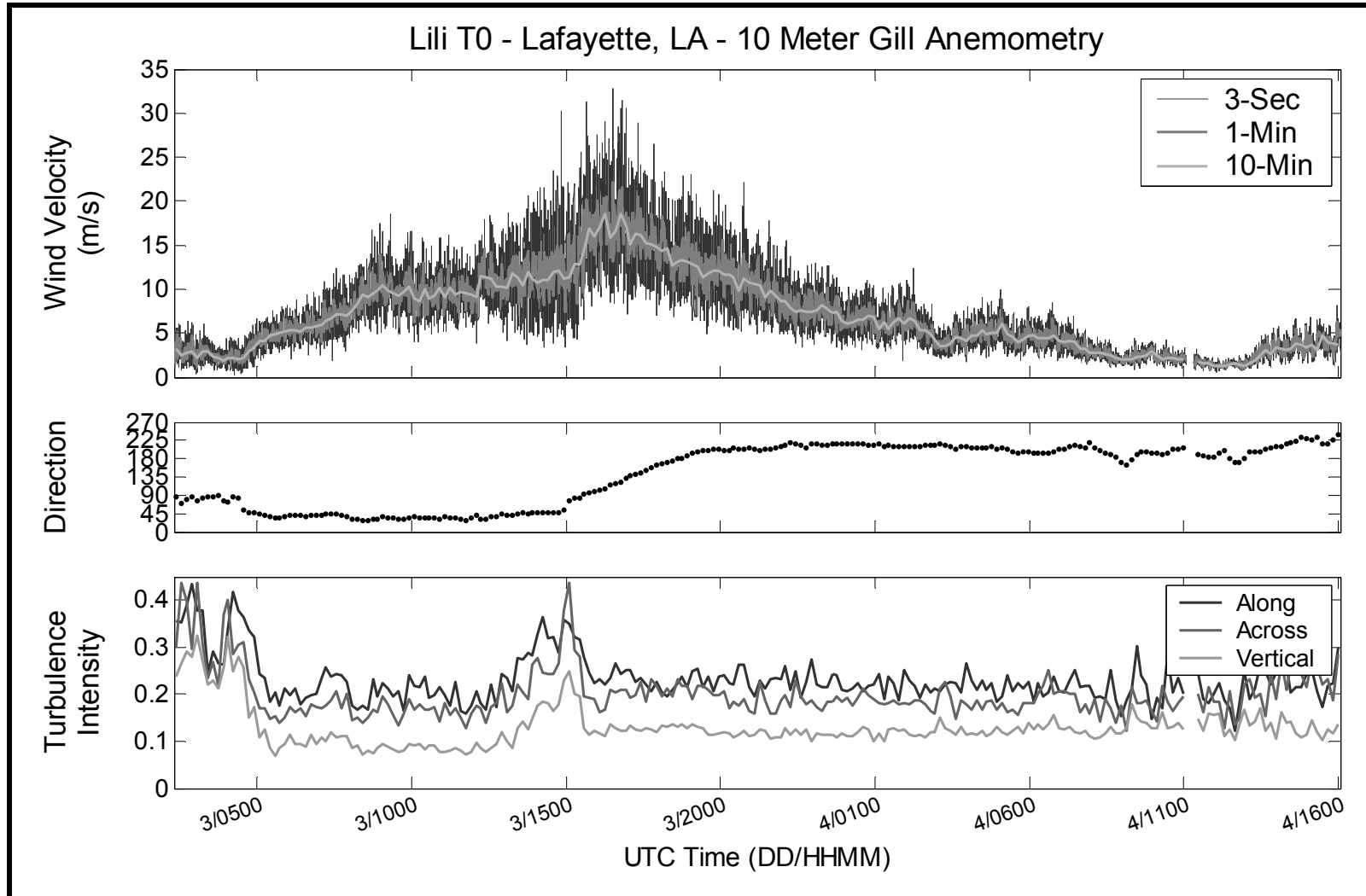


Figure A-5. Velocity and turbulence intensity records from Tower T0 in Hurricane Lili at Lafayette, Louisiana

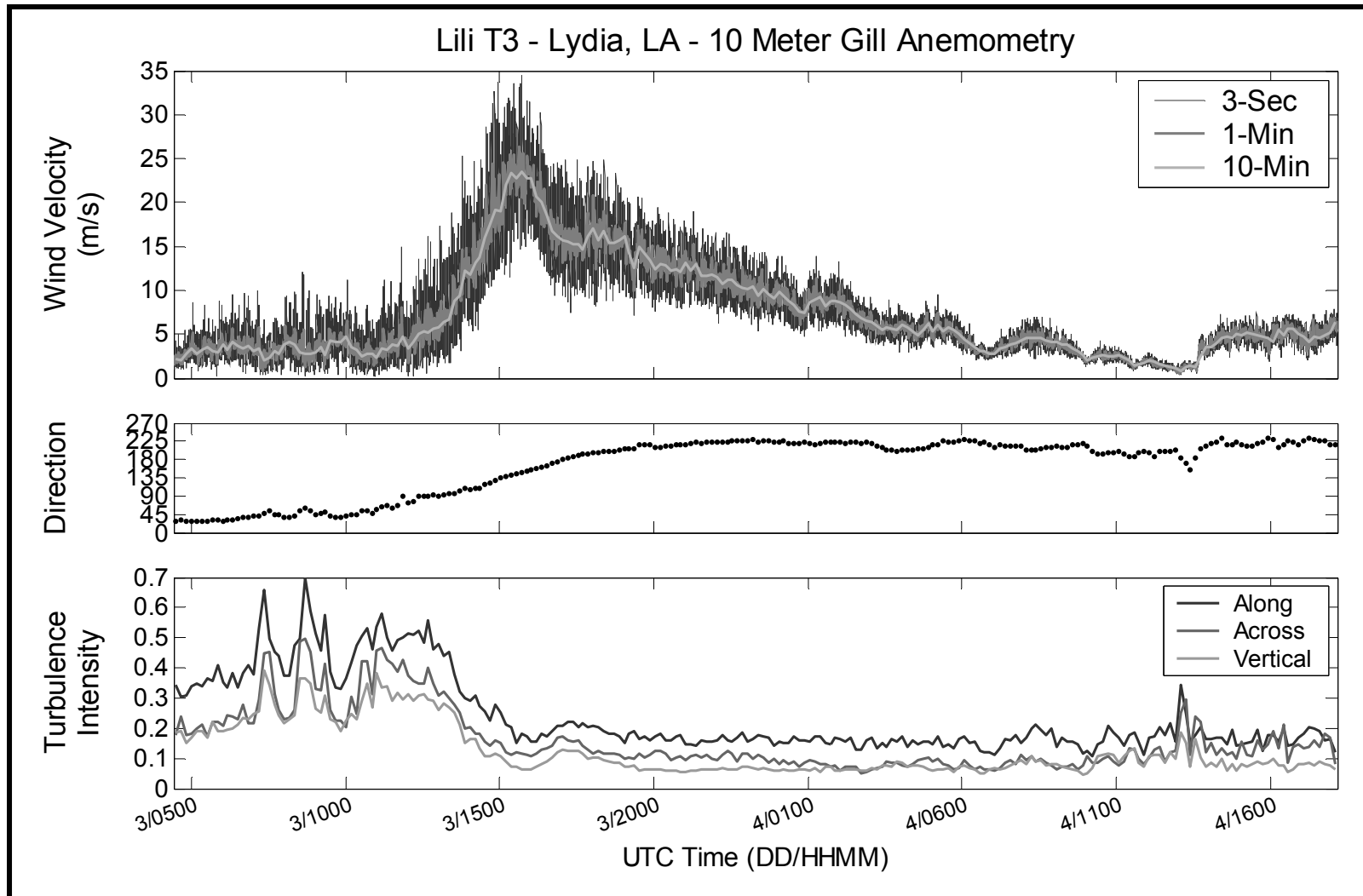


Figure A-6. Velocity and turbulence intensity records from Tower T3 in Hurricane Lili at Lydia, Louisiana

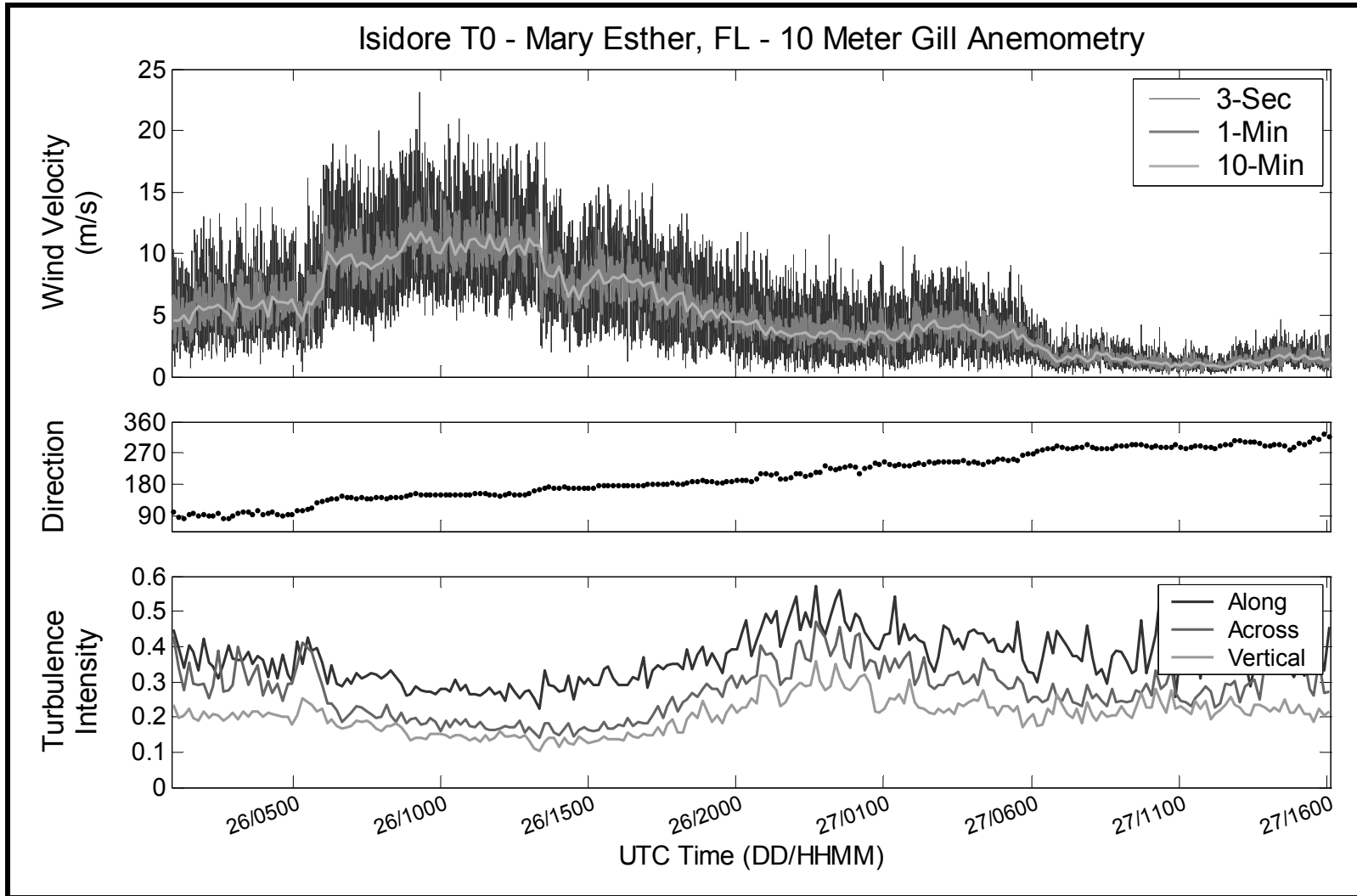


Figure A-7. Velocity and turbulence intensity records from Tower T0 in Tropical Storm Isidore at Mary Esther, Florida

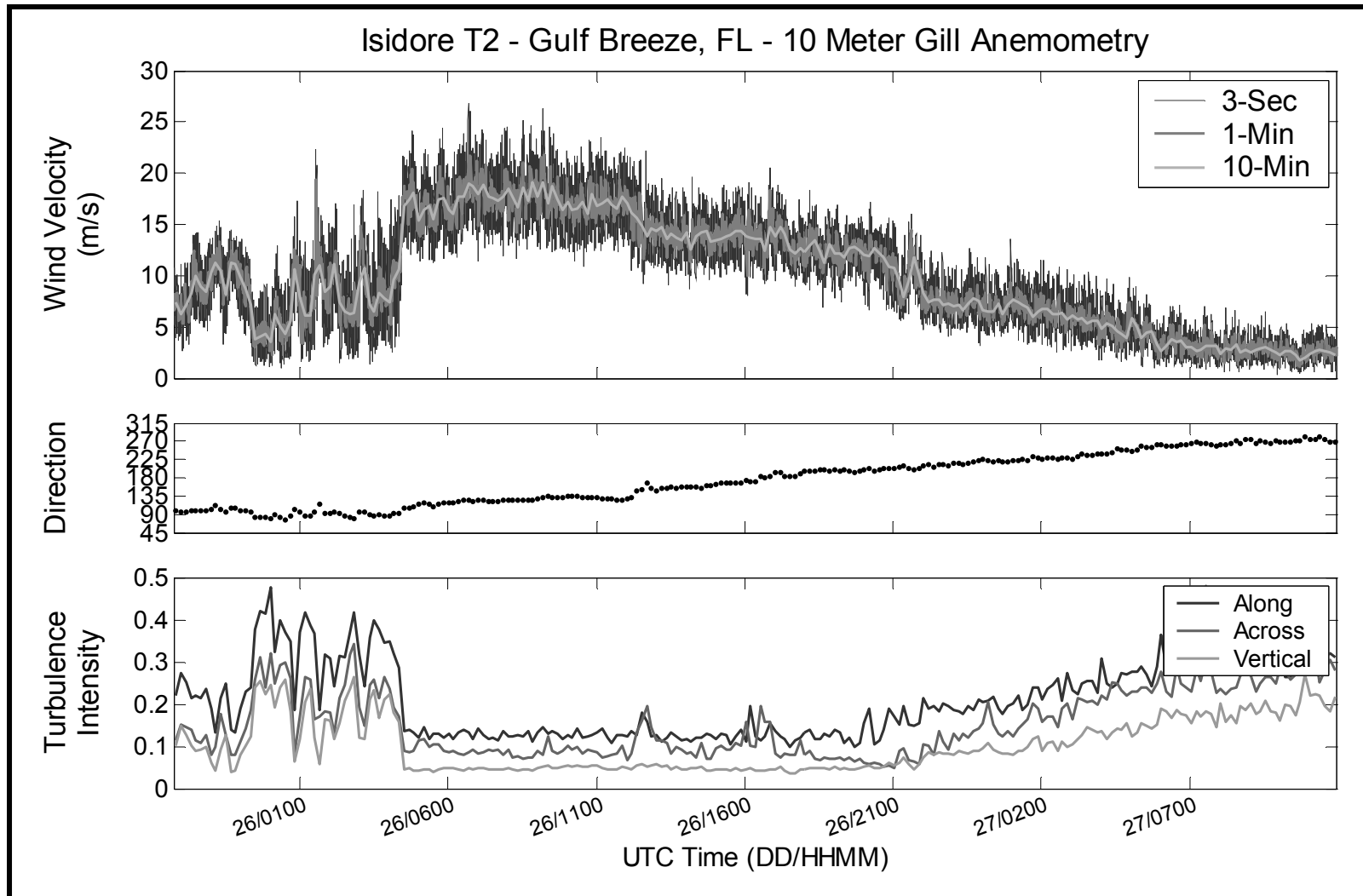


Figure A-8. Velocity and turbulence intensity records from Tower T2 in Tropical Storm Isidore at Gulf Breeze, Florida

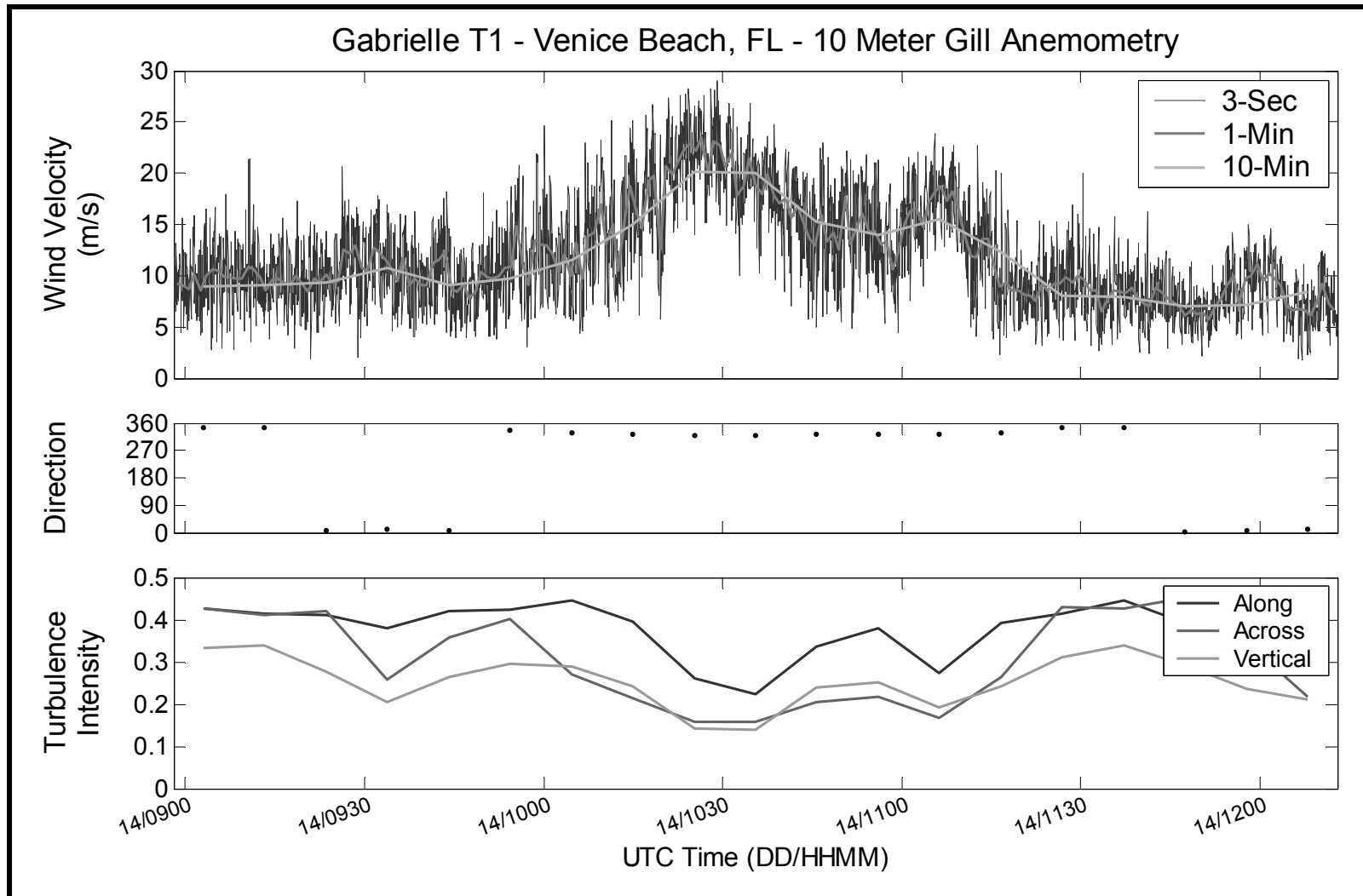


Figure A-9. Velocity and turbulence intensity records from Tower T1 in Tropical Storm Gabrielle at Venice Beach, Florida

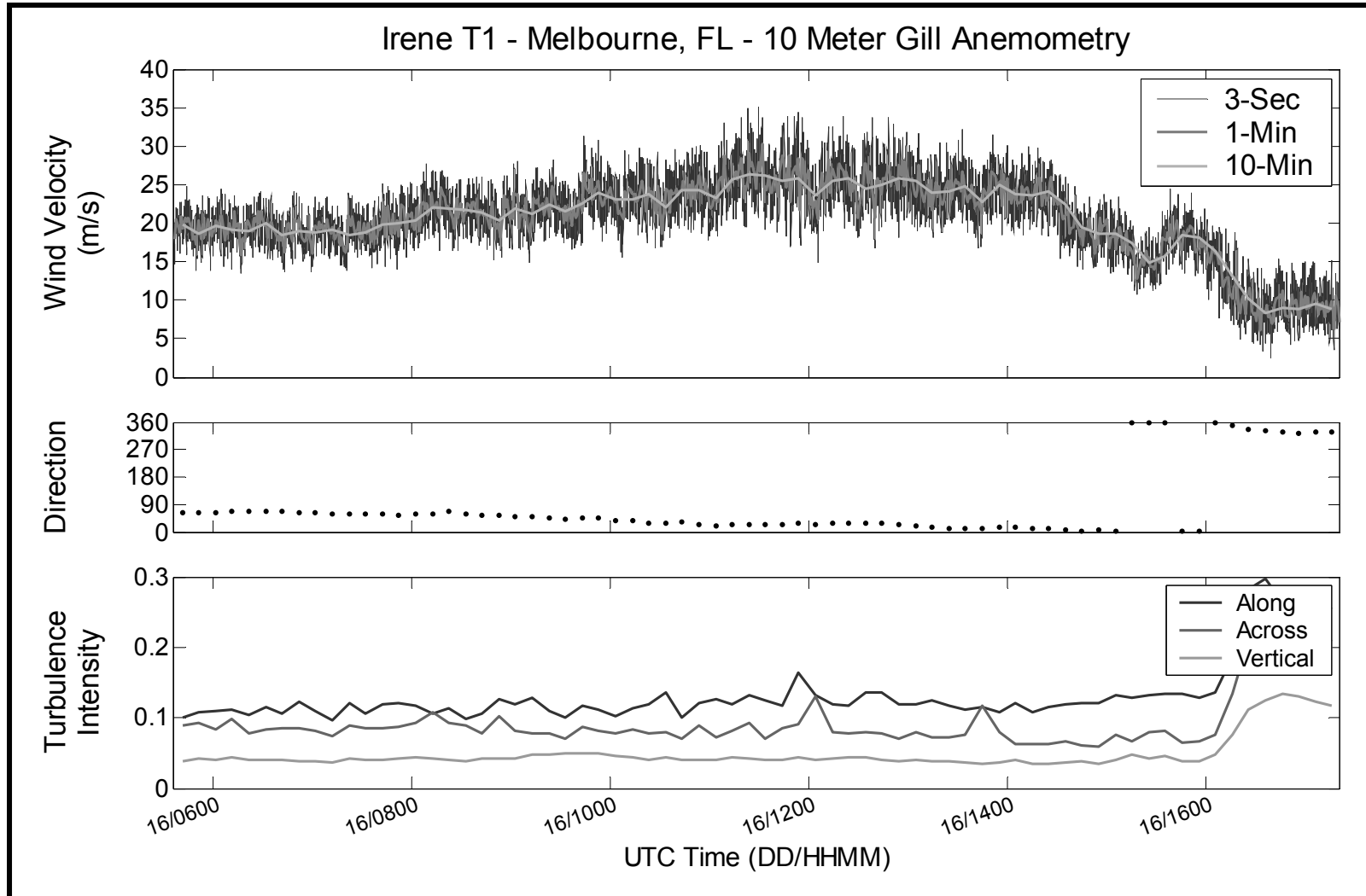


Figure A-10. Velocity and turbulence intensity records from Tower T1 in Tropical Storm Irene at Melbourne Beach, Florida

APPENDIX B AERIAL IMAGERY OF TOWER SITES

This appendix contains selected composite aerial imagery of the terrain surrounding the deployment sites built from digital orthophoto quadrangles (DOQ). These photos are the property of the United States Geological Survey (USGS) and are freely available at Microsoft's Terraserver website: terraserver.microsoft.com.

Lines and rings were added to aerial imagery in AutoCAD to demarcate the upwind fetch. Lines extend radially from the instrumented tower, and the rings are spaced at 250 m intervals. Note that the dates of these photos are included in the right margin of each picture. High resolution (1 m = 1 pixel) versions of these figures (for all deployment sites) are available at the project website: www.ce.ufl.edu/~fcmp.

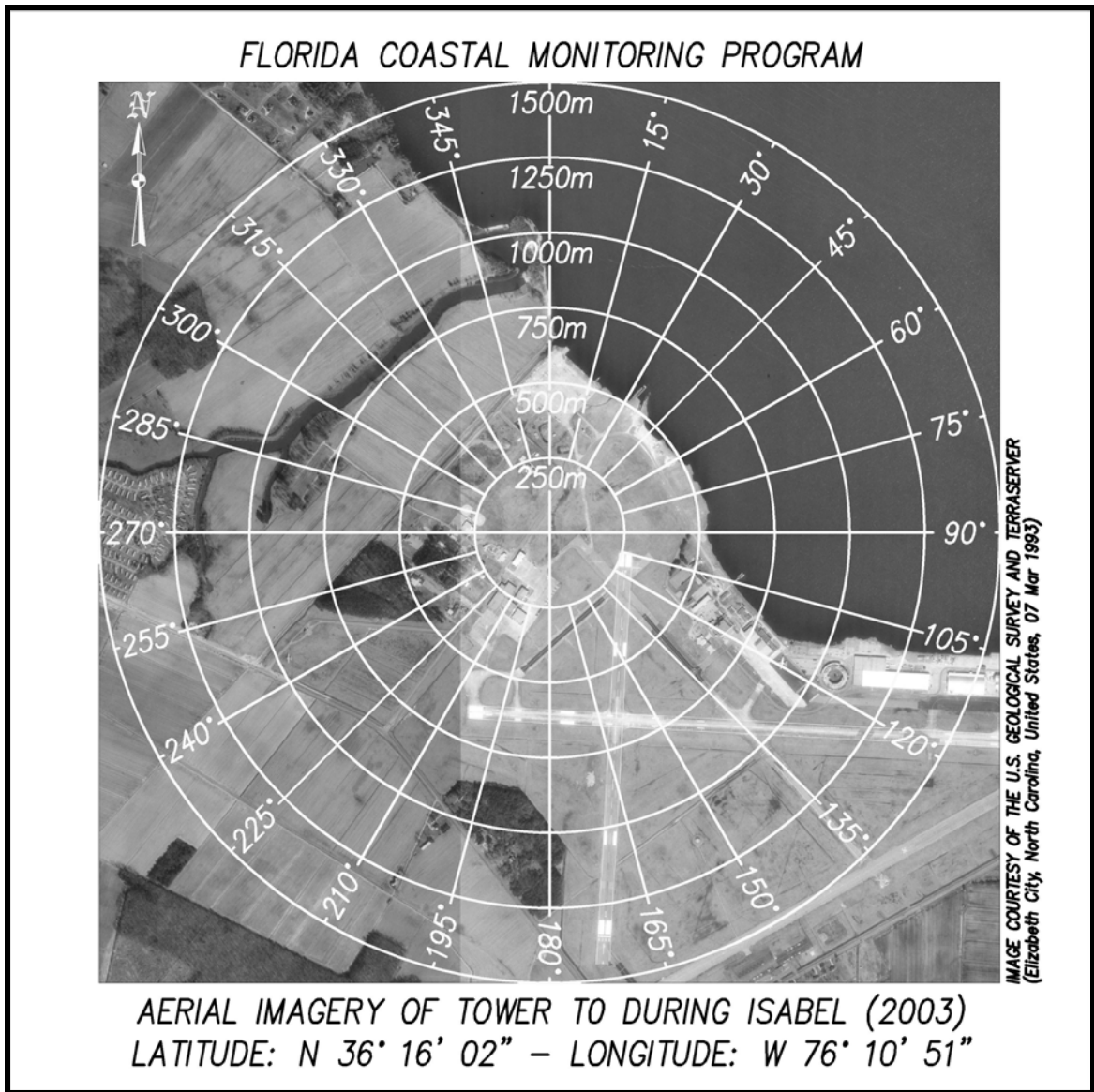


Figure B-1. Aerial Imagery of the terrain surrounding Tower T0 in Hurricane Isabel at Elizabeth City, North Carolina

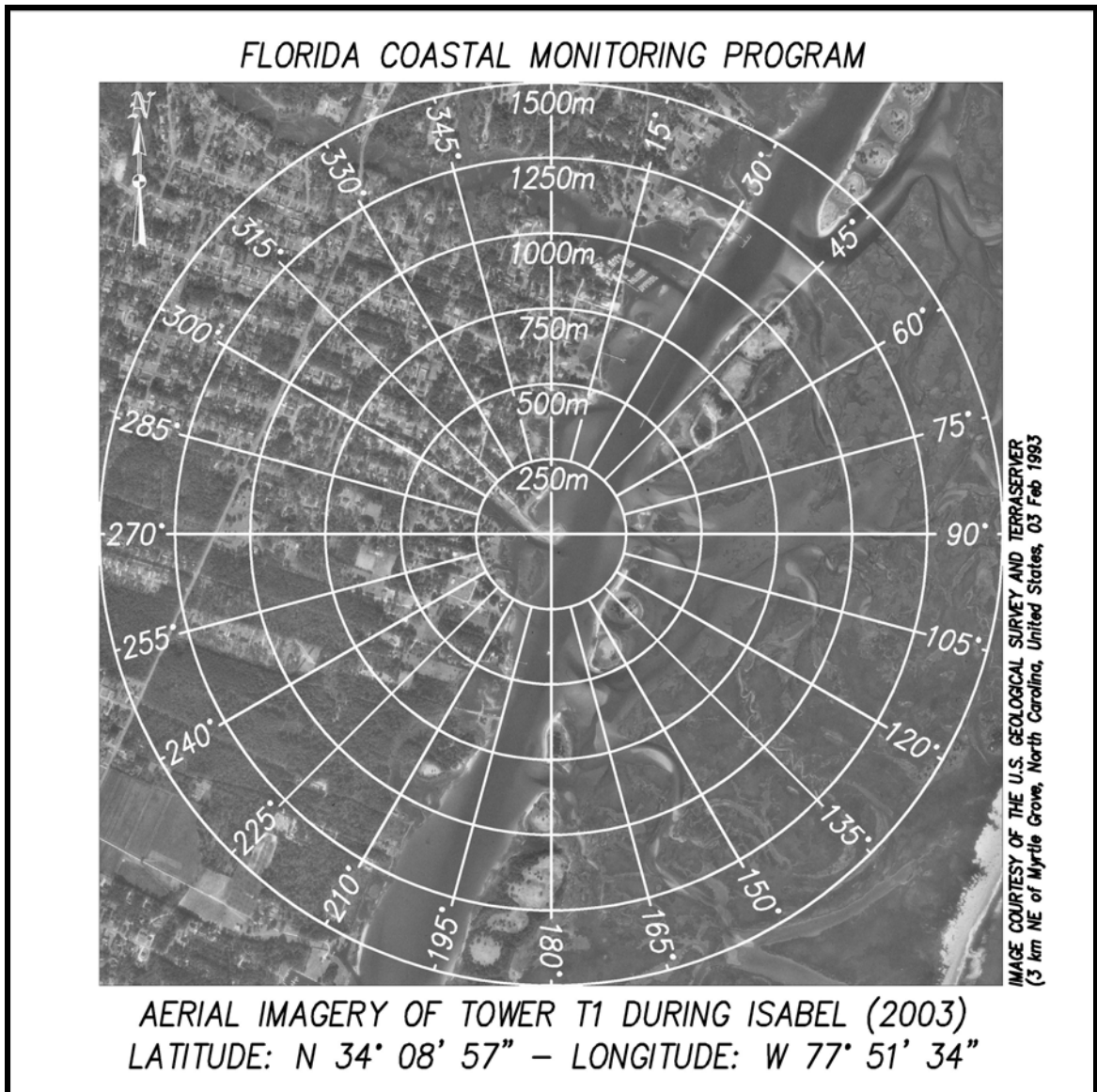


Figure B-2. Aerial Imagery of the terrain surrounding Tower T1 in Hurricane Isabel at Wilmington, North Carolina

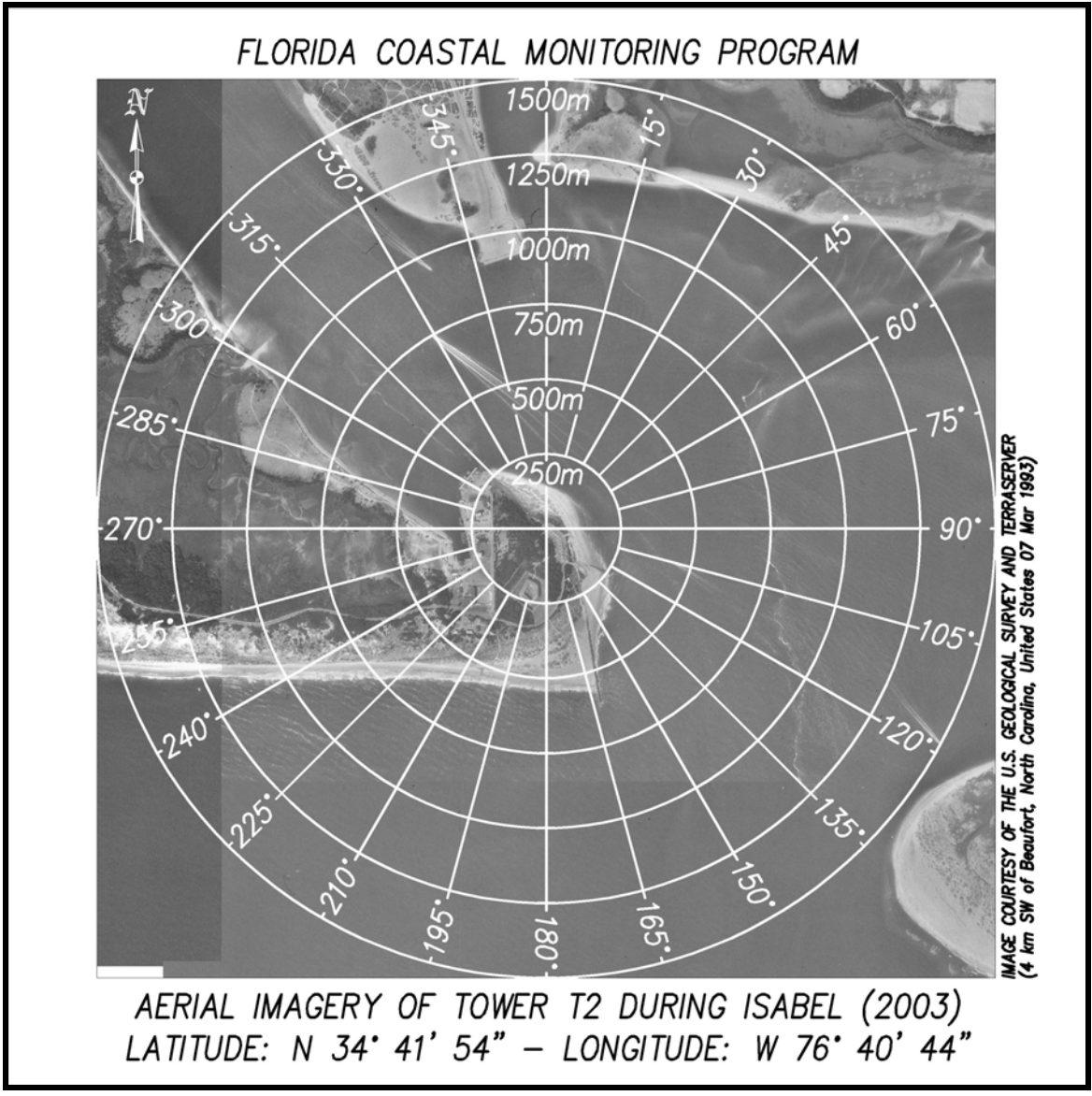


Figure B-3. Aerial Imagery of the terrain surrounding Tower T2 in Hurricane Isabel at Atlantic Beach, North Carolina

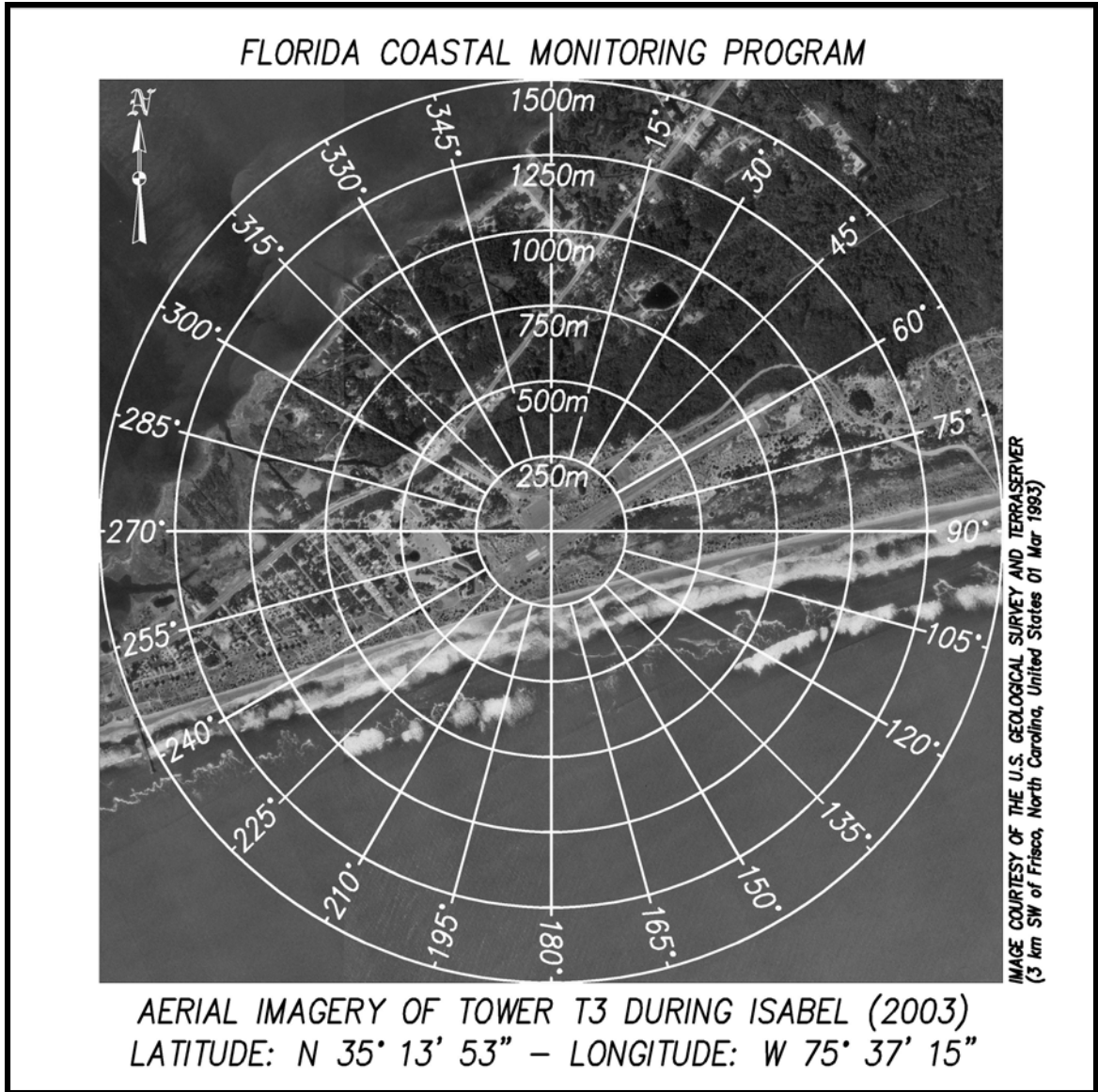


Figure B-4. Aerial Imagery of the terrain surrounding Tower T3 in Hurricane Isabel at Frisco, North Carolina

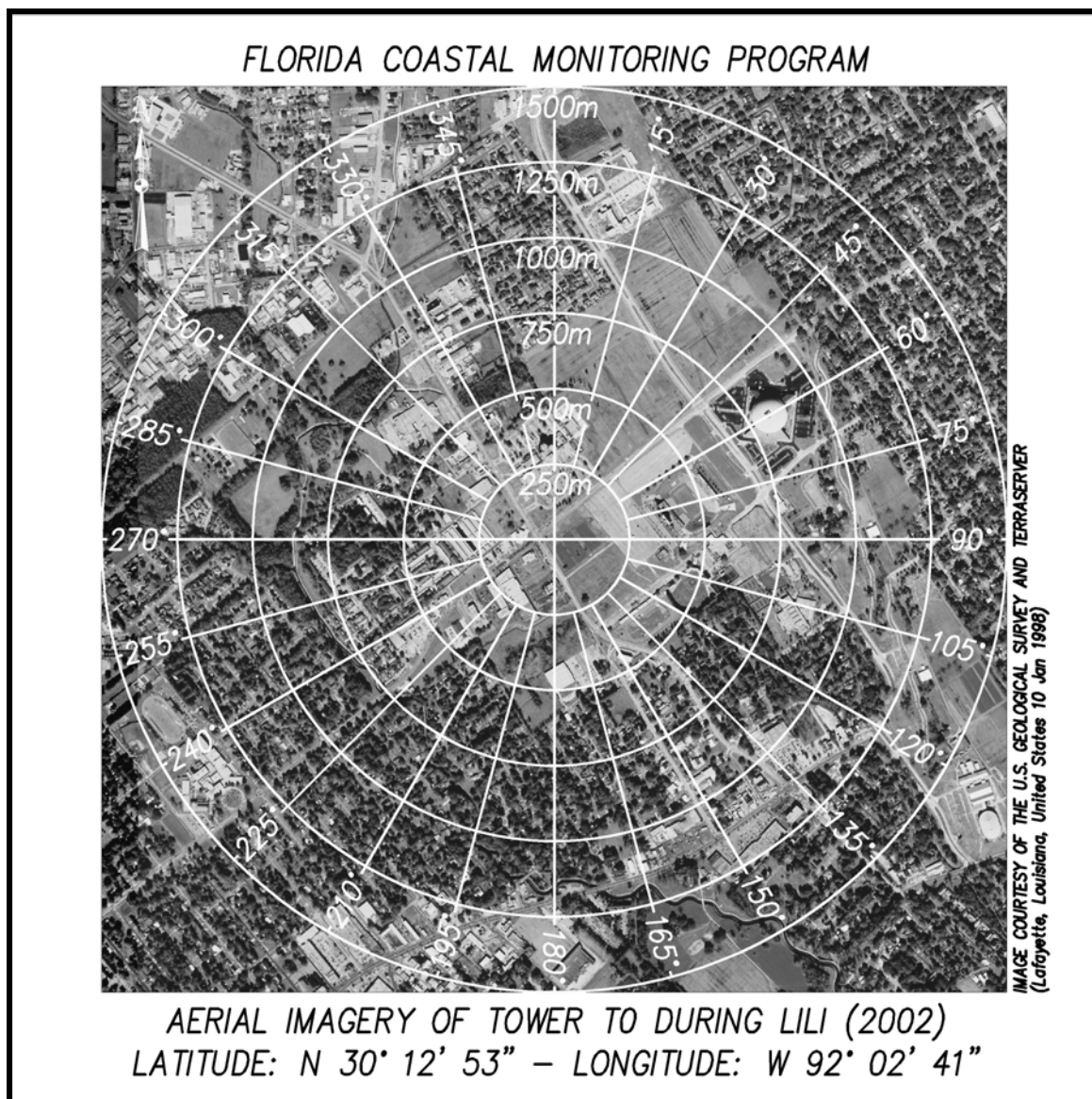


Figure B-5. Aerial Imagery of the terrain surrounding Tower T0 in Hurricane Lili at Lafayette, Louisiana

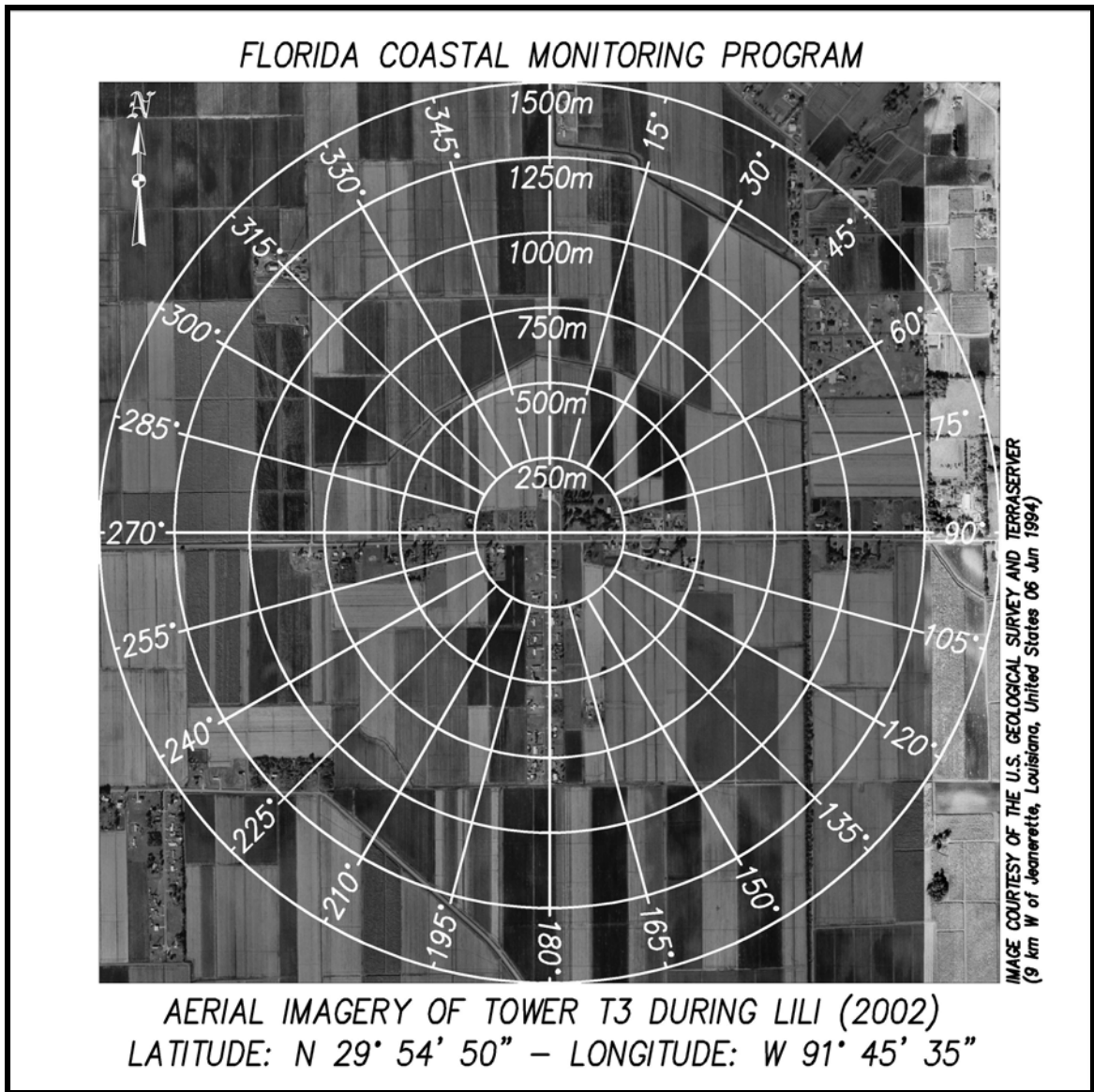


Figure B-6. Aerial Imagery of the terrain surrounding Tower T3 in Hurricane Lili at Lydia, Louisiana

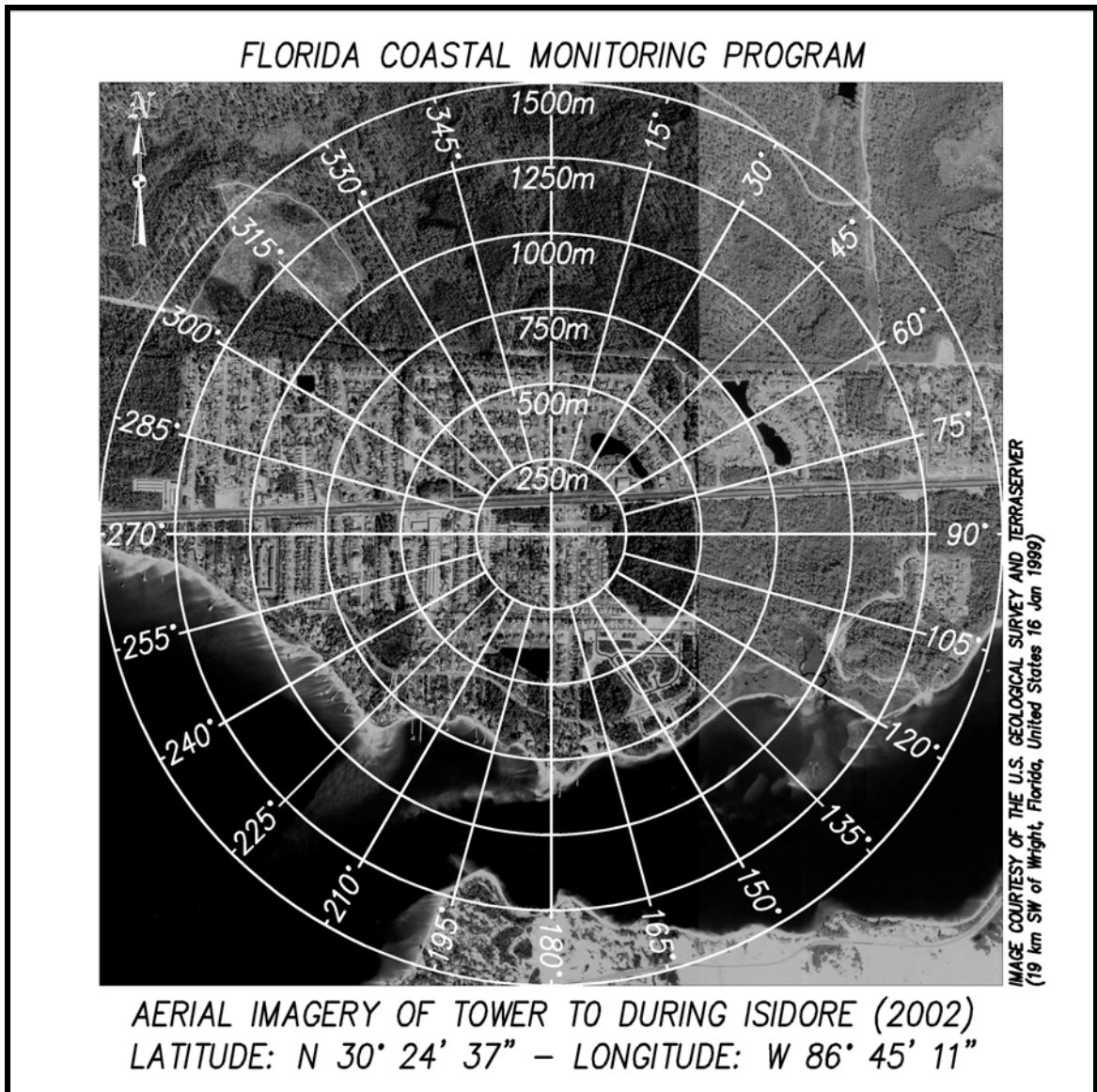


Figure B-7. Aerial Imagery of the terrain surrounding Tower T0 in Tropical Storm Isidore at Mary Esther, Florida

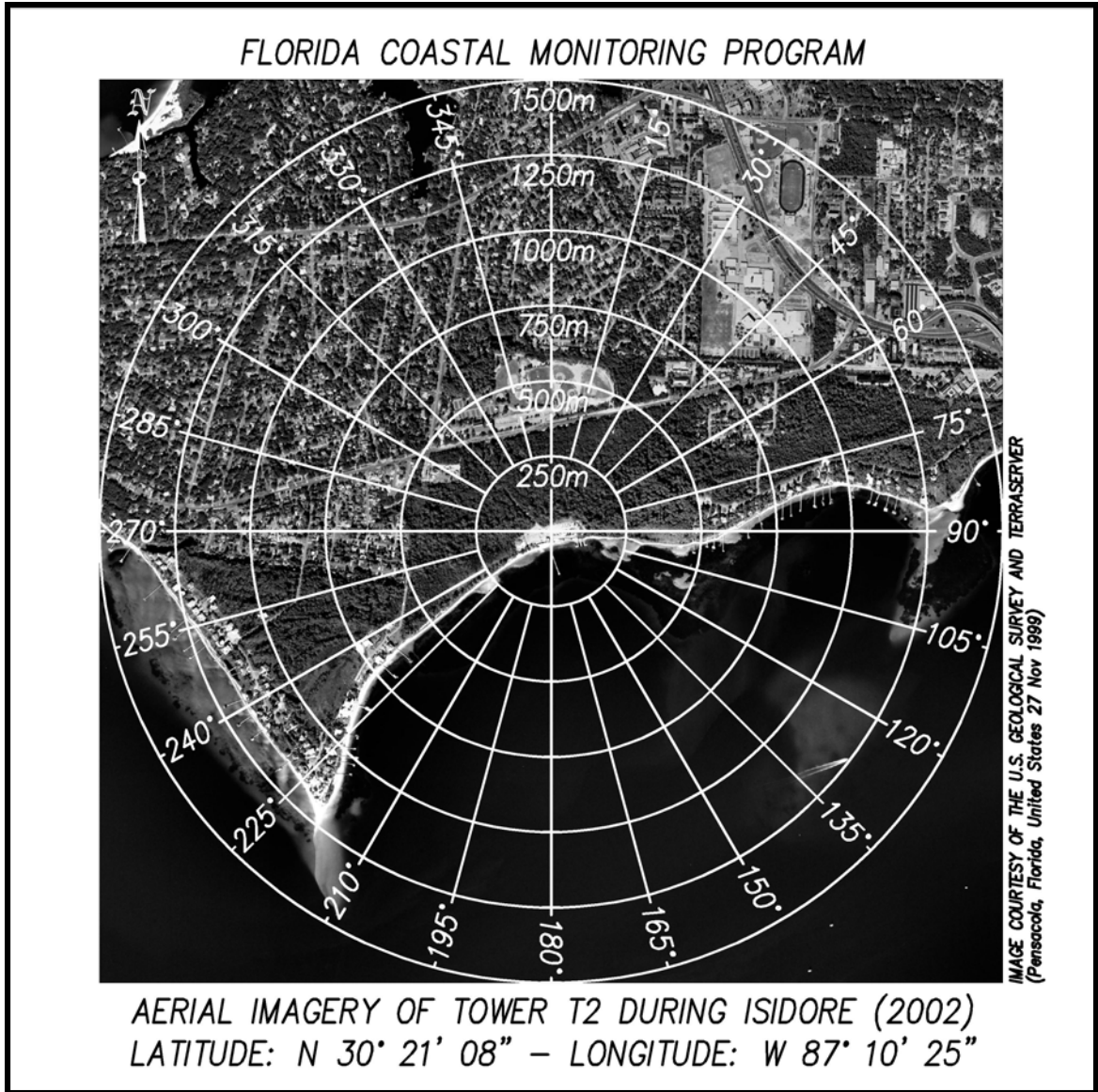


Figure B-8. Aerial Imagery of the terrain surrounding Tower T2 in Tropical Storm Isidore at Gulf Breeze, Florida

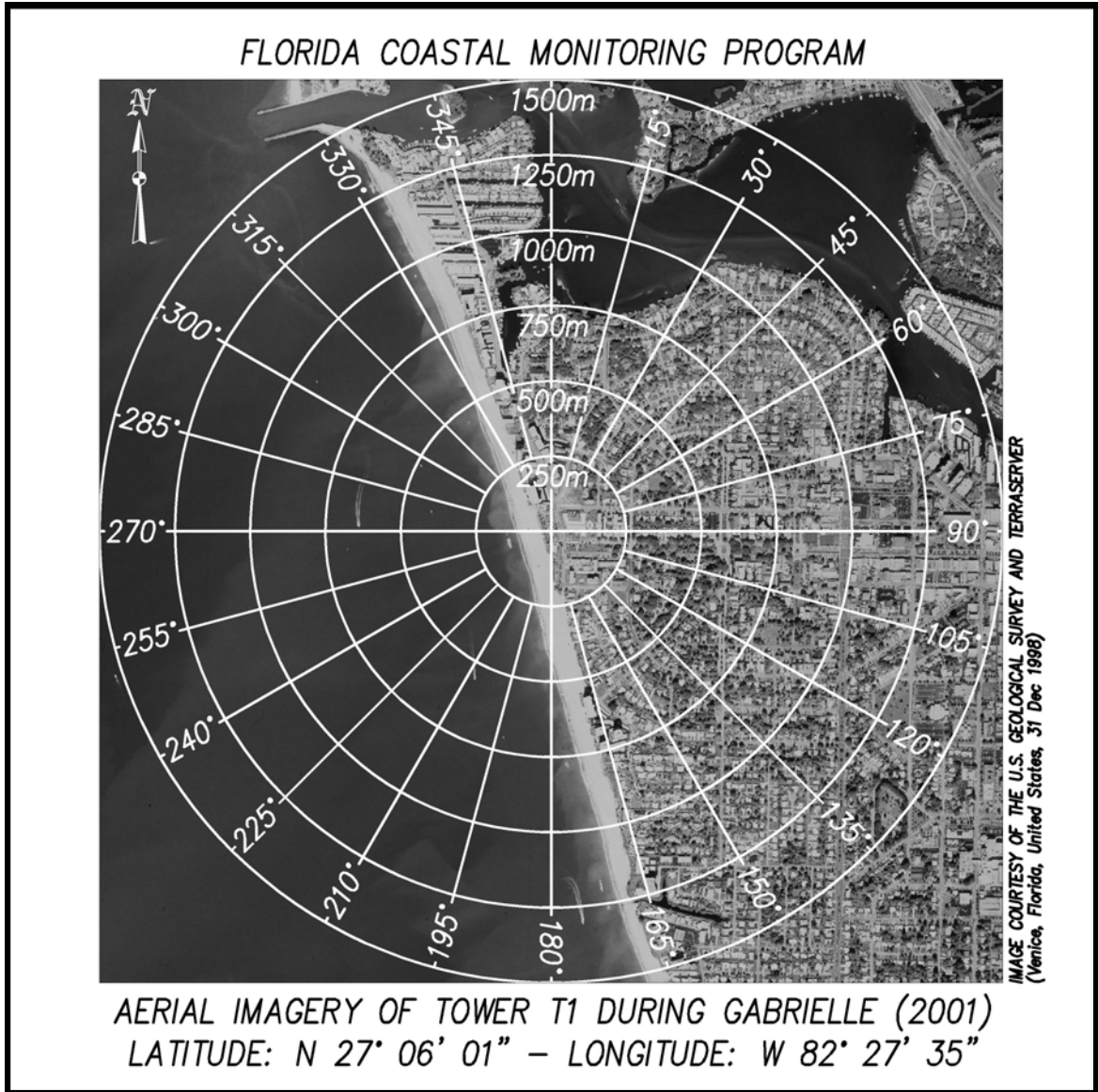


Figure B-9. Aerial Imagery of the terrain surrounding Tower T1 in Tropical Storm Gabrielle at Venice Beach, Florida

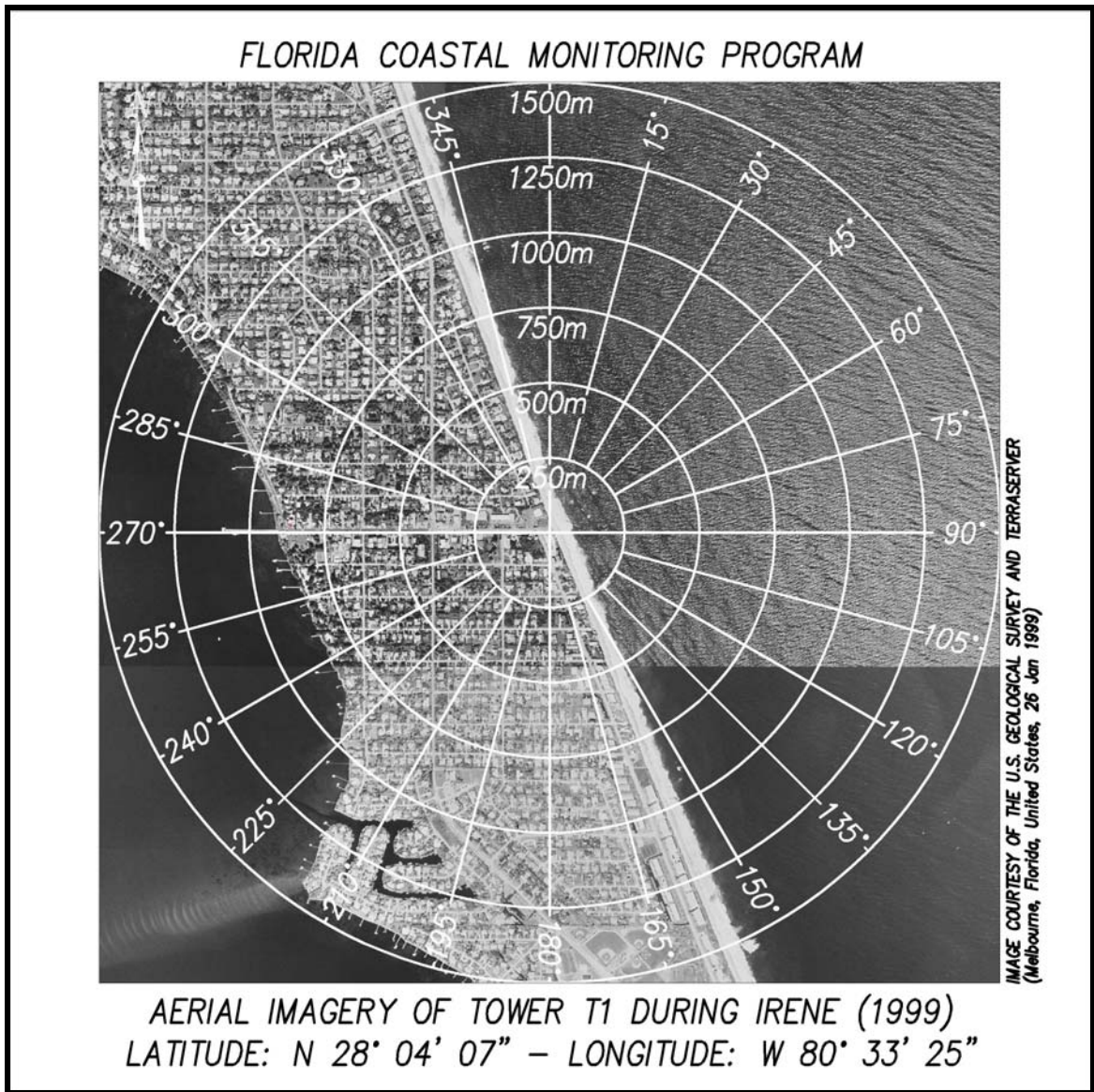


Figure B-10. Aerial Imagery of the terrain surrounding Tower T1 in Tropical Storm Irene at Melbourne Beach, Florida

APPENDIX C
RESULTS FROM PRESSURE TAP SIMULATION OF UWO WIND TUNNEL DATA

This appendix contains the peak pressure coefficients measured from experimental and simulated data for the 12 simulation cases listed in Chapter 6.

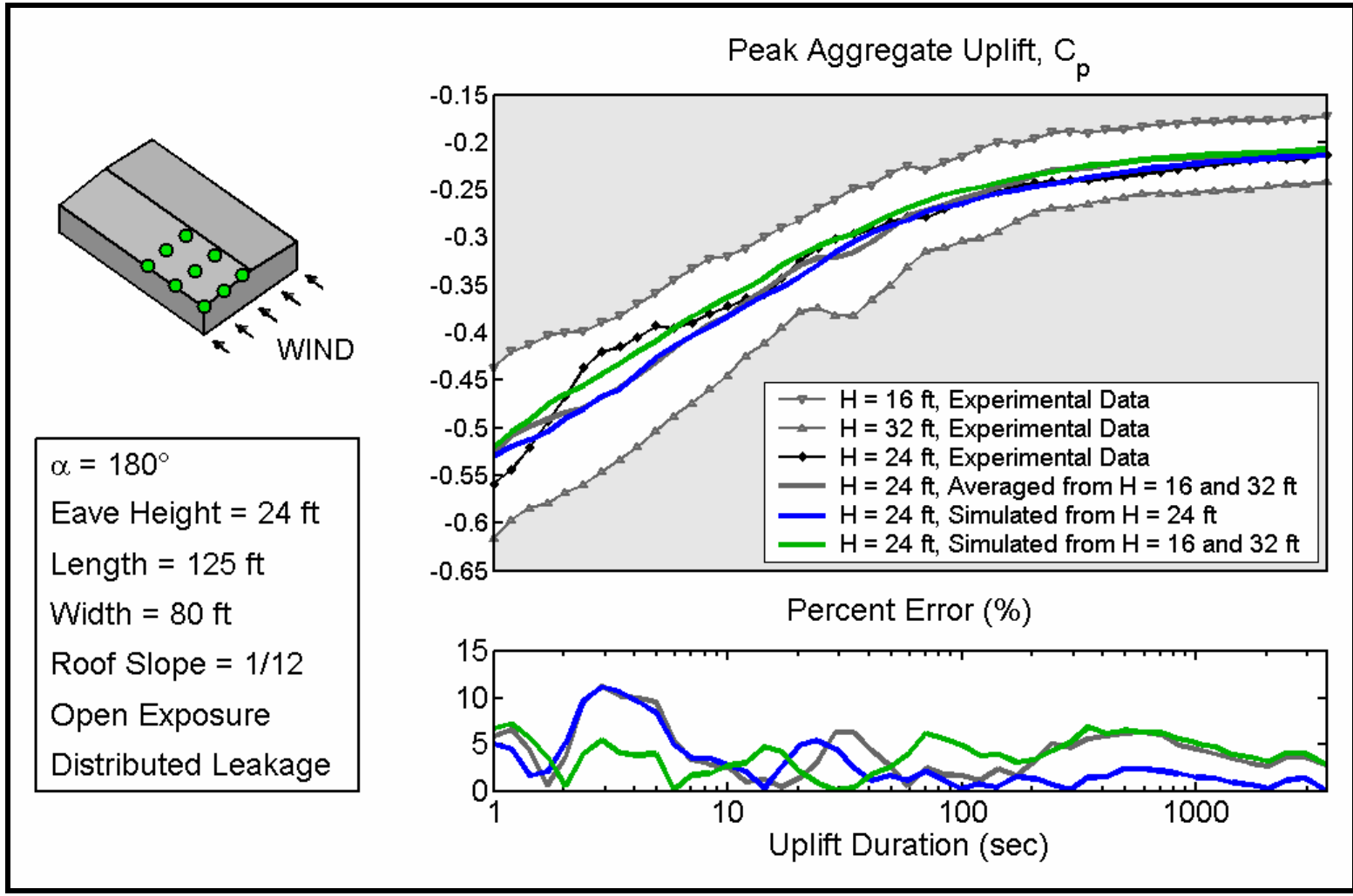


Figure C-1. Comparison of direct and interpolated simulated peak aggregate uplifts to wind tunnel data and simple averaging for winds parallel to the ridgeline on a 125 X 80 ft gable end building with a 24 ft eave height

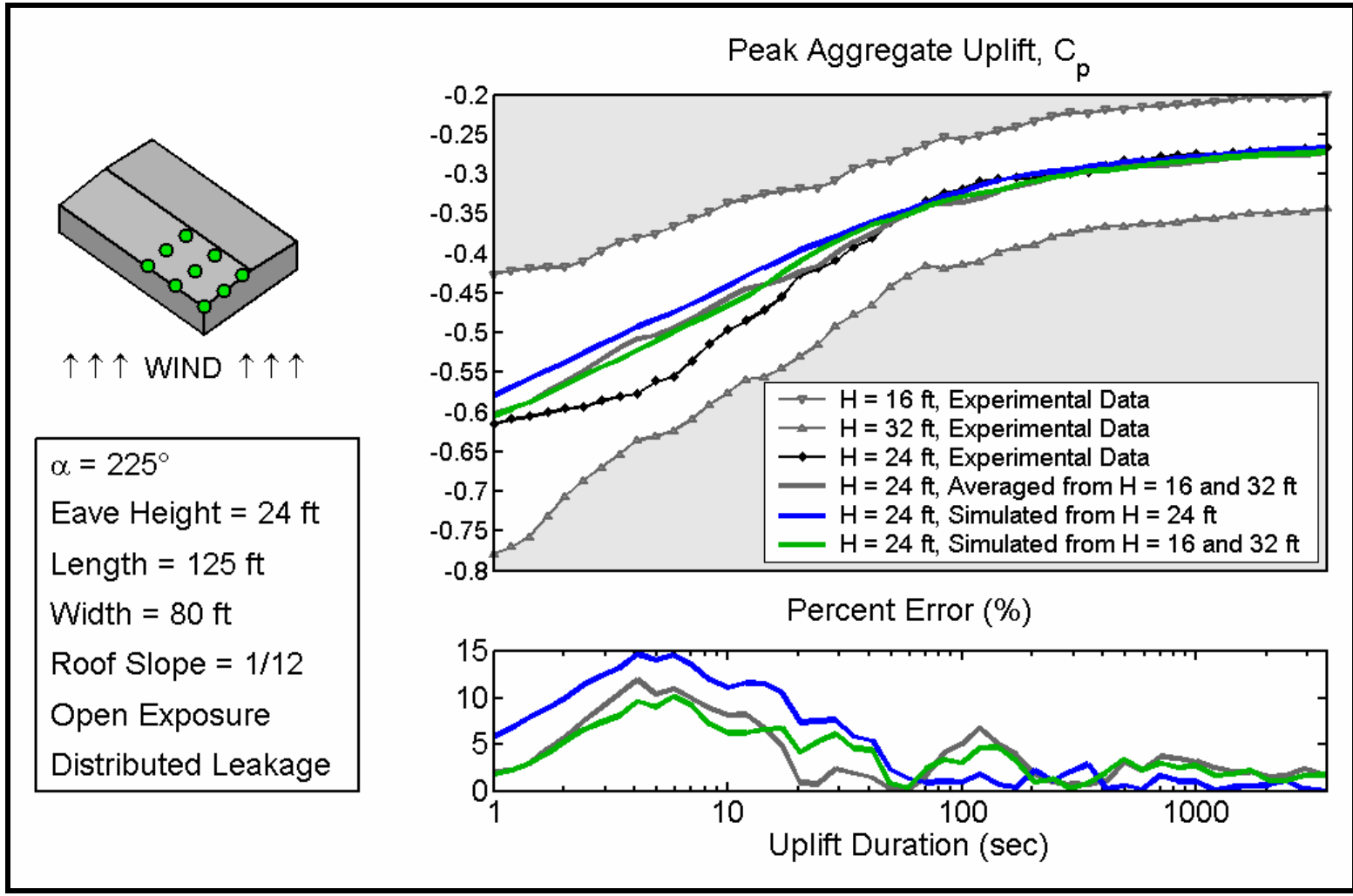


Figure C-2. Comparison of direct and interpolated simulated peak aggregate uplifts to wind tunnel data and simple averaging for cornering winds on a 125 X 80 ft gable end building with a 24 ft eave height

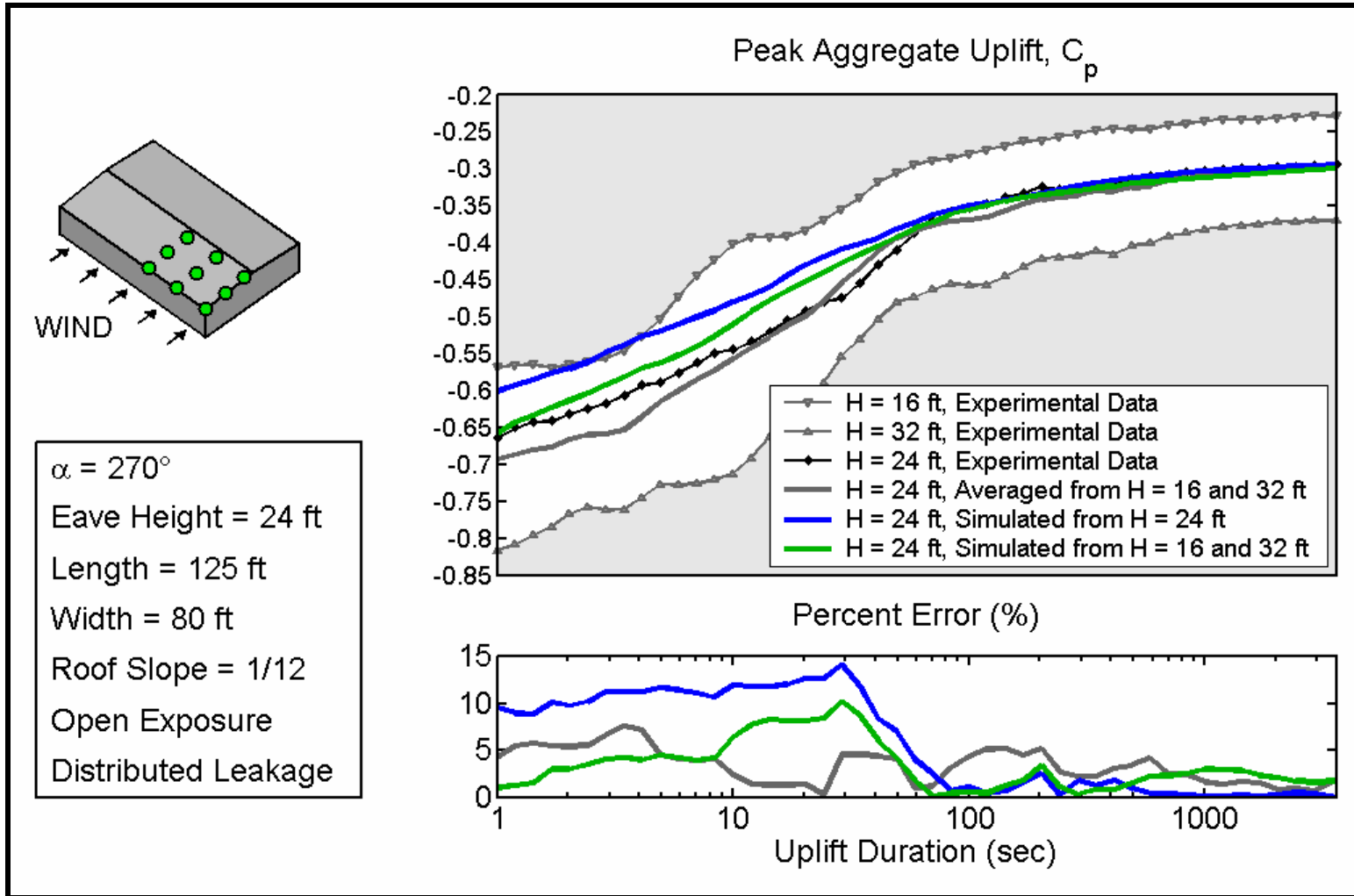


Figure C-3. Comparison of direct and interpolated simulated peak aggregate uplifts to wind tunnel data and simple averaging for winds perpendicular to the ridgeline on a 125 X 80 ft gable end building with a 24 ft eave height

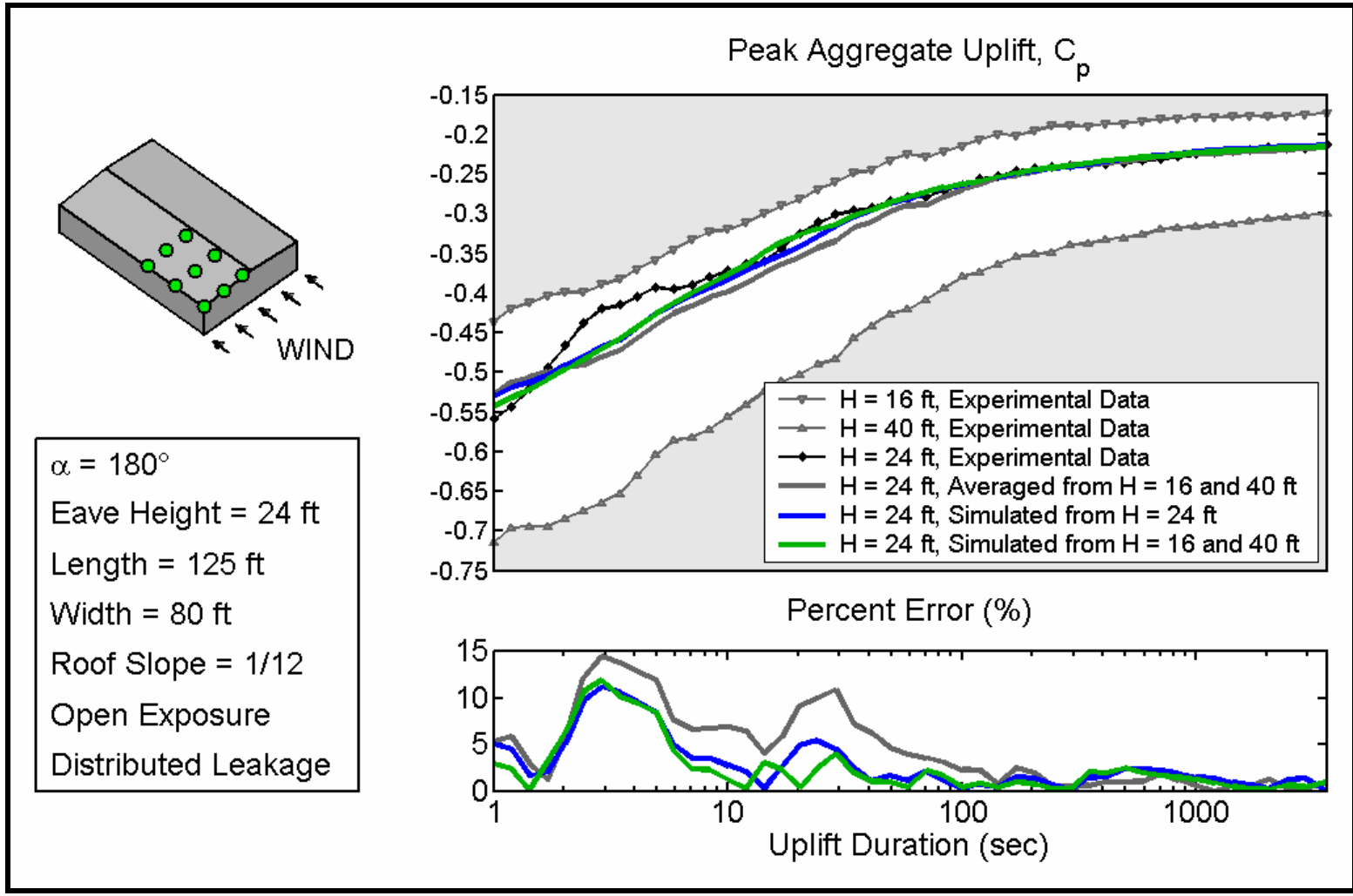


Figure C-4. Comparison of direct and interpolated simulated peak aggregate uplifts to wind tunnel data and simple averaging for winds parallel to the ridgeline on a 125 X 80 ft gable end building with a 24 ft eave height

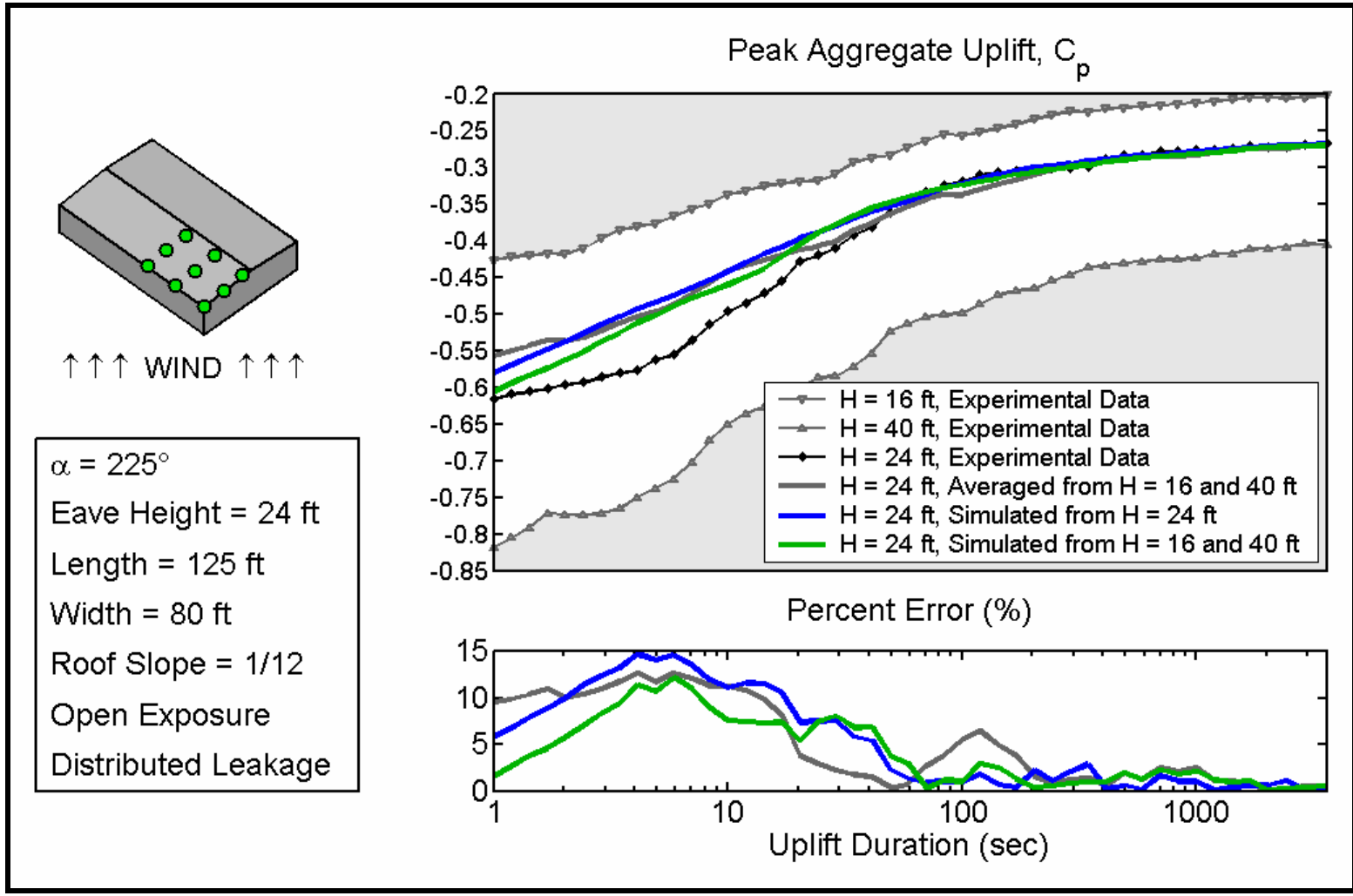


Figure C-5. Comparison of direct and interpolated simulated peak aggregate uplifts to wind tunnel data and simple averaging for cornering winds on a 125 X 80 ft gable end building with a 24 ft eave height

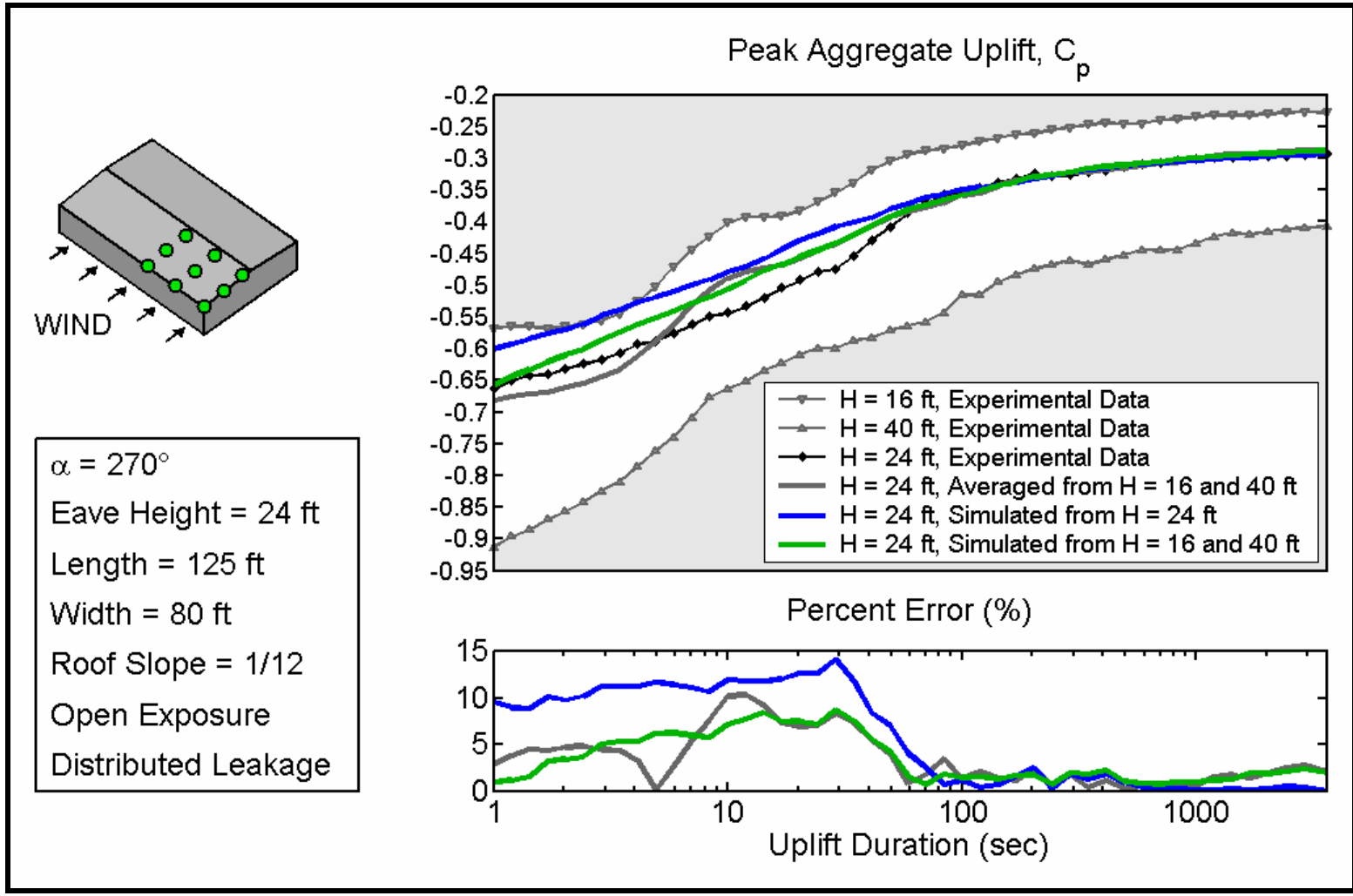


Figure C-6. Comparison of direct and interpolated simulated peak aggregate uplifts to wind tunnel data and simple averaging for winds perpendicular to the ridgeline on a 125 X 80 ft gable end building with a 24 ft eave height

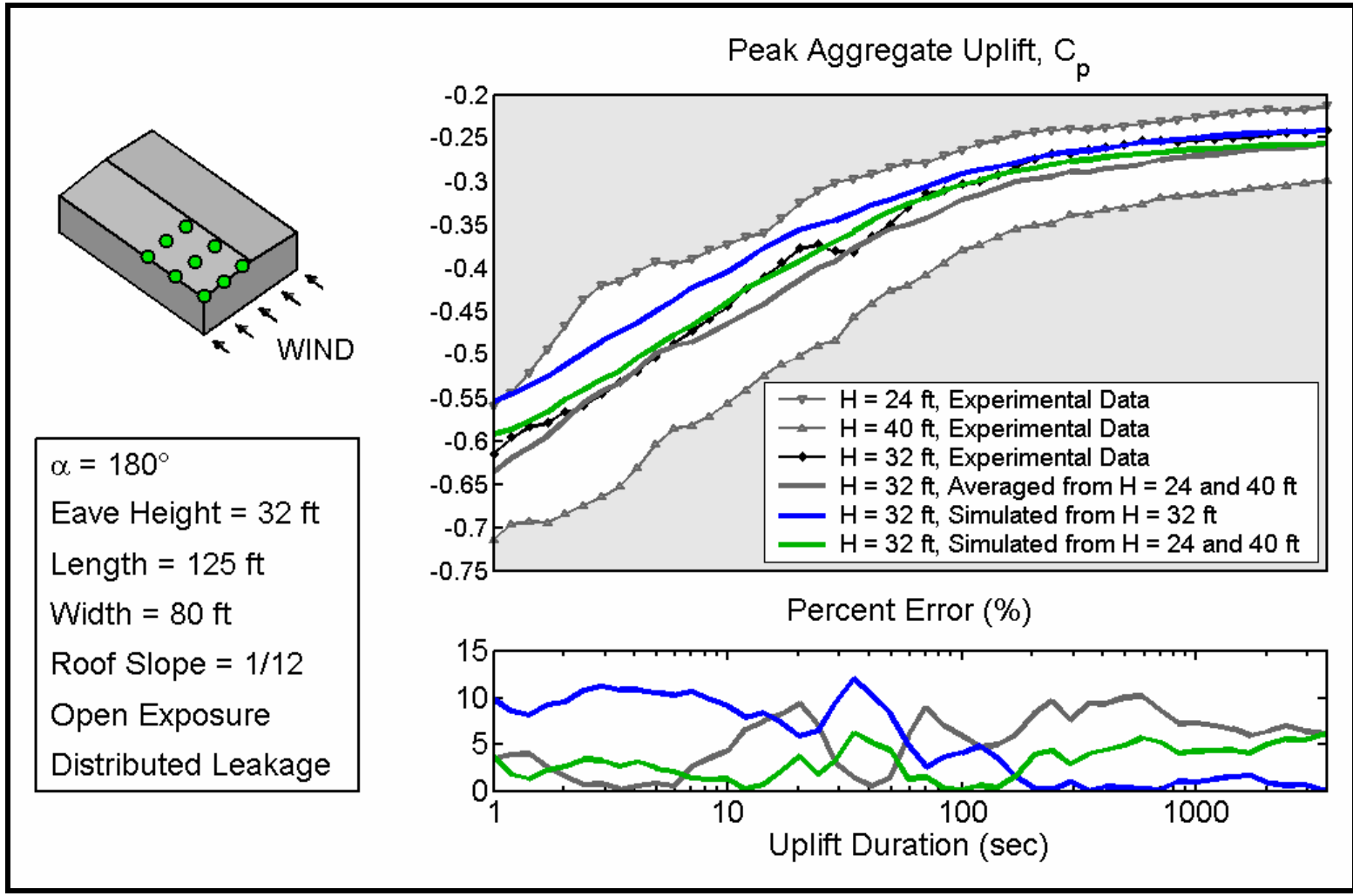


Figure C-7. Comparison of direct and interpolated simulated peak aggregate uplifts to wind tunnel data and simple averaging for winds parallel to the ridgeline on a 125 X 80 ft gable end building with a 32 ft eave height

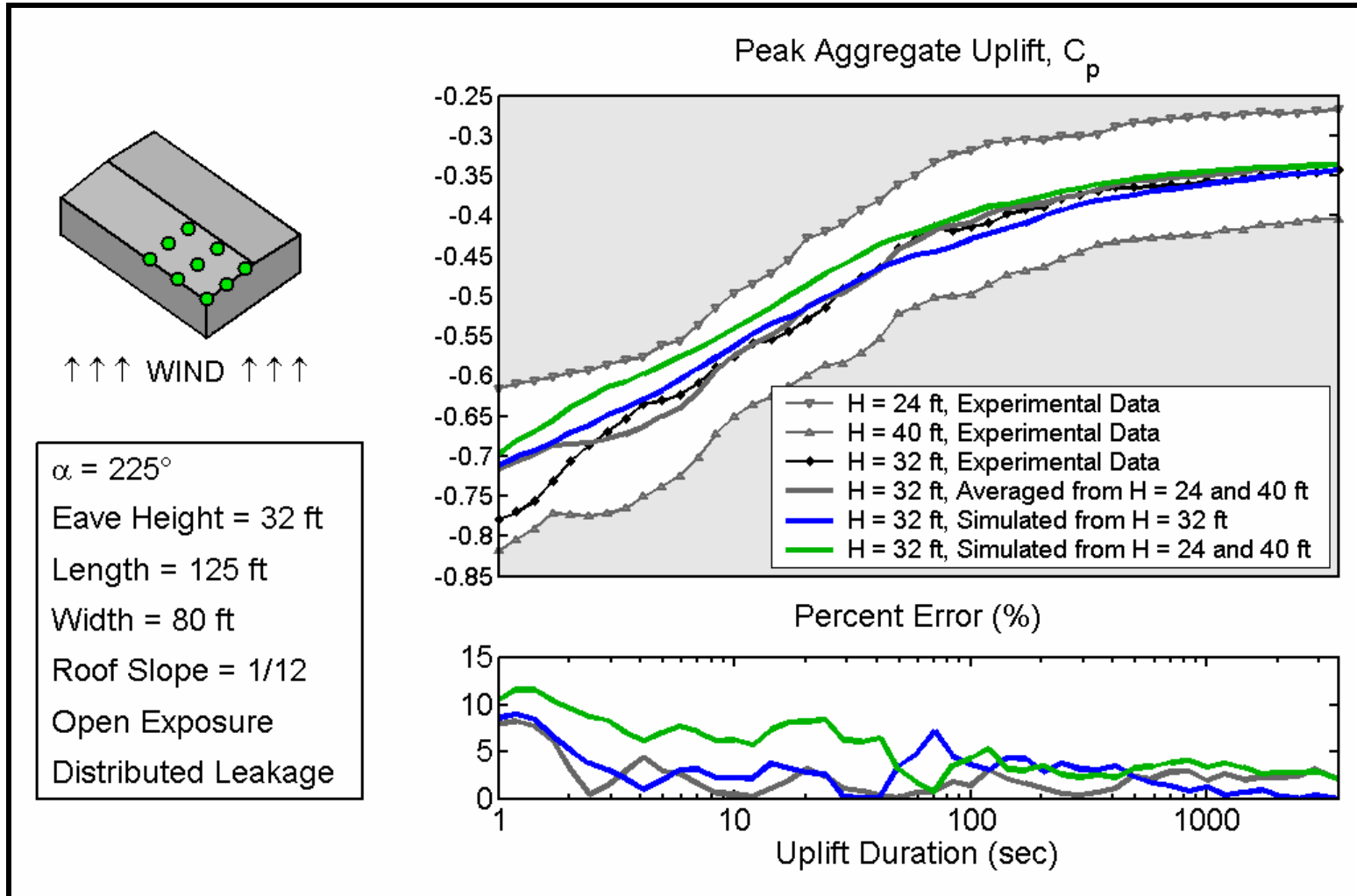


Figure C-8. Comparison of direct and interpolated simulated peak aggregate uplifts to wind tunnel data and simple averaging for cornering winds on a 125 X 80 ft gable end building with a 32 ft eave height

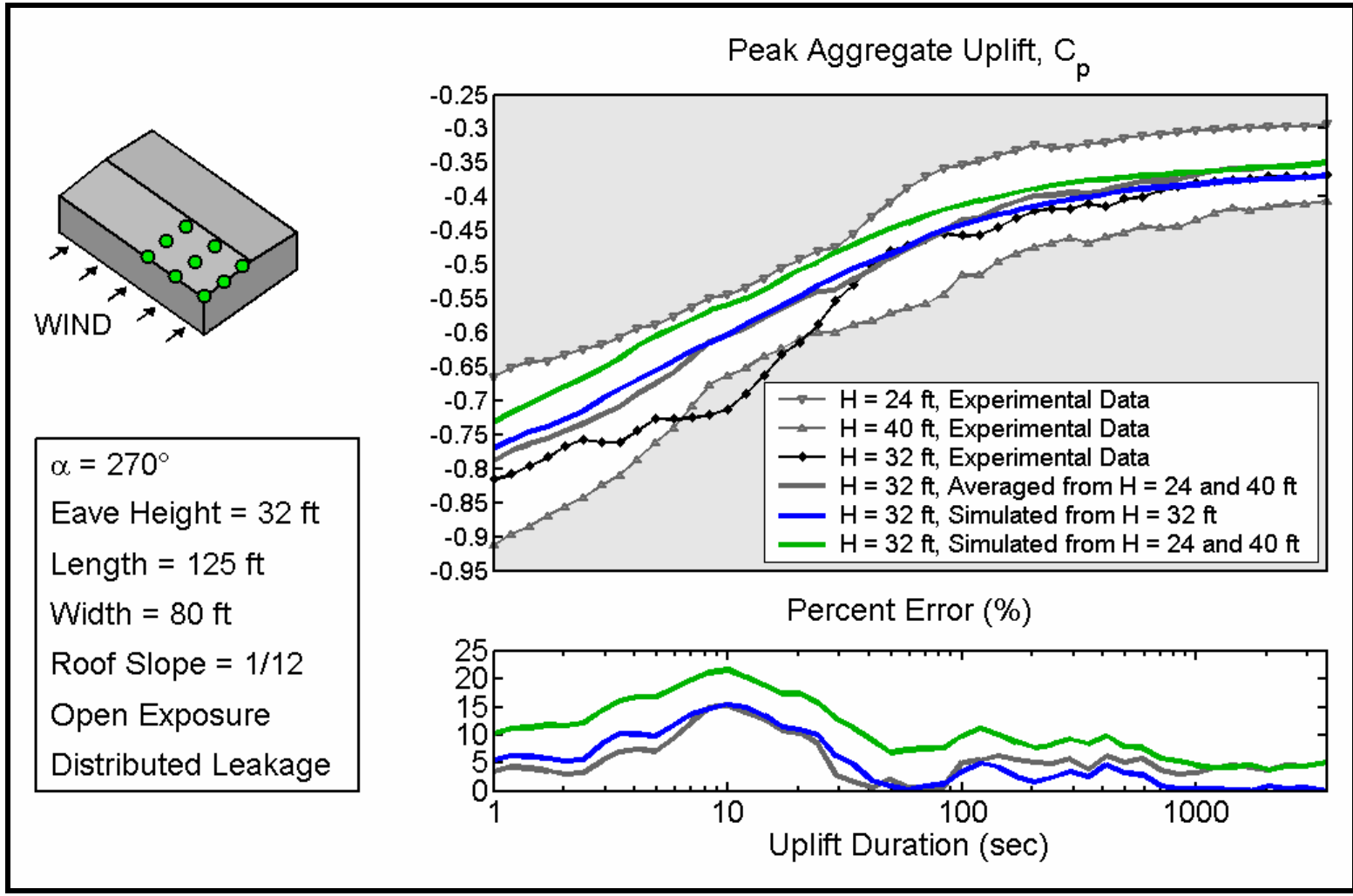


Figure C-9. Comparison of direct and interpolated simulated peak aggregate uplifts to wind tunnel data and simple averaging for winds perpendicular to the ridgeline on a 125 X 80 ft gable end building with a 32 ft eave height

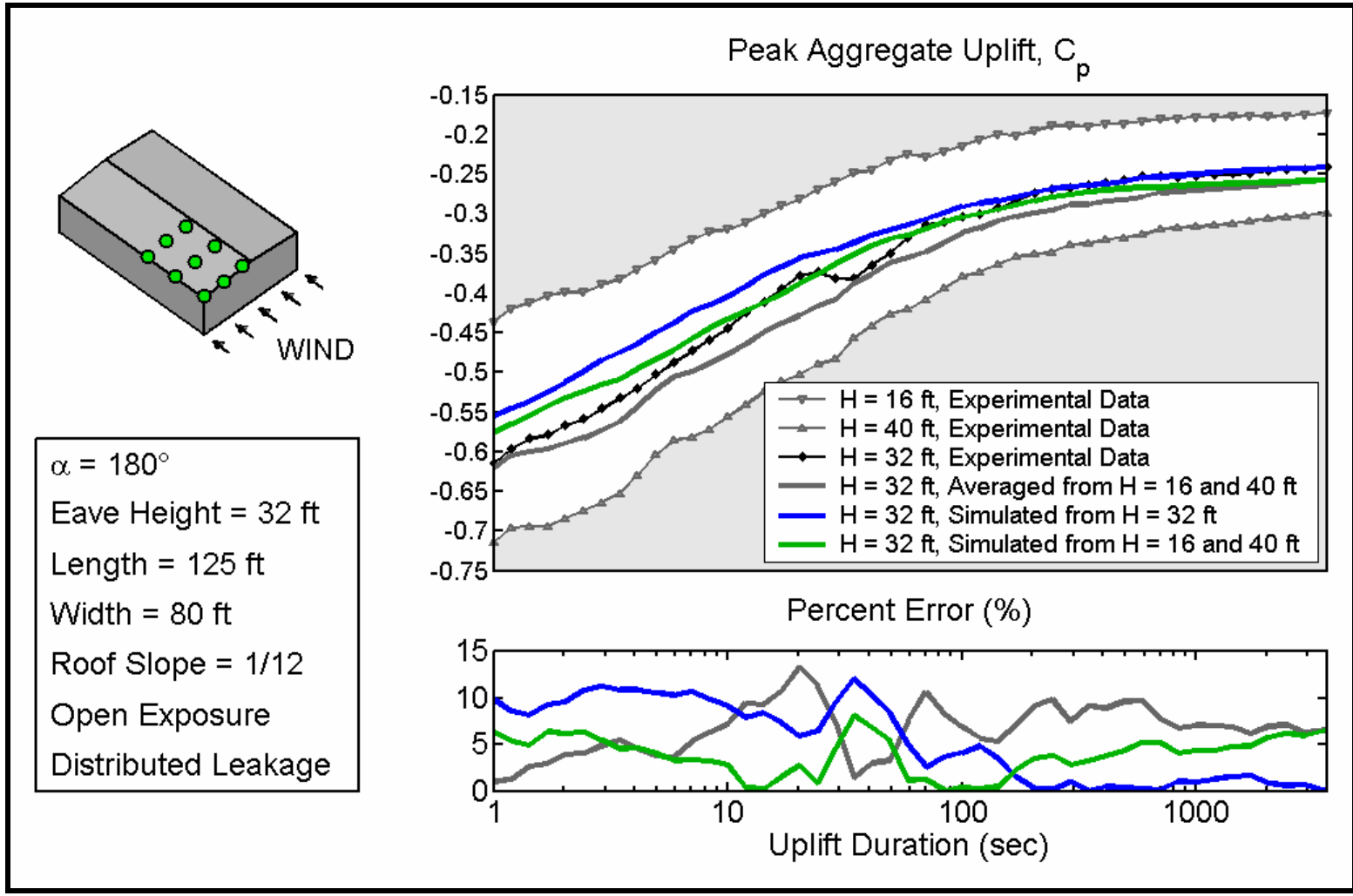


Figure C-10. Comparison of direct and interpolated simulated peak aggregate uplifts to wind tunnel data and simple averaging for winds parallel to the ridgeline on a 125 X 80 ft gable end building with a 32 ft eave height

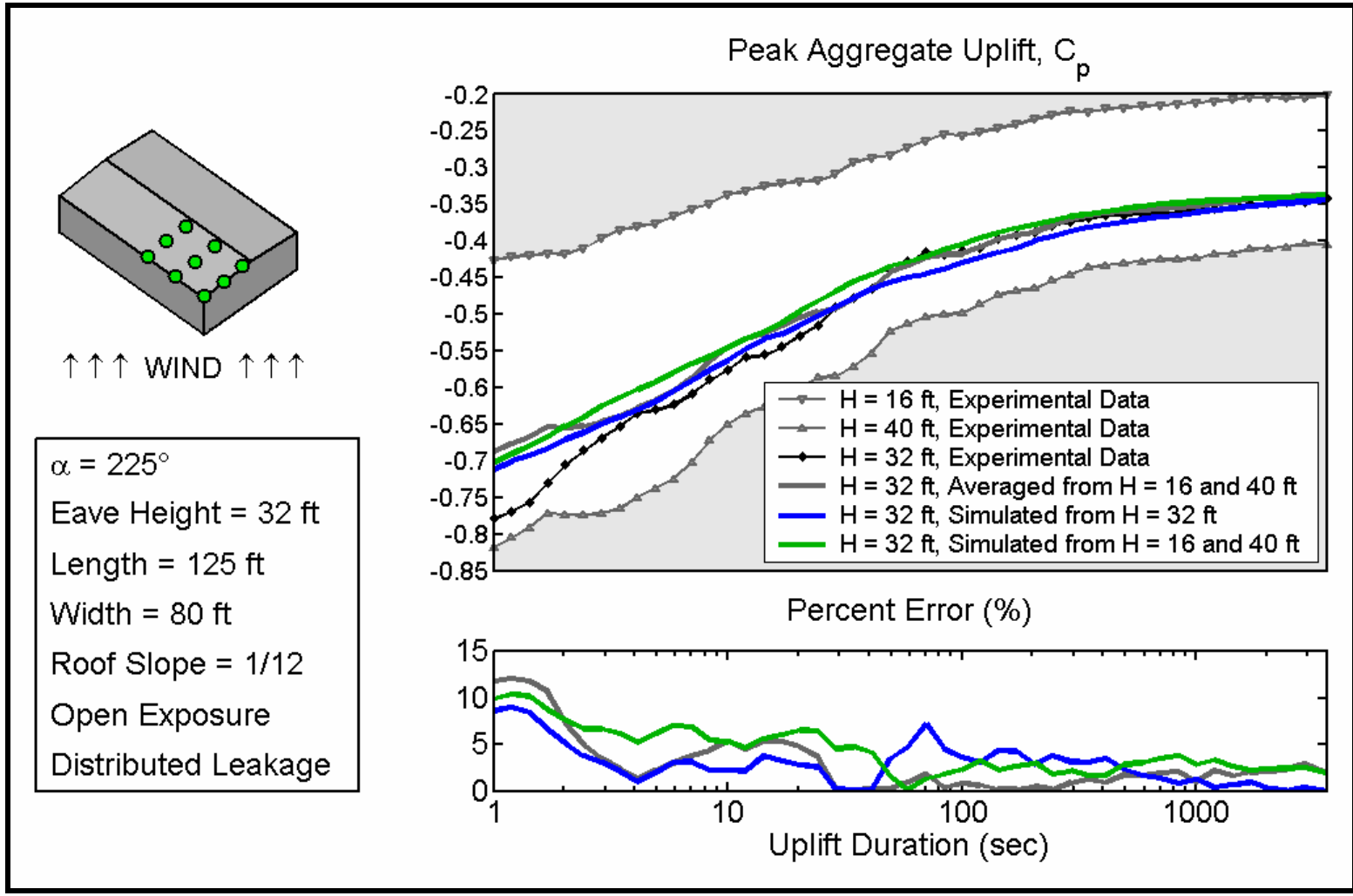


Figure C-11. Comparison of direct and interpolated simulated peak aggregate uplifts to wind tunnel data and simple averaging for cornering winds on a 125 X 80 ft gable end building with a 32 ft eave height

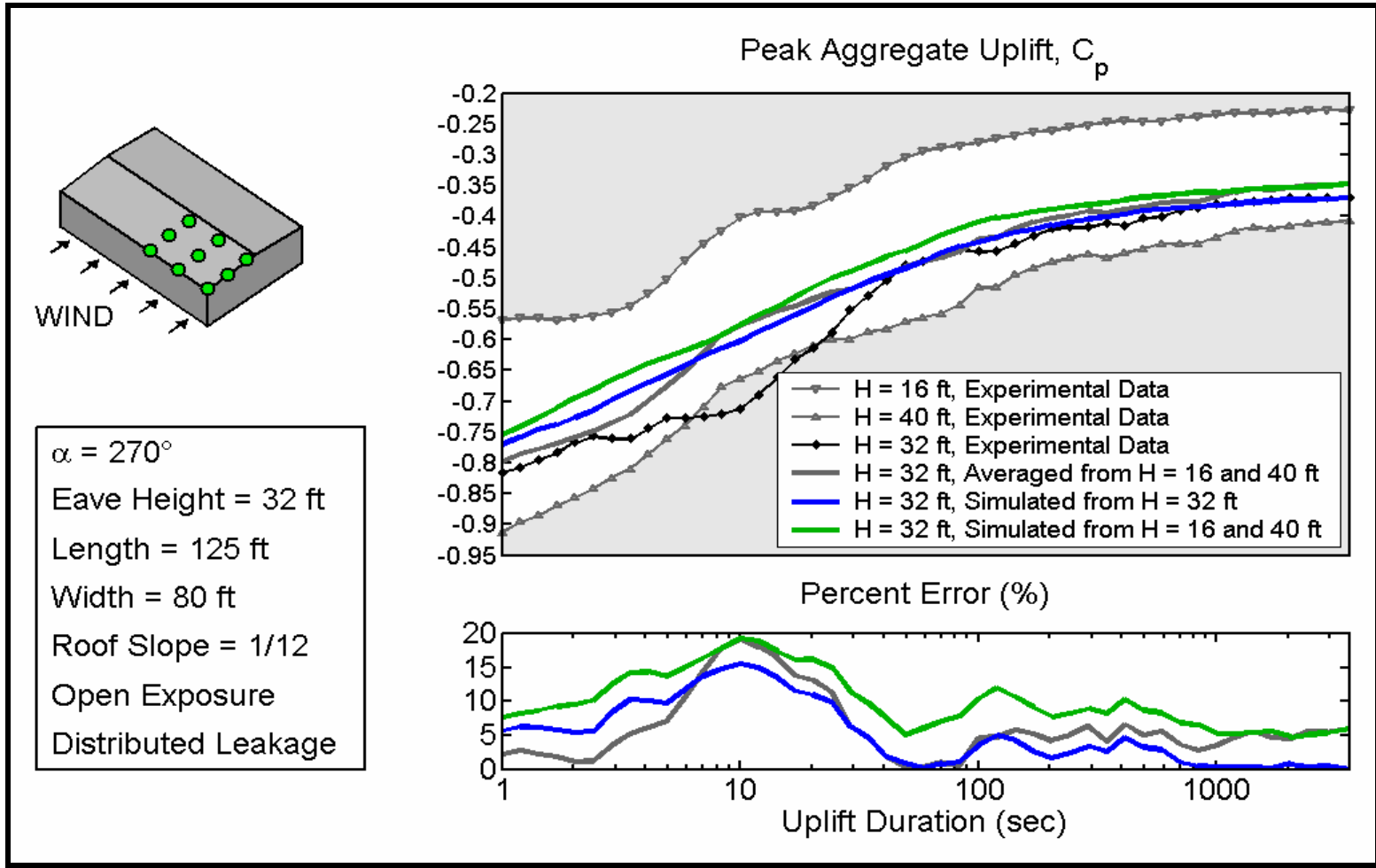


Figure C-12. Comparison of direct and interpolated simulated peak aggregate uplifts to wind tunnel data and simple averaging for winds perpendicular to the ridgeline on a 125 X 80 ft gable end building with a 32 ft eave height

LIST OF REFERENCES

- ASCE 7-02 (2002). Minimum design loads for buildings and other structures. American Society of Civil Engineers, Reston, VA.
- Aponte, L (2004). "Measurement, Validation and Dissemination of Hurricane Wind Data." Masters Report, University of Florida, Department of Civil and Coastal Engineering.
- Barnes, J. (1998). Florida's hurricane history. Chapel Hill, University of North Carolina Press.
- Bendat, J. S. and A. G. Piersol (2000). Random data: analysis and measurement procedures. New York, Wiley.
- Borgman, L. E. (1990). Irregular ocean waves: Kinematics and forces: the sea. B. LeMehaute and D. M. Hanes, John Wiley and Sons. 9: 121-167.
- Cai, G. Q. and Y. K. Lin (1996). "Generation of non-Gaussian stationary stochastic processes." Physical Review E 54(1): 299-303.
- Chen, Y., G.A. Kopp, and D. Surry (2003a), "Interpolation of Pressure Time Series in an Aerodynamic Database for Low Buildings," Journal of Wind Engineering and Industrial Aerodynamics 91: 737-765.
- Chen, Y., G.A. Kopp, and D. Surry (2003b), "The Use of Linear Stochastic Estimation for the Reduction of Data in the NIST Aerodynamic Database," Journal of Wind and Structures 6(2): 107-126.
- Cook, N. J. (1985). The designer's guide to wind loading of building structures. London, Building Research Establishment Department of the Environment
- Cope, A. and R. Gurley (2001). "Spatial characteristics of pressure coefficients on low rise gable structures." The 1st America's Conference on Wind Engineering, Clemson University, Clemson, SC, June 4-6, 2001.
- Counihan, J. (1975). "Adiabatic atmospheric boundary layers - review and analysis of data from period 1880-1972." Atmospheric Environment 9(10): 871-905.
- Davenport, A. G. (1961). "The spectrum of horizontal gustiness near the ground in high winds." Quarterly Journal of the Royal Meteorological Society 87(372): 194-211.

- Davenport, A. G. and J. M. Stagg (1962). "The spectrum of horizontal gustiness near the ground in high winds." *Quarterly Journal of the Royal Meteorological Society* 88(376): 197-198.
- Dearheart, E. A. (2003). Comparison of field and model wind pressures on residential buildings in tropical storm winds. Civil Engineering Department. Clemson, SC, Clemson University.
- Deodatis, G. and R. C. Micaletti (2001). "Simulation of highly skewed non-Gaussian stochastic processes." *ASCE Journal of Engineering Mechanics* 127(12): 1284-1295.
- Durst, C. S. (1960). "Wind speeds over short periods of time." *The Meteorological Magazine* 89: 181-186.
- Dyrbye, C. and S. O. Hansen (1999). *Wind loads on structures*. New York, Wiley.
- Eurocode (1994). *Basis of design and actions on structures..* Commission of the European Communities, Brussels, Belgium.
- Elishakoff, I., Y. J. Ren and M. Shinozuka (1994). "Conditional simulation of non-Gaussian random-fields." *Engineering Structures* 16(7): 558-563.
- FBC (2003). *Florida Building Code*. State of Florida Department of Community Affairs, <http://www.floridabuilding.org/>.
- Forristall, G. Z. (1988). "Wind spectra and gust factors over water." *Offshore Technology Conference*, Houston, TX.
- Franklin, J. L., M. L. Black, and K. Valde (2000). "Eyewall Wind Profiles in Hurricanes Determined By GPS Dropwindsondes." NOAA Tropical Prediction Center. <http://www.nhc.noaa.gov/aboutwindprofile.shtml>.
- Gioffre, M., V. Gusella and M. Grigoriu (2001). "Non-Gaussian wind pressure on prismatic buildings II: Numerical simulation." *ASCE Journal of Structural Engineering* 127(9): 990-995.
- Gray, W. M. and P. J. Klotzbach (2003). "Extended range forecast of Atlantic seasonal hurricane activity and US landfall strike probability for 2004." Fort Collins, CO, Department of Atmospheric Science, Colorado State University.
- Grigoriu, M. (2001). "A class of non-Gaussian processes for Monte Carlo simulation." *Journal of Sound and Vibration* 246(4): 723-735.
- Grigoriu, M. (1984). "Crossings of non-Gaussian translation processes." *ASCE Journal of Engineering Mechanics* 110(4): 610-620.

- Grigoriu, M. (1993). "On the spectral representation method in simulation." *Probabilistic Engineering Mechanics* 8(2): 75-90.
- Grigoriu, M. (1995). "Probabilistic models and simulation methods for seismic ground acceleration." *Meccanica* 30(1): 105-124.
- Grigoriu, M. (1998). "Simulation of stationary non-Gaussian translation processes." *Journal of Engineering Mechanics-Asce* 124(2): 121-126.
- Gurley, K. and A. Kareem (1997). "Analysis interpretation modeling and simulation of unsteady wind pressure data." *Journal of Wind Engineering and Industrial Aerodynamics* 71: 657-669.
- Gurley, K. and A. Kareem (1998a). "Simulation of correlated non-Gaussian pressure fields." *Meccanica* 33(3): 309-317.
- Gurley, K. and A. Kareem (1998b). "A Conditional Simulation of Non-Normal Velocity/Pressure Fields", *Journal of Wind Engineering and Industrial Aerodynamics*, 77-78, pp. 39-51, 1998.
- Gurley, K. R., M. A. Tognarelli and A. Kareem (1997). "Analysis and simulation tools for wind engineering." *Probabilistic Engineering Mechanics* 12(1): 9-31.
- Harris, R. I. (1990). "Some further thoughts on the spectrum of gustiness in strong winds." *Journal of Wind Engineering and Industrial Aerodynamics* 33(3): 461-477.
- Hartwig, R. (2003). *Facts and statistics: catastrophes*.
<http://www.iii.org/media/facts/statsbyissue/catastrophes/>, Insurance Information Institute.
- Hinrichsen, D. (1999). "The coastal population explosion." Coastal Trends Workshop, NOAA's State of the Coast Project.
- Hoshiya, M., S. Noda and H. Inada (1998). "Estimation of conditional non-Gaussian translation stochastic fields." *ASCE Journal of Engineering Mechanics* 124(4): 435-445.
- IBC (2003). *International Building Code 2003*. International Code Council. Delmar Publishers, Kentucky.
- Ishizaki, H. (1983). "Wind profiles, turbulence intensities and gust factors for design in typhoon-prone regions." *Journal of Wind Engineering and Industrial Aerodynamics* 13(1-3): 55-66.
- Kaimal, J. C. and J. J. Finnigan (1994). *Atmospheric boundary layer flows*. New York, Oxford University Press.

- Kaimal, J. C., Y. Izumi, J. C. Wyngaard and R. Cote (1972). "Spectral characteristics of surface-layer turbulence." *Quarterly Journal of the Royal Meteorological Society* 98(417): 563-589.
- Kaplan, E. L. and P. Meier (1958). "Nonparametric-Estimation from Incomplete Observations." *Journal of the American Statistical Association* 53(282): 457-481.
- Krayer, W. R. and R. D. Marshall (1992). "Gust Factors Applied to Hurricane Winds." *Bulletin of the American Meteorological Society* 73(5): 613-617.
- Li, Y. S. and A. Kareem (1997). "Simulation of multivariate nonstationary random processes: Hybrid DFT and digital filtering approach." *Journal of Engineering Mechanics-Asce* 123(12): 1302-1310.
- Lynn, B. A. and T. Stathopoulos (1985). "Wind-induced fatigue on low metal buildings." *ASCE Journal of Structural Engineering* 111(4): 826-839.
- Masters, F. and K. Gurley (2003). "Non-Gaussian simulation: Cumulative distribution function map-based spectral correction." *ASCE Journal of Engineering Mechanics* 129(12): 1418-1428.
- Meade, C. and M. Abbott (2003). "Assessing Federal Research and Development for Hazard Loss Reduction", RAND Report, 2003.
- Merry, M. and H. A. Panofsky (1976). "Statistics of vertical motion over land and water." *Quarterly Journal of the Royal Meteorological Society* 102(431): 255-260.
- Noserale, D. (2001). "USGS talks about America's coastal crisis."
http://www.usgs.gov/public/press/public_affairs/press_releases/pr1516m.html,
United States Geological Survey.
- Peterson, E. W. (1969). "Modification of mean flow and turbulent energy by a change in surface roughness under conditions of neutral stability." *Quarterly Journal of the Royal Meteorological Society* 95(405): 561-575.
- Phoon, K. K., S. P. Huang and S. T. Quek (2002). "Simulation of second-order processes using Karhunen-Loeve expansion." *Computers & Structures* 80(12): 1049-1060.
- Popescu, R., G. Deodatis and J. H. Prevost (1998). "Simulation of homogeneous nonGaussian stochastic vector fields." *Probabilistic Engineering Mechanics* 13(1): 1-13.
- Poss, D. P. (2000). Design and evaluation of a mobile wind instrumentation tower for hurricane wind measurements. Civil Engineering Department. Clemson, SC, Clemson University.
- Priestly, M. B. (1967). "Power spectral analysis of non-stationary processes." *Journal of Sound and Vibration* 6(1): 86-97.

- Powell, M. D. (1993). "Wind measurement and archival under the Automated Surface Observing System (ASOS) - User concerns and opportunity for improvement." *Bulletin of the American Meteorological Society* 74(4): 615-623.
- Powell, M. D. and S. D. Aberson (2001). "Accuracy of United States tropical cyclone landfall forecasts in the Atlantic basin (1976-2000)." *Bulletin of the American Meteorological Society* 82(12): 2749-2767.
- Powell, M. D., T. A. Reinhold and R. D. Marshall (1999). "GPS sonde insights on boundary layer wind structure in hurricanes." The 10th Annual International Conference on Wind Engineering, Copenhagen, Denmark
- Powell, M. D., S. H. Houston and T. A. Reinhold (1996). "Hurricane Andrew's landfall in south Florida: Part 1. Standardizing measurements for documentation of surface wind fields." *Weather and Forecasting*. 11: 304-328.
- Rappaport, E. (1993). "Preliminary report: Hurricane Andrew." National Hurricane Center. <http://www.nhc.noaa.gov/1992andrew.html>.
- Schroeder, J. L. and D. A. Smith (2003). "Hurricane Bonnie wind flow characteristics as determined from WEMITE." *Journal of Wind Engineering and Industrial Aerodynamics* 91(6): 767-789.
- Solari, G. (1990). "A generalized definition of gust factor." *Journal of Wind Engineering and Industrial Aerodynamics* 36: 539-548.
- Rigato, A., P. Chang and E. Simiu (2001). "Database-assisted design, standardization, and wind direction effects." *ASCE Journal of Structural Engineering*. 127: 855-860.
- Sakamoto, S. and R. Ghanem (2002). "Polynomial chaos decomposition for the simulation of non-Gaussian nonstationary stochastic processes." *ASCE Journal of Engineering Mechanics* 128(2): 190-201.
- Sakamoto, S. and R. Ghanem (2002). "Simulation of multi-dimensional non-gaussian non-stationary random fields." *Probabilistic Engineering Mechanics* 17(2): 167-176.
- Scott, R. (2001). *In the wake of Tacoma : suspension bridges and the quest for aerodynamic stability*. Reston, Va, ASCE Press.
- Shinozuka, M. and C. M. Jan (1972). "Digital simulation of random processes and its applications." *Journal of Sound and Vibration* 25(1): 111-128.
- Shinozuka, M. (1971). "Simulation of multivariate and multidimensional random processes." *Journal of the Acoustical Society of America*. 49: 357-367.

- Shinozuka, M. and G. Deodatis (1996). "Simulation of multi-dimensional Gaussian stochastic fields by spectral representation." *ASME Applied Mechanics Review* 49(1): 29-53.
- Shinozuka, M. and G. Deodatis (1991). "Simulation of stochastic processes by spectral representation." *ASME Applied Mechanics Review* 44(4): 191-203.
- Simiu, E. and N. A. Heckert (1998). "Wind direction and hurricane-induced ultimate wind loads." *Journal of Wind Engineering and Industrial Aerodynamics* 74-76: 1037-1046.
- Simiu, E. and R. H. Scanlan (1996). *Wind effects on structures : fundamentals and applications to design*. New York, John Wiley.
- Simpson, R. H. and H. Riehl (1981). *The hurricane and its impact*. Louisiana State University Press.
- Tieleman, H. W. (1995). "Universality of velocity spectra." *Journal of Wind Engineering and Industrial Aerodynamics* 56(1): 55-69.
- van der Hoven, I. (1957). "Power spectrum of horizontal wind speed in the frequency range from 0.0007 to 900 cycles per hour." *Journal of Meteorology* 14(2): 160-164.
- Vanmarcke, E. H. and G. A. Fenton (1991). "Conditioned simulation of local fields of earthquake ground motion." *Structural Safety* 10(1-3): 247-264.
- Von Kármán, T. (1948). "Progress in the statistical theory of turbulence." *Proceedings of the National Academy of Sciences of the United States of America* 34(11): 530-539.
- Xu, Y. L. (1996). "Wind-induced fatigue loading and damage to hip and gable roof claddings." *ASCE Journal of Structural Engineering*: 122(12): 1475-1483.
- Weber, R. O. (1999). "Remarks on the definition and estimation of friction velocity." *Boundary-Layer Meteorology* 93: 197-209.
- Welch, P. D. (1967). "Use of fast Fourier transform for estimation of power spectra - a method based on time averaging over short modified periodograms." *IEEE Transactions on Audio and Electroacoustics* AU-15(2): 70.
- Wieringa, J. (1993). "Representative roughness parameters for homogeneous terrain." *Boundary-Layer Meteorology* 63(4): 323-363.
- Williams, J. (2003). "City database for hurricane landfalls." <http://www.hurricanecity.com/cities.htm>.

- Wittig, L. E. and A. K. Sinha (1975). "Simulation of multicorrelated random processes using FFT algorithm." *Journal of the Acoustical Society of America* 58(3): 630-634.
- Zemen, O. and N. O. Jensen (1987). "Modification of turbulence characteristics in flow over hills." *Quarterly Journal of the Royal Meteorological Society* 113: 55-80.
- Zhang, R. C. and G. Deodatis (1996). "Seismic ground motion synthetics of the 1989 Loma Prieta earthquake." *Earthquake Engineering & Structural Dynamics* 25(5): 465-481.

BIOGRAPHICAL SKETCH

Like the previous twelve generations of his family, Forrest James Masters was born in Saint Augustine, Florida, and from that day, April 8, 1977, to the summer after his graduation from Saint Joseph Academy in 1995, he remained there. In the fall semester of 1995, Masters matriculated into the University of Florida and with the encouragement of Dr. Marc Hoit and joined the Department of Civil and Coastal Engineering shortly thereafter.

During spring of his senior year (1999), Masters was approached by his future mentor, Dr. Kurtis Gurley, to pursue the research topics that would become the foundation of this dissertation. After graduating with high honors in December, he began graduate research and was accepted into the Ph.D. program in the spring of 2000. In the fall, he received a named university presidential fellowship, which supported him until his graduation in the summer of 2004. In addition to conducting wind engineering research at the University of Florida, Masters spent the summer of 2001 in Japan participating in earthquake engineering research under the guidance of Dr. Mitsumasa Midorikawa of the Building Research Institute in Tsukuba and Dr. Masayoshi Nakashima of the Disaster Research Prevention Institute in Kyoto.

Forrest James Masters is a student member of the American Association for Wind Engineering, the American Society of Civil Engineers, Chi Epsilon and Tau Beta Pi.